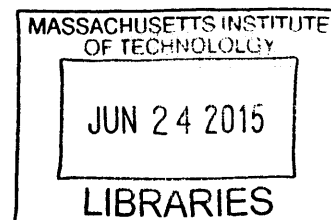


THE FUNCTIONALIZATION OF FULLERENES AND
NANOCARBON MATERIALS FOR PHOTOVOLTAICS
AND OTHER APPLICATIONS

by

GGOCH DDEUL HAN



B.S., Chemistry
Pohang University of Science and Technology, Republic of Korea, 2010

Submitted to the Department of Chemistry
in Partial Fulfillment of the Requirements for the Degree of

DOCTOR OF PHILOSOPHY IN CHEMISTRY

AT THE

MASSACHUSETTS INSTITUTE OF TECHNOLOGY

June 2015

© 2015 Massachusetts Institute of Technology. All rights reserved.

Signature redacted

Signature of Author

Department of Chemistry
May 15, 2015

Signature redacted

Certified by

U Timothy M. Swager
John D. MacArthur Professor of Chemistry
Thesis Supervisor

Signature redacted

Accepted by

Robert W. Field
Haslam and Dewey Professor of Chemistry
Chairman, Departmental Committee of Graduate Studies

This doctoral thesis has been examined by a Committee of the Department of Chemistry as follows:

Professor Mircea Dincă: **Signat̂ure redacted**
Chairman

Professor Timothy M. Swager: **Signature redacted**
Thesis Advisor

Professor Stephen J. Lippard: **Signature redacted**
Department of Chemistry

Dedicated to my family and friends

THE FUNCTIONALIZATION OF FULLERENES AND NANOCARBON MATERIALS FOR PHOTOVOLTAICS AND OTHER APPLICATIONS

by

GGOCH DDEUL HAN

Submitted to the Department of Chemistry
on May 15, 2015 in Partial Fulfillment of the
Requirements for the Degree of Doctor of Philosophy in
Chemistry

ABSTRACT

Fullerenes and other nanocarbon materials such as carbon nanotubes possess interesting chemical and physical properties. In this thesis, we explore various functionalization methods for nanocarbon materials and their potential applications in photovoltaics and fuel cells.

Chapter 1 gives an introduction to the chemistry and applications of fullerenes.

In Chapter 2, the syntheses of cyclobutadiene-functionalized fullerenes are described, and the influence of intramolecular π -interaction on the electronic energy of a molecule is explored. The fullerene derivatives are used as electron acceptors in bulk heterojunction organic photovoltaics with polymer donors.

In Chapter 3, a series of isobenzofulvene-functionalized fullerenes and their photovoltaic performances are presented. We demonstrate that these n-type materials can generate high open-circuit voltages in organic solar cells and produce higher power conversion efficiencies compared to those of standard devices.

In Chapter 4, we utilize fullerene derivatives for electron transport layers in perovskite solar cells. We explore the morphology and stability of fullerene films and demonstrate the fabrication of high performance photovoltaics under low-temperature ambient conditions.

In Chapter 5, we study the improvement of organic solar cell performances by the addition of aryne-functionalized fullerenes to active layers as a minority component.

In Chapter 6, we describe isoxazoline-functionalized fullerenes and carbon nanotubes and explore their transition metal complexes. Co(II) and Fe(II) complexes on carbon nanotubes are used for electrocatalytic oxygen reduction.

Thesis Supervisor: Timothy M. Swager

Title: John D. MacArthur Professor of Chemistry

CONTRIBUTIONS

For Chapter 2, W. R. Collins conducted the preliminary synthesis of fullerene adducts. T. L. Andrew performed device fabrication and characterization including atomic force microscopy (AFM).

For Chapter 3, A. Maurano fabricated devices and conducted AFM, optical characterization, and transient photovoltage-photocurrent measurement. J. G. Weis performed the synthesis of a precursor, 9-isopropylidenebenzonorbornadiene.

For Chapter 4, S. Chang made a major contribution to device fabrication and characterization including scanning electron microscopy. J. G. Weis performed AFM and the synthesis of a precursor, 9-isopropylidenebenzonorbornadiene. H. Park participated in the preliminary device fabrications. P. Mueller contributed to the acquisition of variable-temperature X-ray diffraction patterns.

For Chapter 5, A. Maurano made a major contribution to device fabrication and characterization including AFM. P. Mueller contributed to the acquisition of variable-temperature X-ray diffraction patterns.

For Chapter 6, B. Koo conducted a large-scale synthesis of bipyridinecarbohydroximoyl chloride and preliminary ball-mill functionalization of carbon nanotubes. Y. Inamoto synthesized *m*- and *p*-pyridinecarbohydroximoyl chloride, and performed further ball-mill functionalization of carbon nanotubes. D. Kim conducted density functional theory calculations.

TABLE OF CONTENTS

Title Page	1
Signature Page	2
Dedication.....	3
Abstract.....	4
Contributions.....	5
Table of Contents.....	6
List of Figures, Schemes, Tables, and Spectra.....	9
Chapter 1	21
1.1. Fullerene Chemistry.....	22
1.1.1. Discovery and Formation of Fullerenes.....	22
1.1.2. The Structure of Fullerenes.....	23
1.1.3. The Reactivity of Fullerenes.....	24
1.1.4. Isomers and Multiadducts.....	29
1.2. Electronic Properties of Fullerenes.....	32
1.3. Applications.....	35
1.3.1. Organic Photovoltaic (OPV) Applications.....	35
1.3.2. Model for Nanocarbon Functionalization.....	36
1.3.3. Other Applications.....	37
1.4. References and Notes.....	39
Chapter 2	50
2.1. Introduction.....	51
2.2. Results and Discussion.....	54
2.2.1. Syntheses of Tetraalkylcyclobutadiene-C ₆₀ Adducts.....	54
2.2.2. Electrochemical Properties.....	56
2.2.3. Photophysical Properties.....	58
2.2.4. Thermal Properties.....	60
2.2.5. Organic Photovoltaic Performances.....	66
2.2.6. Elimination of π -Orbital Interaction.....	69
2.3. Conclusions.....	73
2.4. Experimental Section.....	74
2.5. References and Notes.....	80
2.6. Appendix.....	86
Chapter 3	94
3.1. Introduction.....	95
3.2. Results and Discussion.....	96
3.2.1. Syntheses of Isobenzofulvene-C ₆₀ Adducts.....	96
3.2.2. Electrochemical Properties.....	99
3.2.3. Photophysical Properties.....	101

3.2.4.	Thermal Stability.....	103
3.2.5.	Photovoltaic Characterization.....	104
3.2.6.	Transient Photovoltage and Photocurrent Measurement.....	107
3.2.7.	Morphology, UV–Vis absorption, and Photoluminescence of Thin Films.....	109
3.3.	Conclusions.....	112
3.4.	Experimental Section.....	113
3.5.	References and Notes.....	118
3.6.	Appendix.....	122
Chapter 4	129
4.1.	Introduction.....	130
4.2.	Results and Discussion.....	131
4.2.1.	Selection of Electron Transport Materials.....	131
4.2.2.	Morphology of IBF–Ep and PCBM Thin Films and the Perovskite Layers on the Fullerene Films.....	132
4.2.3.	Normal Structure Devices.....	137
4.2.4.	Inverted Structure Devices.....	140
4.3.	Conclusions.....	143
4.4.	Experimental Section.....	144
4.5.	References and Notes.....	147
4.6.	Appendix.....	150
Chapter 5	152
5.1.	Introduction.....	153
5.2.	Results and Discussion.....	155
5.2.1.	Syntheses of Aryne–C ₆₀ Adducts.....	155
5.2.2.	Electrochemical Properties.....	158
5.2.3.	Photophysical Properties.....	159
5.2.4.	Thermal Properties.....	161
5.2.5.	Decomposition Study by NMR.....	165
5.2.6.	DFT Calculations.....	169
5.2.7.	Variable-Temperature Transmission-Mode X-Ray Powder Diffraction.....	170
5.2.8.	Organic Photovoltaic Performances.....	172
5.2.9.	Morphological Study.....	177
5.2.10.	Statistical Analysis of Solar Cell Performances.....	178
5.3.	Conclusions.....	180
5.4.	Experimental Section.....	181
5.5.	References and Notes.....	188
5.6.	Appendix.....	193
Chapter 6	201
6.1.	Introduction.....	202

6.2.	Results and Discussion.....	203
6.2.1.	C ₆₀ Ligands for Metal Chelation.....	203
6.2.2.	Carbon Nanotube Functionalization by 1,3-Dipolar Cycloaddition with Nitrile Oxides: Solution-State and Mechanochemical Syntheses.....	207
6.2.3.	Computation of Isomeric Pyridyl Isoxazoline Structures on CNTs.....	214
6.2.4.	Metal Complexation and Electrocatalytic Performances.....	216
6.2.4.1.	Chelation of Cobalt Ion with Tridentate Ligand.....	216
6.2.4.2.	Axial Coordination of Pyridyl Ligand to Iron Macrocycle.....	222
6.3.	Conclusions.....	225
6.4.	Experimental Section.....	226
6.5.	References and Notes.....	231
6.6.	Appendix.....	235
	Curriculum Vitae.....	237
	Acknowledgements.....	239

LIST OF FIGURES

Figure 1.1.	Two different types of bonds in C ₆₀ fullerene.....	23
Figure 1.2.	Structures of addition products on different C–C bonds.....	26
Figure 1.3.	Illustration of 1,2-adduct and 1,4-adduct positions. The red double bond is introduced to the [5,6] junction as a result of 1,4-addition.....	30
Figure 1.4.	Regioisomeric positions of two substituents on C ₆₀ and the point groups of the resulting bisadducts in the paranthesis.....	31
Figure 1.5.	Electronic structure of C ₆₀ fullerene.....	33
Figure 1.6.	(a) Planar and (b) bulk heterojunction device architectures for organic photovoltaics.....	36
Figure 1.7.	A water-soluble fullerene dendrimer functionalized with hydrophilic solubilizing groups.....	38
Figure 2.1.	Structures of functionalized fullerenes.....	54
Figure 2.2.	Cyclic voltammograms of PCBM and (a) TMCB Mono-, Bis-, and Trisadducts (b) TBCB Mono-, and Bisadducts (under N ₂ , 0.1M Bu ₄ NPF ₆ in toluene/acetonitrile (4:1), Pt (WE), Pt wire (CE), Ag/AgNO ₃ (RE), scan rate 0.1 V/s, Fc/Fc ⁺ internal standard E _{1/2} at 0.20 V).....	56
Figure 2.3.	UV–Vis absorption spectra of PCBM (2.4 x 10 ⁻⁵ M) and (a) TMCB-Mono (2.5 x 10 ⁻⁵ M), Bis (2.4 x 10 ⁻⁵ M), and Tris (2.0 x 10 ⁻⁵ M) (b) TBCB-Mono (2.3 x 10 ⁻⁵ M), and Bis (1.3 x 10 ⁻⁵ M) in CHCl ₃	59
Figure 2.4.	HOMO–LUMO energy diagram of fullerene derivatives. The energy levels were drawn relative to the vacuum level that is by definition set to zero.....	60
Figure 2.5.	TGA analysis of TMCB- and TBCB-adducts with scan rate of 10° C/min from 30° C to 800° C. Temperature of 5% weight loss of each compound is 223.4° C (TMCB-Mono), 326.0° C (TBCB-Mono), 274.7° C (TMCB-Bis and TBCB-Bis), and 424.4° C (TMCB-Tris). At 150° C, a typical annealing temperature of BHJ PSC fabrication, all compounds show reasonable thermal stabilities.....	61
Figure 2.6.	Differential scanning calorimetry (DSC) characteristics of TMCB-Mono, Bis, and Tris on the (a) first and (b) second cycle, and those of TBCB-Mono and Bis on the (c) first and (d) second cycle. All the heat flows were measured at the scan rate of 10° C/min over the range from 25° C or 35° C to 200° C. Curves from the second to the fifth cycle were identical without any endothermic/exothermic features.....	61
Figure 2.7.	Tapping-mode atomic force microscopy (1µm window) phase and topography images of the films prepared from (a) PCBM, (b) TMCB-Mono, (c) TMCB-Bis, and (d) TMCB-Tris. P3HT was used as a donor for all devices. PEDOT:PSS was used as the underlayer. All	

	BHJs were annealed at 150° C for 20 min. Root-mean-square roughness was measured and indicated in the topography images.....	63
Figure 2.8.	¹ H NMR spectra of annealed (a) TMCB-Bis and (b) TMCB-Tris after three DSC cycles. Red dots correspond to the peaks of TMCB-Mono, and blue dots to TMCB-Bis. The gained features after annealing indicate the thermal decomposition of the multiadducts to less-functionalized adducts.....	64
Figure 2.9.	X-ray powder diffraction experiment of (a) TMCB-Mono, Bis and (b) TBCB-Mono, Bis. Decreased 2θ values of the monoadducts from C ₆₀ indicate their larger lattice constants in the microcrystalline phase, and the bisadducts are amorphous due to the presence of the multiple regioisomers. Annealing does not affect the crystallinity of TMCB-Bis.....	66
Figure 2.10.	Current density–voltage (J–V) characteristics of bulk heterojunction PSCs under AM 1.5 illumination at 100 mW/cm ² . ITO (150nm)/ PEDOT:PSS (40nm)/ P3HT:Fullerenes (75nm)/ Ca (25nm)/ Al (80nm) used for device fabrication.....	66
Figure 2.11.	Current density–voltage (J–V) characteristics of bulk heterojunction PSCs under AM 1.5 illumination at 100 mW/cm ² . P3HT blend with TBCB-Mono and Bis after annealing at 90° C or 120° C.....	68
Figure 2.12.	Cyclic voltammograms of C ₆₀ , TMCB-Ep, and TMCB-Mono (under N ₂ , 0.1M Bu ₄ NPF ₆ in Toluene/Acetonitrile(4:1), Pt (WE), Pt wire (CE), Ag/AgNO ₃ (RE), scan rate 0.1 V/s, Fc/Fc ⁺ internal standard E _{1/2} at 0.20 V)	70
Figure 2.13.	(a) The optimized structure of TMCB-Mono (ball-bonds and tube representations) determined at B3LYP/6-31G(d,p) level of DFT calculation. Angle between two four-membered rings (θ) is 113.4°. (b) The optimized structure of TMCB-Ep (θ = 114.5°).....	71
Figure 2.14.	Molecular orbital (MO) energy level diagram and isosurface representations of frontier molecular orbitals (HOMO-1, HOMO, LUMO, LUMO+1, and LUMO+2). (a) TMCB-Mono. LUMO is shown in a side view and a front view for clearer comprehension. (b) TMCB-Ep. LUMO+2 and HOMO are shown in a side view and a front view for clearer comprehension.....	72
Figure 3.1.	Cyclic voltammograms of (a) PCBM, IBF–Mono, IBF–Bis (b) PCBM, IBF–Mono, IBF–Ep (c) PCBM, IBF–Bis, IBF–Bis–Ep1, IBF–Bis–Ep2 (under N ₂ , 0.1M Bu ₄ NPF ₆ in toluene/acetonitrile (4:1), Pt (WE), Pt wire (CE), Ag/AgNO ₃ (RE), scan rate 0.1 V/s, Fc/Fc ⁺ internal standard E _{1/2} at 0.20 V)	100
Figure 3.2.	UV–Vis absorption spectra of (a) PCBM (2.4 x 10 ⁻⁵ M), IBF–Mono (2.2 x 10 ⁻⁵ M), IBF–Bis (2.4 x 10 ⁻⁵ M), IBF–Ep (2.3 x 10 ⁻⁵ M) (b) PCBM (2.4 x 10 ⁻⁵ M), IBF–Bis–Ep1 (2.4 x 10 ⁻⁵ M) and IBF–Bis–Ep2 (2.2 x 10 ⁻⁵ M) in CHCl ₃	101

- Figure 3.3.** HOMO–LUMO energy diagrams of functionalized fullerenes. The MO energy levels were scaled relative to the vacuum level set to zero.....102
- Figure 3.4.** TGA analysis of weight loss (solid line) and its first derivative over temperature (dotted line) on (a) PCBM, IBF–Mono, IBF–Bis and (b) IBF–Ep, IBF–Bis–Ep1, IBF–Bis–Ep2 with scan rate of 20° C/min from 50° C to 900° C.....103
- Figure 3.5.** Box plot of PCE, J_{SC} , V_{OC} and FF of the reference PCBM devices that we fabricated (black line and dots) compared to the values previously reported. The J–V plot in Figure 3.6 (a) corresponds to a device which has a V_{OC} at the median of the distribution (marked by red dots), though other parameters can be off the respective median value (e.g. FF). Overall, the distribution of each parameter of our devices is comparable to the published values over the past 7 years.....104
- Figure 3.6.** (a) Current density as a function of applied voltage for the fullerenes in BHJ architecture for solar cells with P3HT, compared to conventional P3HT:PCBM. (b) Box plot of the V_{OC} values obtained from the devices in (a) where the whiskers indicate the 10th to 90th percentile and the box shows the 25th to 75th percentile containing the median (solid line) and average (dotted line). Except for P3HT:IBF–Mono, the median V_{OC} for the devices with the new fullerenes are higher than conventional P3HT:PCBM devices. The broad distribution of V_{OC} of P3HT:IBF–Mono is due to the low reproducibility, which lowers the median; however, the higher values obtained indicate the intrinsic potential of this material to produce high V_{OC}106
- Figure 3.7.** Relationship between the measured V_{OC} and the LUMO energy levels of fullerenes. The red line passing through P3HT:PCBM value indicates the predicted V_{OC} of other devices based on the LUMO level differences.....107
- Figure 3.8.** Recombination lifetime as a function of the averaged excess charge carrier density measured with transient photovoltage and photocurrent (TPV/TPC). P3HT:PCBM devices exhibit the shortest recombination lifetime, compared at the same averaged excess charge density (dotted lines represent power law fits). The slower recombination of P3HT:IBF–C₆₀ devices contributes to their larger V_{OC} s than ones predicted solely by their effective band gaps. Also, all IBF–C₆₀-based devices are characterized by similar recombination dynamics, which suggests their similar electronic behaviors at the interface with P3HT.....108
- Figure 3.9.** Atomic force microscopy topographic images of the devices analyzed in this study at (a) 1 μ m and (b) 10 μ m scales. The topography at 1 μ m scale shows similar phase separation for all the blends under study, except for P3HT:IBF–Mono where particles are observed. The root-mean-square (RMS) roughness measured on each film is 3.5 nm (PCBM), 20.0 nm

(IBF-Mono), 2.5 nm (IBF-Bis), 3.0 nm (IBF-Ep), and 10.4 nm (IBF-Bis-Ep1). 10 μm scale images also show significant amount of the particles of IBF-Mono that are not fully dissolved.....109

Figure 3.10. Optical characterization of the devices analyzed in this study. Due to the similar results of IBF-Bis-Ep1 and IBF-Bis-Ep2, only IBF-Bis-Ep1 is shown for simplicity. (a) Steady-state spectral UV-Vis absorption of thin films fabricated under the same conditions as used for the devices in Figure 3.6 (a) and normalized for thickness. (b) Steady-state spectral photoluminescence emission of thin films fabricated under the same conditions as used for the devices in Figure 3.6 (a). Excited with monochromatic light at 500 nm and normalized for absorption. All fullerenes quench PL when blended with P3HT, though P3HT:IBF-Mono shows higher level of radiative exciton recombination that could explain its low J_{SC}111

Figure 3.11. Averaged excess charge carrier density as function of the light intensity for all the blends under study.....111

Figure 4.1. DSC traces of PCBM and IBF-Ep powder on the first heating and cooling cycles ranging from 25 $^{\circ}\text{C}$ to 350 $^{\circ}\text{C}$. The decomposition temperatures of both materials are higher than 350 $^{\circ}\text{C}$. Variable-temperature X-ray powder diffraction patterns of (b) IBF-Ep and (c) PCBM powder, packed in a capillary, measured at 25 $^{\circ}\text{C}$ (RT), 150 $^{\circ}\text{C}$, 227 $^{\circ}\text{C}$, and 25 $^{\circ}\text{C}$ again (RT') upon cooling. Dots indicate the peaks that developed after cooling of the capillary.....133

Figure 4.2. X-ray powder diffraction patterns of IBF-Ep and PCBM obtained at various temperatures. Four ranges of 2θ were collected subsequently and stitched together to cover the entire range shown here. The brighter parts represent higher intensities and correspond to the peaks in Figure 4.1 (b) and (c)134

Figure 4.3. AFM topographic images of (a) IBF-Ep and (b) PCBM. SEM images of (c) IBF-Ep and (d) PCBM. Fullerene aggregates were observed in PCBM films. (e-f) AFM topographic images of $\text{CH}_3\text{NH}_3\text{PbI}_{3-x}\text{Cl}_x$ perovskite layers spin-coated under ambient condition on IBF-Ep (e) and PCBM (f). (g-f) SEM images of perovskite layers on IBF-Ep ($70 \pm 5\%$ of perovskite coverage) (g) and PCBM ETLs ($60 \pm 5\%$ of perovskite coverage) (h). Particulates and lower coverage ($60 \pm 5\%$) of perovskite were seen on the films with PCBM ETLs.....136

Figure 4.4. (a) UV-Vis absorption spectra and (b) X-ray diffraction patterns of $\text{CH}_3\text{NH}_3\text{PbI}_{3-x}\text{Cl}_x$ solar cells in a normal device structures measured under ambient conditions.....136

Figure 4.5.	(a) A schematic of the normal $\text{CH}_3\text{NH}_3\text{PbI}_{3-x}\text{Cl}_x$ perovskite solar cell structure. (b) The corresponding energy band diagram. (c) $J-V$ characteristics of the $\text{CH}_3\text{NH}_3\text{PbI}_{3-x}\text{Cl}_x$ perovskite solar cells with PCBM and IBF-Ep organic ETLs (measured under 100 mW/cm^2 AM1.5G illumination)	137
Figure 4.6.	$J-V$ characteristics of $\text{CH}_3\text{NH}_3\text{PbI}_{3-x}\text{Cl}_x$ solar cells in a normal device structures fabricated in air of 90 % of relative humidity.....	139
Figure 4.7.	(a) A schematic of the inverted $\text{CH}_3\text{NH}_3\text{PbI}_{3-x}\text{Cl}_x$ perovskite solar cell structure. (b) The corresponding energy band diagram. (c) An SEM cross section image of a device with an IBF-Ep ETL. (d) $J-V$ characteristics under 100 mW/cm^2 AM1.5G illumination of the inverted $\text{CH}_3\text{NH}_3\text{PbI}_{3-x}\text{Cl}_x$ perovskite solar cell devices with PCBM and IBF-Ep organic ETLs.....	141
Figure 4.8.	SEM images of (a) $\text{CH}_3\text{NH}_3\text{PbI}_{3-x}\text{Cl}_x$ layer on PEDOT:PSS HTL, (b) IBF-Ep ETL, and (c) PCBM ETL on the perovskite layer on PEDOT:PSS HTL in an inverted structure. The images were taken at two different magnifications. (d) $\text{CH}_3\text{NH}_3\text{PbI}_{3-x}\text{Cl}_x$ layer on IBF-Ep and PCBM ETLs.....	142
Figure 4.9.	$J-V$ characteristics of $\text{CH}_3\text{NH}_3\text{PbI}_{3-x}\text{Cl}_x$ solar cells fabricated in air without thermal annealing process of ETL. The decreased performance was obtained for devices with both PCBM and IBF-Ep, compared to the devices with annealed ETLs.....	150
Figure 4.10.	$J-V$ characteristics of $\text{CH}_3\text{NH}_3\text{PbI}_{3-x}\text{Cl}_x$ solar cells fabricated exclusively (a) in a N_2 -filled glove box and (b) in air.....	151
Figure 5.1.	Cyclic voltammograms of PCBM, ThBz- C_{60} , $\text{F}_2\text{Bz-C}_{60}$, MeOBz- C_{60} , and MeBz- C_{60} (under N_2 , 0.1M Bu_4NPF_6 in toluene/acetonitrile (4:1), Pt (WE), Pt wire (CE), Ag/AgNO ₃ (RE), scan rate 0.1 V/s, Fc/Fc^+ internal standard $E_{1/2}$ at 0.20 V) and the corresponding chemical structures of the fullerene derivatives.....	158
Figure 5.2.	UV-Vis absorption spectra of PCBM ($2.4 \times 10^{-5} \text{ M}$), ThBz- C_{60} ($2.3 \times 10^{-5} \text{ M}$), $\text{F}_2\text{Bz-C}_{60}$ ($2.2 \times 10^{-5} \text{ M}$), MeOBz- C_{60} ($2.3 \times 10^{-5} \text{ M}$), and MeBz- C_{60} ($2.4 \times 10^{-5} \text{ M}$) in CHCl_3	160
Figure 5.3.	HOMO-LUMO energy diagrams of functionalized fullerenes. The MO energy levels were scaled relative to the vacuum level set to zero.....	161
Figure 5.4.	TGA of functionalized fullerenes under nitrogen condition with scan rate of 20°C/min from 50°C to 900°C	162
Figure 5.5.	DSC measured on fullerene derivatives at the scan rate of 10°C/min over the range from 25°C to 350°C . (a) Three heating cycles of PCBM, (b) three cooling cycles of PCBM, three heating cycles of (c) MeOBz- C_{60} , (d) ThBz- C_{60} , (e) $\text{F}_2\text{Bz-C}_{60}$ and (f) three cooling	

	cycles of F ₂ Bz-C ₆₀ . There was no endo- or exothermic feature on the cooling cycles of MeOBz-C ₆₀ and ThBz-C ₆₀	163
Figure 5.6.	DSC characteristics of (a) PCBM, (b) MeOBz-C ₆₀ , (c) ThBz-C ₆₀ , and (d) F ₂ Bz-C ₆₀ during the first heating cycle measured at the scan rate of 10° C/min over the range from 25 °C to 400, 425, or 500 °C. There was no endo/exothermic feature in the first cooling cycles and in the following heating/cooling cycles for all the compounds.....	165
Figure 5.7.	¹ H NMR spectrum of PCBM.....	166
Figure 5.8.	¹ H NMR spectrum of PCBM annealed at 425 °C.....	166
Figure 5.9.	¹ H NMR spectrum of MeOBz-C ₆₀	167
Figure 5.10.	¹ H NMR spectrum of MeOBz-C ₆₀ annealed at 400 °C.....	167
Figure 5.11.	¹ H NMR spectrum of ThBz-C ₆₀	167
Figure 5.12.	¹ H NMR spectrum of ThBz-C ₆₀ annealed at 425 °C.....	168
Figure 5.13.	¹ H NMR spectrum of F ₂ Bz-C ₆₀	168
Figure 5.14.	¹ H NMR spectrum of F ₂ Bz-C ₆₀ annealed at 500 °C.....	168
Figure 5.15.	Optimized structures of (a) F ₂ Bz-C ₆₀ , (b) MeOBz-C ₆₀ , and (c) ThBz-C ₆₀ by DFT calculations (B3LYP/ 6-31G (d,p))	169
Figure 5.16.	(a) Experimentally obtained and (b) DFT calculated MO energy levels of ThBz-C ₆₀ , F ₂ Bz-C ₆₀ , and MeOBz-C ₆₀	170
Figure 5.17.	VT-XRD spectra of (a) MeOBz-C ₆₀ , (b)ThBz-C ₆₀ , and (c) F ₂ Bz-C ₆₀	171
Figure 5.18.	The original X-ray powder diffraction patterns of MeOBz-C ₆₀ , ThBz-C ₆₀ , and F ₂ Bz-C ₆₀ obtained at various temperatures. Four ranges of 2θ were collected subsequently and stitched together to cover the entire range shown here. The brighter parts represent higher intensities and correspond to the peaks in Figure 5.17.....	171
Figure 5.19.	The device architecture of bulk heterojunction polymer solar cells.....	172
Figure 5.20.	(a) <i>J-V</i> characteristics of PTB7:PC ₆₁ BM and (b) structure of PTB7 donor.....	173
Figure 5.21.	<i>J-V</i> characteristics of PTB7:PC ₇₁ BM with (a) low and (b) upgraded standard.....	175
Figure 5.22.	<i>J-V</i> characteristics of optimized PTB7:PC ₇₁ BM devices with (a) 0.25% ThBz-C ₆₀ and F ₂ Bz-C ₆₀ and (b) a range of F ₂ Bz-C ₆₀ doping.....	177
Figure 5.23.	The topography (upper row) and phase (lower row) of PTB7:PC ₇₁ BM devices without additive (a, b), with 0.25% (c, d), 1.0% (e, f), 2.0% F ₂ Bz-C ₆₀ (g, h), and 0.25% C ₆₀ (i, j). Each image is 1μm x 1μm in scale. The white particles (high features) shown in the topography correspond to fullerene aggregates.....	178
Figure 5.24.	Statistical analysis of the PTB7:PC ₇₁ BM devices with no additives (standard) and 0.25% and 1.0% of additives (F ₂ Bz-C ₆₀ , ThBz-C ₆₀ , C ₆₀ , IBF-Ep). The number of devices for each	

entry is in the box. The purple line in the box indicates the median of distribution. The top and bottom of box represents the 75th and 25th percentiles, and the top and bottom ends show the 90th and 10th percentiles of the statistics. The purple dots are the outlier data. A broad distribution of standard performance implies a challenge for consistent device reproduction.....179

- Figure 6.1.** Transition-metal complexes of isoxazolinofullerene derivatives.....204
- Figure 6.2.** XPS survey scans of the optimized products with (a) *o*-pyridyl, (b) *m*-pyridyl, (c) *p*-pyridyl, and (d) bipyridyl functional groups.....210
- Figure 6.3.** High-resolution XPS spectra of N1s in (a) the product after one-step filtration and thorough washing, (b) after additional purification steps, (c) byproducts in filtrate, and (d) hydroximoyl chloride reagent.....212
- Figure 6.4.** Raman spectra of covalently functionalized (red) and acid-washed (black) DWCNTs....213
- Figure 6.5.** A representative view of the calculated structures of *p*-pyridyl isoxazoline-functionalized (6,5)-SWCNT.....214
- Figure 6.6.** Calculated structures of *o*-pyridyl isoxazoline-functionalized (6,5)-SWCNT. Top-view and side-view of (a, b) diagonally attached and (c, d) perpendicularly attached *o*-pyridyl isoxazoline ring with respect to the long axis of the CNT. The torsional angle between the pyridine and the isoxazoline ring is 1.4° (a, b) and 12.4° (c, d)215
- Figure 6.7.** Calculated structures of *m*-pyridyl isoxazoline-functionalized (6,5)-SWCNT. Top-view and side-view of (a, b) diagonally attached and (c, d) perpendicularly attached *m*-pyridyl isoxazoline ring with respect to the long axis of the CNT. The torsional angle between the pyridine and the isoxazoline ring is 21.7° (a, b) and 18.5° (c, d)215
- Figure 6.8.** Calculated structures of *p*-pyridyl isoxazoline-functionalized (6,5)-SWCNT. Top-view and side-view of (a, b) diagonally attached and (c, d) perpendicularly attached *p*-pyridyl isoxazoline ring with respect to the long axis of the CNT. The torsional angle between the pyridine and the isoxazoline ring is 33.6° (a, b) and 18.8° (c, d).....216
- Figure 6.9.** (a) Rotating electrode setup: a rotor with electrical connectors to working electrodes, a rotating shaft, a reaction flask, and a speed controller, (b) a GC rotating disk electrode, and (c) a rotating ring-disk electrode with a platinum ring and a GC disk.....217
- Figure 6.10.** Linear sweep voltammograms of oxygen reduction electrocatalysis measured at a constant rotation speed of 400 rpm.....218
- Figure 6.11.** (a) Linear sweep voltammograms of oxygen reduction electrocatalysis measured at various rotation speeds and (b) a K–L plot for DWbpy–Co²⁺219

Figure 6.12. Linear sweep voltammograms of disk-current (red) and ring-current (black) for oxygen reduction electrocatalysis measured at a constant rotation speed of 400 rpm.....	221
Figure 6.13. A Tafel plot of oxygen reduction electrocatalysis measured at a constant rotation speed of 400 rpm.....	222
Figure 6.14. Linear sweep voltammograms of oxygen reduction electrocatalysis measured at a constant rotation speed of 2500 rpm.....	224
Figure 6.15. (a) A representative linear sweep voltammogram of oxygen reduction electrocatalysis measured at various rotation speeds and (b) K–L plot for <i>p</i> -pyridyl isoxazoline-functionalized DWCNT/FePc composite.....	225

LIST OF SCHEMES

Scheme 1.1. Aromatization of pyracyclene units in fullerenes via $2e^-$ reduction or nucleophilic addition.....	25
Scheme 1.2. [2+1] cycloaddition of stabilized carbanion to C_{60}	27
Scheme 1.3. Synthesis of PCBM through cycloaddition of diazo compound followed by nitrogen elimination from the pyrazoline intermediate. During the second step, [5,6]-open structure rearranges to more stable [6,6]-closed isomers.....	27
Scheme 1.4. [2+2] photocycloaddition of alkene to C_{60}	28
Scheme 1.5. [2+2] cycloaddition of aryloxy- and alkoxyketenes to C_{60}	28
Scheme 1.6. 1,3-dipolar cycloaddition of nitrile oxide derivatives to C_{60}	29
Scheme 1.7. Diels–Alder cycloaddition of indene to C_{60}	29
Scheme 1.8. Isoxazoline-functionalized CNTs with various substituents.....	37
Scheme 2.1. $AlCl_3$ -assisted Diels–Alder reaction of alkynes.....	53
Scheme 2.2. Synthesis of TMCB fullerenes.....	53
Scheme 2.3. $AlCl_3$ -assisted Diels–Alder cycloaddition reactions between C_{60} and 3-Hexyne, 4-Octyne, and 5-Decyne.....	56
Scheme 2.4. Epoxidation of TMCB-Mono.....	69
Scheme 3.1. Isobenzofulvene formation and Diels–Alder reaction with C_{60} : synthesis of (a) IBF–Mono and (b) IBF–Bis.....	97
Scheme 3.2. Syntheses of (a) IBF–Ep, (b) IBF–Bis–Ep1, and (c) IBF–Bis–Ep2 by epoxidation reaction.....	98
Scheme 5.1. Various aryne formations and their [2+2] cycloaddition with C_{60}	156
Scheme 6.1. 1,3-dipolar cycloaddition of nitrile oxide derivatives to C_{60}	204
Scheme 6.2. The proposed reaction and product of copper(I) complexation to <i>o</i> -pyridyl isoxazolinofullerene and the change in 1H NMR spectra.....	205
Scheme 6.3. The proposed reaction and product of copper(I) complexation to bipyridyl isoxazolinofullerene and the change in 1H NMR spectra.....	205
Scheme 6.4. The proposed reaction and products of cobalt(II) complexation to bipyridyl isoxazolinofullerene and the change in 1H NMR spectra.....	206
Scheme 6.5. The 1,3-dipolar cycloaddition of nitrile oxide derivatives to CNTs in solution.....	208
Scheme 6.6. Mechanochemical cycloaddition of nitrile oxide derivatives to carbon nanotubes.....	209
Scheme 6.7. Mechanisms of byproduct formation from nitrile oxide intermediates.....	212

LIST OF TABLES

Table 2.1.	HOMO and LUMO Energies Calculated from UV–Vis absorption and Cyclic Voltammetry.....	58
Table 2.2.	Characteristics of OPV Devices.....	68
Table 2.3.	Electrochemical Characteristics and LUMO Energy of C ₆₀ , TMCB-Ep, and TMCB-Mono	70
Table 3.1.	HOMO and LUMO energies of fullerene derivatives calculated from UV–Vis absorption and cyclic voltammetry.....	102
Table 3.2.	OPV characteristics of the devices in Figure 3.6 (a).	106
Table 4.1.	Performance of CH ₃ NH ₃ PbI _{3-x} Cl _x perovskite solar cells in the normal device architecture. For each structure, average values and standard deviation for five measured devices are indicated, as well as the champion device results (in parentheses).....	138
Table 4.2.	Performance of CH ₃ NH ₃ PbI _{3-x} Cl _x perovskite solar cells in the inverted structures device architecture with IBF–Ep ETLs. Average values and standard deviation for five measured devices are indicated, as well as the champion device results (in parentheses).....	142
Table 5.1.	HOMO and LUMO energies of fullerene derivatives calculated from UV–Vis absorption and cyclic voltammetry.....	160
Table 5.2.	OPV characteristics of the devices in Figure 5.20.....	174
Table 5.3.	OPV characteristics of the devices in Figure 5.21.....	176
Table 5.4.	OPV characteristics of the devices in Figure 5.20.....	177

LIST OF SPECTRA

Spectrum 2.1.	¹ H NMR of TMCB-Mono.....	86
Spectrum 2.2.	¹³ C NMR of TMCB-Mono.....	86
Spectrum 2.3.	¹ H NMR of TMCB-Bis.....	87
Spectrum 2.4.	¹³ C NMR of TMCB-Bis.....	87
Spectrum 2.5.	¹ H NMR of TMCB-Tris.....	88
Spectrum 2.6.	¹³ C NMR of TMCB-Tris.....	88
Spectrum 2.7.	¹ H NMR of TBCB-Mono.....	89
Spectrum 2.8.	¹³ C NMR of TBCB-Mono.....	89
Spectrum 2.9.	¹ H NMR of TBCB-Bis.....	90
Spectrum 2.10.	¹³ C NMR of TBCB-Bis.....	90
Spectrum 2.11.	¹ H NMR of TMCB-Ep.....	91
Spectrum 2.12.	¹³ C NMR of TMCB-Ep.....	91
Spectrum 2.13.	HPLC trace of pristine C ₆₀	92
Spectrum 2.14.	HPLC trace of TMCB-Mono.....	92
Spectrum 2.15.	HPLC trace of TMCB-Bis.....	92
Spectrum 2.16.	HPLC trace of TMCB-Tris.....	92
Spectrum 2.17.	HPLC trace of TBCB-Mono.....	93
Spectrum 2.18.	HPLC trace of TBCB-Bis.....	93
Spectrum 3.1.	¹ H NMR of IBF-Mono.....	122
Spectrum 3.2.	¹³ C NMR of IBF-Mono.....	122
Spectrum 3.3.	¹ H NMR of IBF-Bis.....	123
Spectrum 3.4.	¹³ C NMR of IBF-Bis.....	123
Spectrum 3.5.	¹ H NMR of IBF-Ep.....	124
Spectrum 3.6.	¹³ C NMR of IBF-Ep.....	124
Spectrum 3.7.	¹ H NMR of IBF-Bis-Ep1.....	125
Spectrum 3.8.	¹³ C NMR of IBF-Bis-Ep1.....	125
Spectrum 3.9.	¹ H NMR of IBF-Bis-Ep2.....	126
Spectrum 3.10.	¹³ C NMR of IBF-Bis-Ep2.....	126
Spectrum 3.11.	HPLC trace of IBF-Mono.....	127
Spectrum 3.12.	HPLC trace of IBF-Bis.....	127
Spectrum 3.13.	HPLC trace of IBF-Ep.....	127
Spectrum 3.14.	HPLC trace of IBF-Bis-Ep1.....	127

Spectrum 3.15.	HPLC trace of IBF-Bis-Ep2.....	128
Spectrum 3.16.	ATR-FTIR spectra of (a) C ₆₀ reference, IBF-Mono, IBF-Bis, (b) IBF-Ep, IBF-Bis-Ep1, and IBF-Bis-Ep2.....	128
Spectrum 5.1.	¹ H NMR of MeOBz-C ₆₀	193
Spectrum 5.2.	¹³ C NMR of MeOBz-C ₆₀	194
Spectrum 5.3.	¹ H NMR of F ₂ Bz-C ₆₀	194
Spectrum 5.4.	¹³ C NMR of F ₂ Bz-C ₆₀	195
Spectrum 5.5.	¹⁹ F NMR of F ₂ Bz-C ₆₀	195
Spectrum 5.6.	¹ H NMR of MeBz-C ₆₀	196
Spectrum 5.7.	¹³ C NMR of MeBz-C ₆₀	196
Spectrum 5.8.	¹ H NMR of ThBz-C ₆₀	197
Spectrum 5.9.	¹³ C NMR of ThBz-C ₆₀	197
Spectrum 5.10.	¹ H NMR of Bz-C ₆₀	198
Spectrum 5.11.	¹ H NMR of Np-C ₆₀	198
Spectrum 5.12.	¹ H NMR of F ₁ Bz-C ₆₀	199
Spectrum 5.13.	HPLC trace of MeOBz-C ₆₀	199
Spectrum 5.14.	HPLC trace of F ₂ Bz-C ₆₀	199
Spectrum 5.15.	HPLC trace of MeBz-C ₆₀	200
Spectrum 5.16.	HPLC trace of ThBz-C ₆₀	200
Spectrum 6.1.	¹ H NMR of <i>o</i> -pyridinecarbohydroximoyl chloride in DMSO- <i>d</i> ₆	235
Spectrum 6.2.	¹ H NMR of <i>m</i> -pyridinecarbohydroximoyl chloride in DMSO- <i>d</i> ₆	235
Spectrum 6.3.	¹ H NMR of <i>p</i> -pyridinecarbohydroximoyl chloride in DMSO- <i>d</i> ₆	236
Spectrum 6.4.	¹ H NMR of bipyridylamidochloride in DMF- <i>d</i> ₇	236

CHAPTER 1
Introduction to Fullerenes:
Chemistry and Applications

1.1. Fullerene Chemistry

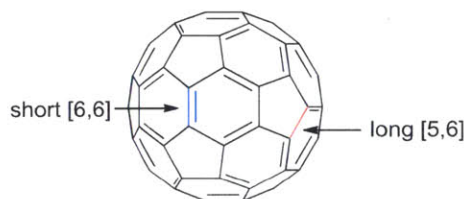
1.1.1. Discovery and Formation of Fullerenes

Three-dimensional carbon allotropes called fullerenes were first synthesized and reported by Kroto et al. in 1985,¹ and this discovery opened new fields of research spanning from fundamental studies to many applications in materials science. As a result of the importance of these new forms of elemental carbon and their unique physical and chemical properties, the 1996 Nobel Prize for Chemistry was awarded to Curl, Kroto, and Smalley for their discovery of fullerenes. Fullerenes were synthesized first by the evaporation of graphite using a pulsed laser (532 nm Nd:YAG in a 5-ns pulse), followed by the Krätschmer–Huffman carbon arc process² for higher-yield production. The mass production affording the commercial use of fullerenes, is now accomplished in a combustion synthesis of benzene and other hydrocarbons which is practiced at a scale of several tons-per-year.³ The continuous energy input and controlled concentration gradient of carbon in these processes result in a kinetically controlled process,⁴ and there have been many mechanisms suggested for the formation of fullerenes.^{5,6} These mechanisms generally involve alkynes in three stages^{4,7}: 1) nucleation through exothermic condensation of *sp* carbon atoms and their conversion to *sp*² centers with the formation of fused pentagons or hexagons, 2) a cage growth through the collapse of polyynes chains to form rings, and 3) cage closure and shrinkage of large defect-rich fullerenes by C₂ evaporation to produce more C₆₀ and C₇₀.⁸ A promising hypothesis suggests that rings and linear carbon chains aggregate and form C₃₈ closed carbon cages which grow by C₂ insertion to C₆₀ or C₇₀.^{9,10} Indeed, the absence of carbon clusters C₂₉ to C₃₇ can be explained by this self-assembly mechanism. The most abundant fullerenes are C₆₀ and C₇₀, and they are the most commonly used forms in research as a result of their commercial availability.

1.1.2. The Structure of Fullerenes

The carbon lattice of fullerenes resembles the shape of a soccer ball and the geodesic spheres/domes popularized by American architect Richard Buckminster Fuller (1895–1983) and hence these structures were named after him. They are still often referred to as “buckyballs”. Fullerenes possess chemical formula C_{2n} with the carbon atoms forming 12 pentagons and $n-10$ hexagons⁷. Within fullerenes, all rings are fused through conjugated double bonds.¹¹ All of the pentagons need to be surrounded exclusively by the hexagons to reduce strain-related instability, a condition called isolated pentagon rule (IPR).¹² When two pentagons are adjacent, 19–24 kcal/mol of destabilization energy is imposed,¹³ and they also form an 8-membered ring (pentalene) with 8π electrons, an anti-aromatic structure.^{14,15} The smallest fullerene that fulfills the IPR is C_{60} , followed by C_{70} , C_{72} , C_{80} , etc. Notably, C_{36} has been also isolated despite its non-IPR structure.¹⁶ For the fullerenes that follow IPR, two different types of bond lengths exist: short [6,6] bonds between two adjacent hexagons and long [5,6] bonds between an adjacent pentagon and hexagon. An X-ray crystal structure¹⁷ of C_{60} demonstrates shorter [6,6] bonds (1.38 Å) than [5,6] bonds (1.45 Å), indicating higher electron density and greater double-bond character on [6,6] compared to [5,6]. For clarity, all the double bonds are therefore drawn to be inside the 6-membered rings as shown in Figure 1.1. Different electron density and double-bond character of [5,6] and [6,6] bonds result in reactivity differences to be discussed in section 1.1.3.

Figure 1.1. Two different types of bonds in C_{60} fullerene.



The icosahedral symmetry (I_h) of C_{60} and 5-fold symmetry (D_{5h}) of C_{70} are well established. Larger fullerenes possess either reduced symmetry and/or isomeric structures. For example, C_{76} possesses D_2 symmetry, the three isomers of C_{78} carry C_{2v} , C'_{2v} , and D_3 symmetry, and two known isomers of C_{80} are within the I_h and D_{5h} point groups.^{18,19} There are other larger fullerenes that are experimentally isolated and stable and some giant fullerenes with icosahedral, but metastable structures (C_{180} , C_{240} , C_{320} , C_{500} , and C_{540}).²⁰⁻²²

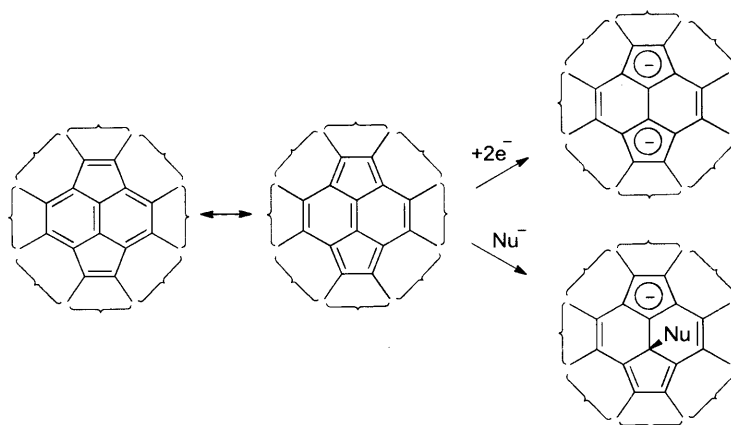
Endohedral metallofullerenes (EMFs) are another class of fullerenes with the chemical formula of (cluster)^{q+}@(C_{2n})^{q-}. They are classified into several groups, encapsulating metal ions ($M@C_{2n}$, $q=3$), dimetallic units ($M_2@C_{2n}$, $q=6$), metallic carbides ($M_2C_2@C_{2n}$, $q=4$), and metallic nitride clusters ($M_3N@C_{2n}$, $q=6$).⁴ M can be a Group 3 element or a lanthanide,^{23,24} and even small molecules such as H_2 , CO , H_2O , NH_3 , or CH_4 ²⁵ have been incorporated in the cages. Many non-IPR EMFs have been synthesized and characterized with their carbon cages usually being structural isomers of the corresponding empty fullerenes due to electron transfer from the HOMO (highest-occupied molecular orbital) of the internal moiety to the LUMO (lowest-unoccupied molecular orbital) of the encapsulating carbon cage.²⁶

1.1.3. The Reactivity of Fullerenes

Since fullerenes are spherical, their double bonds significantly deviate from planarity, thereby introducing large strain energy within the molecules. The relief of strain energy via covalent bonding and the pyramidalization of the sp^2 carbon atoms to their sp^3 form drives exothermic reactions.²⁷ Fullerenes generally exhibit exohedral reactivity and negligible endohedral reactivity, because their π orbitals extend further on the outside than into the interior of the cage.⁴

Fullerenes possess very high reduction potentials and are thus mildly oxidizing.^{28,29} The pyracyclene units (Scheme 1.1) within the structures are $4n \pi$ systems, counting only the circulating electrons. Therefore, it is hypothesized that they are aromatized by the capture of up to two electrons. Scheme 1.1 describes both a direct $2 e^-$ transfer to give $4n+2 \pi$ electron dianionic system and the donation of a lone pair to give cyclopentadienide and a monoadduct by reaction with a nucleophile.³⁰

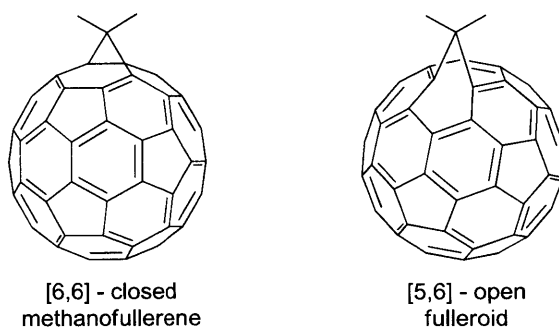
Scheme 1.1. Aromatization of pyracyclene units in fullerenes via $2e^-$ reduction or nucleophilic addition.



The reactivity of fullerenes resembles those of localized electron-deficient polyolefins (electrophilic, dienophilic, and dipolarophilic)³¹ rather than those of aromatic systems. While cycloaddition reactions have been extensively explored (*vide infra*), fullerenes also react with a number of nucleophiles such as amines,³² phosphines,³³ Grignard reagents,^{34,35} organolithium reagents.³⁶ Radical addition reactions³⁷ and transition metal complex formations³⁸ have been reported as well. Most of these chemical reactions are tested on C_{60} as a result of its abundance and highly symmetric structure; only two types of C–C bonds generally lead to a single regioisomer. Larger fullerenes are less symmetric with larger variety of C–C bonds with different reactivities, generating a larger number of regioisomers. As aforementioned, a [6,6] bond has

greater double-bond character than a [5,6] junction, thus the vast majority of reactants target [6,6] over [5,6].^{39,40} The exceptions are the formation of [5,6]-open fulleroids and [6,6]-closed methanofullerene isomers during cyclopropanation reactions (Figure 1.2). The addition of diazomethane initially forms [6,6]-bridged pyrazoline followed by the extrusion of nitrogen, which enables the formation of adducts on a [5,6] junction.⁴¹ Likewise, aziridination reactions by azide additions can initially form [6,6]-bridged triazolines which generate a mixture of [5,6]-open azafulleroids and [6,6]-closed fullerenoaziridine isomers upon nitrogen elimination.^{40,42} Since [6,6] isomers are thermodynamically more stable than [5,6] isomers, the conversion of fulleroids to methanofullerenes can be achieved thermally,^{7,40} electrochemically,⁴³ photochemically,⁴⁴ or via acid-catalysis.⁴⁵ A [5,6]-open isomer has electronic structure maintaining the $60 \pi e^-$ system of pristine C_{60} . By transforming to [6,6]-closed structure, the fullerene core loses 2π electrons and keeps 58π electrons.

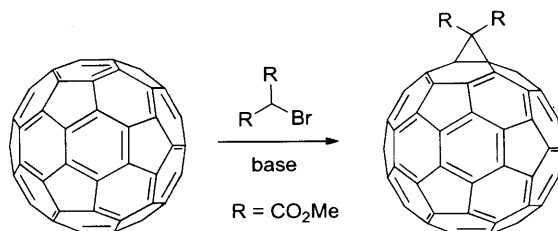
Figure 1.2. Structures of addition products on different C–C bonds.



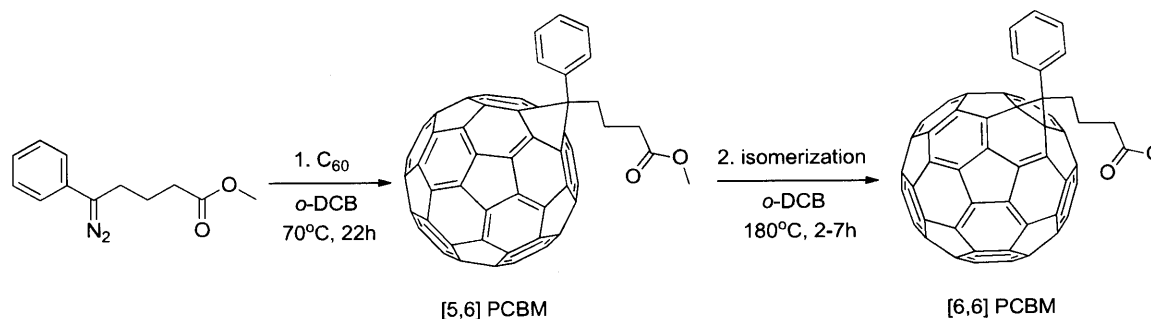
Various [2+n] cycloadditions ($n = 1, 2, 3,$ and 4 most typical) have been investigated, and they are also the major focus of this thesis as functionalization methods. Some of the typical reagents and reaction mechanisms will be described below for reference. [2+1] cycloaddition reactions yield 3-membered carbo- or heterocyclic fragments on fullerenes and produce methanofullerenes, fullerenoaziridines,⁴⁶ fullerenoaxiranes,⁴⁷ and others via the addition of

carbenes, carbanions, nitrenes, etc. There are three classes of reactions for the generation of methanofullerenes. A well-known transformation called the Bingel reaction proceeds by an addition-elimination mechanism involving stabilized carbanions as reagents.⁴⁸ In Scheme 1.2, the treatment of 2-bromomalonic ester by base generates the carbanion intermediate. The second class is the addition of carbenes to the fullerenes.⁷ The third group of reactions is the thermal addition of diazo compounds followed by thermolysis or photolysis of the resulting adducts.⁴⁹ These latter reactions are more complex than the carbene additions, since they form both mixed [6,6]-closed and [5,6]-open isomers as discussed above.⁵⁰ The synthesis of phenyl-C₆₁-butyric acid methyl ester (PCBM) is described in Scheme 1.3 as an example.

Scheme 1.2. [2+1] cycloaddition of stabilized carbanion to C₆₀.



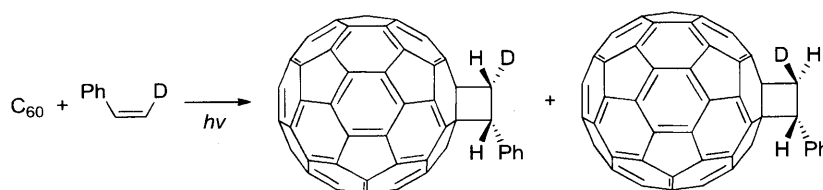
Scheme 1.3. Synthesis of PCBM through cycloaddition of diazo compound followed by nitrogen elimination from the pyrazoline intermediate. During the second step, [5,6]-open structure rearranges to more stable [6,6]-closed isomers.



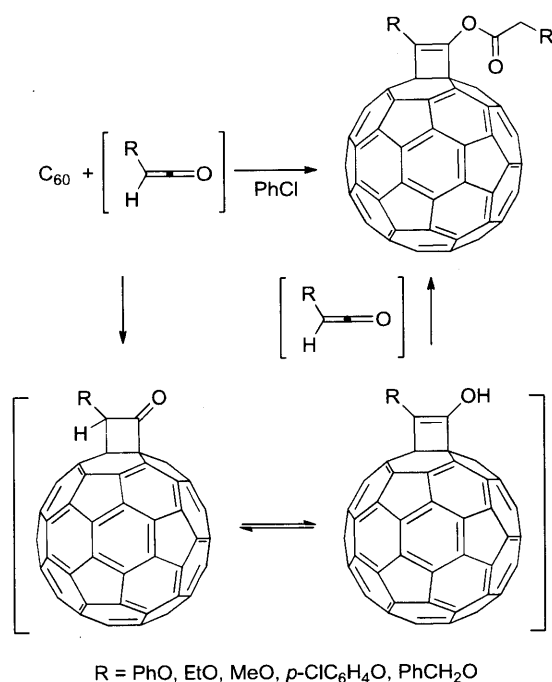
[2+2] photochemical cycloadditions enable the synthesis of cyclobutane-fused C₆₀ structures, and proceed with a stepwise mechanism involving triplet biradical intermediates

(Scheme 1.4).^{51,52} Fullerenes also react with aryloxy- and alkoxyketenes generated *in situ* from the corresponding acid chlorides using triethylamine (Scheme 1.5).⁵³ The ketenes form 2:1 adducts with C₆₀ through formal [2+2] addition followed by enolization and acylation.

Scheme 1.4. [2+2] photocycloaddition of alkene to C₆₀.



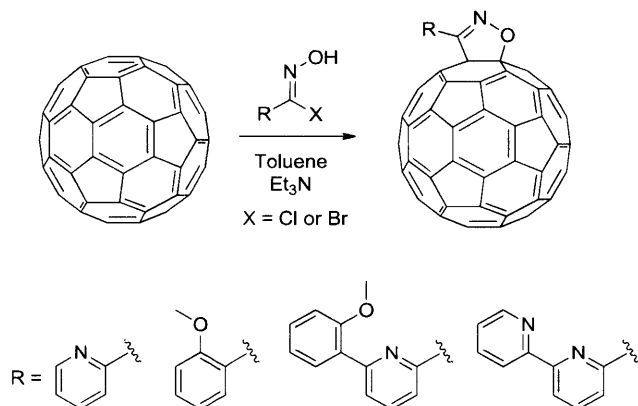
Scheme 1.5. [2+2] cycloaddition of aryloxy- and alkoxyketenes to C₆₀.



[2+3] cycloadditions of various 1,3-dipolar compounds allow for the addition of 5-membered heterocyclic fragments to form fulleropyrazoline,⁵⁴ fullerentriazoline,⁵⁵ fulleropyrrolidines,⁵⁶ fullerenoisoxazoline,^{54,57} etc. Scheme 1.6 depicts the 1,3-dipolar cycloaddition of nitrile oxides generated from the corresponding hydroximoyl halides to

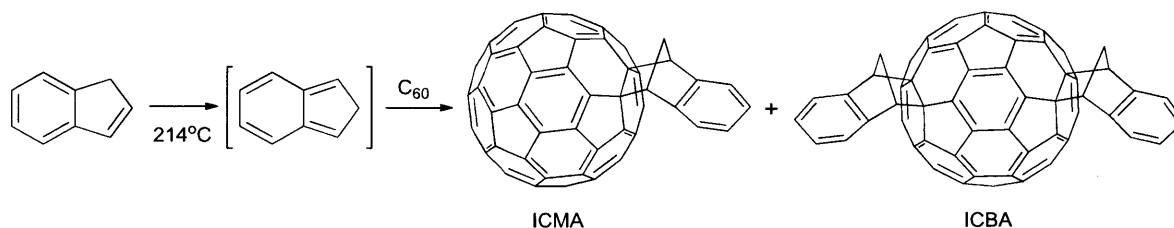
fullerenes, which was developed by Ramírez-Monroy and Swager as a strategy to install pyridyl ligands for transition metal complexation.⁵⁸

Scheme 1.6. 1,3-dipolar cycloaddition of nitrile oxide derivatives to C₆₀.



The most common cycloadditions used to chemically modify fullerenes are [4+2] (Diels–Alder) reactions, which was first demonstrated in a study of using cyclopentadiene⁵⁹ as the diene and a fullerene as the dienophile. For example, indene–C₆₀ adducts (Scheme 1.7) are effective electron acceptors commonly used in organic photovoltaics, and their synthesis involves isomerization of indene to isoindene diene at high temperatures, which undergoes Diels–Alder cycloaddition to C₆₀.⁶⁰

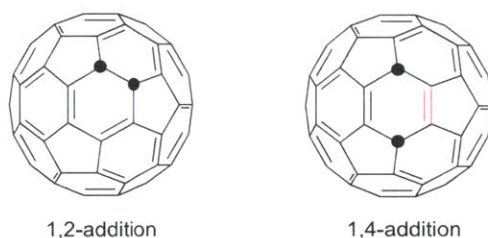
Scheme 1.7. Diels–Alder cycloaddition of indene to C₆₀.



1.1.4. Isomers and Multiadducts

In addition to the [5,6]-open and [6,6]-closed isomers as discussed earlier, the monoaddition to C_{60} can result in 1,2- and 1,4-adduct isomers by nucleophilic addition and the treatment of the initially formed anion NuC_{60}^- with various electrophiles.³⁸ 1,2-adducts are obtained when the addition occurs between two hexagons (at the [6,6] junction), while 1,4-adducts are formed when the addition occurs across a 6-membered ring (Figure 1.3). 1,2-adducts are thermodynamically more stable since they retain all the double bonds within the 6-membered rings. In contrast, 1,4-adducts possess a double bond within a 5-membered ring (marked red in Figure 1.3), which increases the energy of the fullerene by about 8 kcal/mol relative to the 1,2-adducts.^{61,62} 1,4-adducts are, however, favored when bulky groups are added to fullerenes since the steric hindrance is decreased by locating them apart, which compensates for this unfavorable energy increase. 1,2- and 1,4-adducts can be separated by high pressure liquid chromatography (HPLC), and one method to distinguish the isomers is the comparison of their UV-Vis absorption spectra. 1,2-adducts show a weak absorption centered around 432 nm, while 1,4-adducts exhibit a broad absorption band at 445 nm.⁶³⁻⁶⁵

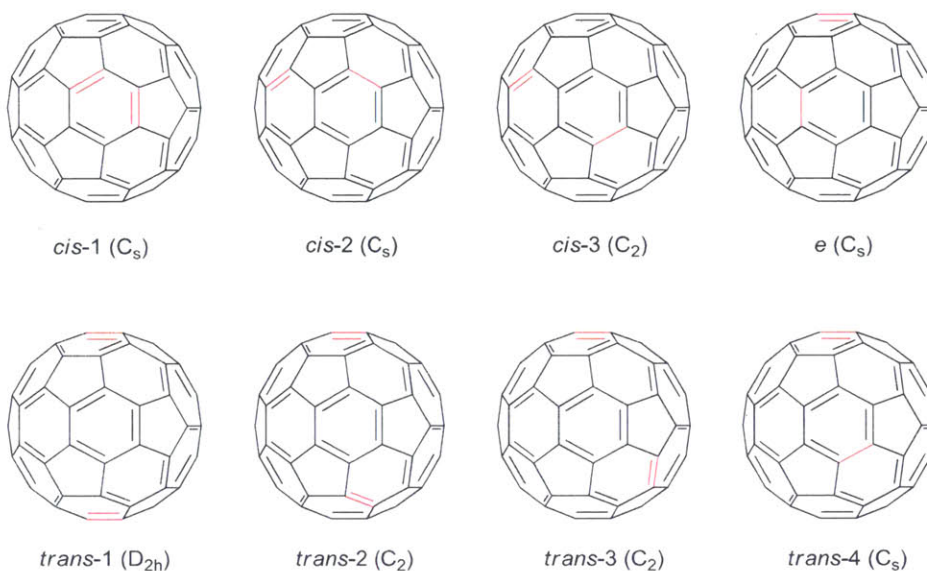
Figure 1.3. Illustration of 1,2-adduct and 1,4-adduct positions. The red double bond is introduced to the [5,6] junction as a result of 1,4-addition.⁶⁴



The Hirsch group conducted a pioneering systematic study aimed at determining the factors that govern the complicated regiochemistry of multiadducts of C_{60} .⁶⁶ There are 8 types of regioisomers for C_{60} bisadducts, and the spatial arrangements of the added groups are

categorized into three sections (marked red in Figure 1.4): two groups on the same hemisphere (*cis*), on the opposite hemispheres (*trans*), and one at the equator (*e*). Three sets of double bonds are available on the same hemisphere, and four sets of double bonds can be on the opposite side. The regioisomers exhibit different yields (more *trans*-3 and *e* isomers than others) and can be isolated by HPLC with a specialized column wherein the order of elution corresponds to the polarities.⁶⁷ Electrochemical isomerization of bisadducts was additionally conducted on each of 6 isolated regioisomeric bis-malonate C₆₀ adducts.⁶⁸ In this study, the cyclopropane rings migrate over the surface of the fullerene, which is called the “walk-on-the-sphere” mechanism, and the resulting relative ratios of the isomers are unchanged from the original distribution.⁶⁹ Thus, it was confirmed that the process is thermodynamically controlled. The symmetry of regioisomers can be resolved by ¹³C nuclear magnetic resonance (NMR) spectroscopy. 32 fullerene carbon peaks for C_s symmetry, 30 peaks for C₂, 8 peaks for D_{2h} are observed with simple substituents such as methano bridges.⁶⁶ In addition, excited-state and time-resolved electron paramagnetic resonance (EPR) spectroscopy^{70,71} can be employed to characterize regioisomers.

Figure 1.4. Regioisomeric positions of two substituents on C₆₀ and the point groups of the resulting bisadducts in the paranthesis.



Higher adducts exhibit enhanced regioselectivity; for example, 7 out of 46 possible isomeric tris-[di(ethoxycarbonyl)methano] C_{60} were isolated.⁷² *Cis* arrangement is unfavorable as 36 *cis* isomers were not detected, and it was found that the third addition prefers the equatorial position (by 40% probability).⁷³ Hexakisadducts with all *e* substitution are synthesized with high yields via stepwise *e* addition onto the purified *e,e,e* trisadduct isomer. Starting from C_{60} and 8 equivalents of diethyl 2-bromomalonate treated with 1,8-diazabicyclo[5.4.0]undec-7-ene (DBU), the hexakisadduct was obtained with 14% yield.⁷⁴ For more effective region- and stereoselective multiadditions on fullerenes, tether-directed remote functionalization strategies were developed by the Diederich group and others.⁷⁵⁻⁷⁷ The covalent template with a designed spacer can direct the mutual arrangement of addends in an elegant and unambiguous way.

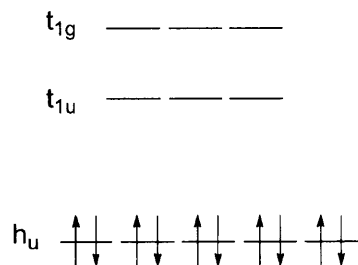
1.2. Electronic Properties of Fullerenes

Fullerenes are known for their high electron affinity and the ability to transport charges effectively.²³ In pioneering studies, the Wudl group systematically studied the electrochemistry of fullerenes, with cyclic voltammetry showing that a pristine C_{60} can reversibly accept up to 6

electrons.^{30,41,43} C₆₀ derivatives generally retain the electronic properties of pristine C₆₀, as they exhibit similar electrochemical characteristics.^{78,79} However, the cyclic voltammograms of C₆₀ derivatives present at most 5 reduction peaks in the accessible potential range, since the reversible peaks are cathodically shifted compared to the pristine C₆₀.⁸⁰⁻⁸² This trend indicates that the fullerene derivatives become generally less electron deficient than their pristine structures, as a result of the saturation of one or more double bonds. The trend not only applies to singlet ground state but also to the singlet and triplet excited states. Adiabatic electron affinity (AEA) was also calculated to examine relative electron affinity of pristine C₆₀ and its derivatives. AEA can be obtained by calculating the difference between the total energy of a neutral molecule and that of an anionic analog (upon 1 e⁻ addition) at equilibrium: $E_{AEA} = E_{C_{60}} - E_{C_{60}^{-1}}$. The decrease in electron affinity upon monosubstitution, influenced by the loss of 2 π electrons (and formation of a [6,6]-closed 58 π e⁻ product), was consistent with the cyclic voltammetry results. Calculated electron affinity (B3LYP/6-31G(d)) decreased from 48.28 kcal/mol for pristine C₆₀ to 46.27 kcal/mol for methanofullerene.⁸³

As shown by electrochemical characterization, fullerenes have low-lying LUMO levels, which makes fullerenes very electron withdrawing. 5-fold degenerate HOMO and 3-fold degenerate LUMO of C₆₀ are described in Figure 1.5.^{84,85} The energy levels of the HOMO and LUMO are reported differently depending on the characterization procedures or calculation methods. The commonly accepted values for C₆₀ are -6.2 eV and -4.5 eV for the HOMO and LUMO, respectively.⁸⁶

Figure 1.5. Electronic structure of C₆₀ fullerene.⁸⁷



Small reorganization energy (λ) of C_{60} compared to that of typical electron acceptors, such as benzoquinone and pyromellitic diimides, was confirmed by the study of the photoexcited charge separation and recombination in donor–acceptor dyads.⁸⁸ Relative to a porphyrin–benzoquinone dyad, the charge separation in the corresponding porphyrin– C_{60} counterpart was accelerated and the charge recombination was retarded. This relative charge transfer dynamics can be interpreted as the result of the reorganization energy differences for the acceptor moiety. Although the unit charge in benzoquinone is concentrated on the oxygen atoms, the charge on C_{60} is delocalized over the whole molecule, decreasing the charge density on each carbon atom. Thus, the solvent reorganization energy (λ_s) of the C_{60} system becomes small. In addition, the rigid framework of C_{60} is unchanged upon reduction to C_{60}^- , which reduces the intramolecular reorganization energy (λ_i) of porphyrin– C_{60} dyad. Therefore, the overall reorganization energy (λ) defined as the combination of λ_s and λ_i is smaller for C_{60} than benzoquinone, enabling enhanced charge transfer from porphyrin donor.⁸⁹

Additionally, hole mobility (μ_h) in C_{60} film is within the range of 10^{-4} $\text{cm}^2/\text{V}\cdot\text{s}$.⁹⁰ As a result of this modest mobility, C_{60} is not classified as a p-type semiconductor. On the other hand, the electron mobility (μ_e) of epitaxially grown C_{60} film is about $0.4\text{--}1$ $\text{cm}^2/\text{V}\cdot\text{s}$,^{91,92} rendering C_{60} one of the most useful carbon-based n-type materials.

1.3. Applications

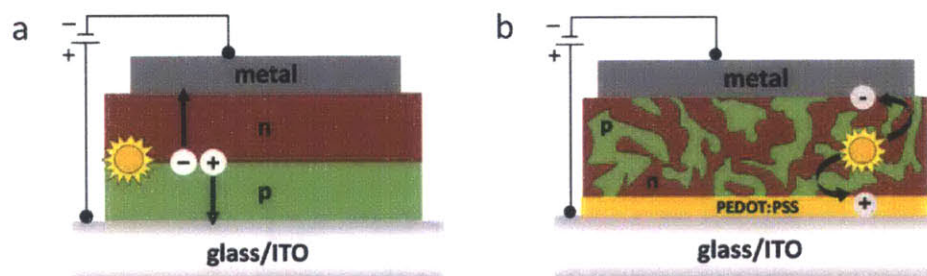
1.3.1. Organic Photovoltaic (OPV) Applications

As a result of their outstanding electron accepting capabilities in photoinduced electron-transfer (ET) processes with electron donors,⁹³ fullerenes have found broad utilities for organic photovoltaics as the n-type materials. As organic materials are limited by a high exciton binding energy of around 0.4 eV⁹⁴ and consequently a short exciton diffusion length on the order of 10 nm,⁹⁵ a bulk heterojunction (BHJ) configuration is preferred to conventional planar heterojunction (PHJ) geometries (Figure 1.6). In a BHJ architecture, two components, usually a p-type polymer and a fullerene, are mixed in solution and spin-coated onto substrates, resulting in bicontinuous phases for efficient extraction of charges and for the maximized interface between donor and acceptor.⁹⁶

Functionalized fullerenes such as PCBM have also been shown to possess excellent electron accepting properties, and C₇₀ derivatives have been employed due to their enhanced light absorption relative to their higher symmetry C₆₀ counterparts. The lowered symmetry of C₇₀ enables forbidden or less-allowed electronic transitions.⁹⁷ The increased ability to absorb light leads to higher short-circuit current densities (J_{sc}) of the devices.⁹⁸ Additionally, the LUMO levels of fullerene derivatives for BHJ devices can be tailored by various chemical modifications, which will be described in Chapters 2 and 3. The change in the LUMO level of electron acceptors affects the built-in potential of device architectures and as a result the open-circuit voltages (V_{oc}) in solar cells.⁹⁹ The fill factor (FF), which is governed by charge recombination and transport dynamics, can be influenced by the resistivity of fullerene derivatives depending on the substituents.¹⁰⁰ In general, long alkyl chain attachments improve the solubility of fullerenes in common organic solvents, but can adversely affect the conductivity of the materials.¹⁰¹ The

role of fullerenes in organic photovoltaics and the importance of their structural design will be the primary focus of this thesis.

Figure 1.6. (a) Planar and (b) bulk heterojunction device architectures for organic photovoltaics¹⁰⁰



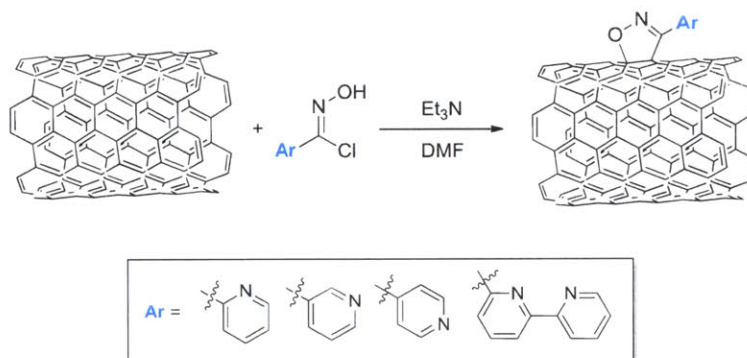
1.3.2. Model for Nanocarbon Functionalization

Fullerenes, particularly C_{60} which exhibits a highly symmetrical structure, are very useful model systems for the carbon nanotube (CNT) and graphene functionalization. As fullerenes are small molecules compared to the much larger 2 or 3 dimensional CNTs and graphenes, they are easier to characterize by common methods such as 1H and ^{13}C NMR spectroscopy, mass spectrometry, and X-ray crystallography. The chemical structures and locations of the functional groups on C_{60} derivatives can thus be determined. In contrast, CNTs and graphenes are materials with length scales on the order of microns, so conventional characterization techniques cannot be applied to them. Some of commonly used procedures to characterize these much larger systems include X-ray photoelectron spectroscopy, infrared spectroscopy, thermogravimetric analysis, Raman spectroscopy, and solid-state NMR spectroscopy. However, these techniques only provide indirect or qualitative evidence of functionalization, and other oxygen-containing moieties (carboxylic acids, ketones, hydroxyl groups, etc.) and impurities in the carbon networks can interfere with the correct assignment of functional groups. Therefore, the functionalization of

CNTs and graphenes benefits from precedent with fullerenes to confirm that the reaction conditions yield the anticipated functionalization. For example, we conducted a CNT functionalization with nitrile oxide derivatives (Scheme 1.8) based on the successful chemistry on the fullerenes (Scheme 1.6).

However, lower reactivity of the planar or less-curved sp^2 networks of graphene and carbon nanotubes relative to fullerenes requires the use of harsher reaction conditions as a result of a smaller driving force for the pyramidalization of their sp^2 carbons.¹⁰² In addition, carbon nanotubes and graphenes tend to bundle and stack, thus exhibiting extremely low solubility and dispersibility in organic and/or aqueous solvents. Therefore, the dispersion of the materials prior to and during the heterogeneous reaction is crucial for obtaining high yields, and generally a larger excess of reactants is used than is required for fullerene chemistry.

Scheme 1.8. Isoxazoline-functionalized CNTs with various substituents.

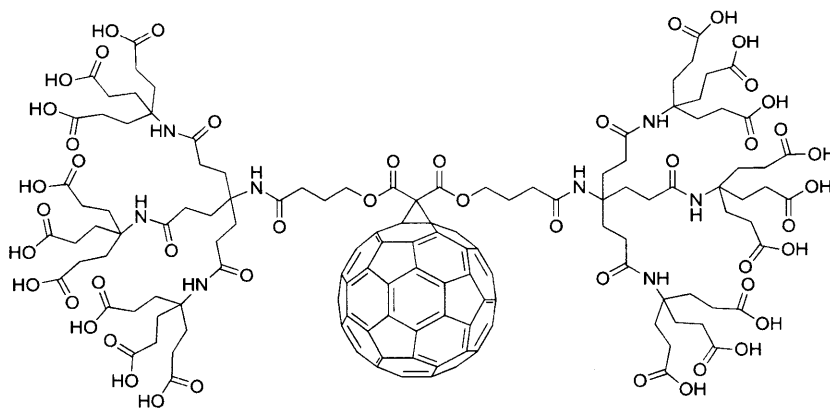


1.3.3. Other Applications

Thin films of fullerenes have potential applications in various fields that rely on their non-linear optical,^{103,104} ferromagnetic,¹⁰⁵ and superconducting^{17,106,107} properties. Medicinal chemistry¹⁰⁸ is another area which makes use of fullerene's suitable size, three-dimensionality, hydrophobicity, and electronic properties. The hydrophobicity enables fullerene's coordination

to the hydrophobic regions of enzymes or cells. However, functionalization of fullerenes with water-solubilizing groups is necessary for their use in biological environments. An example of water-soluble dendrimers for fullerenes are depicted in Figure 1.7 (solubility of 34 mg/mL at pH 7.4, and 254 mg/mL at pH 10).¹⁰⁹ It is hypothesized that C₆₀ derivatives can capture radicals for therapeutic treatment of neurodegenerative diseases.¹¹⁰ Fullerenes containing amino acids and peptides are also of great interest.¹¹¹

Figure 1.7. A water-soluble fullerene dendrimer functionalized with hydrophilic solubilizing groups.



Fullerenes have distinct photophysical properties suitable for photodynamic therapy. First, photo-excited fullerenes are good triplet sensitizer which can generate singlet oxygen to cleave DNA: $^3(C_{60}) + O_2 \rightarrow C_{60} + (^1O_2)$.¹¹² They can also directly oxidize biomolecules by electron transfer, leading to cytotoxicity.¹¹³ Second, light absorption around 700 nm by the functionalized fullerenes allows for the efficient penetration of longer-wavelength light through tissues.¹¹⁴ Fullerenes have been demonstrated to exhibit cytotoxicity only under irradiation for HeLa S3 tumor cell *in vitro* assays¹¹⁵ and contributed to fibrous tumor treatment in mice by local irradiation without skin injury.¹¹⁶ Fullerenes were also detected to have excellent vascular

permeability and to accumulate in a tumor. The biological and medicinal applications of fullerenes have been reviewed in the literature.

1.4. References and Notes

1. Kroto, H. W.; Heath, J. R.; O'Brien, S. C.; Curl, R. F.; Smalley, R. E. C₆₀: Buckminsterfullerene. *Nature* **1985**, *318*, 162-163.
2. Kratschmer, W.; Lamb, L. D.; Fostiropoulos, K.; Huffman, D. R. Solid C₆₀: a new form of carbon. *Nature* **1990**, *347*, 354-358.
3. Howard, J. B.; McKinnon, J. T.; Makarovsky, Y.; Lafleur, A. L.; Johnson, M. E. Fullerenes C₆₀ and C₇₀ in flames. *Nature* **1991**, *352*, 139-141.
4. Rodriguez-Forteza, A.; Irle, S.; Poblet, J. M.: Fullerenes: formation, stability, and reactivity. *Wires Comput. Mol. Sci.* **2011**, *1*, 350-367.
5. Wakabayashi, T.; Achiba, Y.: A model for the C₆₀ and C₇₀ growth mechanism. *Chem. Phys. Lett.* **1992**, *190*, 465-468.
6. Smalley, R. E.: Self-assembly of the fullerenes. *Acc. Chem. Res.* **1992**, *25*, 98-105.
7. Diederich, F.; Isaacs, L.; Philp, D.: Syntheses, structures, and properties of methanofullerenes. *Chem. Soc. Rev.* **1994**, *23*, 243-255.
8. Zheng, G. S.; Wang, Z.; Irle, S.; Morokuma, K.: Quantum chemical molecular dynamics study of "Shrinking" of Hot Giant fullerenes. *J. Nanosci. Nanotechnol.* **2007**, *7*, 1662-1669.
9. Zhang, Q. L.; O'Brien, S. C.; Heath, J. R.; Liu, Y.; Curl, R. F.; Kroto, H. W.; Smalley, R. E.: Reactivity of large carbon clusters: spheroidal carbon shells and their possible relevance to the formation and morphology of soot. *J. Phys. Chem.* **1986**, *90*, 525-528.
10. von Helden, G.; Gotts, N. G.; Bowers, M. T.: Experimental evidence for the formation of fullerenes by collisional heating of carbon rings in the gas phase. *Nature* **1993**, *363*, 60-63.

11. Prato, M.: [60]Fullerene chemistry for materials science applications. *J. Mater. Chem.* **1997**, *7*, 1097-1109.
12. Schmalz, T. G.; Seitz, W. A.; Klein, D. J.; Hite, G. E.: C₆₀ carbon cages. *Chem. Phys. Lett.* **1986**, *130*, 203-207.
13. Albertazzi, E.; Domene, C.; W. Fowler, P.; Heine, T.; Seifert, G.; Van Alsenoy, C.; Zerbetto, F.: Pentagon adjacency as a determinant of fullerene stability. *Phys. Chem. Chem. Phys.* **1999**, *1*, 2913-2918.
14. Liu, X.; Schmalz, T. G.; Klein, D. J.: Favorable structures for higher fullerenes. *Chem. Phys. Lett.* **1992**, *188*, 550-554.
15. Klein, D. J.; Schmalz, T. G.; Hite, G. E.; Seitz, W. A.: Resonance in C₆₀ buckminsterfullerene. *J. Am. Chem. Soc.* **1986**, *108*, 1301-1302.
16. Slanina, Z.; Zhao, X.; Uhlík, F.; Ōsawa, E.: Non-IPR fullerenes: C₃₆ and C₇₂. *AIP Conference Proceedings* **1999**, *486*, 179-182.
17. Haddon, R. C.: Electronic structure, conductivity and superconductivity of alkali metal doped C₆₀. *Acc. Chem. Res.* **1992**, *25*, 127-133.
18. Hennrich, F. H.; Michel, R. H.; Fischer, A.; Richard-Schneider, S.; Gilb, S.; Kappes, M. M.; Fuchs, D.; Bürk, M.; Kobayashi, K.; Nagase, S.: Isolation and Characterization of C₈₀. *Angew. Chem. Int. Ed. Eng.* **1996**, *35*, 1732-1734.
19. Wang, C.-R.; Sugai, T.; Kai, T.; Tomiyama, T.; Shinohara, H.: Production and isolation of an ellipsoidal C fullerene. *Chem. Commun.* **2000**, 557-558.
20. Dunlap, B. I.; Zope, R. R.: Efficient quantum-chemical geometry optimization and the structure of large icosahedral fullerenes. *Chem. Phys. Lett.* **2006**, *422*, 451-454.
21. Scuseria, G. E.: The equilibrium structures of giant fullerenes: faceted or spherical shape? An ab initio Hartree-Fock study of icosahedral C₂₄₀ and C₅₄₀. *Chem. Phys. Lett.* **1995**, *243*, 193-198.
22. Calaminici, P.; Geudtner, G.; Köster, A. M.: First-Principle Calculations of Large Fullerenes. *J. Chem. Theor. Comput.* **2009**, *5*, 29-32.

23. Chaur, M. N.; Valencia, R.; Rodríguez-Fortea, A.; Poblet, J. M.; Echegoyen, L.: Trimetallic Nitride Endohedral Fullerenes: Experimental and Theoretical Evidence for the $M_3N_6^+@C_{2n}^{6-}$ model. *Angew. Chem. Int. Ed.* **2009**, *48*, 1425-1428.
24. Stevenson, S.; Fowler, P. W.; Heine, T.; Duchamp, J. C.; Rice, G.; Glass, T.; Harich, K.; Hajdu, E.; Bible, R.; Dorn, H. C.: Materials science: A stable non-classical metallofullerene family. *Nature* **2000**, *408*, 427-428.
25. Osuna, S.; Swart, M.; Sola, M.: The reactivity of endohedral fullerenes. What can be learnt from computational studies? *Phys. Chem. Chem. Phys.* **2011**, *13*, 3585-3603.
26. Tan, Y.-Z.; Xie, S.-Y.; Huang, R.-B.; Zheng, L.-S.: The stabilization of fused-pentagon fullerene molecules. *Nat. Chem.* **2009**, *1*, 450-460.
27. Haddon, R. C.: Chemistry of the Fullerenes - the Manifestation of Strain in a Class of Continuous Aromatic-Molecules. *Science* **1993**, *261*, 1545-1550.
28. Haufler, R. E.; Conceicao, J.; Chibante, L. P. F.; Chai, Y.; Byrne, N. E.; Flanagan, S.; Haley, M. M.; O'Brien, S. C.; Pan, C.; et al.: Efficient production of C_{60} (buckminsterfullerene), $C_{60}H_{36}$, and the solvated buckide ion. *J. Phys. Chem.* **1990**, *94*, 8634-8636.
29. Allemand, P. M.; Koch, A.; Wudl, F.; Rubin, Y.; Diederich, F.; Alvarez, M. M.; Anz, S. J.; Whetten, R. L.: Two different fullerenes have the same cyclic voltammetry. *J. Am. Chem. Soc.* **1991**, *113*, 1050-1051.
30. Wudl, F.: The Chemical-Properties of Buckminsterfullerene (C_{60}) and the Birth and Infancy of Fulleroids. *Acc. Chem. Res.* **1992**, *25*, 157-161.
31. Yurovskaya, M. A.; Trushkov, I. V.: Cycloaddition to buckminsterfullerene C_{60} : advancements and future prospects. *Russ. Chem. Bull.* **2002**, *51*, 367-443.
32. Schick, G.; Kampe, K.-D.; Hirsch, A.: Reaction of [60]fullerene with morpholine and piperidine: preferred 1,4-additions and fullerene dimer formation. *J. Chem. Soc., Chem. Commun.* **1995**, 2023-2024.
33. Yamago, S.; Yanagawa, M.; Nakamura, E.: Tertiary phosphines and P-chiral phosphinites bearing a fullerene substituent. *J. Chem. Soc., Chem. Commun.* **1994**, 2093-2094.

34. Hirsch, A.; Soi, A.; Karfunhel, H. R.: Titration of C₆₀: A Method for the Synthesis of Organofullerenes. *Angew. Chem. Int. Ed. Eng.* **1992**, *31*, 766-768.
35. Hirsch, A.; Grösser, T.; Skiebe, A.; Soi, A.: Synthesis of Isomerically Pure Organodihydrofullerenes. *Chem. Ber.* **1993**, *126*, 1061-1067.
36. Fagan, P. J.; Krusic, P. J.; Evans, D. H.; Lerke, S. A.; Johnston, E.: Synthesis, chemistry, and properties of a monoalkylated buckminsterfullerene derivative, tert-BuC₆₀ anion. *J. Am. Chem. Soc.* **1992**, *114*, 9697-9699.
37. Troshin, P. A.; Lyubovskaya, R. N.: Organic chemistry of fullerenes: The major reactions, types of fullerene derivatives and prospects for practical use. *Usp. Khim.* **2008**, *77*, 323-369.
38. Hirsch, A.: Addition Reactions of Buckminsterfullerene (C₆₀). *Synthesis* **1995**, *1995*, 895-913.
39. Pang, L. S. K.; Wilson, M. A.: Reactions of fullerenes C₆₀ and C₇₀ with cyclopentadiene. *J. Phys. Chem.* **1993**, *97*, 6761-6763.
40. Prato, M.; Lucchini, V.; Maggini, M.; Stimpfl, E.; Scorrano, G.; Eiermann, M.; Suzuki, T.; Wudl, F.: Energetic preference in 5,6 and 6,6 ring junction adducts of C₆₀: fulleroids and methanofullerenes. *J. Am. Chem. Soc.* **1993**, *115*, 8479-8480.
41. Suzuki, T.; Li, Q.; Khemani, K. C.; Wudl, F.; Almarsson, O.: Systematic Inflation of Buckminsterfullerene C₆₀- Synthesis of Diphenyl Fulleroids C₆₁ to C₆₆. *Science* **1991**, *254*, 1186-1188.
42. Isaacs, L.; Wehrsig, A.; Diederich, F.: Improved Purification of C₆₀ and Formation of σ- and π-Homoaromatic methano-bridged fullerenes by reaction with alkyl diazoacetates. *Helv. Chim. Acta.* **1993**, *76*, 1231-1250.
43. Eiermann, M.; Wudl, F.; Prato, M.; Maggini, M.: Electrochemically Induced Isomerization of a Fulleroid to a Methanofullerene. *J. Am. Chem. Soc.* **1994**, *116*, 8364-8365.
44. Janssen, R. A. J.; Hummelen, J. C.; Wudl, F.: Photochemical Fulleroid to Methanofullerene Conversion via the Di-π-methane (Zimmerman) Rearrangement. *J. Am. Chem. Soc.* **1995**, *117*, 544-545.
45. Gonzalez, R.; Hummelen, J. C.; Wudl, F.: The Specific Acid-Catalyzed and Photochemical Isomerization of a Robust Fulleroid to a Methanofullerene. *J. Org. Chem.* **1995**, *60*, 2618-2620.

46. Banks, M. R.; Cadogan, J. I. G.; Gosney, I.; Hodgson, P. K. G.; Langridge-Smith, P. R. R.; Millar, J. R. A.; Taylor, A. T.: Aziridino[2[prime or minute],3[prime or minute] : 1,2][60]fullerene. *J. Chem. Soc., Chem. Commun.* **1995**, 885-886.
47. Murray, R. W.; Iyanar, K.: Oxidation of [60]fullerene by the methyltrioxorhenium-hydrogen peroxide system. *Tetrahedron Lett.* **1997**, 38, 335-338.
48. Bingel, C.: Cyclopropanierung von Fullerenen. *Chem. Ber.* **1993**, 126, 1957-1959.
49. Hall, M. H.; Lu, H.; Shevlin, P. B.: Observation of Both Thermal First-Order and Photochemical Zero-Order Kinetics in the Rearrangement of [6,5] Open Fulleroids to [6,6] Closed Fullerenes. *J. Am. Chem. Soc.* **2001**, 123, 1349-1354.
50. Osterodt, J.; Windscheif, P.-M.; Vögtle, F.; Nieger, M.: Verkronte-Fullerene. *Chem. Ber.* **1993**, 126, 2331-2336.
51. Vassilikogiannakis, G.; Orfanopoulos, M.: Stereochemistry and Isotope Effects of the [2+2] Photocycloadditions of Arylalkenes to C₆₀. A Stepwise Mechanism. *J. Am. Chem. Soc.* **1997**, 119, 7394-7395.
52. Vassilikogiannakis, G.; Hatzimarinaki, M.; Orfanopoulos, M.: Mechanism of the [2+2] Photocycloaddition of Fullerene C₆₀ with Styrenes. *J. Org. Chem.* **2000**, 65, 8180-8187.
53. Matsui, S.; Kinbara, K.; Saigo, K.: A novel reaction of [60]fullerene. A formal [2+2] cycloaddition with aryloxy- and alkoxyketenes. *Tetrahedron Lett.* **1999**, 40, 899-902.
54. Muthu, S.; Maruthamuthu, P.; Ragnathan, R.; Vasudeva Rao, P. R.; Mathews, C. K.: Reaction of buckminsterfullerene with 1,3-diphenylnitrilimine : Synthesis of pyrazoline derivatives of fullerene. *Tetrahedron Lett.* **1994**, 35, 1763-1766.
55. Guldi, D. M.; González, S.; Martín, N.; Antón, A.; Garín, J.; Orduna, J.: Efficient Charge Separation in C₆₀-Based Dyads: Triazolino[4',5':1,2][60]fullerenes. *J. Org. Chem.* **2000**, 65, 1978-1983.
56. Maggini, M.; Scorrano, G.; Prato, M.: Addition of azomethine ylides to C₆₀: synthesis, characterization, and functionalization of fullerene pyrrolidines. *J. Am. Chem. Soc.* **1993**, 115, 9798-9799.

57. Meier, M. S.; Poplawska, M.: Addition of nitrile oxides to C₆₀: formation of isoxazoline derivatives of fullerenes. *J. Org. Chem.* **1993**, *58*, 4524-4525.
58. Ramirez-Monroy, A.; Swager, T. M.: Metal Chelates Based on Isoxazoline[60]fullerenes. *Organometallics* **2011**, *30*, 2464-2467.
59. Wudl, F.; Hirsch, A.; Khemani, K. C.; Suzuki, T.; Allemand, P. M.; Koch, A.; Eckert, H.; Srdanov, G.; Webb, H. M.: Survey of Chemical-Reactivity of C₆₀, Electrophile and Dieno Polarophile Par Excellence. *Fullerenes : Synthesis, Properties, and Chemistry of Large Carbon Clusters* **1992**, *481*, 161-175.
60. He, Y. J.; Chen, H. Y.; Hou, J. H.; Li, Y. F.: Indene-C₆₀ Bisadduct: A New Acceptor for High-Performance Polymer Solar Cells. *J. Am. Chem. Soc.* **2010**, *132*, 5532-5532.
61. Matsuzawa, N.; Dixon, D. A.; Fukunaga, T.: Semiempirical Calculations of Dihydrogenated Buckminsterfullerenes, C₆₀H₂. *J. Phys. Chem.* **1992**, *96*, 7594-7604.
62. Cahill, P. A.; Rohlffing, C. M.: Theoretical studies of derivatized buckyballs and buckytubes. *Tetrahedron* **1996**, *52*, 5247-5256.
63. Murata, Y.; Komatsu, K.; Wan, T. S. M.: The reaction of [60]fullerene with lithium fluorene: Formation of a novel 1,4-adduct of [60]fullerene. *Tetrahedron Lett.* **1996**, *37*, 7061-7064.
64. Kadish, K. M.; Gao, X.; Van Caemelbecke, E.; Suenobu, T.; Fukuzumi, S.: Effect of addition pattern on the electrochemical and spectroscopic properties of neutral and reduced 1,2- and 1,4-(C₆H₅CH₂)₂C₆₀ isomers. *J. Phys. Chem. A* **2000**, *104*, 3878-3883.
65. Tajima, Y.; Hara, T.; Honma, T.; Matsumoto, S.; Takeuchi, K.: Lewis Acid-Assisted Nucleophilic Substitution of Fullerene Epoxide. *Org. Lett.* **2006**, *8*, 3203-3205.
66. Hirsch, A.; Lamparth, I.; Karfunkel, H. R.: Fullerene Chemistry in Three Dimensions: Isolation of Seven Regioisomeric Bisadducts and Chiral Trisadducts of C₆₀ and Di(ethoxycarbonyl)methylene. *Angew. Chem. Int. Ed. Eng.* **1994**, *33*, 437-438.

67. Hirsch, A.; Lamparth, I.; Karfunkel, H. R.: Fullerene Chemistry in 3 Dimensions - Isolation of 7 Regioisomeric Bisadducts and Chiral Trisadducts of C₆₀ and Di(Ethoxycarbonyl)Methylene. *Angew. Chem. Int. Ed. Eng.* **1994**, *33*, 437-438.
68. Kessinger, R.; Gomez-Lopez, M.; Boudon, C.; Gisselbrecht, J. P.; Gross, M.; Echegoyen, L.; Diederich, F.: Walk on the sphere: Electrochemically induced isomerization of C₆₀ bis-adducts by migration of Di(alkoxycarbonyl)methano bridges. *J. Am. Chem. Soc.* **1998**, *120*, 8545-8546.
69. Isaacs, L.; Haldimann, R. F.; Diederich, F.: Tether-Directed Remote Functionalization of Buckminsterfullerene: Regiospecific Hexaadduct Formation. *Angew. Chem. Int. Ed. Eng.* **1994**, *33*, 2339-2342.
70. Pasimeni, L.; Hirsch, A.; Lamparth, I.; Herzog, A.; Maggini, M.; Prato, M.; Corvaja, C.; Scorrano, G.: Use of Transient EPR Spectroscopy of Excited Triplet State for the Structural Assignment of Bisadducts of Fullerene C₆₀. *J. Am. Chem. Soc.* **1997**, *119*, 12896-12901.
71. Pasimeni, L.; Segre, U.; Ruzzi, M.; Maggini, M.; Prato, M.; Kordatos, K.: Preferential Orientation of Fulleropyrrolidine Bisadducts in E7 Liquid Crystal: A Time-Resolved Electron Paramagnetic Resonance Study. *J. Phys. Chem. B* **1999**, *103*, 11275-11281.
72. Echegoyen, L. E.; Djojo, F. D.; Hirsch, A.; Echegoyen, L.: Electrochemical studies of seven regioisomers of tris[di(ethoxycarbonyl)methano][60]fullerene: Umpolung of regiochemistry in retro-bingel reactions and walk-on-the-sphere rearrangements. *J. Org. Chem.* **2000**, *65*, 4994-5000.
73. Hirsch, A.; Lamparth, I.; Grosser, T.; Karfunkel, H. R.: Regiochemistry of Multiple Additions to the Fullerene Core - Synthesis of a T-H-Symmetrical Hexakisadduct of C₆₀ with Bis(Ethoxycarbonyl)Methylene. *J. Am. Chem. Soc.* **1994**, *116*, 9385-9386.
74. Lamparth, I.; Maichlemossmar, C.; Hirsch, A.: Reversible Template-Directed Activation of Equatorial Double-Bonds of the Fullerene Framework - Regioselective Direct Synthesis, Crystal-Structure, and Aromatic Properties of T_h-C₆₆(COOEt)₁₂. *Angew. Chem. Int. Ed. Eng.* **1995**, *34*, 1607-1609.
75. Isaacs, L.; Seiler, P.; Diederich, F.: Solubilized Derivatives of C₁₉₅ and C₂₆₀: The First Members of a New Class of Carbon Allotropes C_{n(60+5)}. *Angew. Chem. Int. Ed. Eng.* **1995**, *34*, 1466-1469.

76. Cardullo, F.; Seiler, P.; Isaacs, L.; Nierengarten, J.-F.; Haldimann, R. F.; Diederich, F.; Mordasini-Denti, T.; Thiel, W.; Boudon, C.; Gisselhrcht, J.-P.; Gross, M.: Bis- through Tetrakis-Adducts of C_{60} by Reversible Tether-Directed Remote Functionalization and systematic investigation of the changes in fullerene properties as a function of degree, pattern, and nature of functionalization. *Helv. Chim. Acta.* **1997**, *80*, 343-371.
77. Isaacs, L.; Diederich, F.; Haldimann, R. F.: Multiple Adducts of C_{60} by Tether-Directed Remote Functionalization and synthesis of soluble derivatives of new carbon allotropes $C_{n(60 + s)}$. *Helv. Chim. Acta.* **1997**, *80*, 317-342.
78. Prato, M.; Suzuki, T.; Foroudian, H.; Li, Q.; Khemani, K.; Wudl, F.; Leonetti, J.; Little, R. D.; White, T.: [3 + 2] and [4 + 2] Cycloadditions of fullerene C_{60} . *J. Am. Chem. Soc.* **1993**, *115*, 1594-1595.
79. Prato, M.; Li, Q. C.; Wudl, F.; Lucchini, V.: Addition of azides to fullerene C_{60} : synthesis of azafulleroids. *J. Am. Chem. Soc.* **1993**, *115*, 1148-1150.
80. Arias, F.; Xie, Q.; Echegoyen, L.; Wu, Y.; Lu, Q.; Wilson, S. R.: Kinetic Effects in the Electrochemistry of Fullerene Derivatives at Very Negative Potentials. *J. Am. Chem. Soc.* **1994**, *116*, 6388-6394.
81. Arias, F.; Echegoyen, L.; Wilson, S. R.; Lu, Q.; Lu, Q.: Methanofullerenes and Methanofulleroids Have Different Electrochemical Behavior at Negative Potentials. *J. Am. Chem. Soc.* **1995**, *117*, 1422-1427.
82. Paolucci, F.; Marcaccio, M.; Roffia, S.; Orlandi, G.; Zerbetto, F.; Prato, M.; Maggini, M.; Scorrano, G.: Electrochemical Monitoring of Valence Bond Isomers Interconversion in Bipyridyl- C_{61} Anions. *J. Am. Chem. Soc.* **1995**, *117*, 6572-6580.
83. Zhang, Z.; Han, P.; Liu, X.; Zhao, J.; Jia, H.; Zeng, F.; Xu, B.: First Principle Calculations of the Electronic Properties of the Fullerene Derivative as an Electron Acceptor in Organic Solar Cells. *J. Phys. Chem. C* **2008**, *112*, 19158-19161.
84. Haddon, R. C.; Brus, L. E.; Raghavachari, K.: Rehybridization and π -orbital alignment: the key to the existence of spheroidal carbon clusters. *Chem. Phys. Lett.* **1986**, *131*, 165-169.

85. Haddon, R. C.: π -Electrons in three dimensions. *Acc. Chem. Res.* **1988**, *21*, 243-249.
86. Chu, C.-W.; Shrotriya, V.; Li, G.; Yang, Y.: Tuning acceptor energy level for efficient charge collection in copper-phthalocyanine-based organic solar cells. *Appl. Phys. Lett.* **2006**, *88*, 153504.
87. Diener, M. D.; Alford, J. M.: Isolation and properties of small-bandgap fullerenes. *Nature* **1998**, *393*, 668-671.
88. Hiroshi, I.; Kiyoshi, H.; Tsuyoshi, A.; Masanori, A.; Seiji, T.; Tadashi, O.; Masahiro, S.; Yoshiteru, S.: The small reorganization energy of C₆₀ in electron transfer. *Chem. Phys. Lett.* **1996**, *263*, 545-550.
89. Imahori, H.; Tkachenko, N. V.; Vehmanen, V.; Tamaki, K.; Lemmetyinen, H.; Sakata, Y.; Fukuzumi, S.: An Extremely Small Reorganization Energy of Electron Transfer in Porphyrin–Fullerene Dyad. *J. Phys. Chem. A* **2001**, *105*, 1750-1756.
90. Könenkamp, R.; Priebe, G.; Pietzak, B.: Carrier mobilities and influence of oxygen in C₆₀ films. *Phys. Rev. B* **1999**, *60*, 11804-11808.
91. Singh, T. B.; Marjanović, N.; Matt, G. J.; Günes, S.; Sariciftci, N. S.; Moutagne Ramil, A.; Andreev, A.; Sitter, H.; Schwödiauer, R.; Bauer, S.: High-mobility n-channel organic field-effect transistors based on epitaxially grown C₆₀ films. *Org. Electron.* **2005**, *6*, 105-110.
92. Kitamura, M.; Kuzumoto, Y.; Kamura, M.; Aomori, S.; Arakawa, Y.: High-performance fullerene C₆₀ thin-film transistors operating at low voltages. *Appl. Phys. Lett.* **2007**, *91*, 183514.
93. Kawauchi, H.; Suzuki, S.; Kozaki, M.; Okada, K.; Islam, D. M. S.; Araki, Y.; Ito, O.; Yamanaka, K.-i.: Photoinduced Charge-Separation and Charge-Recombination Processes of Fullerene[60] Dyads Covalently Connected with Phenothiazine and Its Trimer. *J. Phys. Chem. A* **2008**, *112*, 5878-5884.
94. Brédas, J.-L.; Cornil, J.; Heeger, A. J.: The exciton binding energy in luminescent conjugated polymers. *Adv. Mater.* **1996**, *8*, 447-452.
95. Brabec, C. J.; Heeney, M.; McCulloch, I.; Nelson, J.: Influence of blend microstructure on bulk heterojunction organic photovoltaic performance. *Chem. Soc. Rev.* **2011**, *40*, 1185-1199.

96. Yu, G.; Gao, J.; Hummelen, J. C.; Wudl, F.; Heeger, A. J.: Polymer Photovoltaic Cells - Enhanced Efficiencies Via a Network of Internal Donor-Acceptor Heterojunctions. *Science* **1995**, *270*, 1789-1791.
97. Wienk, M. M.; Kroon, J. M.; Verhees, W. J. H.; Knol, J.; Hummelen, J. C.; van Hal, P. A.; Janssen, R. A. J.: Efficient methano[70]fullerene/MDMO-PPV bulk heterojunction photovoltaic cells. *Angew. Chem. Int. Ed.* **2003**, *42*, 3371-3375.
98. Troshin, P. A.; Hoppe, H.; Peregudov, A. S.; Egginger, M.; Shokhovets, S.; Gobsch, G.; Sariciftci, N. S.; Razumov, V. F.: [70]Fullerene-Based Materials for Organic Solar Cells. *Chemosuschem* **2011**, *4*, 119-124.
99. Brabec, C. J.; Cravino, A.; Meissner, D.; Sariciftci, N. S.; Fromherz, T.; Rispen, M. T.; Sanchez, L.; Hummelen, J. C.: Origin of the open circuit voltage of plastic solar cells. *Adv. Funct. Mater.* **2001**, *11*, 374-380.
100. Mishra, A.; Bäuerle, P.: Small Molecule Organic Semiconductors on the Move: Promises for Future Solar Energy Technology. *Angew. Chem. Int. Ed.* **2012**, *51*, 2020-2067.
101. Han, G. D.; Collins, W. R.; Andrew, T. L.; Bulovic, V.; Swager, T. M.: Cyclobutadiene-C₆₀ Adducts: N-Type Materials for Organic Photovoltaic Cells with High V_{OC}. *Adv. Funct. Mater.* **2013**, *23*, 3061-3069.
102. Lin, T.; Zhang, W.-D.; Huang, J.; He, C.: A DFT Study of the Amination of Fullerenes and Carbon Nanotubes: Reactivity and Curvature. *J. Phys. Chem. B* **2005**, *109*, 13755-13760.
103. Kajzar, F.; Taliani, C.; Danieli, R.; Rossini, S.; Zamboni, R.: Wave-dispersed third-order nonlinear optical properties of C₆₀ thin films. *Chem. Phys. Lett.* **1994**, *217*, 418-422.
104. Tutt, L. W.; Kost, A.: Optical limiting performance of C₆₀ and C₇₀ solutions. *Nature* **1992**, *356*, 225-226.
105. Allemand, P. M.; Khemani, K. C.; Koch, A.; Wudl, F.; Holczer, K.; Donovan, S.; Gruner, G.; Thompson, J. D.: Organic Molecular Soft Ferromagnetism in a Fullerene-C₆₀. *Science* **1991**, *253*, 301-303.

106. Holczer, K.; Klein, O.; Huang, S.-m.; Kaner, R. B.; Fu, K.-j.; Whetten, R. L.; Diederich, F.: Alkali-Fulleride Superconductors: Synthesis, Composition, and Diamagnetic Shielding. *Science* **1991**, 252, 1154-1157.
107. Hebard, A. F.; Rosseinsky, M. J.; Haddon, R. C.; Murphy, D. W.; Glarum, S. H.; Palstra, T. T. M.; Ramirez, A. P.; Kortan, A. R.: Superconductivity at 18 K in potassium-doped C₆₀. *Nature* **1991**, 350, 600-601.
108. Da Ros, T.; Prato, M.: Medicinal chemistry with fullerenes and fullerene derivatives. *Chem. Commun.* **1999**, 663-669.
109. Brettreich, M.; Hirsch, A.: A highly water-soluble dendro[60]fullerene. *Tetrahedron Lett.* **1998**, 39, 2731-2734.
110. Pellicciari, R.; Costantino, G.; Marinozzi, M.; Natalini, B.: Modulation of glutamate receptor pathways in the search for new neuroprotective agents1. *Il Farmaco* **1998**, 53, 255-261.
111. An, Y. Z.; Anderson, J. L.; Rubin, Y.: Synthesis of .alpha.-amino acid derivatives of C₆₀ from 1,9-(4-hydroxycyclohexano)buckminsterfullerene. *J. Org. Chem.* **1993**, 58, 4799-4801.
112. Guldi, D. M.: Probing the Electron-Accepting Reactivity of Isomeric Bis(pyrrolidinium) Fullerene Salts in Aqueous Solutions. *J. Phys. Chem. B* **2000**, 104, 1483-1489.
113. Arbogast, J. W.; Darmanyan, A. P.; Foote, C. S.; Diederich, F. N.; Whetten, R. L.; Rubin, Y.; Alvarez, M. M.; Anz, S. J.: Photophysical properties of sixty atom carbon molecule (C₆₀). *J. Phys. Chem.* **1991**, 95, 11-12.
114. Sharma, S. K.; Chiang, L. Y.; Hamblin, M. R.: Photodynamic therapy with fullerenes in vivo: reality or a dream? *Nanomedicine* **2011**, 6, 1813-1825.
115. Tokuyama, H.; Yamago, S.; Nakamura, E.; Shiraki, T.; Sugiura, Y.: Photoinduced biochemical activity of fullerene carboxylic acid. *J. Am. Chem. Soc.* **1993**, 115, 7918-7919.
116. Tabata, Y.; Murakami, Y.; Ikada, Y.: Antitumor Effect of Poly(Ethylene Glycol)-Modified Fullerene. *Fullerene Sci. Techn.* **1997**, 5, 989-1007.

CHAPTER 2

Cyclobutadiene–C₆₀ Adducts: N-Type Materials for Organic Photovoltaics with High V_{OC}

Adapted and reprinted in part from:

G. D. Han, W. R. Collins, T. L. Andrew, V. Bulović, and T. M. Swager.

“Cyclobutadiene–C₆₀ Adducts: N-Type Materials for Organic Photovoltaic Cells with High V_{OC}.”

Adv. Funct. Mater. **2013**, *23*, 3061-3069.

2.1. Introduction

Bulk heterojunction (BHJ) polymer solar cells (PSCs), composed of conjugated polymer donors and small or macromolecule acceptors, are leading compositions in the quest for practical organic photovoltaic cells.^{1,2} The bicontinuous nature of the phases in BHJ creates a large surface to volume ratio for efficient exciton dissociation, and facile and low-cost fabrication methods are compatible with large scale production.^{3,4} Despite extensive efforts to improve the properties of the constituent materials and morphologies of BHJ systems, competing with the power conversion efficiency (PCE) of silicon-based solar cells remains a challenge.⁵ In pursuit of ideal BHJ electronic structures, researchers have developed low band gap p-type polymers that strongly absorb high fractions of the solar spectrum and assemble into desirable film morphologies.^{6,7} Efforts to improve n-type acceptor components have included BHJs with small molecules such as 9,9'-bifluorenylidenes, perylenediimides, and vinazenes.⁸⁻¹⁰ Nevertheless, fullerenes are presently the most widely used and highest performing materials in part due to their high electron affinities and low reorganization energies for electron transfer.¹¹ Tailoring the electronic structure of fullerene is therefore of interest, and reactions with organometallic reagents, radicals, and transition-metal complexation have been investigated to create new fullerenes for BHJs.¹²⁻¹⁴ The reactivity of fullerene resembles that of an electron-deficient polyolefin, and as such, a dominant functionalization strategy has been to use cycloaddition reactions.^{15,16} Noteworthy examples include the synthesis of PCBM ([6,6]-phenyl- C_{61} -butyric acid methyl ester) via 1,3-dipolar cycloaddition and indene- C_{60} adducts from Diels-Alder reactions.¹⁷⁻¹⁹

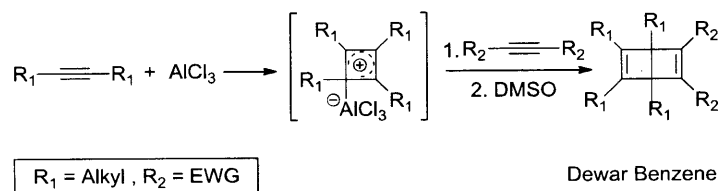
Less-than-optimal band offsets at the BHJs can lead to energy loss and low open-circuit voltages in solar cells. In order to increase power conversion efficiencies, there have been efforts

to increase the HOMO_D-LUMO_A (A: acceptor, D: donor) gap which is often considered to be proportional to the open-circuit voltage.²⁰ Many polymer donors with alternating electron-rich and electron-poor units have been designed for optimized absorption of the solar spectrum. Decreasing the HOMO energy of the donor polymers can be accomplished by simple modifications of the electron-rich repeating units, but this typically leads to an expanded band gap that reduces the solar absorption efficiency, thereby giving a smaller short-circuit current density (J_{SC}).²¹⁻²³ As a result, an alternative, and perhaps more predictive, method is to increase the LUMO energy level of the fullerenes to create increased V_{OC} s. Most C_{60} functionalization methods, including cycloaddition reactions, break the full conjugation of the C_{60} π -system and generally decrease the electron affinity and raise the LUMO level.²⁴ The extent of this change varies depending on the nature of the functional groups attached to the C_{60} core. The decreased relative electron affinity of C_{60} is measured by the change of the onset reduction potential or the calculated LUMO level.^{25,26} In this context, there has recently been interest in indene- C_{60} acceptors because these materials exhibit ca. 50–170 mV reduced electron affinities (higher LUMO) relative to PCBM.²⁷ It would appear that the short distance between the C_{60} π -system and the π -orbitals of the addend aromatic ring of the indene affects the LUMO energy.

To expand upon the hypothesis that cofacial π -orbital interactions between C_{60} and an attached group can effectively raise the fullerene LUMO levels, we have targeted a new functionalization method that makes use of the well-known zwitterionic $AlCl_3$ -cyclobutadiene adducts. The release of the cyclobutadienes by treatment of alkyne- $AlCl_3$ adducts with weak Lewis bases has been found to result in Diels-Alder reactions with alkynes (Scheme 2.1)²⁸ to give Dewar benzene products that have fairly small angles (114.6–114.9°) between two

cyclobutene rings.²⁹ As a result, we rationalized that Diels–Alder adducts of similarly generated cyclobutadiene adducts with fullerenes could give rise to strong cofacial π -orbital interactions.

Scheme 2.1. $AlCl_3$ -assisted Diels–Alder reaction of alkynes



In this study we report the syntheses of mono- and multiadducts of tetramethylcyclobutadienes (Scheme 2.2) and tetrabutylcyclobutadienes to fullerenes (Figure 2.1). The electrochemical, photophysical, and thermal properties of these new fullerenes have been studied, and their use in photovoltaic devices with poly(3-hexylthiophene) (P3HT) has been evaluated in comparison with PCBM. Tetramethylcyclobutadiene- C_{60} mono-, bis-, and trisadducts (TMCB-Mono, TMCB-Bis, and TMCB-Tris) all exhibited higher open-circuit voltages than that of PCBM, and TMCB-Mono showed comparable power conversion efficiency (2.49%) to PCBM (2.57%) devices under the identical conditions. Lastly, the π -orbital interactions between cyclobutene and the C_{60} cage were probed by removing the appended double bond by epoxidation. The increased electron affinity of the cyclobutane–epoxide- C_{60} was measured by cyclic voltammetry and calculated using density functional theory. All of our results are consistent with the hypothesis that π - π orbital interactions are an effective means to adjust the fullerene LUMO levels.

Scheme 2.2. Synthesis of TMCB fullerenes

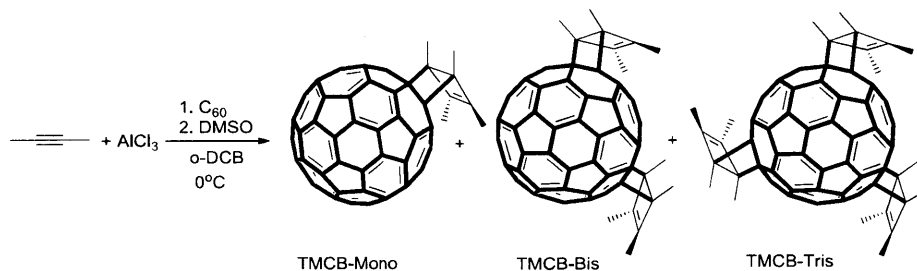
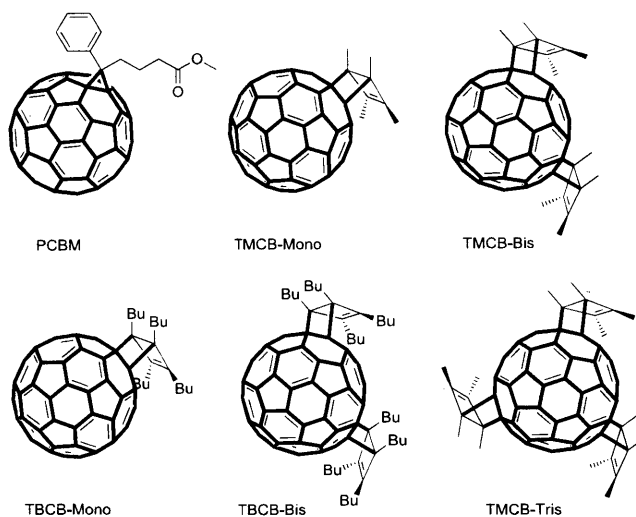


Figure 2.1. Structures of functionalized fullerenes



2.2. Results and Discussion

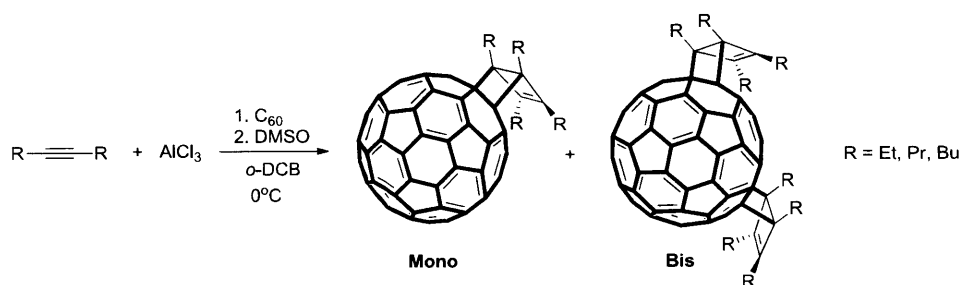
2.2.1. Syntheses of Tetraalkylcyclobutadiene- C_{60} Adducts

It is well-known that aluminum chloride reacts with internal alkynes to generate cyclobutadiene intermediates with a σ -bonded aluminum moiety (Scheme 2.1).²⁸ The intermediate cyclobutadiene, which is liberated by addition of dimethylsulfoxide, is very reactive in [4+2] cycloaddition reactions either as a diene (Scheme 2.1) or as a reactive alkene.³⁰ C_{60} is a potent dienophile³¹ and new n-type C_{60} derivatives are created via Diels-Alder reactions with the *in situ* generated tetraalkylcyclobutadienes.

The reactions were run under moisture-free conditions wherein the reaction of 2-butyne and aluminum chloride was first combined with C_{60} and subsequent treatment with DMSO produced tetramethylcyclobutadiene- C_{60} mono-, bis-, and trisadducts (Scheme 2.2). By varying the molar ratio of the alkyne, aluminum chloride, and C_{60} , we were able to selectively increase the yield of each product in the mixture. In many cases, the syntheses of functionalized fullerenes involve tens of equivalents of the non-fullerene reagents to ensure a high-yielding functionalization.^{27,32} In contrast, four equivalents of 2-butyne relative to C_{60} produce monoadduct and bisadduct in isolated respective yields of 32 % and 17 % after rigorous purification. Generation of four equivalents of cyclobutadiene (8 eq. of 2-butyne) increases the isolated yield of the pure trisadduct to 8 %. It is also the case that the syntheses of fullerene derivatives by Diels-Alder reactions often require long reaction times,³³ and high temperatures such as refluxing *o*-dichlorobenzene (b.p. 180.5° C).³² The cyclobutadiene addition was carried out at low temperatures (between 0° C and room temperature) with reaction times of less than 2 hours. After the reaction, the mixture of fullerene adducts was separated by HPLC using a 5PBB Cosmosil column with toluene elution. ^1H and ^{13}C nuclear magnetic resonance (NMR) spectroscopy as well as mass spectrometry (MS) confirmed the attachment of the cyclobutene moiety. The similar procedure provided other tetraalkylcyclobutadiene- C_{60} adducts starting with symmetric internal alkynes such as 3-hexyne, 4-octyne, and 5-decyne (Scheme 2.3). The longer alkyl products provide for high solubility in organic solvents such as chloroform, dichloromethane, and toluene. Longer chains disfavor trisadduct formation, presumably due to the steric strain on the C_{60} surface. For example, for the functionalization starting with 5-decyne, we could not observe the trisadduct even when using 16 equivalents of this alkyne. Figure 2.1

details the representative five new functionalized fullerenes selected for further investigation and the well-known PCBM.

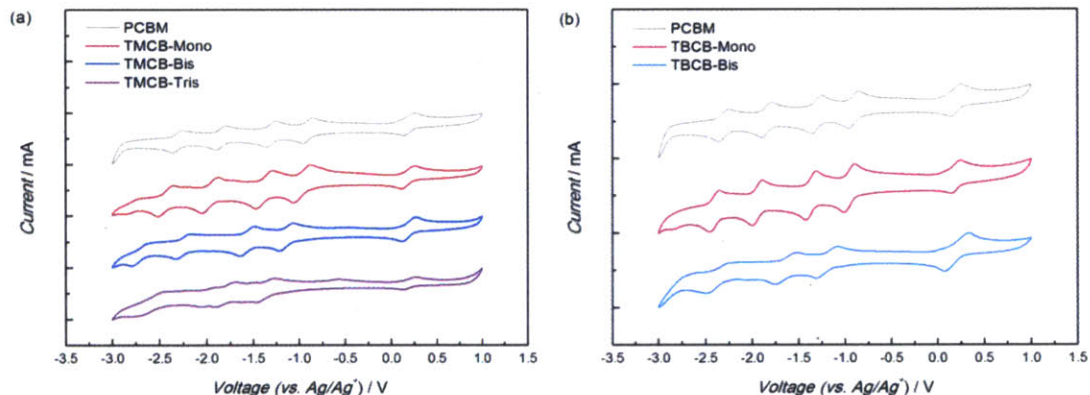
Scheme 2.3. $AlCl_3$ -assisted Diels-Alder cycloaddition reactions between C_{60} and 3-Hexyne, 4-Octyne, and 5-Decyne



2.2.2. Electrochemical Properties

C_{60} has triply-degenerated low-lying LUMO energy levels and thereby can be reduced by up to six electrons.³⁴ A series of cyclic voltammograms in Figure 2.2 shows that three or four reversible redox waves are retained in the functionalized fullerenes under anhydrous air-free conditions, relative to the ferrocene/ferrocenium (Fc/Fc^+) internal standard peaks at ca. 200 mV (± 0.5 mV).

Figure 2.2. Cyclic voltammograms of PCBM and (a) TMCB Mono-, Bis-, and Trisadducts (b) TBCB Mono-, and Bisadducts (under N_2 , 0.1M Bu_4NPF_6 in toluene/acetonitrile (4:1), Pt (WE), Pt wire (CE), $Ag/AgNO_3$ (RE), scan rate 0.1 V/s, Fc/Fc^+ internal standard $E_{1/2}$ at 0.20 V).



The monoadducts (TMCB-Mono and TBCB-Mono) exhibited four reversible redox peaks (Figure 2.2 (a) and (b)), which are all shifted to negative potentials by ca. 100 mV as compared to PCBM, and the bisadducts showed an additional ca. 200 mV shift relative to the monoadducts. The measured half-wave potentials are listed in Table 2.1, together with the estimated LUMO energy levels relative to the vacuum level.

The cyclic voltammogram of the trisadduct contained three major sets of the redox peaks, as well as another set of peaks, which we assume to be a persistent tetrakisadduct impurity (Figure 2.2 (a)). Despite the less defined features, it is clear that the three main redox waves are further shifted by about 200 mV as compared to the bisadduct. The reversible sets of redox curves shown in Figure 2.2 (a) and (b) confirm that the functionalization preserves the key electronic accepting characteristics of C_{60} . The pronounced negative shifts of redox curves and the corresponding increase of LUMO energy levels relative to PCBM (90 meV for TMCB-Mono, 260 meV for TMCB-Bis, and 450 meV for TMCB-Tris) are considerably greater than the indene- C_{60} mono- and bisadducts (50 meV and 170 meV, respectively).²⁷ This behavior is consistent with our designs that make use of the small angles between fused four-membered rings, which increases the π -orbital interaction between the pendant cyclobutene moiety and C_{60} centered states. It is not straightforward to explain the difference in LUMO shifts of indene- C_{60}

and cyclobutadiene–C₆₀. The proximity of the addend π -orbitals to C₆₀ surface, or the angle between two rings, of either compound has not been determined and crystal structures have not been obtained to date. The different extent of LUMO shifts could be also influenced by other factors, given two dissimilar addend structures.

The cyclic voltammograms of TMCB-adducts and TBCB-adducts are similar in terms of the shape and the positions of potentials, but the TBCB-adducts exhibit slightly more negative redox potentials. Considering the higher LUMOs of the TBCB-series we expect a slightly higher V_{OC} in photovoltaic devices relative to those obtained for TMCB-adducts.

Table 2.1. HOMO and LUMO Energies Calculated from UV–Vis absorption and Cyclic Voltammetry

C ₆₀ derivative	E ₁ [V][a]	E ₂ [V]	E ₃ [V]	E _{onset} [V][b]	LUMO[eV][c]	λ_{onset} [nm][d]	HOMO[eV][e]	E _{gap} [eV][f]
PCBM	-0.90	-1.31	-1.85	-0.77	-3.83	723	-5.55	1.72
TMCB-Mono	-0.96	-1.38	-1.97	-0.86	-3.74	738	-5.42	1.68
TMCB-Bis	-1.14	-1.57	-2.25	-1.03	-3.57	746	-5.24	1.67
TMCB-Tris	-1.37	-1.79	-2.57	-1.22	-3.38	697	-5.16	1.78
TBCB-Mono	-0.96	-1.36	-1.94	-0.88	-3.72	740	-5.40	1.68
TBCB-Bis	-1.19	-1.64	-2.38	-1.10	-3.50	751	-5.15	1.65

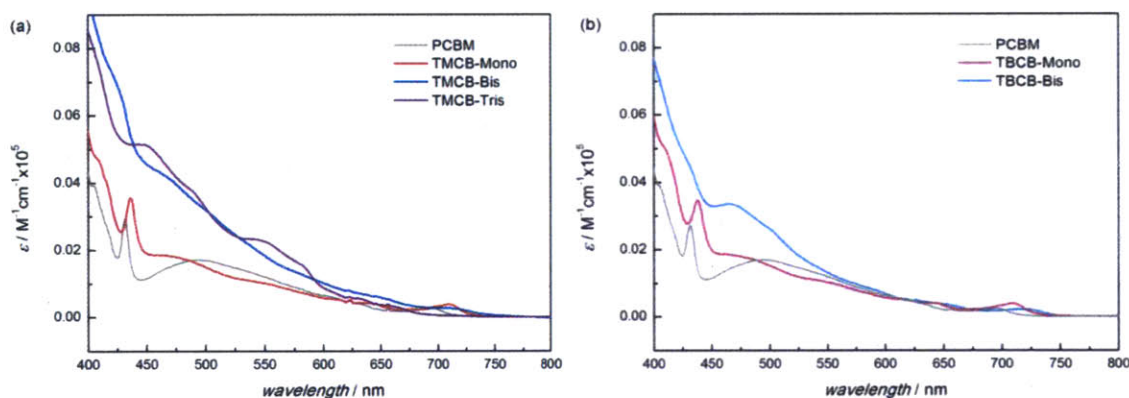
[a] Half-wave potential, 0.5 (Ep.a.+Ep.c.); Ep.a., anodic peak potential; Ep.c. cathodic peak potential; [b] Onset reduction potential; [c] LUMO (eV) = $-e (E_{\text{onset}}+4.60)$; [d] Onset absorption wavelength; [e] HOMO = LUMO–E_{gap} [eV]; [f] Band gap = $hc/\lambda_{\text{onset}}$, converted [J] to [eV]; h, Planks constant; c, speed of light.

2.2.3. Photophysical Properties

The visible and near-infrared spectral absorptions of BHJ devices are a major determinant of solar cell efficiencies. J_{SC} is dependent on the number of charge carriers generated and their mobility.²⁰ Considerable efforts have focused on creating donor polymers with band gaps that match the solar spectrum. Although J_{SC} is generally dominated by the photon collection of the

donor polymer, stronger visible light absorption of the acceptors can also contribute to light harvesting. Specifically, the weak optical absorptions of PCBM are considered a limitation and have led to interest in more costly C_{70} acceptor materials.³⁵ In Figure 2.3, we show comparative absorption spectra (400 nm–800 nm) of our new fullerene derivatives relative to PCBM. The cyclobutadiene functionalized fullerenes exhibited the similar or higher absorptivity relative to PCBM. A more intense absorption was observed for the higher adducts, which is consistent with desymmetrization of fullerenes.

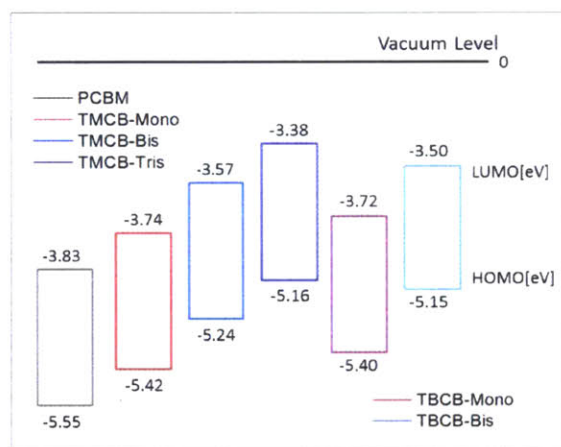
Figure 2.3. UV–Vis absorption spectra of PCBM (2.4×10^{-5} M) and (a) TMCB-Mono (2.5×10^{-5} M), Bis (2.4×10^{-5} M), and Tris (2.0×10^{-5} M) (b) TBCB-Mono (2.3×10^{-5} M), and Bis (1.3×10^{-5} M) in $CHCl_3$.



The weak spikes around 430 nm for TMCB- and TBCB-Mono are characteristic for 1,2-addition products, which confirms the structures depicted in Scheme 2.2. A hypothetical 1,4-adduct, which would form if C_{60} acted as a diene and cyclobutadiene as a dienophile, would exhibit a broad absorption band around 450 nm, instead.³⁶⁻³⁹ The absorption peaks around 430 nm are slightly red-shifted from those of PCBM. Additionally, the bis- and trisadducts showed broader absorptions as a result of the fact that they are a mixture of regioisomers. Based upon their absorption properties these new fullerene derivatives appear to offer advantages over

PCBM in terms of the higher absorptivity and the red-shifted absorption edge around 700 nm. The absorption edge wavelengths, λ_{onset} , vary from 697 nm to 751 nm, and longer wavelengths were observed for bisadducts than monoadducts and PCBM (Table 2.1.). The trisadduct is a 56- π -electron fullerene and deviates from the trend with a small value of λ_{onset} . The band gaps and the HOMO energy levels of the fullerenes were calculated from λ_{onset} and the first reduction wave, and are summarized in Figure 2.4 and Table 2.1.

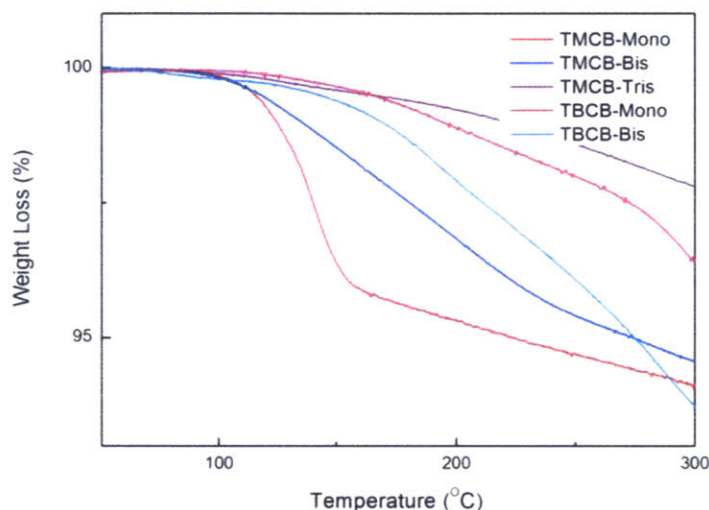
Figure 2.4. HOMO–LUMO energy diagram of fullerene derivatives. The energy levels were drawn relative to the vacuum level that is by definition set to zero.



2.2.4. Thermal Properties

The thermal stability of the molecules was determined by thermogravimetric analysis (TGA), which revealed weight loss of less than 5% at 200° C under N₂ atmosphere (Figure 2.5). All functionalized fullerenes are less stable than pristine C₆₀, which has outstanding thermal stability up to 500–600° C.⁴⁰ C₆₀ derivatives often display a change in morphology or decomposition at around 150° C, and the typical annealing temperatures used in polymer solar cell fabrications affect their performance.

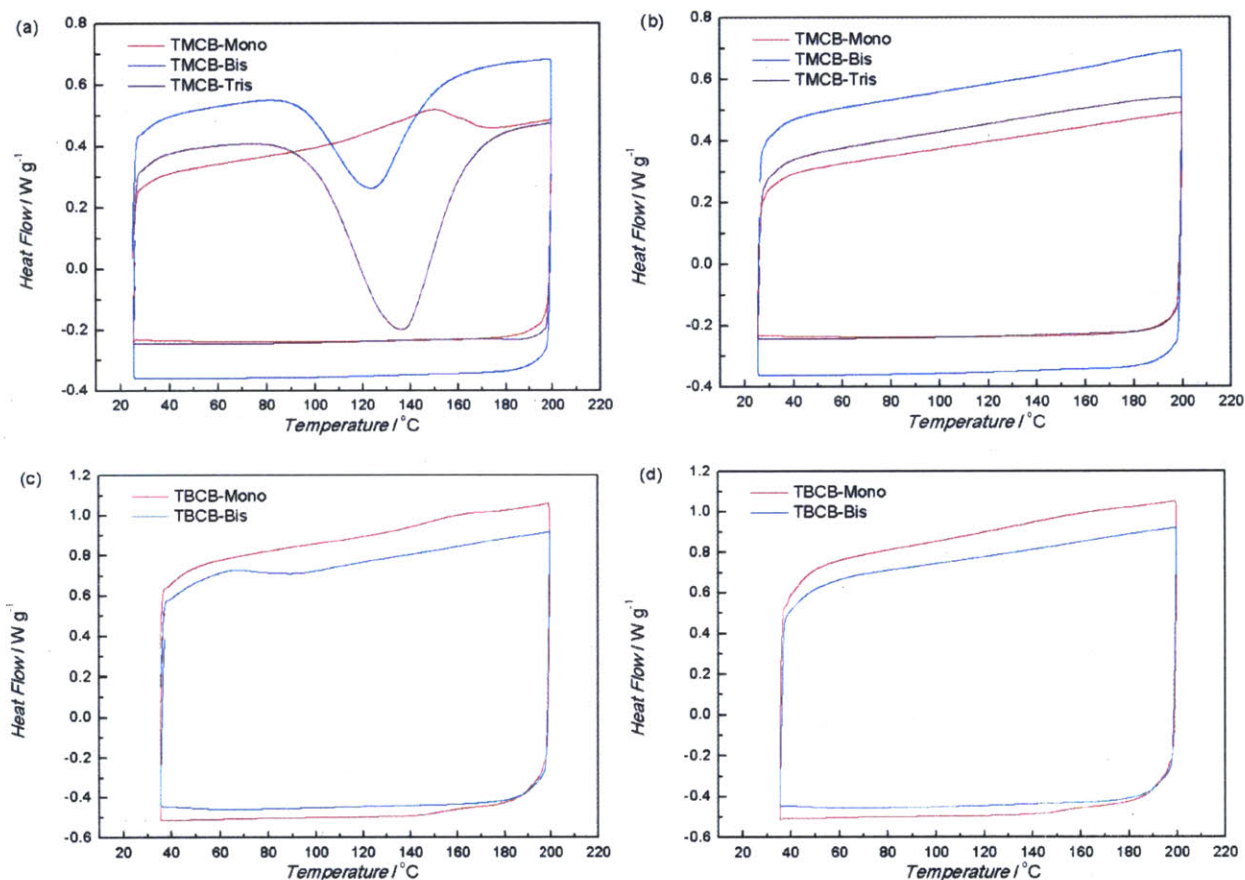
Figure 2.5. TGA analysis of TMCB- and TBCB-adducts with scan rate of $10^{\circ}\text{C}/\text{min}$ from 30°C to 800°C . Temperature of 5% weight loss of each compound is 223.4°C (TMCB-Mono), 326.0°C (TBCB-Mono), 274.7°C (TMCB-Bis and TBCB-Bis), and 424.4°C (TMCB-Tris). At 150°C , a typical annealing temperature of BHJ PSC fabrication, all compounds show reasonable thermal stabilities.



To further investigate the thermal properties of the fullerene adducts and the effects of annealing, we conducted differential scanning calorimetry (DSC) experiments over the range from 25°C to 200°C (Figure 2.6). In the first cycle, a strong and broad exothermic heat flow was observed for TMCB-Bis and Tris from 90°C to 150°C and 80°C to 190°C , respectively (Figure 2.6 (a)). In contrast, the TMCB-Mono displays a small endothermic peak which starts to appear at ca. 110°C , which is likely due to loss of residual toluene (b.p. 111°C). The second DSC cycles were featureless for all of the compounds (Figure 2.6 (b)). The mono- and bisadducts of tetrabutylcyclobutadiene exhibited relatively featureless heat flow to their tetramethyl counterparts (Figure 2.6 (c, d)).

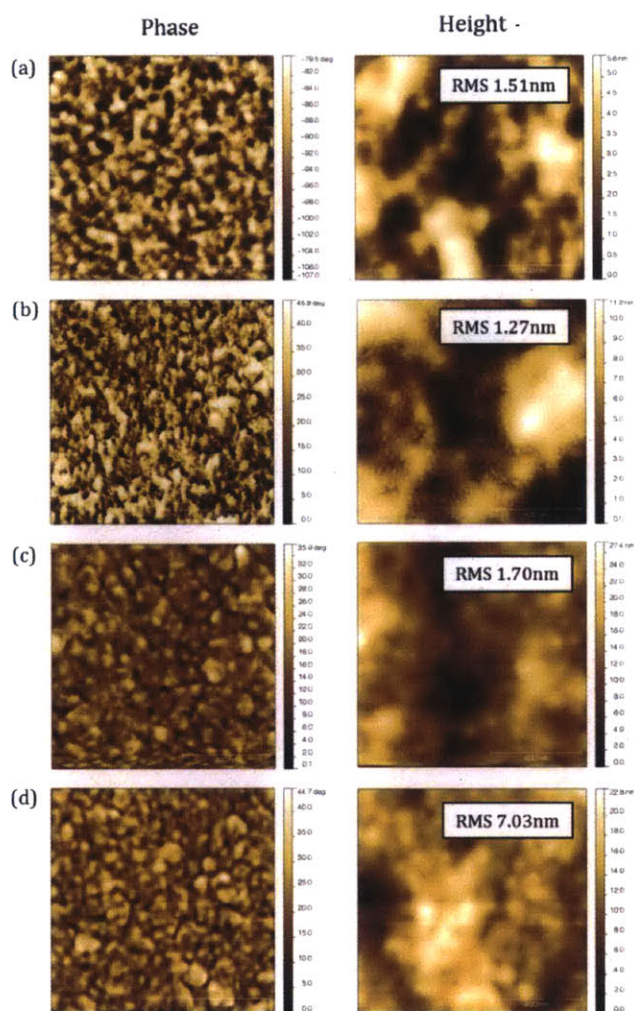
Figure 2.6. Differential scanning calorimetry (DSC) characteristics of TMCB-Mono, Bis, and Tris on the (a) first and (b) second cycle, and those of TBCB-Mono and Bis on the (c) first and (d) second cycle. All the heat flows were measured at the scan rate of $10^{\circ}\text{C}/\text{min}$ over the range

from 25° C or 35° C to 200° C. Curves from the second to the fifth cycle were identical without any endothermic/exothermic features.



BHJs formed with P3HT after annealing at 150° C for 20 min were studied by atomic force microscopy (AFM) (Figure 2.7). The larger grain sizes (root-mean-square roughness) and more pronounced phase separation were observed in the films with higher adducts. The P3HT/TMCB-Mono morphology most closely resembled the roughness of the P3HT/PCBM blend. We were interested in determining if any of the features observed for the higher adducts in the DSC and AFM reflected thermal decomposition or only morphology changes. Indeed our new fullerene derivatives could be susceptible to retro-cycloaddition reactions as other fullerene cycloadducts.^{41,42}

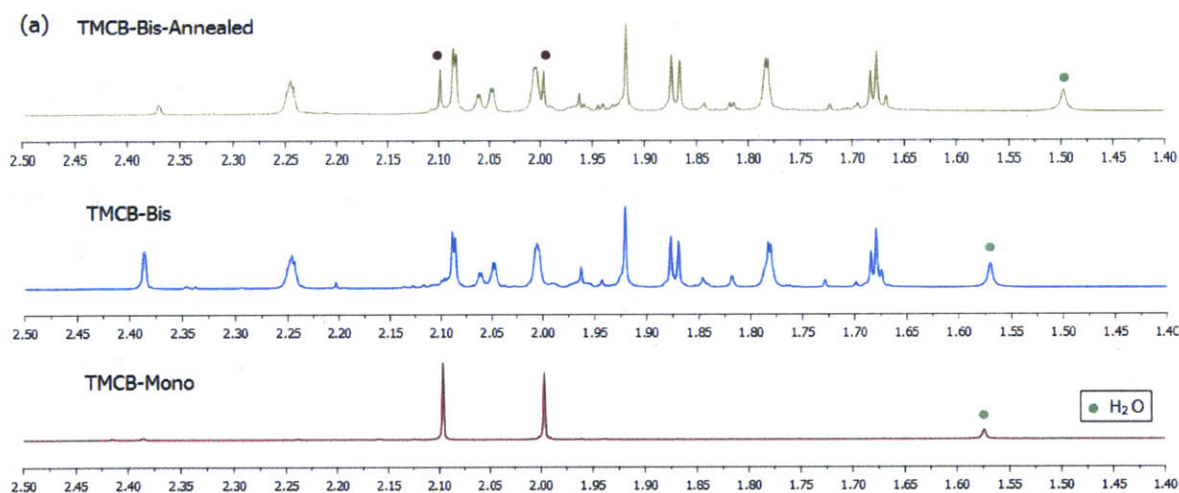
Figure 2.7. Tapping-mode atomic force microscopy (1 μ m window) phase and topography images of the films prepared from (a) PCBM, (b) TMCB-Mono, (c) TMCB-Bis, and (d) TMCB-Tris. P3HT was used as a donor for all devices. PEDOT:PSS was used as the underlayer. All BHJs were annealed at 150 $^{\circ}$ C for 20 min. Root-mean-square roughness was measured and indicated in the topography images.

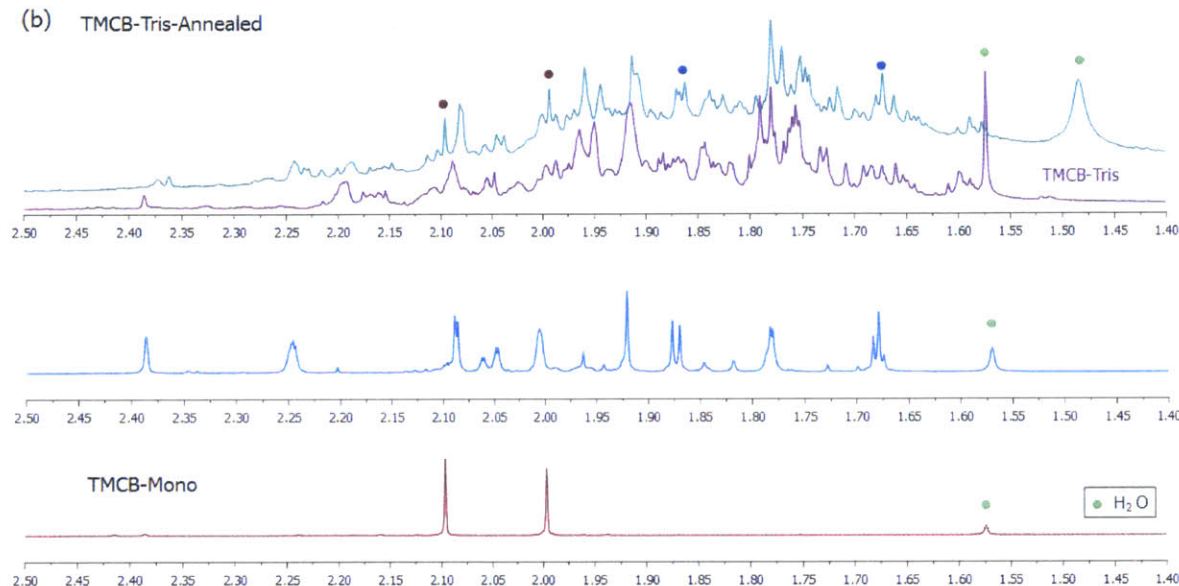


In order to investigate this, we measured the ^1H NMR spectra of the fullerene derivatives after three DSC cycles (25 $^{\circ}$ C–200 $^{\circ}$ C, 10 $^{\circ}$ C/min) (Figure 2.8 (a, b)). The TMCB-Bis gained the peaks assignable to TMCB-Mono, and TMCB-Tris gained the peaks indicating the generation of TMCB-Mono and TMCB-Bis. As a result, it is possible that larger phase separation of the BHJ

layers with the multiadducts is related to conversion of the fullerene multiadducts into less-functionalized adducts upon annealing. The ^1H NMR spectra of the TMCB-Mono, TBCB-Mono, and TBCB-Bis after being subjected to three DSC cycles did not display any detectable changes thereby reconfirming their superior thermal stability as compared to the TMCB multiadducts.

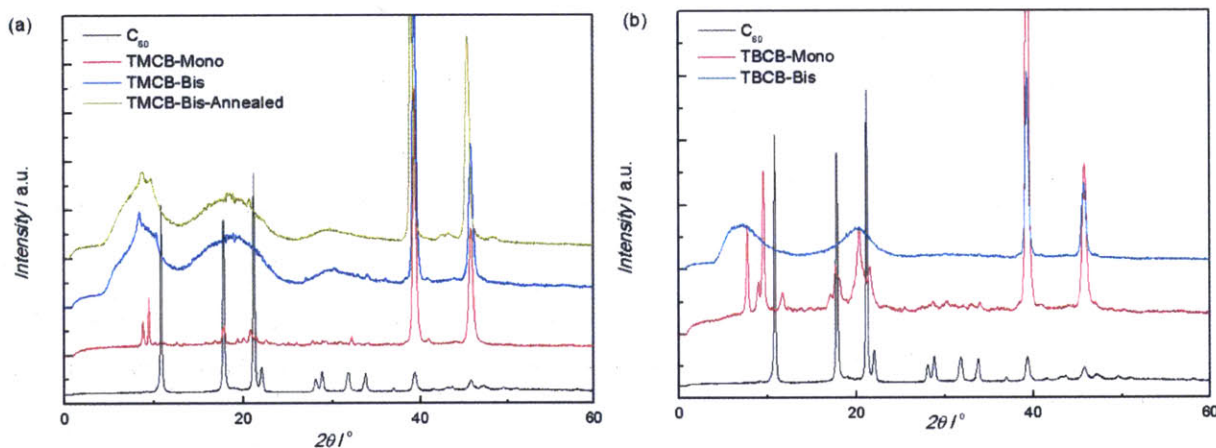
Figure 2.8. ^1H NMR spectra of annealed (a) TMCB-Bis and (b) TMCB-Tris after three DSC cycles. Red dots correspond to the peaks of TMCB-Mono, and blue dots to TMCB-Bis. The gained features after annealing indicate the thermal decomposition of the multiadducts to less-functionalized adducts.





To determine if crystallization might also be responsible for the exothermic DSC transitions of the TMCB multiadducts at high temperatures, we conducted X-ray diffraction experiments (Figure 2.9 (a, b)). TMCB and TBCB monoadducts are a single regioisomer, presumably fused to C_{60} in [6,6]-closed fashion as usual Diels–Alder cycloaddition products of C_{60} ,⁴³⁻⁴⁵ and exhibit microcrystallinity. The butyl groups on cyclobutadiene- C_{60} , as expected, produce a larger lattice spacing (11.2 Å) than methyl groups (10.1 Å). For multiadducts, the mixture of isomers reduced the crystallinity of the sample, and TMCB-Bis remained in an amorphous state even after three DSC cycles. As a result, the observed DSC exothermic transitions for the multiadducts are most likely the result of retro-cycloaddition reactions. In an attempt to produce a more stable analog, the reaction of C_{60} and naphthocyclobutadiene was conducted. However, the reaction did not proceed, presumably as a result of the fact that the tetraalkylcyclobutadiene behaves as the diene in the Diels Alder reaction and naphthocyclobutadiene would only be expected to behave as the dienophile.

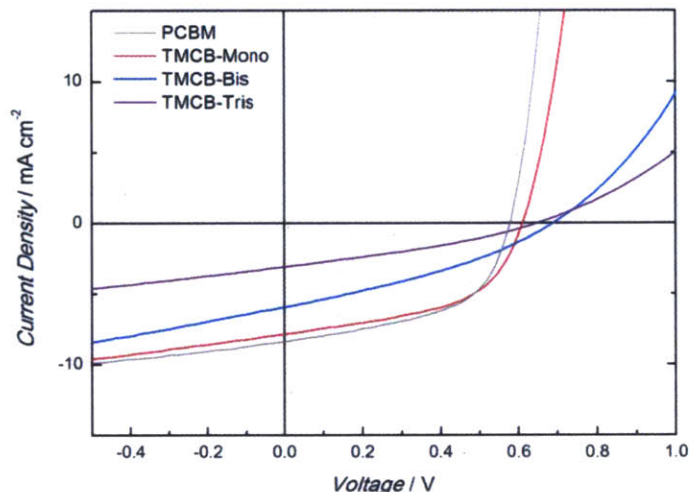
Figure 2.9. X-ray powder diffraction experiment of (a) TMCB-Mono, Bis and (b) TBCB-Mono, Bis. Decreased 2θ values of the monoadducts from C_{60} indicate their larger lattice constants in the microcrystalline phase, and the bisadducts are amorphous due to the presence of the multiple regioisomers. Annealing does not affect the crystallinity of TMCB-Bis.



2.2.5. Organic Photovoltaic Performances

Figure 2.10 details current density versus voltage (J - V) characteristics under illumination of select P3HT/fullerene BHJ solar cells. Specifically TMCB-Mono, Bis, and Tris are compared to the well-known P3HT/PCBM system. As predicted based on the LUMO energy levels, TMCB-Mono gives a higher open-circuit voltage than PCBM. The P3HT/TMCB-Mono system also displays a short-circuit current density, fill factor, and PCE (η) comparable to the P3HT/PCBM device. The J - V curve of TMCB-Bis displays a higher V_{OC} , consistent with its higher LUMO level, but a much lower J_{SC} and decreased fill factor lead to poor efficiency. We expect that the thermal instabilities of the higher fullerene cyclobutadiene adducts contributes to lower efficiencies. The performance of the P3HT/TMCB-Tris cell displays even lower J_{SC} .

Figure 2.10. Current density-voltage (J - V) characteristics of bulk heterojunction PSCs under AM 1.5 illumination at 100 mW/cm^2 . ITO (150nm)/ PEDOT:PSS (40nm)/ P3HT:Fullerenes (75nm)/ Ca (25nm)/ Al (80nm) used for device fabrication.



Field-effect mobilities of electrons are also decreased for the higher adducts in comparison to TMCB-Mono and the standard PCBM. $2.53 \times 10^{-3} \text{ cm}^2/\text{V}\cdot\text{s}$ for PCBM, $1.08 \times 10^{-3} \text{ cm}^2/\text{V}\cdot\text{s}$ for TMCB-Mono, $1.07 \times 10^{-5} \text{ cm}^2/\text{V}\cdot\text{s}$ for TMCB-Bis, and $1.34 \times 10^{-6} \text{ cm}^2/\text{V}\cdot\text{s}$ for TMCB-Tris were obtained. An interesting feature is that the open-circuit voltage of TMCB-Tris is smaller than that of TMCB-Bis. This discrepancy might result from the excessive decomposition of Tris upon annealing. In general, the open-circuit voltages of the BHJ polymer-fullerene films are influenced by intermolecular interactions in the solid state. Thus, they can exhibit quantitatively non-linear correlation with $\text{HOMO}_D\text{-LUMO}_A$ gaps, predicted by the solution-state measurements. Additionally, we note that the V_{OC} in organic BHJ solar cells is recombination limited.⁴⁶ Since we observe non-ideal BHJ morphologies with some of our fullerene adducts, which increases the rate of bimolecular recombination across the donor-acceptor interface, we hypothesize that part of the observed discrepancy in V_{OC} trends is also due to increased recombination. Correspondingly, the PCE (Table 2.2) of P3HT/TMCB-Mono (2.49%), comparable with that of P3HT/PCBM (2.57%), and the smaller values for P3HT/TMCB-Bis (1.35%) and P3HT/TMCB-Tris (0.65%) were consistent with the degree of phase separation and root-mean-square roughness discovered on AFM images.

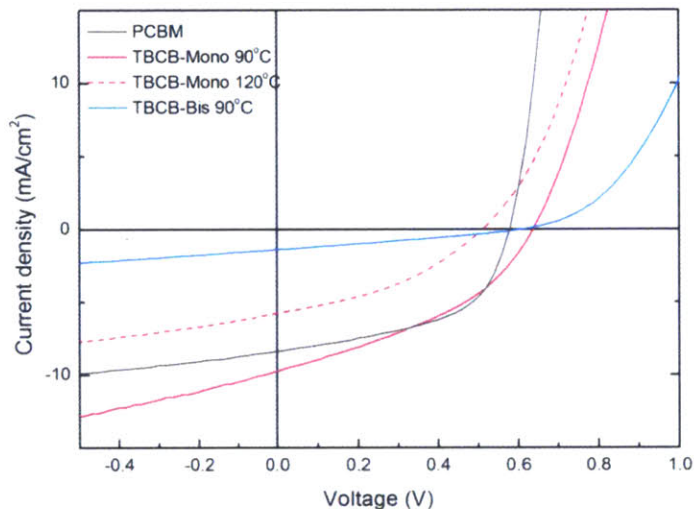
Table 2.2. Characteristics of OPV Devices [a]

	TMCB-Mono	Bis	Tris	PCBM
J_{SC} [mA/cm ²]	7.86	5.92	3.13	8.35
V_{OC} [V]	0.61	0.69	0.65	0.58
FF [%]	0.52	0.33	0.32	0.53
η [%]	2.49	1.35	0.65	2.57

[a] Definitions: short-circuit current density, J_{SC} ; open-circuit voltage, V_{OC} ; fill factor, FF; PCE, η .

In order to obtain the optimized performance of fullerene adducts with longer alkyl chains, we annealed the devices with TBCB-Mono and TBCB-Bis at 90° C (Figure 2.11). P3HT/TBCB-Mono blend produced higher V_{OC} (0.64 V) and J_{SC} (9.72 mA/cm²) compared to P3HT/PCBM, but the increased resistance in the blend resulted in lower fill factor and comparable PCE (2.43%). The decreased V_{OC} (0.61 V) and J_{SC} (1.37 mA/cm²) of P3HT/TBCB-Bis cell led to poor PCE (0.23%), thus reconfirming that less desirable performances are obtained from our multiadducts. In addition, the comparison of the J–V curves from different annealing conditions (90° C and 120° C) reflected the destructive effect of thermal annealing at high temperatures on the cells.

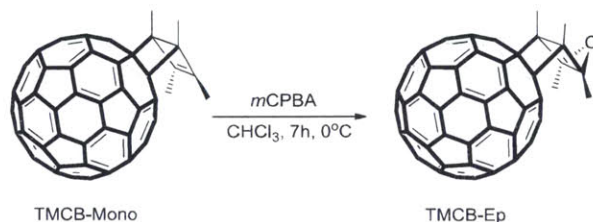
Figure 2.11. Current density–voltage (J–V) characteristics of bulk heterojunction PSCs under AM 1.5 illumination at 100 mW/cm². P3HT blend with TBCB-Mono and Bis after annealing at 90° C or 120° C.



2.2.6. Elimination of π -Orbital Interaction

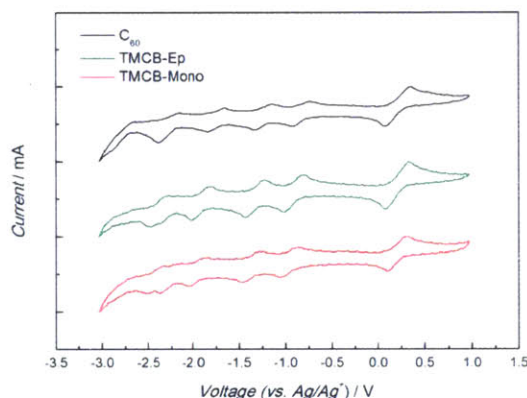
In order to chemically probe our hypothesis that large decrease in electron affinity in the cyclobutadiene-fullerenes is the result of strong interactions between the cyclobutene double bond and the C_{60} π -system, we devised a simple experiment to remove the double bond. Several reactions were attempted, but the most straightforward and the highest-yielding reaction was epoxidation with 3-chloroperbenzoic acid (*m*CPBA) (Scheme 2.4). The reaction proceeded with 96% yield, and the product (TMCB-EP) had significantly different polarity from the starting material, which facilitated purification. The identity of the product was supported by ^1H and ^{13}C NMR spectra (detailed in experimental section and appendix) as well as MS. Epoxidation of TBCB-Mono was unsuccessful presumably as a result of steric hindrance around the reaction site, and only starting material was recovered.

Scheme 2.4. Epoxidation of TMCB-Mono



Cyclic voltammetry of TMCB-Ep (Figure 2.12) exhibited four reversible redox peaks like other monoadducts, but half-wave potentials were located approximately half way between those of pristine C_{60} and the TMCB-Mono compound.

Figure 2.12. Cyclic voltammograms of C_{60} , TMCB-Ep, and TMCB-Mono (under N_2 , 0.1M Bu_4NPF_6 in Toluene/Acetonitrile(4:1), Pt (WE), Pt wire (CE), Ag/AgNO₃ (RE), scan rate 0.1 V/s, Fc/Fc⁺ internal standard $E_{1/2}$ at 0.20 V)



In Table 2.3, the half-wave potentials of TMCB-Ep were summarized. The difference between LUMO energy levels of C_{60} and TMCB-Ep is 60 meV, and the gap between those of TMCB-Ep and TMCB-Mono is 50 meV. From this observation, we conclude that orbital interactions between the cofacial cyclobutene and C_{60} π -systems contribute to the observed LUMO raising. The electron affinity of TMCB-Ep was still lower than that of C_{60} and this is presumably the result of the σ - π hyperconjugative interactions.

Table 2.3. Electrochemical Characteristics and LUMO Energy of C_{60} , TMCB-Ep, and TMCB-Mono

E_1 [V][a]	E_2 [V]	E_3 [V]	E_{onset} [V][b]	LUMO[eV][c]
--------------	-----------	-----------	--------------------	-------------

C ₆₀	-0.84	-1.24	-1.75	-0.75	-3.85
TMCB-Ep	-0.91	-1.34	-1.92	-0.81	-3.79
TMCB-Mono	-0.97	-1.38	-1.95	-0.86	-3.74

[a] Half-wave potential (V), 0.5 (Ep.a.+Ep.c.); Ep.a., anodic peak potential; Ep.c. cathodic peak potential; [b] Onset reduction potential; [c] LUMO (eV) = -e (E_{onset}+4.60).

To further support this assertion, we conducted quantum-chemical density functional theory (DFT) calculations (B3LYP functional/6-31G (d,p) basis set) of TMCB-Mono and TMCB-Ep. The geometry optimized structures (Figure 2.13 (a), (b)) had HOMO and LUMO energy levels of -5.57 eV and -3.04 eV for TMCB-Mono, and -5.69 eV and -3.16 eV for TMCB-Ep (Figure 2.14 (a), (b)). These results also indicated that epoxidation of the cyclobutene moiety decreased the LUMO level. The calculated distances between C₆₀ cage and the attached functional groups were 3.05 Å and 3.10 Å for TMCB-Mono and TMCB-Ep, sufficiently short to allow for cofacial π -orbital interactions.⁴⁷ It is apparent in the LUMO representations (side and front views on Figure 2.14 (a)) of TMCB-Mono that the wavefunction on the double bond of the cyclobutene moiety and that on the adjacent C₆₀ π -orbital possess the opposite signs. It is believed that the LUMO level of C₆₀ is raised effectively due to this close π - π interaction between the two moieties. On the other hand, for TMCB-Ep (Figure 2.14 (b)), the hyperconjugative interaction between the C–H σ -bonds of methyl groups and C₆₀ π -system is outstanding for most of the MOs rather than cofacial π interaction. Therefore, we could theoretically support the concept of the structural design of cyclobutadiene–C₆₀ for efficient cofacial π interaction and the experimental results.

Figure 2.13. (a) The optimized structure of TMCB-Mono (ball-bonds and tube representations) determined at B3LYP/6-31G(d,p) level of DFT calculation. Angle between two four-membered rings (θ) is 113.4°. (b) The optimized structure of TMCB-Ep ($\theta = 114.5^\circ$).

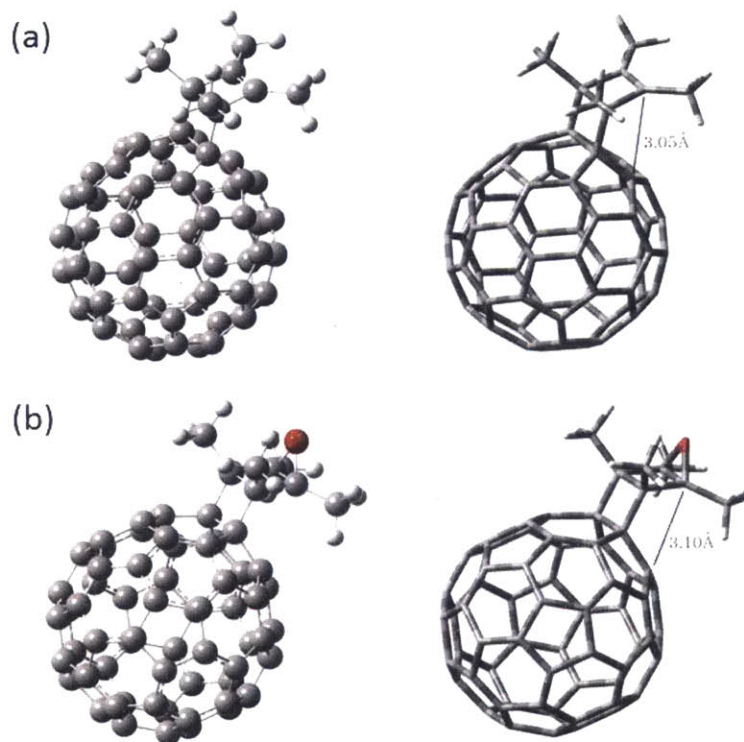
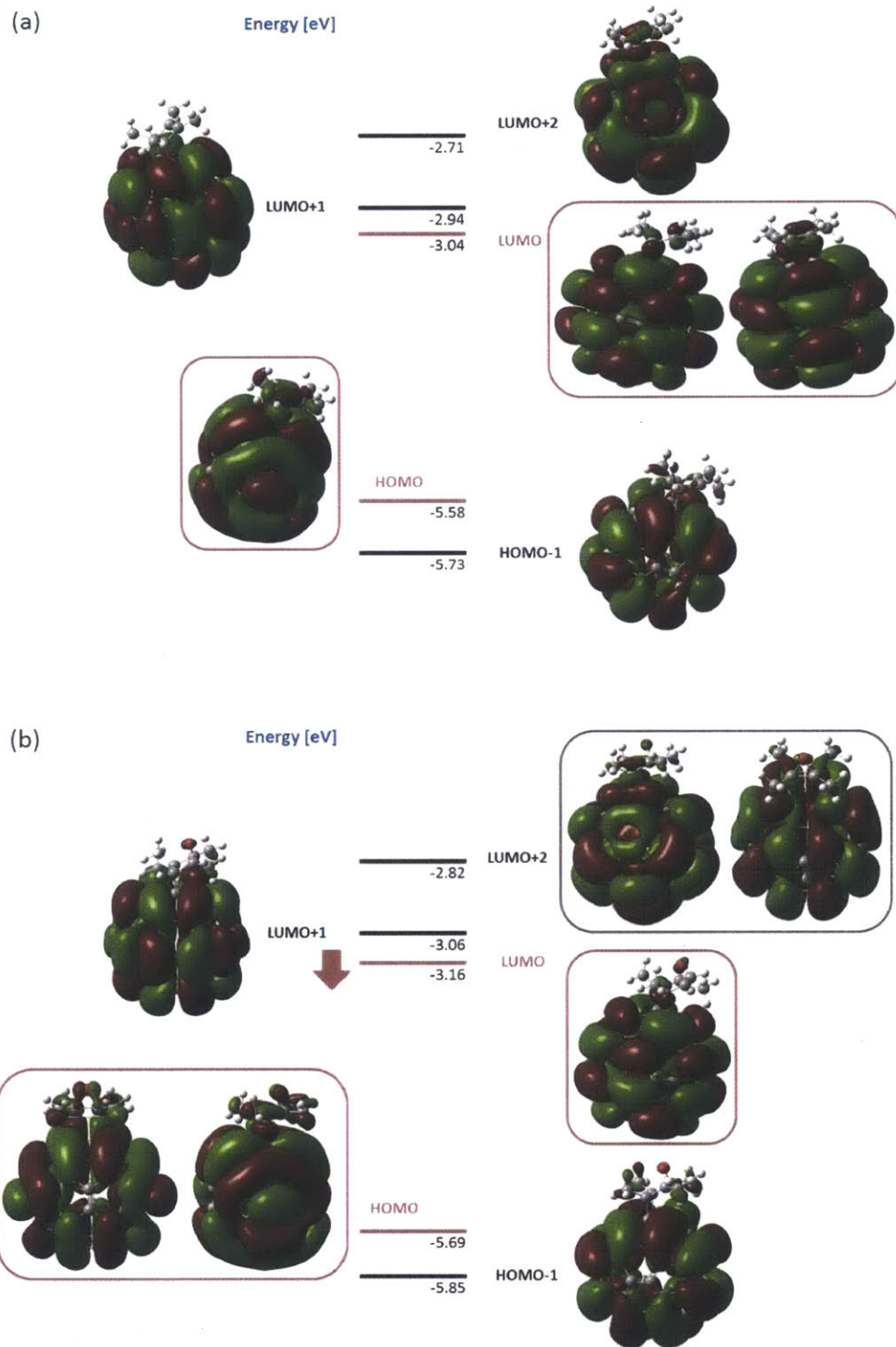


Figure 2.14. Molecular orbital (MO) energy level diagram and isosurface representations of frontier molecular orbitals (HOMO-1, HOMO, LUMO, LUMO+1, and LUMO+2). (a) TMCB-Mono. LUMO is shown in a side view and a front view for clearer comprehension. (b) TMCB-Ep. LUMO+2 and HOMO are shown in a side view and a front view for clearer comprehension.



2.3. Conclusions

Two families of tetraalkylcyclobutadiene- C_{60} adducts were generated via Diels-Alder cycloaddition reactions between *in situ* generated cyclobutadiene intermediates and C_{60} . The

mono-, bis-, and trisadducts of C_{60} with tetraalkylcyclobutadiene groups were formed, and their electrochemical, photophysical, and thermal properties were compared. The thermal annealing process in device fabrication was revealed to be destructive for the new fullerene bis- and trisadducts, leading to large phase separation and low PCEs. Epoxidation of cyclobutene confirmed that strong cofacial π -orbital interactions between C_{60} π -system and the double bond π -orbital contribute to raising the LUMO levels. Our results show that n-type materials for bulk heterojunction polymer solar cells can be chemically modified to fine-tune their electronic properties and thus the resulting open-circuit voltages in organic solar cells.

2.4. Experimental Section

Materials. C_{60} was purchased from SES Research, and aluminum chloride and alkynes were purchased from Sigma-Aldrich and used as received. Other materials including solvents and electrolyte salt were commercially available. Anhydrous solvents were obtained from a solvent purification system (Innovative Technologies).

Measurements. Reaction mixtures containing multiadducts of fullerenes were separated by 5PBB Cosmosil column (10 mm x 250 mm) from Nacalai Tesque, Inc. installed in Agilent Technologies ProsStar 210 High Pressure Liquid Chromatography (HPLC) system with 4mL/min elution of toluene. ^1H and ^{13}C NMR spectra were taken on Varian Inova-500 spectrometers. Chemical shifts were reported in ppm and referenced to residual solvent peaks (CDCl_3 : 7.26 ppm for ^1H , 77.20 ppm for ^{13}C). Thermally assisted direct analysis in real time (TA-DART)⁴⁸ mass spectrometry (MS) was measured on LCQ DECA (Thermo-Finnigan LLC) with ID-CUBE source (IonSense, Inc.). Capillary temperature was 200° C, and the capillary voltage was set to 15V in positive-ion mode. Helium was used as the ionization gas. Bruker

Daltonics Omnistar MALDI-TOF mass spectrometer was also used for mass determination. The matrix was prepared following a literature procedure⁴⁹, containing 7,7,8,8-tetracyanoquinodimethane in THF (10 mg/mL) with 1 % silver trifluoroacetate as a promoter. Molecules were dissolved in THF to 0.1 mg/mL concentration and the solution (2 μ L) was mixed with matrix (20 μ L). UV-Vis absorption spectra were obtained using Agilent 8453 diode-array spectrophotometer. Electrochemical measurements were carried out in a glove box under nitrogen, using an Autolab PGSTAT 10 or PGSTAT 20 potentiostat (Eco Chemie) in a three-electrode cell configuration. A Pt button (1.6 mm in diameter) electrode, a Pt wire, and a quasi-internal Ag wire submerged in 0.01M $AgNO_3$ /0.1M tetrabutylammonium hexafluorophosphate (TBAPF₆) in acetonitrile were used as a working electrode, a counter electrode, and a reference electrode, respectively, in 0.1M TBAPF₆ toluene/acetonitrile (4:1) solution. The ferrocene/ferrocenium (Fc/Fc⁺) redox couple was used as an internal standard, with the half-wave potentials observed between 0.195–0.203 V vs Ag/Ag^+ in toluene/acetonitrile (4:1) solution. Differential Scanning Calorimetry (DSC) was measured on a TA Instruments Q1000 DSC at scan rate of 10° C/min over the range of 25° C to 200° C or 35° C to 200° C. Thermogravimetric Analyses were performed with a TGA Q50 apparatus (TA Instruments) under nitrogen. Samples were heated at 10° C/min from 30° C to 800° C. X-ray diffraction was measured using Cu K α radiation on an Inel CPS 120 position-sensitive detector with a XRG 3000 generator using aluminum substrate during ca. 20 minute collection time. Gaussian 03 software package was used for the structure optimization and the frequency calculation at the DFT level. B3LYP functional/6-31G (d,p) basis set was used for the computation.

Syntheses of TMCB-Mono and TMCB-Bis. In a flame dried 100 mL Schlenk flask, $AlCl_3$ (148 mg, 1.11 mmol) was dissolved in dry *o*-dichlorobenzene (*o*-DCB) (10 mL) and stirred at 0 °C under Ar. 2-Butyne (174 μ L, 2.22 mmol) was added to the solution dropwise, and then *o*-DCB solution (20 mL) of C_{60} (400 mg, 0.555 mmol) was added. After 1 hour of stirring to ensure formation of homogeneous phase, DMSO (0.2 mL, 2.33 mmol) was added dropwise and the solution was slowly warmed up to room temperature. Ethanol (50 mL) was poured, and the precipitate was filtered and washed with ethanol several times, and then dissolved in toluene/hexane (1:1, 100 mL). The solution was passed through silica gel pad (5 cm), and concentrated in vacuo. Monoadduct and Bisadduct were separated by 5PBB Cosmosil column in toluene (4 mL/min) with yields of 31.9 % (146.6 mg) and 16.5 % (86.0 mg), respectively.

TMCB-Mono 1H NMR (500 MHz, $CDCl_3$, δ): 2.07 (s, 6H), 1.97 (s, 6H). ^{13}C NMR (500 MHz, $CDCl_3$, δ): 28 peaks found for C_{60} sp^2 carbons (154.62, 154.21, 147.24, 146.94, 146.91, 146.22, 146.14, 146.06, 145.53, 145.46, 145.39, 145.37, 145.35, 145.26, 144.69, 144.58, 143.21, 143.05, 142.79, 142.49, 142.35, 142.31, 142.25, 142.11, 140.43, 140.37, 139.06, 137.75), 129.22 (1C), 128.41 (1C), 74.38 (C_{60} sp^3), 60.38 (2C), 53.62 (CH_2Cl_2), 14.07 (2C), 11.56 (2C).

TMCB-Bis 1H NMR (500 MHz, $CDCl_3$, δ): 2.22 (m, 3H), 2.05 (m, 3H), 2.03-2.02 (m, 3H), 1.98 (m, 3H), 1.89 (s, 3H), 1.85-1.84 (m, 3H), 1.75 (m, 3H), 1.66-1.64 (m, 3H). ^{13}C NMR (500 MHz, $CDCl_3$, δ): 160-137 (C_{60} sp^2), 129-125 (alkene), 73.61 (C_{60} sp^3), 61-60 (cyclobutene sp^3), 14-11 (CH_3).

MS (ESI, m/z): Monoadduct $[M+H]^+$ calcd for $C_{68}H_{12}$, 829.1012; found, 829.04, Bisadduct $[M]^+$ calcd for $C_{76}H_{24}$, 937.0060; found, 936.99)

Synthesis of TMCB-Tris. In a flame dried 200 mL Schlenk flask, $AlCl_3$ (741 mg, 5.56 mmol) was dissolved in dry *o*-DCB (25 mL) and stirred at 0° C under Ar. 2-Butyne (0.88 mL, 11.1 mmol) was added to the solution dropwise, and then *o*-DCB solution (50 mL) of C_{60} (1.0 g, 1.39 mmol) was added. After 1 hour of stirring, DMSO (0.89 mL, 11.4 mmol) was added dropwise and the solution was slowly warmed up to room temperature. Ethanol (100 mL) was poured, and the precipitate was filtered and washed with ethanol several times, and then dissolved in toluene/hexane (1:1, 250 mL). The solution was passed through silica gel pad (5 cm), and concentrated in vacuo. 115 mg (7.9 %) of the product was obtained after purification by 5PBB Cosmosil column in toluene (4 mL/min). 1H NMR (500 MHz, $CDCl_3$, δ): 2.16-1.57 (m, 36H). ^{13}C NMR (500 MHz, $CDCl_3$, δ): 160-140 (C_{60} sp^2), 115-114 (alkene), 99.99 (C_{60} sp^3), 60-59 (cyclobutene sp^3), 29.91 (acetone), 14-11 (CH_3).

MS (MALDI-TOF, m/z): $[M]^+$ calcd for $C_{84}H_{36}$, 1045.1871; found, 1045.22

Synthesis of TMCB-Ep. TMCB-Mono (102mg, 0.123mmol) was dissolved in chloroform (15 mL) in a 50 mL round-bottom flask in which a solution of 3-chloroperbenzoic acid (max. 77 % purity, 76 mg, 0.339 mmol) in chloroform (5 mL) was added dropwise at 0 °C. The solution was slowly warmed up to room temperature during 7 hours of stirring, and a major product spot was detected on a TLC plate. The reaction mixture was diluted with dichloromethane (75 mL), and extracted with NaOH aqueous solution several times. The organic layer was dried with $MgSO_4$ and concentrated in vacuo. 100 mg (96.1 %) of the product was isolated after gradient silica column with 1:13 to 1:1 toluene/hexane eluent.

1H NMR (500 MHz, $CDCl_3$, δ): 1.98 (s, 6H), 1.87 (s, 6H). ^{13}C NMR (500 MHz, $CDCl_3$, δ): 29 peaks found for C_{60} sp^2 carbons (153.77, 153.69, 147.20, 146.76, 146.57, 146.30, 146.22, 146.21,

145.69, 145.55, 145.51, 145.43, 145.39, 144.75, 144.70, 143.35, 143.34, 142.94, 142.90, 142.55, 142.49, 142.26, 142.10, 142.19, 141.87, 140.64, 140.62, 138.87, 137.31), 71.38 (C_{60} sp³), 71.20 (2C), 62.46 (2C), 29.90 (acetone), 12.87 (2C), 12.12 (2C).

MS (ESI, m/z): $[M+H]^+$ calcd for $C_{68}H_{12}O$, 845.0961; found, 845.12

Syntheses of TBCB-Mono and TBCB-Bis. In a flame dried 50 mL Schlenk flask, $AlCl_3$ (150 mg, 1.12 mmol) was dissolved in dry *o*-DCB (15 mL) and stirred at 0° C under Ar. 5-Decyne (0.41 mL, 2.28 mmol) was added to the solution dropwise, and then *o*-DCB solution (50 mL) of C_{60} (200 mg, 0.28 mmol) was added. After 1 hour of stirring, DMSO (0.2 mL, 2.33 mmol) was added dropwise and the solution was slowly warmed up to room temperature. Ethanol (35 mL) was poured, and the precipitate was filtered and washed with ethanol several times, and then dissolved in toluene/hexane (1:4, 150 mL). The solution was passed through silica gel pad (5 cm), and concentrated in vacuo. Monoadduct and Bisadduct were separated by 5PBB Cosmosil column in toluene (4 mL/min) with yields of 40.1 % (111.1 mg) and 24.1 % (85.1 mg), respectively. 17.7 % (35.5 mg) of C_{60} was recovered.

TBCB-Mono ¹H NMR (500 MHz, $CDCl_3/CS_2$ 1:1, δ): 2.69-2.63 (m, 4H), 2.47-2.41 (m, 2H), 2.30-2.24 (m, 2H), 2.02-1.98 (m, 2H), 1.91-1.73 (m, 6H), 1.54-1.50 (m, 8H), 1.04-1.01 (t, 12H). ¹³C NMR (500 MHz, $CDCl_3/CS_2$ 1:1, δ): 30 peaks found for C_{60} sp² carbons (155.19, 153.81, 149.58, 147.25, 146.71, 146.23, 146.06, 145.99, 145.96, 146.87, 145.35, 145.33, 145.30, 145.18, 145.16, 144.53, 144.41, 143.08, 142.74, 142.71, 142.62, 142.31, 142.19, 142.09, 142.08, 141.95, 140.30, 140.09, 138.77, 137.78), 143.03 (1C), 142.89 (1C), 73.98 (C_{60} sp³), 64.00 (2C), 31.46 (2C), 31.43 (2C), 29.51 (2C), 28.90 (2C), 24.34 (2C), 23.83 (2C), 14.31 (2C), 14.28 (2C).

TBCB-Bis ^1H NMR (500 MHz, $\text{CDCl}_3/\text{CS}_2$ 1:1, δ): 2.55-1.34 (m, 42H), 1.01-0.90 (m, 24H). ^{13}C NMR (500 MHz, $\text{CDCl}_3/\text{CS}_2$ 1:1, δ): 160-137 (C_{60} sp^2 , alkene), 74-73 (C_{60} sp^3), 64-63 (cyclobutene sp^3), 35-14 (alkane).

MS (ESI, m/z): $[\text{M}+\text{H}]^+$ calcd for $\text{C}_{80}\text{H}_{36}$, 997.2890; found, 997.23

MS (MALDI-TOF, m/z): $[\text{M}]^+$ calcd for $\text{C}_{100}\text{H}_{72}$, 1273.6448; found, 1273.62

Device Fabrication. Pre-patterned indium tin oxide (ITO)-coated glass substrates (Thin Film Devices, Inc.) were sonicated in acetone (30 min) and isopropanol (30 min) and oxygen plasma-cleaned (3 min) immediately prior to deposition of the PEDOT:PSS layer. PEDOT:PSS (2–5 wt% in water, Aldrich) was spin-coated in a nitrogen atmosphere at 4000 rpm and annealed at 150°C (using a hotplate) for 15 min under nitrogen. A 40 nm PEDOT layer was thus obtained. Film thickness was determined by ellipsometry measurements on separate films prepared on silicon substrates. For the active layer, a 10 mg/mL solution of 1:1.2 P3HT:fullerene in 1,2-dichlorobenzene (DCB) was employed (in a representative example, P3HT (1.9 mg) and fullerene (2.3 mg) were dissolved in DCB (0.2 mL)). This solution (60 μL) was then spin-coated onto the PEDOT layer at 1000 rpm under nitrogen. The substrate was taken from the spin chuck and immediately placed under an inverted Petri dish inside the glovebox for 10 minutes to encourage solvent annealing from the small amount of residual DCB on the substrate. Next, the solar cells were placed on a 150°C hotplate and annealed for 20 min under nitrogen. A 70 ± 5 nm active layer was thus obtained. Following this deposition procedure, the top electrode was deposited by thermal evaporation of a 25 nm thick film of Ca followed by 80 nm thick film of Al. The device area, as defined by the anode-cathode overlap, is 1.21 mm^2 .

Device Characterization. Current density–voltage (J–V) measurements were recorded by a Keithley 6487 picoammeter both in the dark and under illumination. The devices were illuminated through the glass substrate using an Oriel 91191 150 W full spectrum solar simulator. The illumination intensity was calibrated to 100 mW/cm² using an NREL-certified silicon photodiode. Spectral mismatch was not corrected for in these measurements.

FET electron mobility measurement. Bottom-gate, bottom-contact FETs were made on Si substrates with a thermally-grown SiO₂ layer (500 nm) and 10 μm channel lengths.(PCBM and TMCB-Mono) Top-gate, bottom-contact FETs were made on glass substrates with a PMMA layer (465 nm) top gate and 10 μm channel lengths. (TMCB-bis and TMCB-tris)

2.5. References and Notes

1. Roncali, J. Molecular Bulk Heterojunctions: An Emerging Approach to Organic Solar Cells. *Acc. Chem. Res.* **2009**, *42*, 1719-1730.
2. Chen, J.; Cao, Y. Development of Novel Conjugated Donor Polymers for High-Efficiency Bulk-Heterojunction Photovoltaic Devices. *Acc. Chem. Res.* **2009**, *42*, 1709-1718.
3. Thompson, B. C.; Frechet, J. M. J. Organic photovoltaics- Polymer-Fullerene Composite Solar Cells. *Angew. Chem. Int. Edit.* **2008**, *47*, 58-77.
4. Yu, G.; Gao, J.; Hummelen, J. C.; Wudl, F.; Heeger, A. J. Polymer Photovoltaic Cells - Enhanced Efficiencies Via a Network of Internal Donor-Acceptor Heterojunctions. *Science* **1995**, *270*, 1789-1791.
5. Brabec, C. J.; Heeney, M.; McCulloch, I.; Nelson, J. *Chem.Soc.Rev.* Influence of blend microstructure on bulk heterojunction organic photovoltaic performance. **2011**, *40*, 1185-1199.
6. Muhlbacher, D.; Scharber, M.; Morana, M.; Zhu, Z. G.; Waller, D.; Gaudiana, R.; Brabec, C. High Photovoltaic Performance of a Low-Bandgap Polymer. *Adv. Mater.* **2006**, *18*, 2884-2889.

7. Scharber, M. C.; Wuhlbacher, D.; Koppe, M.; Denk, P.; Waldauf, C.; Heeger, A. J.; Brabec, C. L. Design Rules for Donors in Bulk-Heterojunction Solar Cells- Towards 10 % Energy-Conversion Efficiency. *Adv. Mater.* **2006**, *18*, 789-794.
8. Brunetti, F. G.; Gong, X.; Tong, M.; Heeger, A. J.; Wudl, F. Strain and Huckel Aromaticity: Driving Forces for a Promising New Generation of Electron Acceptors in Organic Electronics. *Angew. Chem. Int. Edit.* **2010**, *49*, 532-536.
9. Dittmer, J. J.; Marseglia, E. A.; Friend, R. H. Electron trapping in dye/polymer blend photovoltaic cells. *Adv. Mater.* **2000**, *12*, 1270-1274.
10. Woo, C. H.; Holcombe, T. W.; Unruh, D. A.; Sellinger, A.; Frechet, J. M. J. Phenyl vs Alkyl Polythiophene: A Solar Cell Comparison Using a Vinazene Derivative as Acceptor. *Chem. Mater.* **2010**, *22*, 1673-1679.
11. Segura, J. L.; Martin, N.; Guldi, D. M. Materials for organic solar cells: the C_{60} /pi-conjugated oligomer approach. *Chem. Soc. Rev.* **2005**, *34*, 31-47.
12. Champeil, E.; Crean, C.; Larraya, C.; Pescitelli, G.; Proni, G.; Ghosez, L. Functionalization of C_{60} via organometallic reagents. *Tetrahedron* **2008**, *64*, 10319-10330.
13. Penicaud, A.; Hsu, J.; Reed, C. A.; Koch, A.; Khemani, K. C.; Allemand, P. M.; Wudl, F. C_{60} with Coordination Compounds (Tetraphenylporphinato)Chromium(III) Fulleride. *J. Am. Chem. Soc.* **1991**, *113*, 6698-6700.
14. Tzirakis, M. D.; Orfanopoulos, M. Acyl Radical Reactions in Fullerene Chemistry: Direct Acylation of [60]Fullerene through an Efficient Decatungstate-Photomediated Approach. *J. Am. Chem. Soc.* **2009**, *131*, 4063-4069.
15. Diederich, F.; Thilgen, C. Covalent fullerene chemistry. *Science* **1996**, *271*, 317-323.
16. Yurovskaya, M. A.; Trushkov, I. V. Cycloaddition to buckminsterfullerene C-60: advancements and future prospects. *Russ. Chem. Bull.* **2002**, *51*, 367-443.
17. Hummelen, J. C.; Knight, B. W.; Lepeq, F.; Wudl, F.; Yao, J.; Wilkins, C. L. Preparation and Characterization of Fulleroid and Methanofullerene Derivatives. *J. Org. Chem.* **1995**, *60*, 532-538.

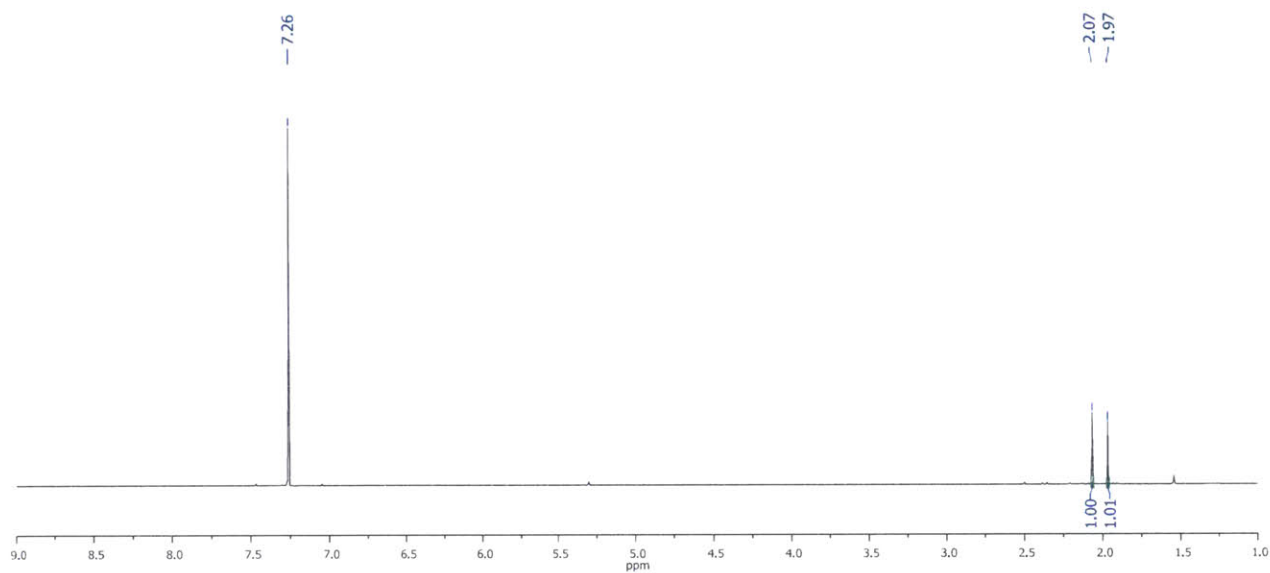
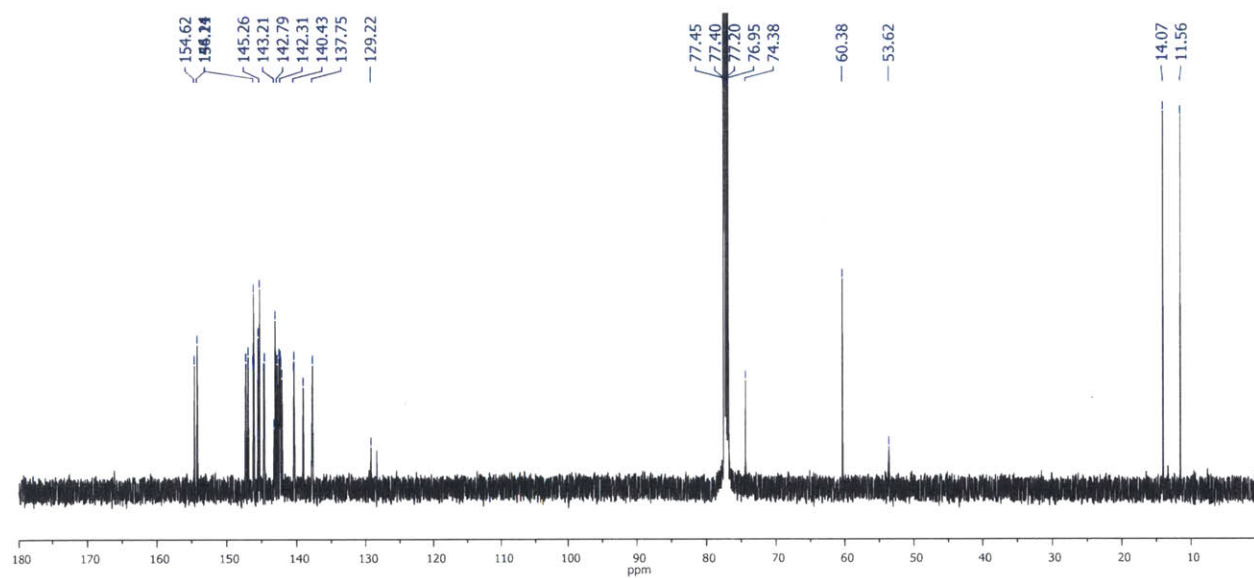
18. Laird, D. W. R., H.; Vejins, V.; Scott, L. T.; Lada, T. A. Organic photovoltaic devices comprising fullerenes and derivatives thereof and improved methods of making fullerene derivatives. *Patent* WO/2008/018931 A2.
19. Puplovskis, A.; Kacens, J.; Neilands, O. New route for [60]fullerene functionalisation in [4+2] cycloaddition reaction using indene. *Tetrahedron Lett.* **1997**, *38*, 285-288.
20. Brabec, C. J.; Cravino, A.; Meissner, D.; Sariciftci, N. S.; Fromherz, T.; Rispen, M. T.; Sanchez, L.; Hummelen, J. C. Origin of the open circuit voltage of plastic solar cells. *Adv. Funct. Mater.* **2001**, *11*, 374-380.
21. Huang, F.; Chen, K.-S.; Yip, H.-L.; Hau, S. K.; Acton, O.; Zhang, Y.; Luo, J.; Jen, A. K. Y. Development of New Conjugated Polymers with Donor- π -Bridge-Acceptor Side Chains for High Performance Solar Cells. *J. Am. Chem. Soc.* **2009**, *131*, 13886-13887.
22. Piliago, C.; Holcombe, T. W.; Douglas, J. D.; Woo, C. H.; Beaujuge, P. M.; Fréchet, J. M. J. Synthetic Control of Structural Order in N-Alkylthieno[3,4-c]pyrrole-4,6-dione-Based Polymers for Efficient Solar Cells. *J. Am. Chem. Soc.* **2010**, *132*, 7595-7597.
23. Woo, C. H.; Beaujuge, P. M.; Holcombe, T. W.; Lee, O. P.; Fréchet, J. M. J. Incorporation of Furan into Low Band-Gap Polymers for Efficient Solar Cells. *J. Am. Chem. Soc.* **2010**, *132*, 15547-15549.
24. Zhang, Y.; Matsuo, Y.; Li, C. Z.; Tanaka, H.; Nakamura, E. A Scalable Synthesis of Methano[60]fullerene and Congeners by the Oxidative Cyclopropanation Reaction of Silylmethylfullerene. *J. Am. Chem. Soc.* **2011**, *133*, 8086-8089.
25. Khlyabich, P. P.; Burkhart, B.; Thompson, B. C. Efficient Ternary Blend Bulk Heterojunction Solar Cells with Tunable Open-Circuit Voltage. *J. Am. Chem. Soc.* **2011**, *133*, 14534-14537.
26. Kooistra, F. B.; Knol, J.; Kastenberg, F.; Popescu, L. M.; Verhees, W. J. H.; Kroon, J. M.; Hummelen, J. C. Increasing the Open Circuit Voltage of Bulk-Heterojunction Solar Cells by Raising the LUMO Level of the Acceptor. *Org. Lett.* **2007**, *9*, 551-554.

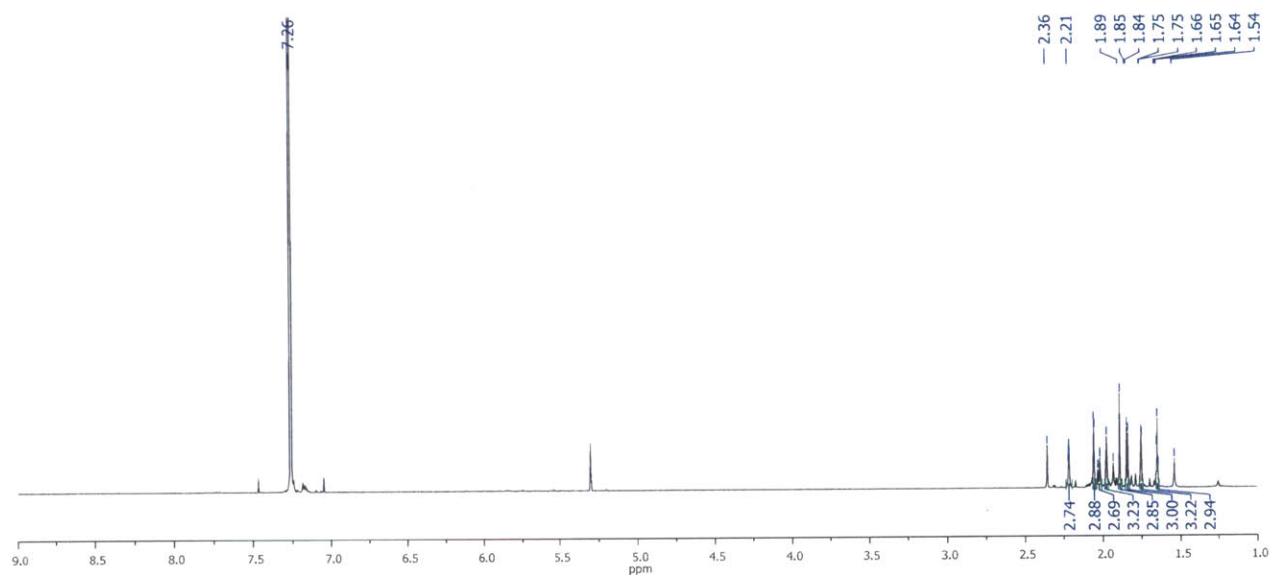
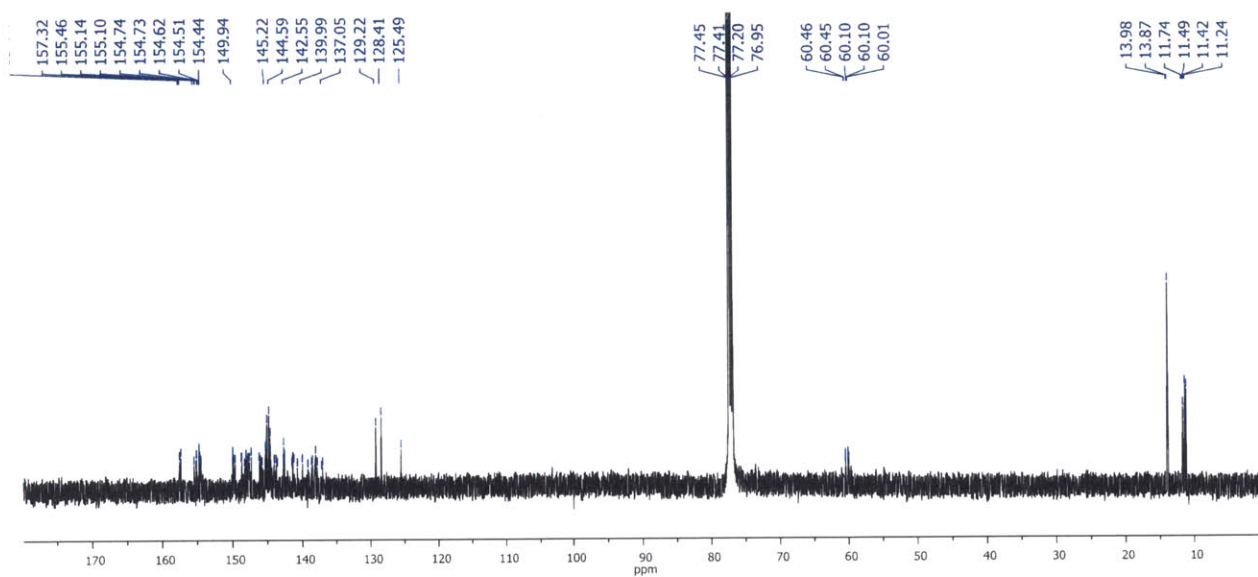
27. He, Y. J.; Chen, H. Y.; Hou, J. H.; Li, Y. F. Indene- C_{60} Bisadduct: A New Acceptor for High-Performance Polymer Solar Cells. *J. Am. Chem. Soc.* **2010**, *132*, 1377-1382.
28. Driessen, P. B. J.; Hogeveen, H. $AlCl_3$ Sigma-Complexes of Cyclobutadienes. *J. Am. Chem. Soc.* **1978**, *100*, 1193-1200.
29. Jankova, S.; Cisarova, I.; Uhlik, F.; Stepnicka, P.; Kotora, M. Synthesis and characterisation of Dewar benzene-ferrocene conjugates. *Dalton Trans.* **2009**, 3137-3139.
30. Jankova, S.; Dracinsky, M.; Cisarova, I.; Kotora, M. Synthesis and rearrangement of Dewar benzenes into biaryls: Experimental evidence for conrotatory ring opening. *Eur. J. Org. Chem.* **2008**, 47-51.
31. Wudl, F. The Chemical Properties of Buckminsterfullerene (C_{60}) and the Birth and Infancy of Fulleroids. *Acc. Chem. Res.* **1992**, *25*, 157-161.
32. He, Y.; Zhao, G.; Peng, B.; Li, Y. High-Yield Synthesis and Electrochemical and Photovoltaic Properties of Indene- C_{70} Bisadduct. *Adv. Funct. Mater.* **2010**, *20*, 3383-3389.
33. Liu, C.; Xiao, S.; Shu, X.; Li, Y.; Xu, L.; Liu, T.; Yu, Y.; Zhang, L.; Liu, H.; Li, Y. Synthesis and Photovoltaic Properties of Novel Monoadducts and Bisadducts Based on Amide Methanofullerene. *ACS Appl. Mater. Interfaces* **2012**, *4*, 1065-1071.
34. Guldi, D. M. Probing the electron-accepting reactivity of isomeric bis(pyrrolidinium) fullerene salts in aqueous solutions. *J. Phys. Chem. B* **2000**, *104*, 1483-1489.
35. Wienk, M. M.; Kroon, J. M.; Verhees, W. J. H.; Knol, J.; Hummelen, J. C.; van Hal, P. A.; Janssen, R. A. J. Efficient Methano[70]fullerene/MDMO-PPV Bulk Heterojunction Photovoltaic Cells. *Angew. Chem., Int. Edit.* **2003**, *42*, 3371-3375.
36. Kadish, K. M.; Gao, X.; Caemelbecke, E. V.; Suenobu, T.; Fukuzumi, S. Effect of Addition Pattern on the Electrochemical and Spectroscopic Properties of Neutral and Reduced 1,2- and 1,4- $(C_6H_5CH_2)_2C_{60}$ Isomers. *J. Phys. Chem. A* **2000**, *104*, 3878-3883.
37. Murata, Y.; Komatsu, K.; Wan, T. S. M. The reaction of [60]fullerene with lithium fluorenyl: Formation of a novel 1,4-adduct of [60]fullerene. *Tetrahedron Lett.* **1996**, *37*, 7061-7064.

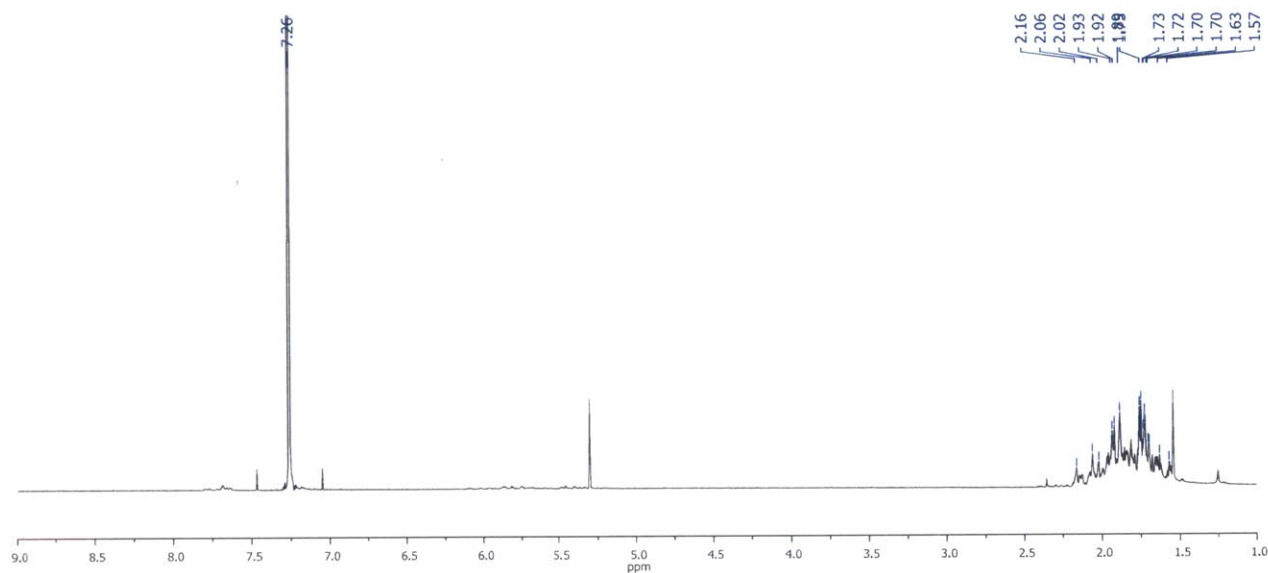
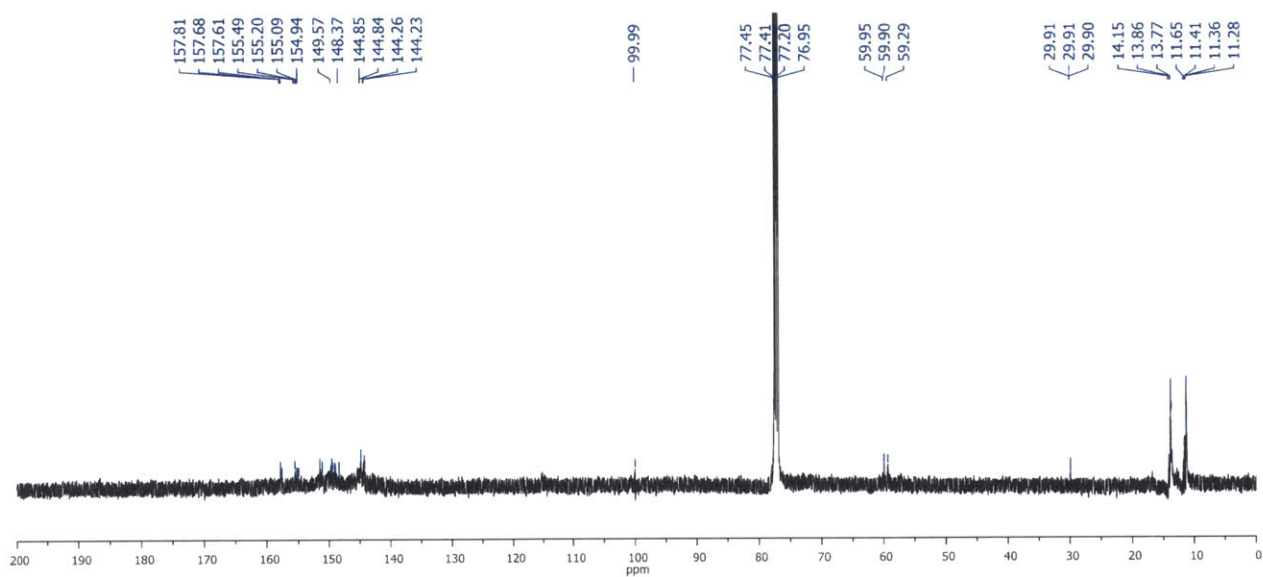
38. Chen, Z.-X.; Wang, G.-W.: One-Pot Sequential Synthesis of Acetoxyated [60]Fullerene Derivatives. *J. Org. Chem.* **2005**, *70*, 2380-2383.
39. Tajima, Y.; Hara, T.; Honma, T.; Matsumoto, S.; Takeuchi, K. Lewis Acid-Assisted Nucleophilic Substitution of Fullerene Epoxide. *Org. Lett.* **2006**, *8*, 3203-3205.
40. Milliken, J.; Keller, T. M.; Baronavski, A. P.; Mcelvany, S. W.; Callahan, J. H.; Nelson, H. H. Thermal and Oxidative Analyses of Buckminsterfullerene, C_{60} . *Chem. Mater.* **1991**, *3*, 386-387.
41. Delgado, J. L.; Oswald, F.; Cardinali, F.; Langa, F.; Martin, N. On the Thermal Stability of [60]Fullerene Cycloadducts: Retro-Cycloaddition Reaction of 2-Pyrazolino[4,5:1,2][60]fullerenes. *J. Org. Chem.* **2008**, *73*, 3184-3188.
42. Martin, N.; Altable, M.; Filippone, S.; Martin-Domenech, A.; Echegoyen, L.; Cardona, C. M. Retro-Cycloaddition Reaction of Pyrrolidinofullerenes. *Angew. Chem. Int. Edit.* **2006**, *45*, 110-114.
43. Osuna, S.; Houk, K. N. Cycloaddition Reactions of Butadiene and 1,3-Dipoles to Curved Arenes, Fullerenes, and Nanotubes: Theoretical Evaluation of the Role of Distortion Energies on Activation Barriers. *Chem. Eur. J.* **2009**, *15*, 13219-13231.
44. Osuna, S.; Morera, J.; Cases, M.; Morokuma, K.; Sola, M. Diels-Alder Reaction between Cyclopentadiene and C_{60} : An Analysis of the Performance of the ONIOM Method for the Study of Chemical Reactivity in Fullerenes and Nanotubes. M. Sola, *J. Phys. Chem. A* **2009**, *113*, 9721-9726.
45. Solá, M.; Mestres, J.; Martí, J.; Duran, M. An AM1 study of the reactivity of buckminsterfullerene (C_{60}) in a Diels-Alder model reaction. *Chem. Phys. Lett.* **1994**, *231*, 325-330.
46. Maurano, A.; Hamilton, R.; Shuttle, C. G.; Ballantyne, A. M.; Nelson, J.; O'Regan, B.; Zhang, W. M.; McCulloch, I.; Azimi, H.; Morana, M.; Brabec, C. J.; Durrant, J. R. Recombination Dynamics as a Key Determinant of Open Circuit Voltage in Organic Bulk Heterojunction Solar Cells: A Comparison of Four Different Donor Polymers. *Adv. Mater.* **2010**, *22*, 4987-4992.
47. Hunter, C. A.; Sanders, J. K. M. The Nature of Pi-Pi Interactions. *J. Am. Chem. Soc.* **1990**, *112*, 5525-5534.

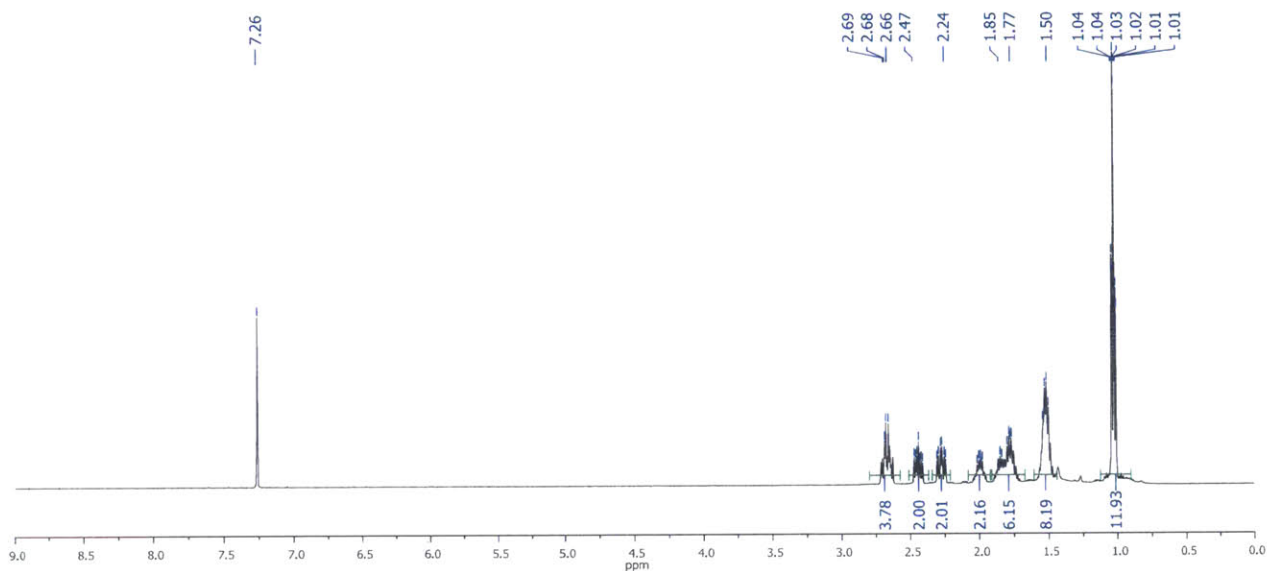
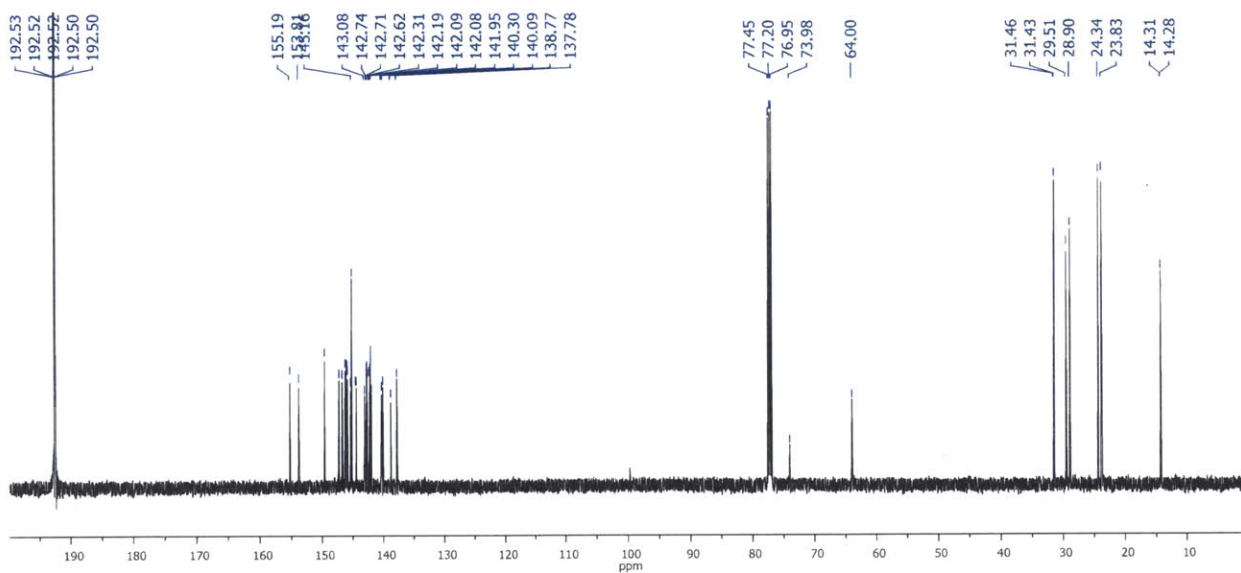
48. Krechmer, J.; Tice, J.; Crawford, E.; Musselman, B. Increasing the rate of sample vaporization in an open air desorption ionization source by using a heated metal screen as a sample holder. *Rapid Commun. Mass Spectrom.* **2011**, *25*, 2384-2388.
49. Jasti, R.; Bhattacharjee, J.; Neaton, J. B.; Bertozzi, C. R. Synthesis, Characterization, and Theory of [9]-, [12]-, and [18]Cycloparaphenylene: Carbon Nanohoop Structures. *J. Am. Chem. Soc.* **2008**, *130*, 17646-17647.

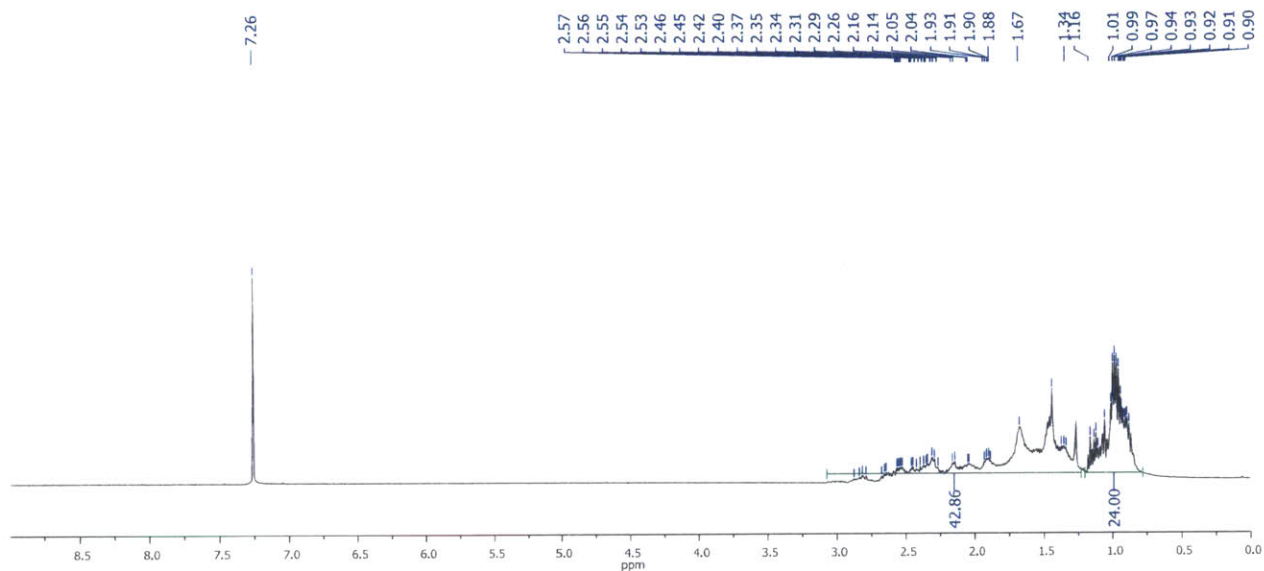
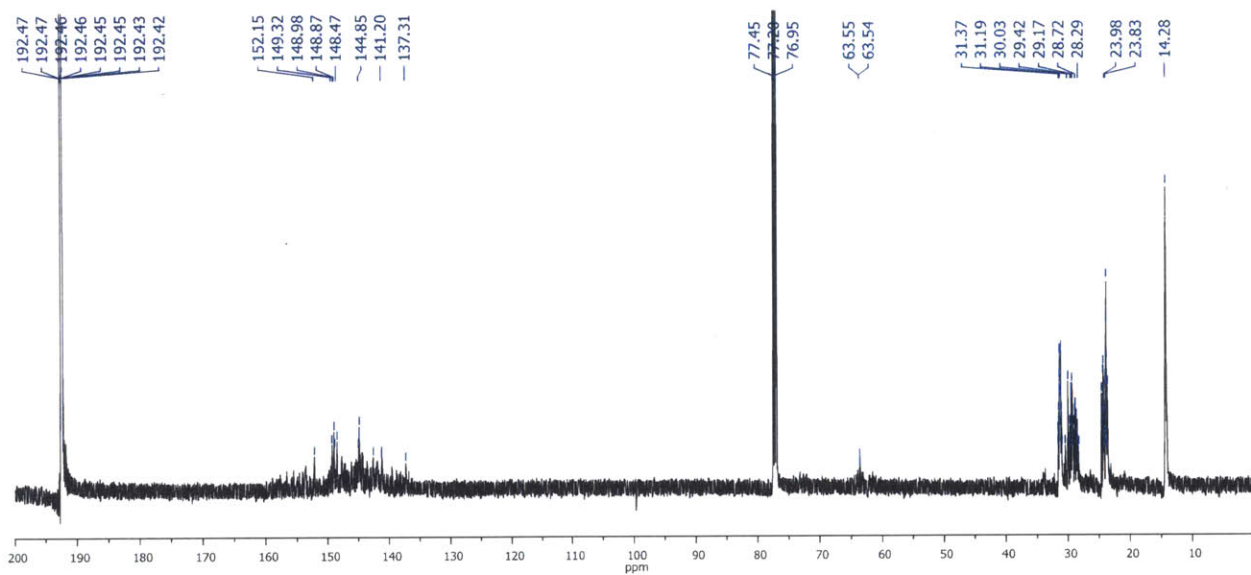
2.6. Appendix

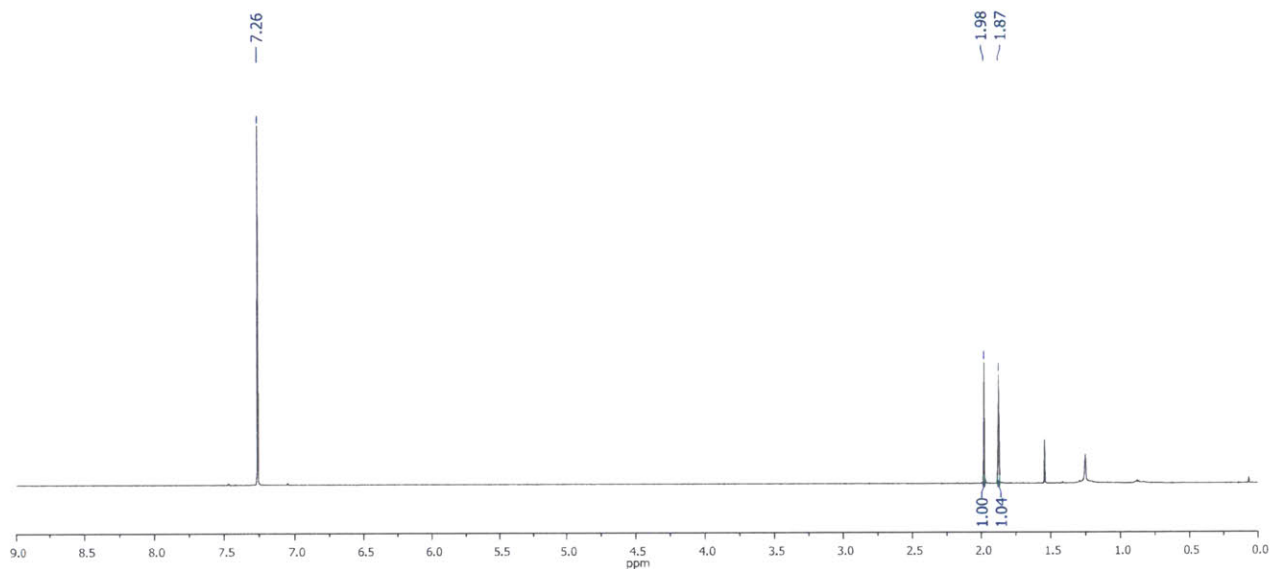
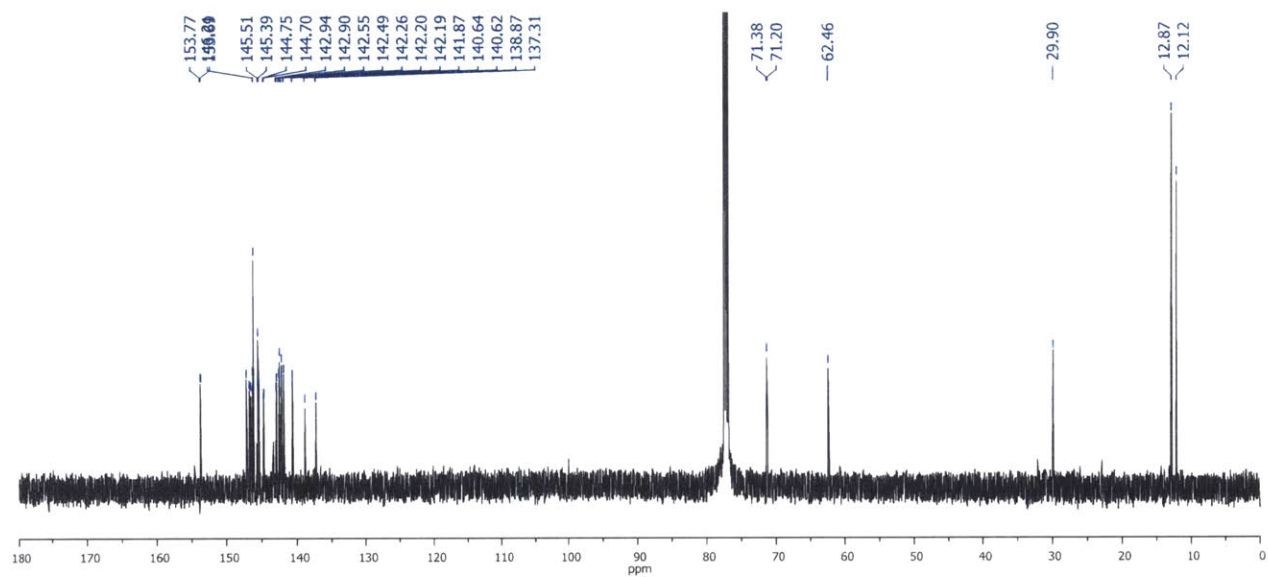
Spectrum 2.1. ^1H NMR of TMCB-MonoSpectrum 2.2. ^{13}C NMR of TMCB-Mono

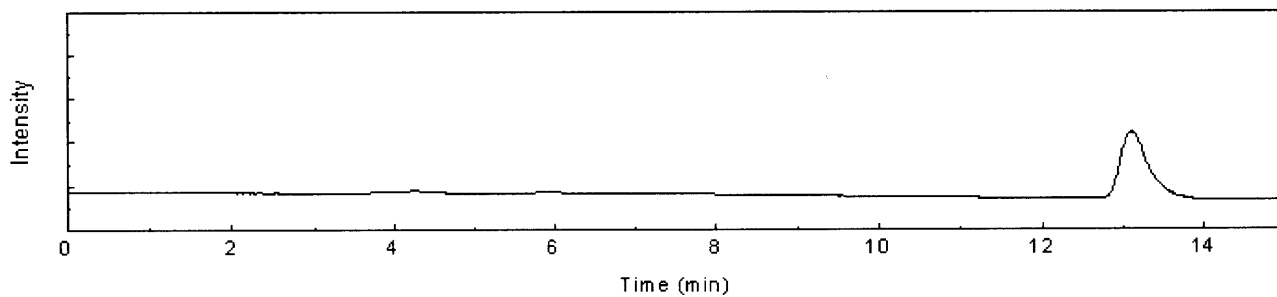
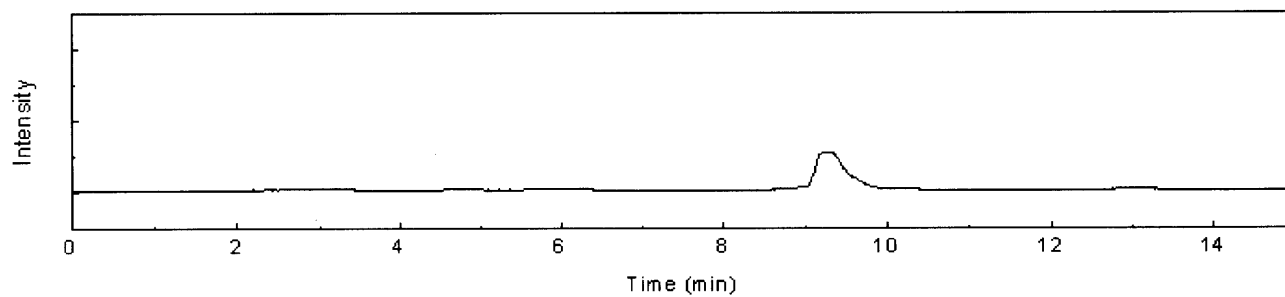
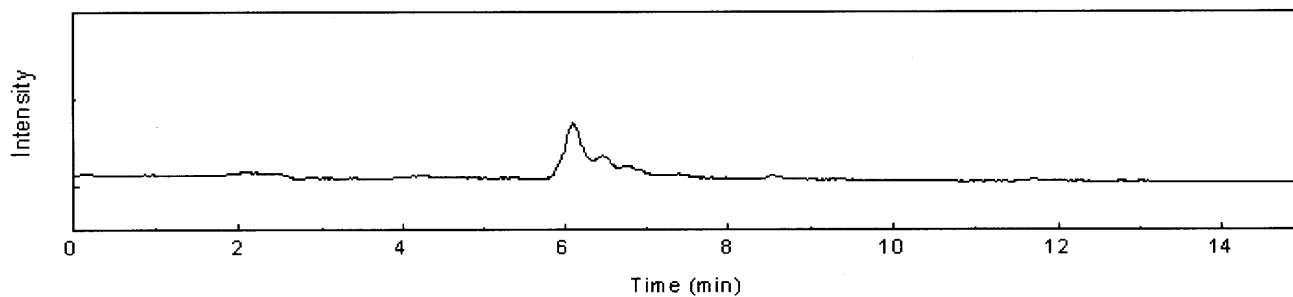
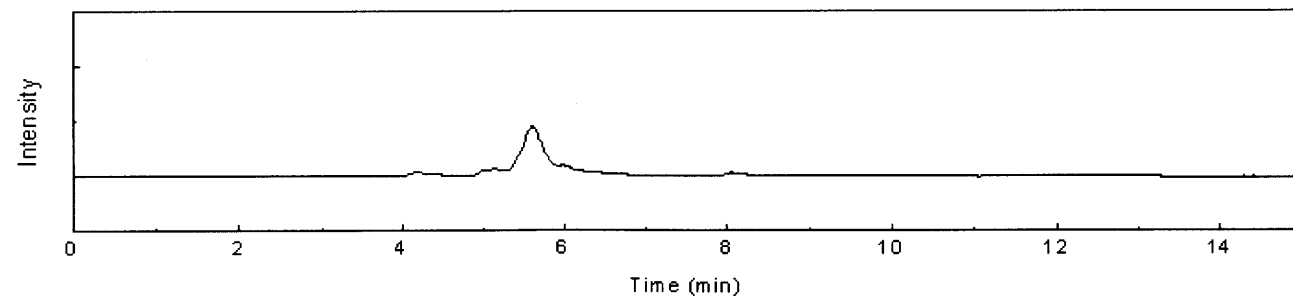
Spectrum 2.3. ^1H NMR of TMCB-Bis**Spectrum 2.4.** ^{13}C NMR of TMCB-Bis

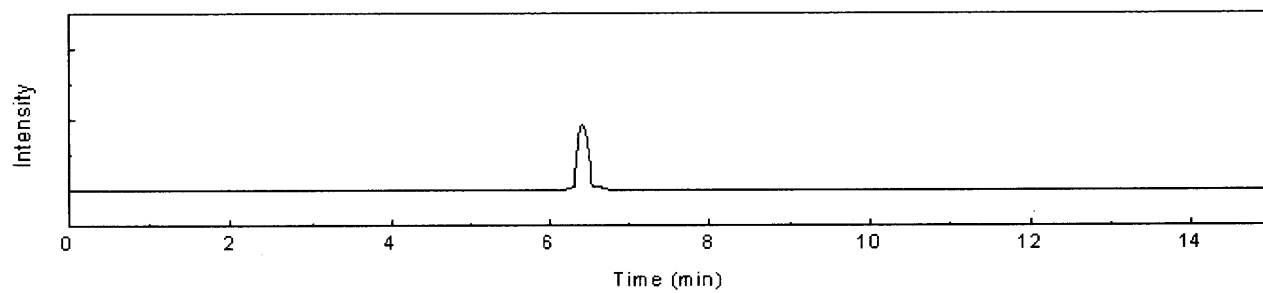
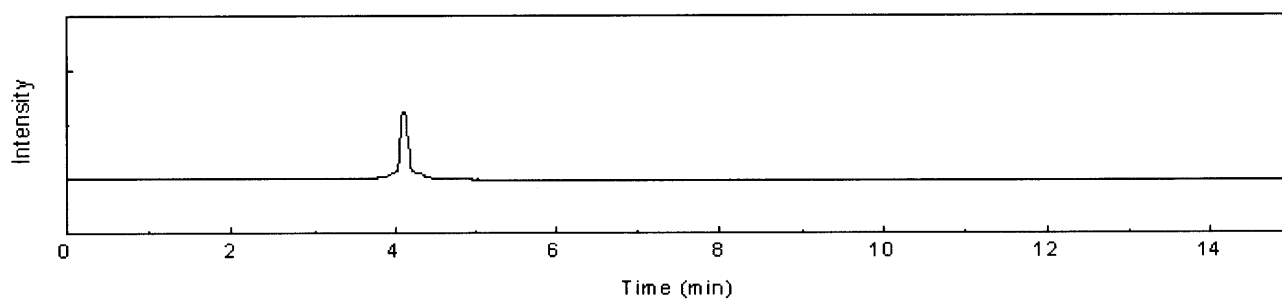
Spectrum 2.5. ¹H NMR of TMCB-TrisSpectrum 2.6. ¹³C NMR of TMCB-Tris

Spectrum 2.7. ^1H NMR of TBCB-MonoSpectrum 2.8. ^{13}C NMR of TBCB-Mono

Spectrum 2.9. ^1H NMR of TBCB-BisSpectrum 2.10. ^{13}C NMR of TBCB-Bis

Spectrum 2.11. ^1H NMR of TMCB-EpSpectrum 2.12. ^{13}C NMR of TMCB-Ep

Spectrum 2.13. HPLC trace of pristine C_{60} **Spectrum 2.14.** HPLC trace of TMCB-Mono**Spectrum 2.15.** HPLC trace of TMCB-Bis**Spectrum 2.16.** HPLC trace of TMCB-Tris

Spectrum 2.17. HPLC trace of TBCB-Mono**Spectrum 2.18.** HPLC trace of TBCB-Bis

CHAPTER 3

V_{OC} Enhancement in Polymer Solar Cells with Isobenzofulvene–C₆₀ Adducts

Adapted and reprinted in part from:

G. D. Han[†], A. Maurano[†], J. G. Weis, V. Bulović, and T. M. Swager.

“V_{OC} Enhancement in Polymer Solar Cells with Isobenzofulvene–C₆₀ Adducts.”

[†]Equal Contribution.

3.1. Introduction

Polymer solar cells with bulk heterojunction (BHJ) active layers continue to be a focus in organic photovoltaic research as a result of the large interfacial area to volume ratio, potential tunability, and ease of fabrication.¹⁻⁴ There is however limited knowledge about structure and property relationships of BHJ needed to optimize the power conversion efficiency (PCE). Research on p-type conjugated polymers has progressed considerably in recent years for the optimized transport and tailoring of the optical band gaps to capture the majority of the solar spectrum.⁵⁻⁷ However, there has not been as much progress in the n-type acceptors which have been mainly focused on small molecules and fullerenes designed to electronically complement their p-type counterparts.⁸ Among n-type molecules, covalently functionalized fullerenes such as PCBM ([6,6]-phenyl- C_{61} -butyric acid methyl ester) and ICBA (Indene- C_{60} Bisadducts) are widely used and generate promising PCEs in combination with optimized polymer counterparts.⁹ In particular, notably high open-circuit voltages (V_{OC}) of P3HT:ICBA BHJ solar cells have been attributed to the high-lying LUMO level of ICBA, since the V_{OC} correlates with the effective band gap at the BHJ interface ($HOMO_{Donor}-LUMO_{Acceptor}$).¹⁰ As a result, there is a continuing interest in the design of n-type materials with LUMO levels that produce high V_{OC} when matched with appropriate p-type polymers.

Most functionalized fullerenes have decreased electron affinities (raised LUMOs) as a result of the decreased π -delocalization.¹¹ However, the extent of this change can also be influenced by the structural and electronic properties of the specific fullerene derivative. In a previous study on tetraalkylcyclobutadiene- C_{60} adducts,¹² cofacial interactions between C_{60} and a pendant π -orbital were found to induce a significant change of the fullerene's LUMO energy levels. Indene- C_{60} adducts also display π -orbital interactions between the aromatic ring and the

C_{60} π -surface and display improved V_{OC} and PCE with a P3HT donor.⁹ In an effort to create larger increases in the fullerene LUMO levels, we designed new C_{60} derivatives (isobenzofulvene- C_{60} , IBF- C_{60}), which contain both a strong alkene-fullerene interaction similar to the cyclobutene adducts as well as an aromatic-fullerene interaction similar to the indene- C_{60} scaffold. These new IBF- C_{60} s were synthesized by cycloaddition reactions between a highly reactive isobenzofulvene and pristine C_{60} . Furthermore, we derivatized IBF- C_{60} s by epoxidation of the alkene to increase their solubility and processability, which further gave rise to more efficient charge separation at the BHJ (increased J_{SC}) and an enhanced PCE.

In this study, we report the syntheses of isobenzofulvene- C_{60} mono-, bisadducts (IBF-Mono, IBF-Bis) and their epoxide derivatives (IBF-Ep, IBF-Bis-Ep1, IBF-Bis-Ep2), together with their performance in BHJ solar cells. The optical, electronic, and thermal properties of the fullerenes have been studied by cyclic voltammetry, UV-Vis absorption spectroscopy, thermogravimetric analysis, and differential scanning calorimetry. The organic photovoltaic (OPV) performance has been investigated by measurements of current-voltage responses ($J-V$), photoluminescence, transient recombination dynamics, and morphology by atomic force microscopy (AFM). In devices with P3HT, most of the newly synthesized fullerenes showed higher open-circuit voltages than that of PCBM. Furthermore, IBF-Ep resulted in ~20% enhancement of PCE compared to PCBM, as a result of its higher J_{SC} and V_{OC} .

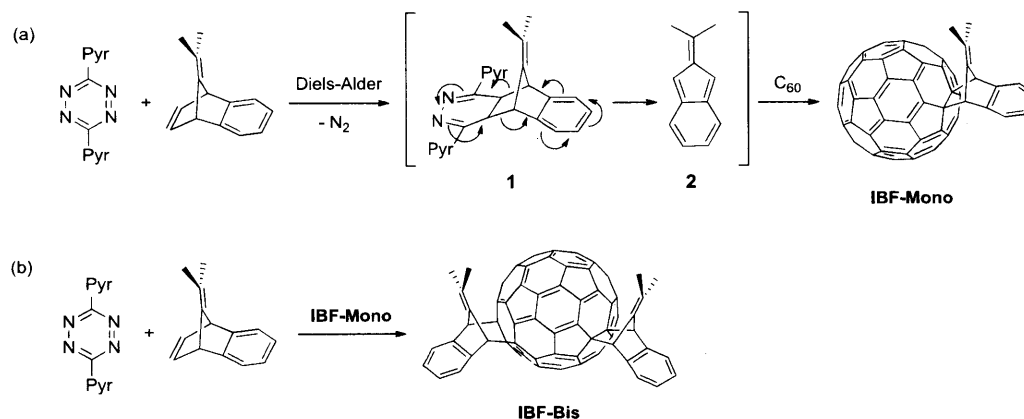
3.2. Results and Discussion

3.2.1. Syntheses of Isobenzofulvene- C_{60} Adducts

C_{60} is a potent dienophile¹³ for Diels-Alder cycloadditions and provided access to the indene- C_{60} adducts, which gave high V_{OC} and PCE in BHJ photovoltaics with P3HT.^{14,15}

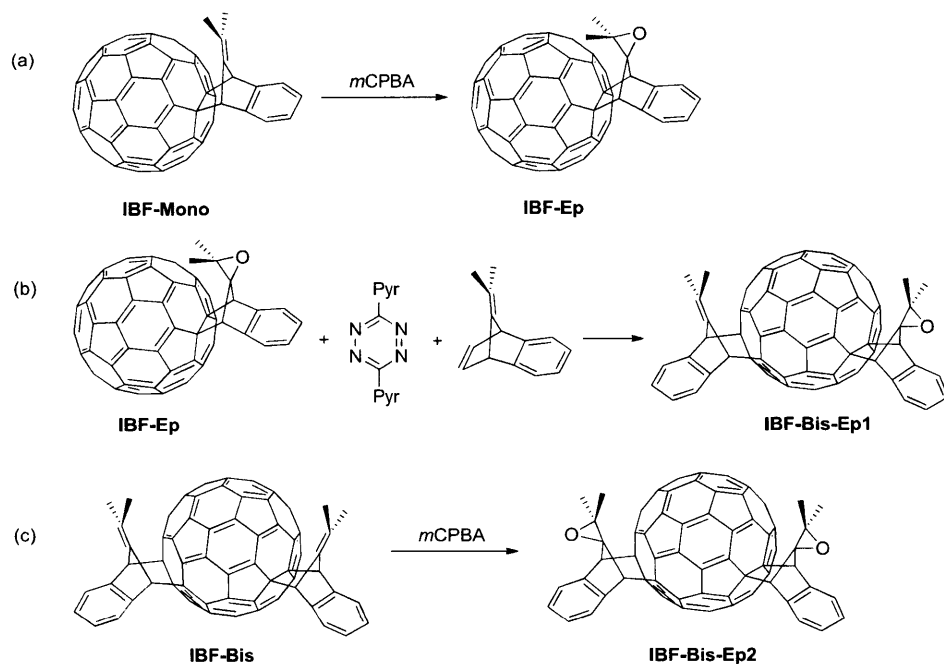
Considering the performance of indene- C_{60} , it was reasoned that the structural similarities of the isobenzofulvene- C_{60} (Scheme 3.1) should similarly produce enhancements and also further raise the LUMO levels through π -orbital interactions. The synthesis is initiated by generating the potent dieneophile 8,8-dimethylisobenzofulvene¹⁶ intermediate **2** via electrocyclic fragmentation of compound **1**, which is a Diels-Alder adduct of 9-isopropylidenebenzonorbornadiene and 3,6-di-2-pyridyl-1,2,4,5-tetrazine (Scheme 3.1 (a)).¹⁷ The [4+2] cycloaddition with two equivalents of isobenzofulvene to C_{60} was conducted at reduced temperatures (0 °C to room temperature) to produce dominantly the monoadduct (IBF-Mono) with minor amounts of the bisadducts (IBF-Bis). IBF-Mono is purified via column chromatography on silica gel by elution with CS_2 /hexane solvent mixture. IBF-Bis (Scheme 3.1 (b)) is a mixture of regioisomers as revealed by 1H and ^{13}C nuclear magnetic resonance (NMR) spectra (see Appendix). These bisadducts exhibit enhanced solubility relative to IBF-Mono in dichloromethane, chloroform, toluene, chlorobenzene, and *o*-dichlorobenzene, and are easily purified by HPLC using a 5PBB Cosmosil column with toluene elution. The disruption in the π -system by two successive cycloaddition reactions produces elevated LUMO energy levels, which in turn translates to higher V_{OC} compared to those of the monoadduct.^{18,19}

Scheme 3.1. Isobenzofulvene formation and Diels-Alder reaction with C_{60} : synthesis of (a) IBF-Mono and (b) IBF-Bis



The electron-rich double bond on the isobenzofulvene moiety can be selectively functionalized and epoxidation of the monoadduct generates IBF-Ep as shown in Scheme 3.2 (a). The increased polarity of IBF-Ep provides increased solubility in organic solvents relative to IBF-Mono. We also synthesized epoxide derivatives of IBF-Bis (Scheme 3.2 (b, c)) in order to take advantage of high V_{OC} characteristics of the bisadducts and to observe the effect of epoxide groups on J_{SC} . For the optimal yields and ease of purification, IBF-Bis-Ep1 was synthesized by adding an isobenzofulvene addend to IBF-Ep scaffold, and IBF-Bis-Ep2 was prepared by the complete epoxidation of IBF-Bis. The structures of the synthesized compounds were characterized by 1H and ^{13}C NMR spectroscopy as well as mass spectrometry (see Appendix).

Scheme 3.2. Syntheses of (a) IBF-Ep, (b) IBF-Bis-Ep1, and (c) IBF-Bis-Ep2 by epoxidation reaction.

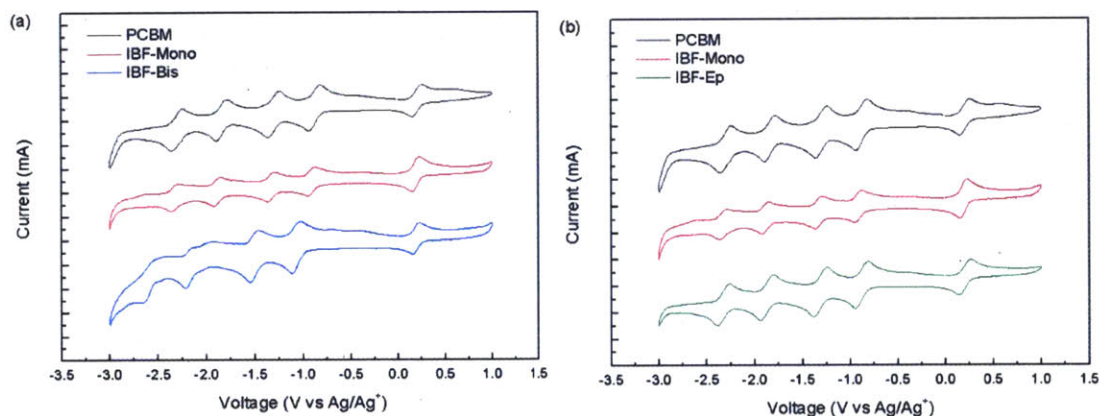


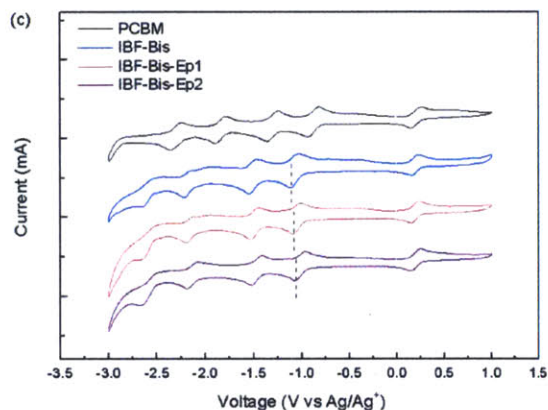
3.2.2. Electrochemical Properties

Cyclic voltammetry was conducted to measure the relative reduction potentials of the new C_{60} derivatives under anhydrous, air-free conditions with a ferrocene/ferrocenium (Fc/Fc^+) internal standard. In 0.1 M TBAPF₆ toluene/acetonitrile (4:1) solution, four reversible redox peaks are observed for each compound, and the relative positions of the onset reduction potentials are used to compare the LUMO energy levels (Figure 3.1).^{20,21} Relative to PCBM, the reduction onset potentials of IBF-Mono and IBF-Bis are respectively shifted toward negative potentials by ca. 60 mV and 180 mV (Figure 3.1 (a)) which are slightly higher than the indene- C_{60} mono- and bisadducts (50 mV and 170 mV, respectively).⁹ These raised LUMO levels, plotted in Figure 3.3 (a), illustrate the increased effective band gap and V_{OC} for BHJ solar cells. We hypothesize that the π - π interactions between C_{60} surface and the attached functional groups (aromatic ring and double bond) contribute to the large decreases in the electron affinity of fullerene.

Epoxidation of IBF-Mono removes the π - π interaction between C_{60} and the pendant double bond. The reduced π - π interaction and the presence of the electron-withdrawing epoxide group manifest slightly increased electron affinity (less negative reduction potential) of IBF-Ep relative to those of IBF-Mono (Figure 3.1 (b)). Similar phenomena are observed for the epoxide derivatives of IBF-Bis, and the redox behaviors of IBF-Bis, IBF-Bis-Ep1, and IBF-Bis-Ep2 are plotted relative to PCBM in Figure 3.1 (c). The slight differences in the first reduction peaks and the onset reduction potentials are as marked by the dotted lines as a visual aid. The incorporation of epoxide groups increases the electron affinity of the fullerenes and lowers the LUMO energy levels as indicated in Figure 3.3.

Figure 3.1. Cyclic voltammograms of (a) PCBM, IBF-Mono, IBF-Bis (b) PCBM, IBF-Mono, IBF-Ep (c) PCBM, IBF-Bis, IBF-Bis-Ep1, IBF-Bis-Ep2 (under N_2 , 0.1M Bu_4NPF_6 in toluene/acetonitrile (4:1), Pt (WE), Pt wire (CE), $Ag/AgNO_3$ (RE), scan rate 0.1 V/s, Fc/Fc^+ internal standard $E_{1/2}$ at 0.20 V).





3.2.3. Photophysical Properties

The optical properties of the new fullerenes are of interest and the absorption of visible light by the acceptors can contribute to the increased J_{SC} of solar cells.²² The comparative absorption spectra of our new fullerene derivatives and PCBM are plotted over the range of 400–800 nm in Figure 3.2. The monoadducts (IBF-Mono, IBF-Ep) exhibit weak peaks around 430–440 nm that are characteristic for 1,2-addition derived fullerene derivatives. The peaks and the absorption onset wavelengths, λ_{onset} , of the monoadducts are red-shifted from those of PCBM. The bisadducts show longer onset wavelengths (smaller band gaps) and broader absorption characteristics than the monoadducts as a result of their regioisomeric mixtures. They also have higher absorptivity as a result of their lowered symmetry. The band gaps are used to approximate the HOMO energy levels of the fullerenes by being subtracted from the LUMO levels derived from cyclic voltammetry. The values obtained from the aforementioned experiments are summarized in Table 3.1, and the MO energy level diagrams of the fullerenes are depicted in Figure 3.3.

Figure 3.2. UV-Vis absorption spectra of (a) PCBM (2.4×10^{-5} M), IBF-Mono (2.2×10^{-5} M), IBF-Bis (2.4×10^{-5} M), IBF-Ep (2.3×10^{-5} M) (b) PCBM (2.4×10^{-5} M), IBF-Bis-Ep1 (2.4×10^{-5} M) and IBF-Bis-Ep2 (2.2×10^{-5} M) in $CHCl_3$.

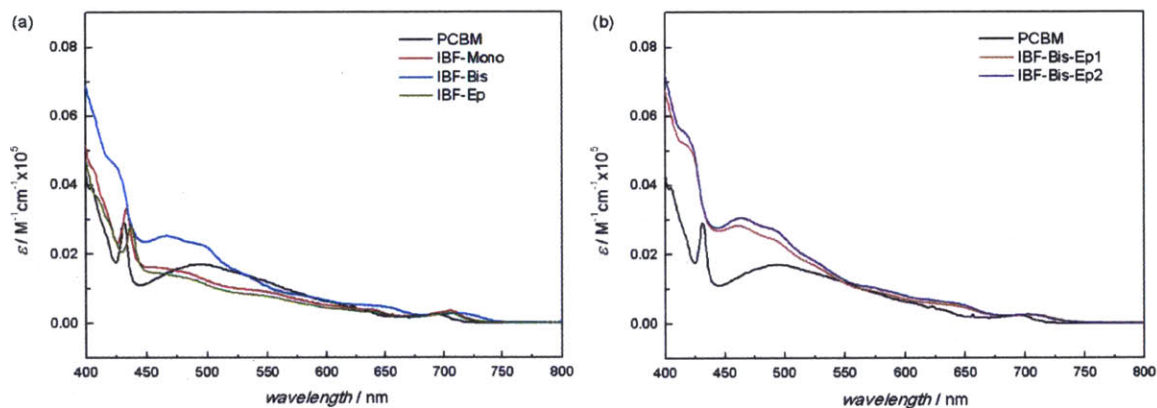


Figure 3.3. HOMO–LUMO energy diagrams of functionalized fullerenes. The MO energy levels were scaled relative to the vacuum level set to zero.

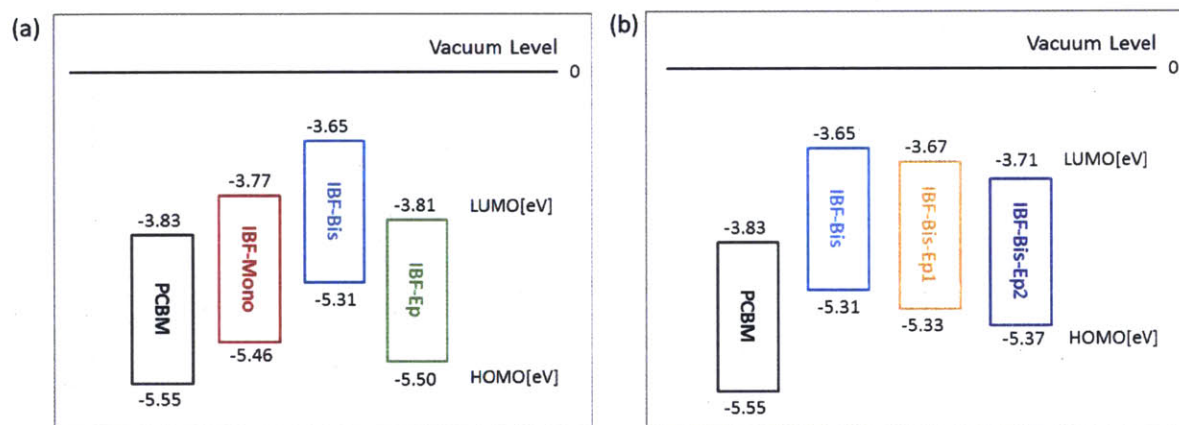


Table 3.1. HOMO and LUMO energies of fullerene derivatives calculated from UV–Vis absorption and cyclic voltammetry

C_{60} derivative	E_1 [V][a]	E_2 [V]	E_3 [V]	E_{onset} [V][b]	LUMO[eV][c]	λ_{onset} [nm][d]	HOMO[eV][e]	E_{gap} [eV][f]
PCBM	-0.87	-1.30	-1.83	-0.77	-3.83	723	-5.55	1.72
IBF–Mono	-0.92	-1.33	-1.89	-0.83	-3.77	737	-5.46	1.69
IBF–Bis	-1.08	-1.51	-2.18	-0.95	-3.65	750	-5.31	1.66
IBF–Ep	-0.88	-1.32	-1.87	-0.79	-3.81	733	-5.51	1.70
IBF–Bis–Ep1	-1.05	-1.49	-2.16	-0.93	-3.67	749	-5.33	1.66
IBF–Bis–Ep2	-1.02	-1.47	-2.14	-0.89	-3.71	749	-5.37	1.66

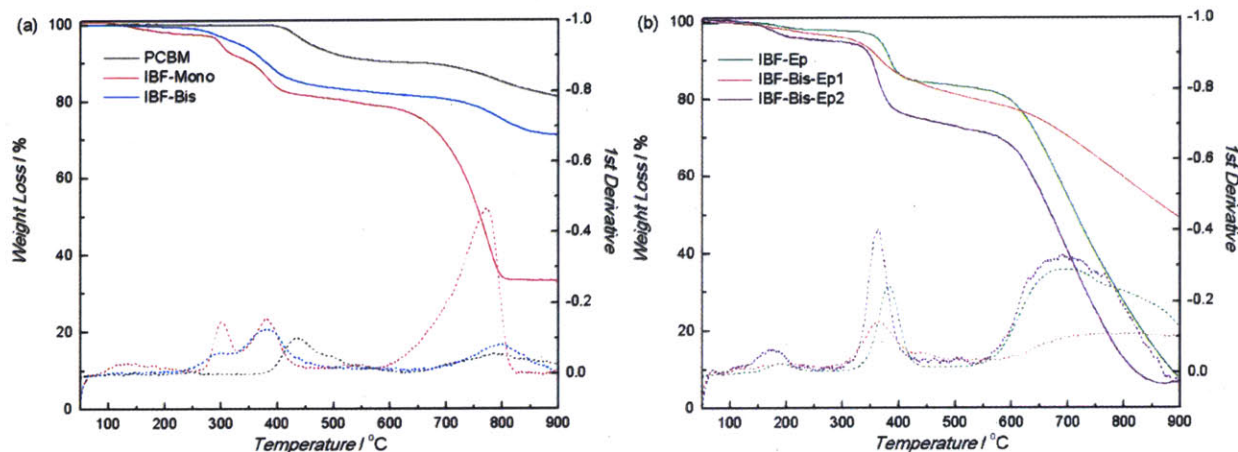
[a] Half-wave potential, 0.5 (Ep.a.+Ep.c.); Ep.a., anodic peak potential; Ep.c. cathodic peak potential; [b] Onset reduction potential; [c] LUMO (eV) = $-e(E_{\text{onset}}+4.60)$; [d] Onset absorption wavelength; [e]

HOMO = LUMO- E_{gap} [eV]; [f] Band gap = $hc/\lambda_{\text{onset}}$, converted [J] to [eV]; h, Planks constant; c, speed of light.

3.2.4. Thermal Stability

The thermal stability of the fullerenes was examined by thermogravimetric analysis (TGA) experiments over the range from 50 °C to 900 °C (Figure 3.4). In Figure 3.4 (a), PCBM displays the first thermal decomposition around 400 °C, but both IBF-Mono and IBF-Bis exhibit first weight loss at the lower temperatures around 300 °C. The weight loss corresponds to the processes of retro-cycloaddition^{23,24} and decomposition of the functional groups. The loss at higher temperatures around 700–800 °C indicate the fullerene sublimation.²⁵ Figure 3.4 (b) shows similar behavior of IBF-Ep, IBF-Bis-Ep1, and IBF-Bis-Ep2 with the first decomposition around 300–400 °C and the sublimation at higher temperatures. It is notable that the fullerene derivatives with isobenzofulvene moieties (IBF-Mono, IBF-Bis, IBF-Bis-Ep1) display two steps of functional group decomposition around 300–400 °C, while those with only the epoxy moieties (IBF-Ep, IBF-Bis-Ep2) have a single step in the range. We can assume that the isobenzofulvene moiety undergoes two-step process of thermal decomposition. The minor weight loss below 260 °C observed for IBF-Mono and IBF-Bis-Ep2 is likely from the residual solvent, toluene, contained in the crystalline phase of the fullerenes as reported in the literature.²⁶

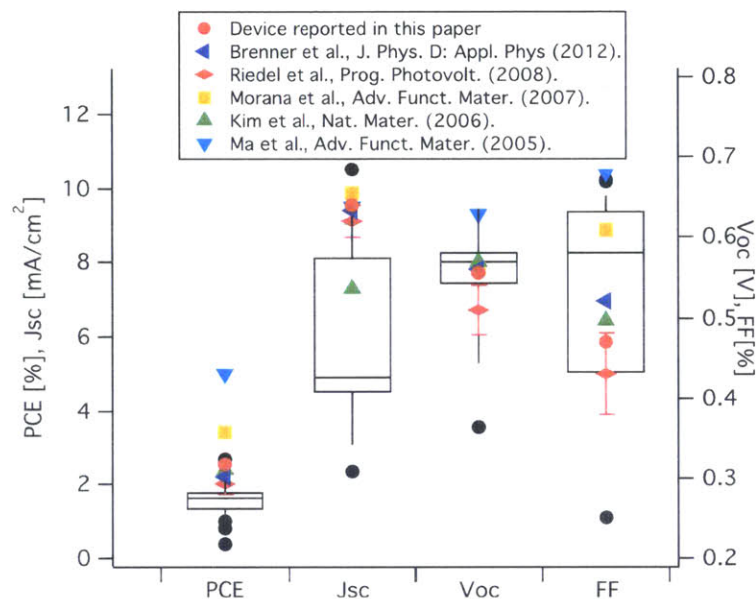
Figure 3.4. TGA analysis of weight loss (solid line) and its first derivative over temperature (dotted line) on (a) PCBM, IBF-Mono, IBF-Bis and (b) IBF-Ep, IBF-Bis-Ep1, IBF-Bis-Ep2 with scan rate of 20 °C/min from 50 °C to 900 °C.



3.2.5. Photovoltaic Characterization

We used IBF-Mono, IBF-Bis, IBF-Ep, IBF-Bis-Ep1, and IBF-Bis-Ep2 as electron acceptors in BHJ solar cells with P3HT as donor, and their performances were compared to conventional P3HT:PCBM devices. We note that we used P3HT donor in order to show that we can obtain enhanced performances with a benchmark material for polymer solar cells. In future publications, we will illustrate our ongoing studies aiming at pairing these high performance n-type acceptors with low-band gap polymers. Experimental details of device fabrication can be found in the experimental section. The comparison made between the performance of our reference P3HT:PCBM devices with the reported values is shown in Figure 3.5.

Figure 3.5. Box plot of PCE, J_{SC} , V_{OC} and FF of the reference PCBM devices that we fabricated (black line and dots) compared to the values previously reported. The J-V plot in Figure 3.6 (a) corresponds to a device which has a V_{OC} at the median of the distribution (marked by red dots), though other parameters can be off the respective median value (e.g. FF). Overall, the distribution of each parameter of our devices is comparable to the published values over the past 10 years.



The device performances (current density as a function of applied voltage ($J-V$)) are shown in Figure 3.6 (a), and the relative parameters are listed in Table 3.2. Devices containing our new fullerenes generally exhibit larger median V_{OC} as in Figure 3.6 (b) (except for IBF-Mono) than that of conventional P3HT:PCBM devices. The broad distribution of the V_{OC} of P3HT:IBF-Mono devices is a result of the low reproducibility due to its low solubility (as discussed below), but the higher values that we obtained suggest that this material has intrinsic potential to produce a high V_{OC} . The replacement of PCBM with IBF-Mono or IBF-Bis reduces the J_{SC} . However, the epoxidation of the isobenzofulvene moieties improves J_{SC} significantly, as illustrated by the difference in current between IBF-Bis and its epoxides (IBF-Bis-Ep1/IBF-Bis-Ep2). Moreover, the epoxidation of IBF-Mono (which creates IBF-Ep) not only generates higher current in a device than that of P3HT:PCBM, but also increases the solubility of IBF-Mono and the reproducibility of the $J-V$ graphs (given by the small V_{OC} distribution of IBF-Ep in Figure 3.6 (b)). Finally, we observed the similar fill factors (FF) for all the devices studied,

which suggests that the combined transport and recombination properties are similar among them.

Figure 3.6. (a) Current density as a function of applied voltage for the fullerenes in BHJ architecture for solar cells with P3HT, compared to conventional P3HT:PCBM. (b) Box plot of the V_{OC} values obtained from the devices in (a) where the whiskers indicate the 10th to 90th percentile and the box shows the 25th to 75th percentile containing the median (solid line) and average (dotted line). Except for P3HT:IBF-Mono, the median V_{OC} for the devices with the new fullerenes are higher than conventional P3HT:PCBM devices. The broad distribution of V_{OC} of P3HT:IBF-Mono is due to the low reproducibility, which lowers the median; however, the higher values obtained indicate the intrinsic potential of this material to produce high V_{OC} .

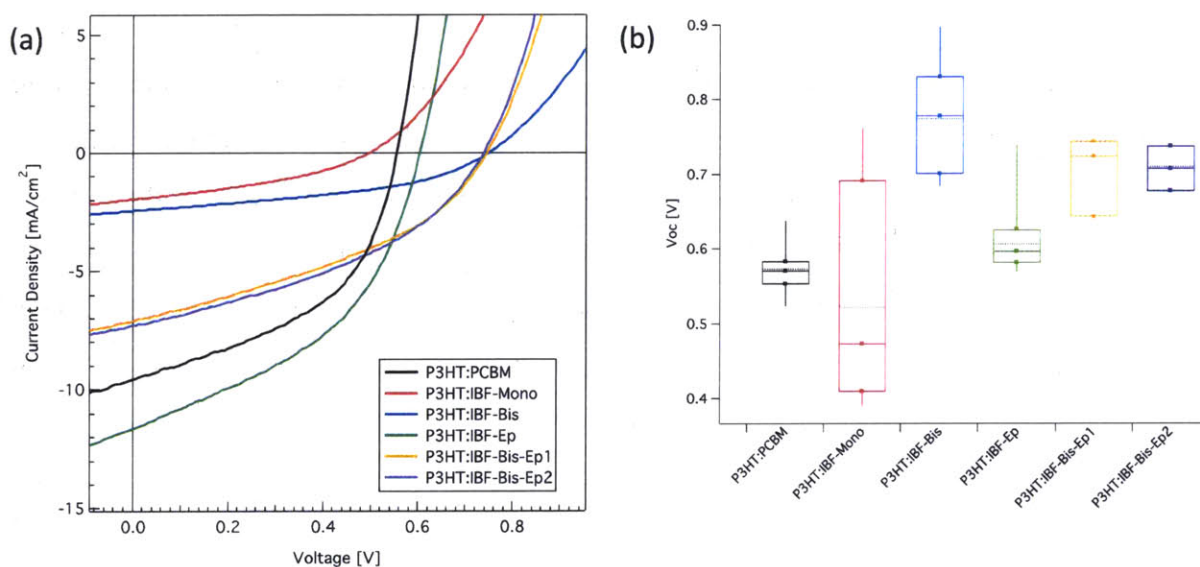


Table 3.2. OPV characteristics of the devices in Figure 3.6 (a).

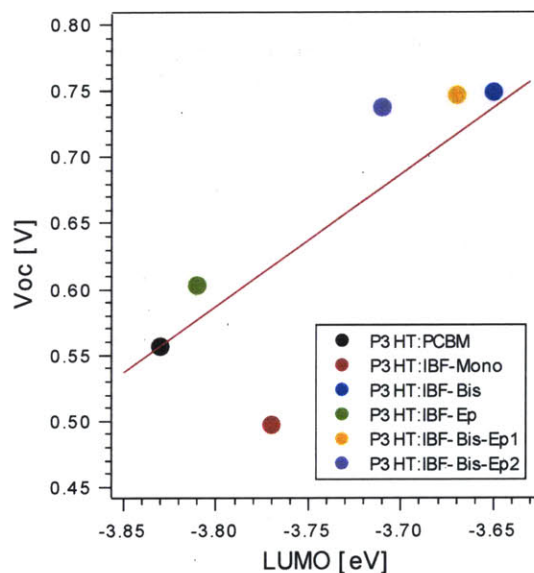
	IBF-Mono	IBF-Bis	IBF-Ep	IBF-Bis-Ep1	IBF-Bis-Ep2	PCBM
J_{SC} [mA/cm ²]	1.97	2.45	11.66	7.10	7.29	9.56
V_{OC} [V]	0.497	0.749	0.603	0.743	0.737	0.557
FF [%]	0.36	0.43	0.44	0.38	0.40	0.47
η [%]	0.36	0.78	3.10	2.02	2.12	2.52

Definitions: short-circuit current density, J_{SC} ; open-circuit voltage, V_{OC} ; fill factor, FF; PCE, η .

3.2.6. Transient Photovoltage and Photocurrent Measurement

The difference of V_{OC} between the bisadducts and PCBM is in accord with the large differences in LUMO levels. However, all the V_{OC} values cannot be solely explained by their LUMO level differences relative to that of PCBM. All the IBF- C_{60} -based devices (except for IBF-Mono where the variation in the V_{OC} values prevents proper comparison) have higher V_{OC} compared to the predicted values based on the LUMO level energy (given by the red line in Figure 3.7).

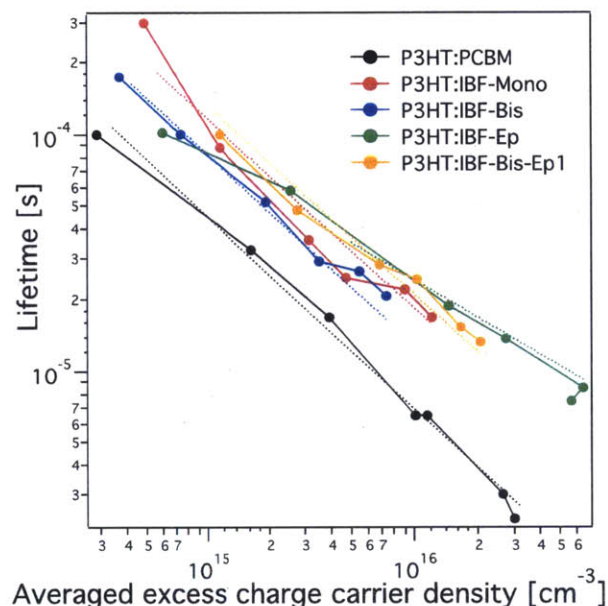
Figure 3.7. Relationship between the measured V_{OC} and the LUMO energy levels of fullerenes. The red line passing through P3HT:PCBM value indicates the predicted V_{OC} of other devices based on the LUMO level differences.



In order to address this discrepancy, we undertook the recombination measurements. Transient photovoltage (TPV) and photocurrent (TPC) measurements are routinely employed to evaluate charge carrier recombination at an open circuit and to relate V_{OC} to charge carrier recombination dynamics.²⁷ We measured recombination lifetimes at an open circuit as a function of excess charge carrier density as in Figure 3.8. P3HT:PCBM devices exhibit a shorter

recombination lifetime compared to other devices at the same averaged excess charge density. The slower recombination dynamics of IBF- C_{60} -based devices have the overall effect of increasing the V_{OC} compared to the values predicted solely by their LUMO energy levels. As such recombination is most likely to occur at the interface between the p- and n-type materials, the similar recombination dynamics of IBF- C_{60} -based devices suggest their distinct interface with P3HT, relative to the interface between PCBM and P3HT. In summary, we attribute the generation of large V_{OC} in P3HT:IBF- C_{60} devices to the combination of increased LUMO levels and slower recombination dynamics caused by the improved electronic interface behavior between IBF- C_{60} derivatives and P3HT.

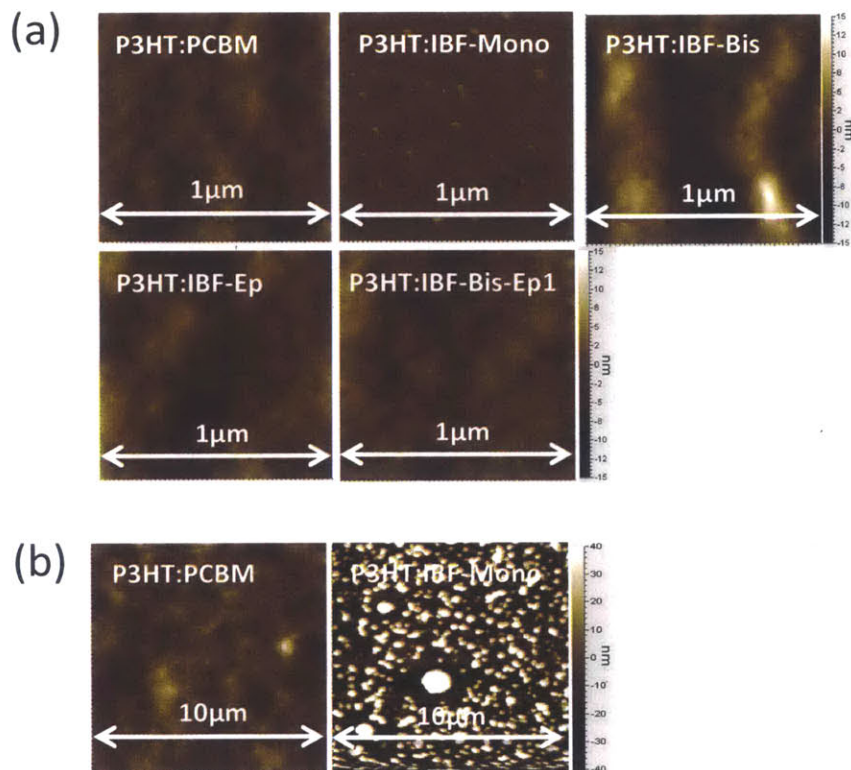
Figure 3.8. Recombination lifetime as a function of the averaged excess charge carrier density measured with transient photovoltage and photocurrent (TPV/TPC). P3HT:PCBM devices exhibit the shortest recombination lifetime, compared at the same averaged excess charge density (dotted lines represent power law fits). The slower recombination of P3HT:IBF- C_{60} devices contributes to their larger V_{OC} s than ones predicted solely by their effective band gaps. Also, all IBF- C_{60} -based devices are characterized by similar recombination dynamics, which suggests their similar electronic behaviors at the interface with P3HT.



3.2.7. Morphology, UV-Vis absorption, and Photoluminescence of Thin Films

To better understand the mechanisms determining the J_{SC} of our devices, we first measured their morphology by atomic force microscopy (AFM). Topographic images at 1 μm scale in Figure 3.9 (a) show that the phase separation of donor and acceptor domains is similar for all blends under study (together with their RMS reported in the legend), except for P3HT:IBF-Mono where particles of IBF-Mono are present. This is consistent with the low solubility of IBF-Mono and the low J_{SC} of the device. Figure 3.9 (b) at 10 μm scale also indicates the suboptimal phase separation of P3HT and IBF-Mono domains, as opposed to P3HT:PCBM.

Figure 3.9. Atomic force microscopy topographic images of the devices analyzed in this study at (a) 1 μm and (b) 10 μm scales. The topography at 1 μm scale shows similar phase separation for all the blends under study, except for P3HT:IBF-Mono where particles are observed. The root-mean-square (RMS) roughness measured on each film is 3.5 nm (PCBM), 20.0 nm (IBF-Mono), 2.5 nm (IBF-Bis), 3.0 nm (IBF-Ep), and 10.4 nm (IBF-Bis-Ep1). 10 μm scale images also show significant amount of the particles of IBF-Mono that are not fully dissolved.



In order to understand the improved J_{SC} of P3HT:IBF-Ep devices, we examined the UV-Vis absorption and photoluminescence (PL) of thin films fabricated under the same conditions as used for the devices in Figure 3.6 (a). The UV-Vis absorption spectra of thin films plotted in Figure 3.10 (a) reveal the reduced absorption of devices with IBF- C_{60} s compared to P3HT:PCBM (at equal thickness). The absorption characteristics of devices with IBF-Mono, IBF-Bis, IBF-Bis-Ep1, and IBF-Bis-Ep2 can explain their low J_{SC} s. In addition to the reduced absorption, P3HT:IBF-Mono device exhibits less-quenched PL (Figure 3.10 (b)) that might indicate higher radiative recombination in BHJ compared to other blends where emission is more quenched. The PL characteristic of P3HT:IBF-Mono film is also consistent with its low J_{SC} . In this case, finite exciton diffusion lengths and competitive relaxation (emission or thermalization) limits the device efficiency.²⁸ Morphology, UV-Vis absorption, and PL explain the mechanisms behind the low J_{SC} of IBF-Mono, IBF-Bis, IBF-Bis-Ep1, and IBF-Bis-Ep2 devices. The high

J_{SC} of P3HT:IBF-Ep devices, on the other hand, could be attributed to their higher charge carrier density compared to P3HT:PCBM reference devices. In fact in Figure 3.8, the data point corresponding to the shortest lifetime for each blend indicates the averaged excess charge carrier density at V_{OC} under the light intensity of 1 Sun (as also shown in Figure 3.11). The trend in the averaged excess charge carrier density at 1 Sun seems to suggest that the larger averaged excess charge carrier density in P3HT:IBF-Ep devices could indeed explain their higher J_{SC} .

Figure 3.10. Optical characterization of the devices analyzed in this study. Due to the similar results of IBF-Bis-Ep1 and IBF-Bis-Ep2, only IBF-Bis-Ep1 is shown for simplicity. (a) Steady-state spectral UV-Vis absorption of thin films fabricated under the same conditions as used for the devices in Figure 3.6 (a) and normalized for thickness. (b) Steady-state spectral photoluminescence emission of thin films fabricated under the same conditions as used for the devices in Figure 3.6 (a). Excited with monochromatic light at 500 nm and normalized for absorption. All fullerenes quench PL when blended with P3HT, though P3HT:IBF-Mono shows higher level of radiative exciton recombination that could explain its low J_{SC} .

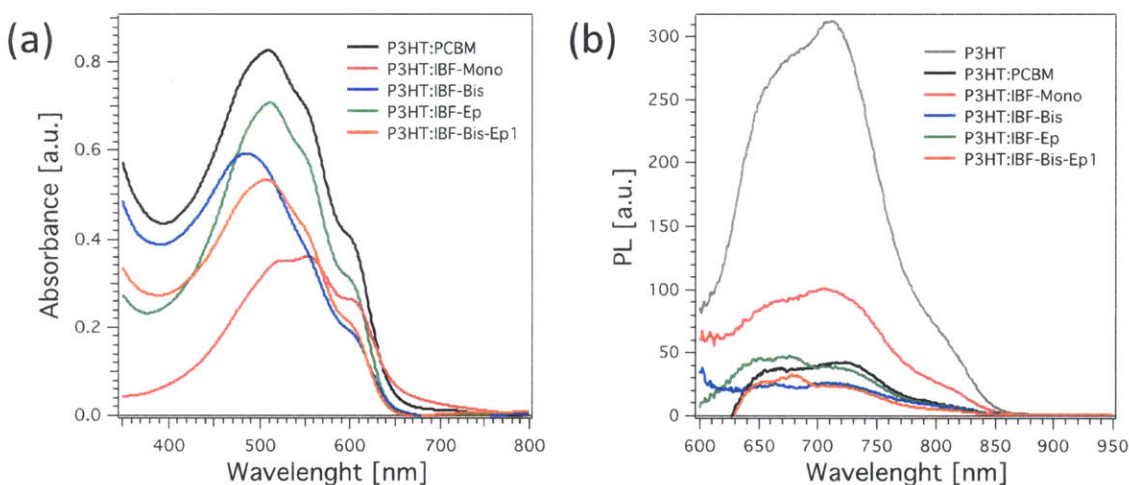
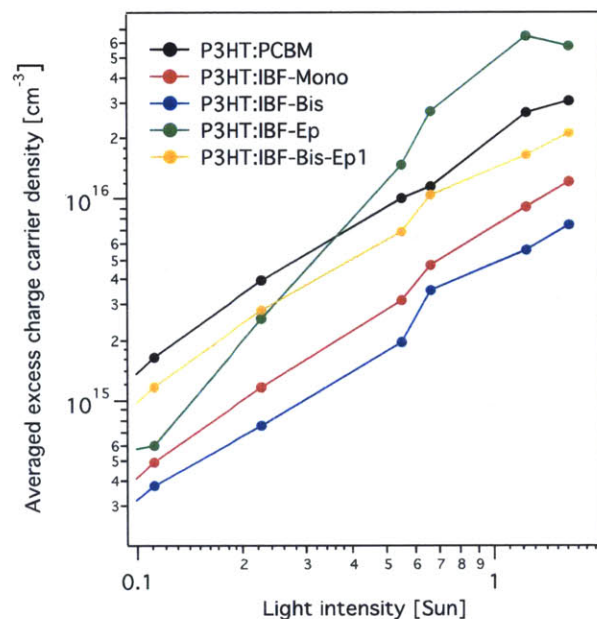


Figure 3.11. Averaged excess charge carrier density as function of the light intensity for all the blends under study.



3.3. Conclusions

A set of isobenzofulvene- C_{60} derivatives was synthesized by [4+2] cycloadditions of C_{60} with a reactive isobenzofulvene intermediate. The fullerene derivatives display cofacial π -interactions that produce elevated LUMO energy levels and higher V_{OC} s in photovoltaic devices than PCBM. The isobenzofulvene- C_{60} derivatives exhibit desirably slower recombination dynamics in the photovoltaic devices relative to PCBM, which also contributes to generating high V_{OC} . Epoxidation was carried out to further functionalize the isobenzofulvene- C_{60} s, and the epoxide derivatives exhibited the improved solubility as well as the increased J_{SC} in photovoltaic devices. The concomitant increase of V_{OC} and J_{SC} observed for P3HT:IBF-Ep devices relative to P3HT:PCBM standard cells resulted in ~20% enhancement of PCE. Ongoing studies are directed at pairing these new high performance n-type acceptors with low-band gap polymers to produce enhanced efficiency solar cells.

3.4. Experimental Section

Materials. C_{60} was purchased from SES Research. $PC_{61}BM$, and P3HT were purchased from Sigma-Aldrich. PEDOT:PSS were purchased from Ossila. 3,6-Di-2-pyridyl-1,2,4,5-tetrazine was purchased from Alfa Aesar. All the compounds purchased from commercial sources were used as received. Other materials including solvents and electrolyte salt were commercially available. Anhydrous solvents were obtained from a solvent purification system (Innovative Technologies).

Measurements. Reaction mixtures containing multiadducts of fullerenes were separated by 5PBB Cosmosil column (10 mm x 250 mm) from Nacalai Tesque, Inc. installed in Agilent Technologies ProsStar 210 High Pressure Liquid Chromatography (HPLC) system with 4mL/min elution of toluene. 1H and ^{13}C NMR spectra were taken on Varian Inova-500 spectrometers. Chemical shifts were reported in ppm and referenced to residual solvent peaks (CD_2Cl_2 : 5.33 ppm for 1H , 53.84 ppm for ^{13}C , $CDCl_3$: 7.26 ppm for 1H , 77.16 ppm for ^{13}C). Bruker Daltonics Omnistar MALDI-TOF mass spectrometer was used for mass determination without the use of a matrix. UV-Vis absorption spectra were obtained using a Cary 4000 UV-Vis spectrophotometer. Electrochemical measurements were carried out in a glove box under nitrogen, using an Autolab PGSTAT 10 or PGSTAT 20 potentiostat (Eco Chemie) in a three-electrode cell configuration. A Pt button (1.6 mm in diameter) electrode, a Pt wire, and a quasi-internal Ag wire submerged in 0.01M $AgNO_3$ /0.1M tetrabutylammonium hexafluorophosphate ($TBAPF_6$) in acetonitrile were used as a working electrode, a counter electrode, and a reference electrode, respectively, in 0.1M $TBAPF_6$ toluene/acetonitrile (4:1) solution. The ferrocene/ferrocenium (Fc/Fc^+) redox couple was used as an internal standard, with the half-

wave potentials observed between 0.193–0.205 V vs Ag/Ag⁺ in toluene/acetonitrile (4:1) solution. Thermogravimetric Analyses were performed with a Discovery TGA (TA Instruments) under nitrogen. Samples were heated at 20° C/min from 50° C to 900° C.

Synthesis of 9-Isopropylidenebenzonorbornadiene. The compound was prepared according to a modified literature procedure.²⁹ To a refluxing solution of 6,6-dimethylfulvene (5.00 g, 5.7 mL, 47 mmol) and isoamyl nitrite (8.3 g, 9.5 mL, 71 mmol) in 1,2-dichloroethane (40 mL) was added dropwise a solution of anthranilic acid (9.7 g, 71 mmol) in 30 mL acetone. The mixture was then refluxed for 90 minutes before removing the solvents under reduced pressure and extracting with hot hexanes. The product was chromatographed on a column of silica gel (hexanes, $R_f=0.25$) and recovered as a colorless powder (3.4 g, 40%).

Synthesis of IBF-Mono. In a 200 mL round-bottom flask, 3,6-di-2-pyridyl-1,2,4,5-tetrazine (396 mg, 1.67 mmol) was dissolved in dichloromethane (25 mL) and stirred at 0°C under air. 9-Isopropylidenebenzonorbornadiene (305 mg, 1.67 mmol) was dissolved in toluene (10 mL) and added to the tetrazine solution dropwise. The solution was stirred for 30 min and turned lighter, and then toluene/*o*-dichlorobenzene solution (70 mL/10 mL) of C_{60} (602 mg, 0.835 mmol) was added. After overnight stirring, the solution was evaporated under reduced pressure. Ethanol (400 mL) was poured into the reaction mixture to precipitate brown solid. The solid was purified via SiO₂ column chromatography with CS₂/hexane (1:3 v/v) elution, and 170 mg (23.2%) of product was obtained.

¹H NMR (500 MHz, CD₂Cl₂/CS₂, δ): 7.67 (dd, 2H), 7.46 (dd, 2H), 5.43 (s, 2H), 2.20 (s, 6H) ¹³C NMR (500 MHz, CDCl₃/CS₂, δ): 192.35 (CS₂), 29 peaks found for C_{60} sp² carbons (155.63,

153.70, 147.08, 146.12, 146.01, 146.00, 145.92, 145.86, 145.55, 145.43, 145.22, 145.19, 145.18, 145.10, 144.95, 144.94, 144.45, 144.26, 142.47, 142.43, 142.34, 142.13, 142.00, 141.87, 141.73, 141.60, 141.50, 139.81, 139.53), 137.81 (1C), 137.16 (1C), 127.11 (2C), 123.21 (2C), 120.13 (2C), 77.11 ($CDCl_3$), 75.16 (C_{60} sp^3), 57.96 (2C), 20.75 (2C).

MS (MALDI-TOF, m/z): $[M+H]^+$ calcd for $C_{72}H_{12}$, 877.1017; found, 876.9678

Synthesis of IBF-Ep. IBF-Mono (170 mg, 0.194 mmol) was dissolved in CS_2 (25 mL) in a 100 mL round-bottom flask in which a solution of 3-chloroperbenzoic acid (max. 77% purity, 130 mg, 0.753 mmol) in dichloromethane (20 mL) was added dropwise at room temperature. After overnight stirring, a major product spot was detected on a TLC plate. The reaction mixture was dried under reduced pressure, re-dissolved in dichloromethane (30 mL), and extracted with NaOH aqueous solution several times. The organic layer was dried with $MgSO_4$ and concentrated in vacuo. 94.0 mg (54.3%) of the product was isolated after gradient silica column with 1:1 to 3:1 toluene/hexane elution.

1H NMR (500 MHz, CD_2Cl_2/CS_2 , δ): 7.75 (dd, 2H), 7.55 (dd, 2H), 4.78 (s, 2H), 1.87 (s, 6H).

^{13}C NMR (500 MHz, CD_2Cl_2/CS_2 , δ): 192.92 (CS_2), 29 peaks found for C_{60} sp^2 carbons (155.07, 153.74, 147.78, 146.81, 146.66, 146.61, 146.54, 146.19, 146.13, 146.00, 145.89, 145.79, 145.78, 145.69, 145.68, 145.09, 144.91, 144.61, 143.39, 143.11, 143.02, 142.45, 142.40, 142.38, 142.25, 142.20, 14.062, 140.29, 137.90), 137.60 (2C), 128.33 (2C), 125.18 (2C), 87.59 (1C), 72.99 (C_{60} sp^3), 66.01 (1C), 58.42 (2C), 30.46 (grease), 23.74 (2C).

MS (MALDI-TOF, m/z): $[M]^+$ calcd for $C_{72}H_{12}O$, 892.0888; found, 892.4482

Synthesis of IBF-Bis. In a 100 mL round-bottom flask, 3,6-Di-2-pyridyl-1,2,4,5-tetrazine (40 mg, 0.17 mmol) was dissolved in dichloromethane (8 mL) and stirred at room temperature. 9-Isopropylidenebenzonorbornadiene (31 mg, 0.17 mmol) was dissolved in toluene and added to the tetrazine solution dropwise. The solution was stirred for 30 min, and the CS_2 solution (10 mL) of IBF-Mono (150 mg, 0.17 mmol) was added. After overnight stirring, the solution was evaporated under reduced pressure. The reaction mixture was dissolved in toluene and purified by HPLC with 5PBB Cosmosil column (toluene/hexane 1:1 elution). For the further purification, the product was passed through SiO_2 column with CS_2 /hexane (1:3 v/v) elution, and 40 mg (22.8 %) of product was obtained.

1H NMR (500 MHz, CD_2Cl_2/CS_2 , δ): 7.94-7.24 (m, 8H), 5.74-5.02 (m, 4H), 2.40-1.89 (12H).

^{13}C NMR (500 MHz, CD_2Cl_2/CS_2 , δ): 192.92 (CS_2), 160-140 (C_{60} sp^2), 140-130 (alkene), 130-115 (aromatic), 80-70 (C_{60} sp^3), 60-55 (bridgehead), 30.47 (grease), 22-20 (CH_3).

MS (MALDI-TOF, m/z): $[M]^+$ calcd for $C_{84}H_{24}$, 1032.1878; found, 1032.5122

Synthesis of IBF-Bis-Ep1. In a 50 mL round-bottom flask, 3,6-Di-2-pyridyl-1,2,4,5-tetrazine (10.9 mg, 0.046 mmol) was dissolved in dichloromethane (2 mL) and stirred at 0°C under air. 9-Isopropylidenebenzonorbornadiene (8.4 mg, 0.046 mmol) was also dissolved in dichloromethane (5 mL) and added to the tetrazine solution dropwise. The solution was stirred for 1h and turned lighter, and then IBF-Ep (41 mg, 0.046 mmol) dissolved in CS_2 (5 mL) was added to the solution dropwise. After overnight stirring, the solution was concentrated in vacuo. The product was purified by silica column chromatography by the elution of dichloromethane/hexane (1:2), and further purified by HPLC with 5PBB Cosmosil column by toluene/hexane (1:1) elution. The purified product was obtained with the yield of 22.8 % (11 mg).

^1H NMR (500 MHz, CD_2Cl_2 , δ): 7.61-7.32 (m, 8H), 5.13-4.33 (m, 4H), 2.05-1.61 (12H).

^{13}C NMR (500 MHz, CD_2Cl_2 , δ): 160-140 (C_{60} sp^2), 140-130 (alkene), 130-115 (aromatic), 90-70 (epoxide), 70-65 (C_{60} sp^3), 60-55 (bridgehead), 25-20 (CH_3).

MS (MALDI-TOF, m/z): $[\text{M}]^+$ calcd for $\text{C}_{84}\text{H}_{24}\text{O}$, 1048.1827; found, 1048.3863

Synthesis of IBF-Bis-Ep2. IBF-Bis (26 mg, 0.025 mmol) was dissolved in dichloromethane (10 mL) in a 50 mL round-bottom flask in which a solution of 3-chloroperbenzoic acid (*m*CPBA) (max. 77 % purity, 34 mg, 0.197 mmol) in dichloromethane (10 mL) was added dropwise at room temperature. After overnight stirring, a major product spot was detected on a TLC plate. The reaction mixture was extracted with NaOH aqueous solution several times. The organic layer was dried with MgSO_4 and concentrated in vacuo. 14 mg (52.2 %) of the product was isolated after gradient silica column with 2:1 dichloromethane/hexane and 100% dichloromethane elution.

^1H NMR (500 MHz, CD_2Cl_2 , δ): 7.91-7.34 (m, 8H), 4.79-4.35 (m, 4H), 2.05-1.70 (12H).

^{13}C NMR (500 MHz, CD_2Cl_2 , δ): 160-140 (C_{60} sp^2), 140-120 (aromatic), 90-85 (epoxide), 75-70 (C_{60} sp^3), 70-65 (epoxide), 60-55 (bridgehead), 25-20 (CH_3).

MS (MALDI-TOF, m/z): $[\text{M}+\text{H}]^+$ calcd for $\text{C}_{84}\text{H}_{24}\text{O}_2$, 1065.1855; found, 1065.4214

Device Fabrication. Pre-patterned indium tin oxide (ITO)-coated glass substrates (Thin Film Devices, Inc.) were sonicated in deionized water (10 min), acetone (10 min) and isopropanol (10 min) and oxygen plasma-cleaned (3 min) immediately prior to deposition of the PEDOT:PSS layer. PEDOT:PSS (2–5 wt% in water) was spin-coated at 4000 rpm and annealed at 150 °C (using a hotplate) for 20 min. For the active layer, a 25 mg/mL solution of P3HT:fullerene with

an optimized ratio varying from 1: 0.5 to 1:1 in chlorobenzene (CB) was spin-coated onto the PEDOT:PSS layer at 1000 rpm under nitrogen and annealed on a 150 °C hotplate for 20 min under nitrogen. Finally, 25 nm Ca followed by 100 nm Al electrode was deposited by thermal evaporation.

Device Characterization. Current density–voltage (J–V) measurements were recorded by a Keithley 6487 picoammeter both in the dark and under illumination. The devices were illuminated through the glass substrate using an Oriel 91191 150 W full spectrum solar simulator. The illumination intensity was calibrated to 100 mW/cm² using an NREL-certified silicon photodiode. The optical absorption and photoluminescence spectra of devices were obtained by using a Cary 5E UV-vis-NIR dual-beam spectrophotometer. Transient photocurrents and recombination lifetime measurement were conducted with a Newport laser diode (830 nm) driven by an Agilent 33220. A function generator was used as a second light source to provide square wave modulated illumination. This illumination was filtered through a neutral density filter before reaching the device to ensure a small illumination perturbation. V_{OC} decay transients were recorded on a Tektronix TDS 3054B digital oscilloscope.

3.5. References and Notes

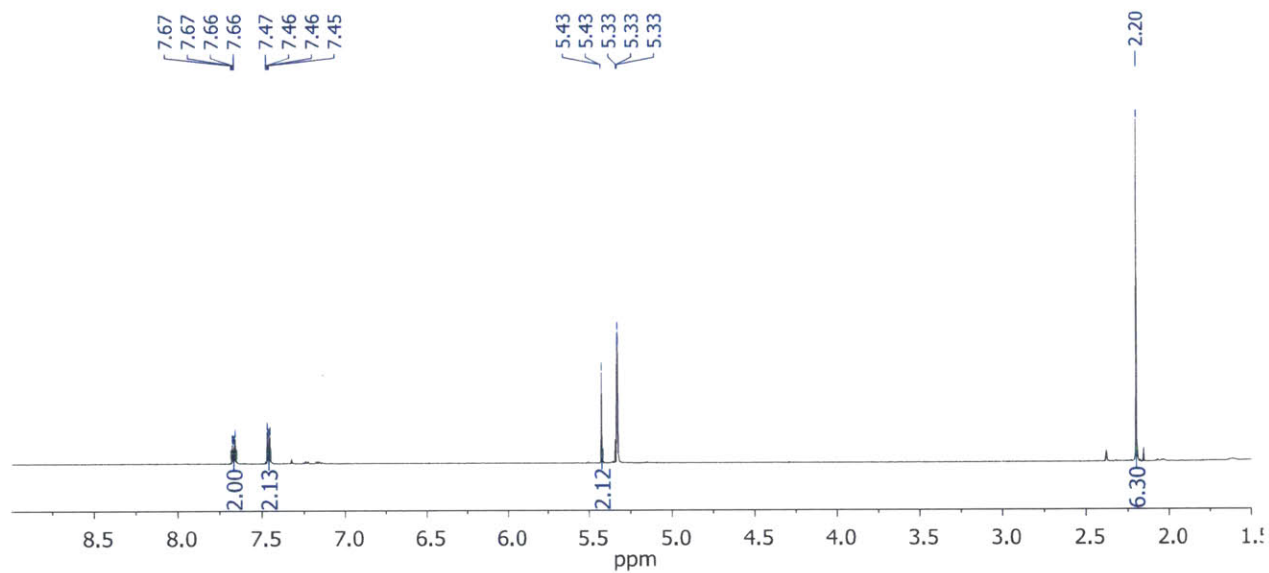
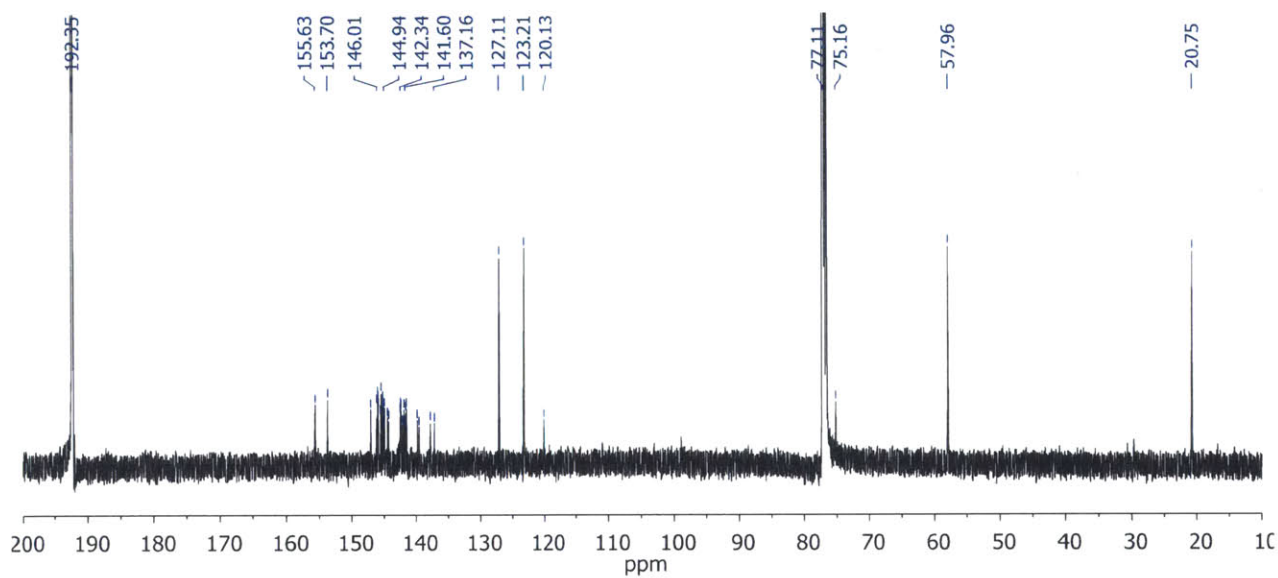
1. Chen, J.; Cao, Y. Development of Novel Conjugated Donor Polymers for High-Efficiency Bulk-Heterojunction Photovoltaic Devices. *Acc. Chem. Res.* **2009**, *42*, 1709-1718.
2. Roncali, J. Molecular Bulk Heterojunctions: An Emerging Approach to Organic Solar Cells. *Acc. Chem. Res.* **2009**, *42*, 1719-1730.
3. Thompson, B. C.; Frechet, J. M. J. Organic photovoltaics- Polymer-Fullerene Composite Solar Cells. *Angew. Chem. Int. Edit.* **2008**, *47*, 58-77.

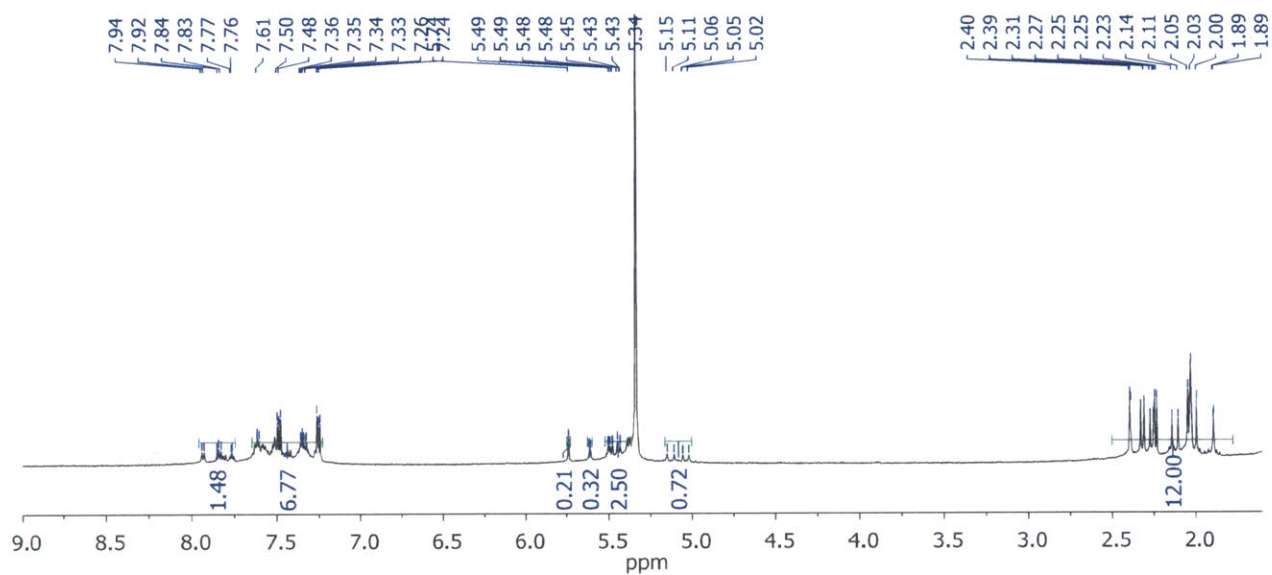
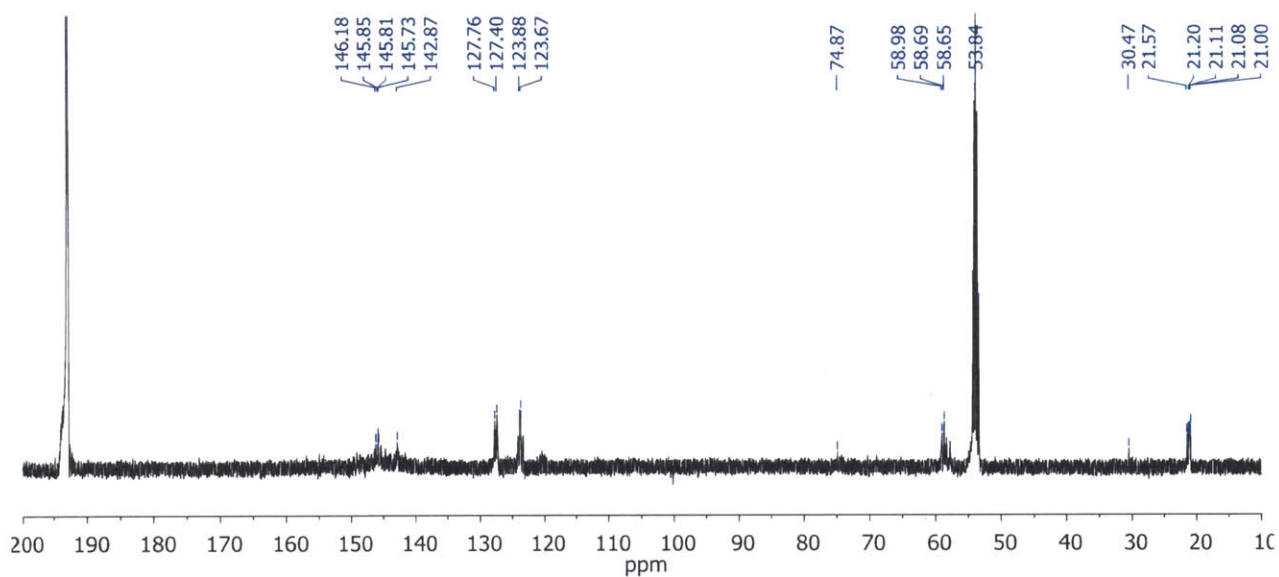
4. Yu, G.; Gao, J.; Hummelen, J. C.; Wudl, F.; Heeger, A. J. Polymer Photovoltaic Cells - Enhanced Efficiencies Via a Network of Internal Donor-Acceptor Heterojunctions. *Science* **1995**, *270*, 1789-1791.
5. Cheng, Y. J.; Yang, S. H.; Hsu, C. S. Synthesis of Conjugated Polymers for Organic Solar Cell Applications. *Chem. Rev.* **2009**, *109*, 5868-5923.
6. Muhlbacher, D.; Scharber, M.; Morana, M.; Zhu, Z. G.; Waller, D.; Gaudiana, R.; Brabec, C. High Photovoltaic Performance of a Low-Bandgap Polymer. *Adv. Mater.* **2006**, *18*, 2884-2889.
7. Scharber, M. C.; Wuhlbacher, D.; Koppe, M.; Denk, P.; Waldauf, C.; Heeger, A. J.; Brabec, C. L. Design Rules for Donors in Bulk-Heterojunction Solar Cells- Towards 10 % Energy-Conversion Efficiency. *Adv. Mater.* **2006**, *18*, 789-794.
8. Chochos, C. L.; Tagmatarchis, N.; Gregoriou, V. G. Rational Design on N-Type Organic Materials for High Performance Organic Photovoltaics. *RSC Adv.* **2013**, *3*, 7160-7181.
9. He, Y. J.; Chen, H. Y.; Hou, J. H.; Li, Y. F. Indene-C₆₀ Bisadduct: A New Acceptor for High-Performance Polymer Solar Cells. *J. Am. Chem. Soc.* **2010**, *132*, 1377-1382.
10. Brabec, C. J.; Cravino, A.; Meissner, D.; Sariciftci, N. S.; Fromherz, T.; Rispen, M. T.; Sanchez, L.; Hummelen, J. C. Origin of the open circuit voltage of plastic solar cells. *Adv. Funct. Mater.* **2001**, *11*, 374-380.
11. Zhang, Y.; Matsuo, Y.; Li, C. Z.; Tanaka, H.; Nakamura, E. A Scalable Synthesis of Methano[60]fullerene and Congeners by the Oxidative Cyclopropanation Reaction of Silylmethylfullerene. *J. Am. Chem. Soc.* **2011**, *133*, 8086-8089.
12. Han, G. D.; Collins, W. R.; Andrew, T. L.; Bulovic, V.; Swager, T. M. Cyclobutadiene-C₆₀ Adducts: N-Type Materials for Organic Photovoltaic Cells with High V_{OC}. *Adv. Funct. Mater.* **2013**, *23*, 3061-3069.
13. Wudl, F. The Chemical Properties of Buckminsterfullerene (C₆₀) and the Birth and Infancy of Fullerenes. *Acc. Chem. Res.* **1992**, *25*, 157-161.

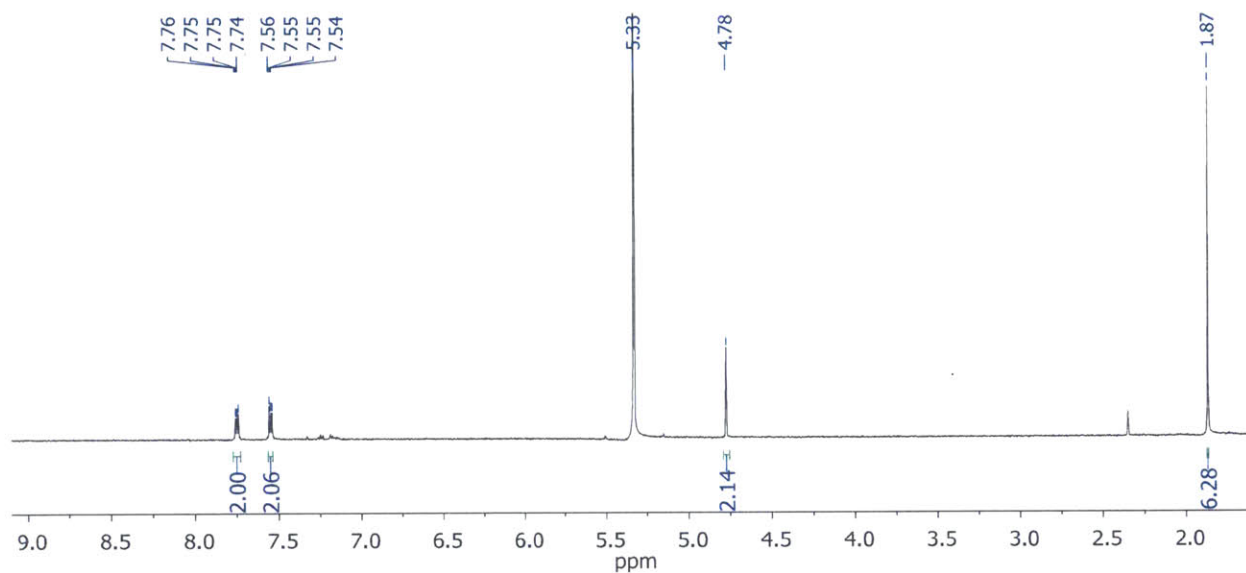
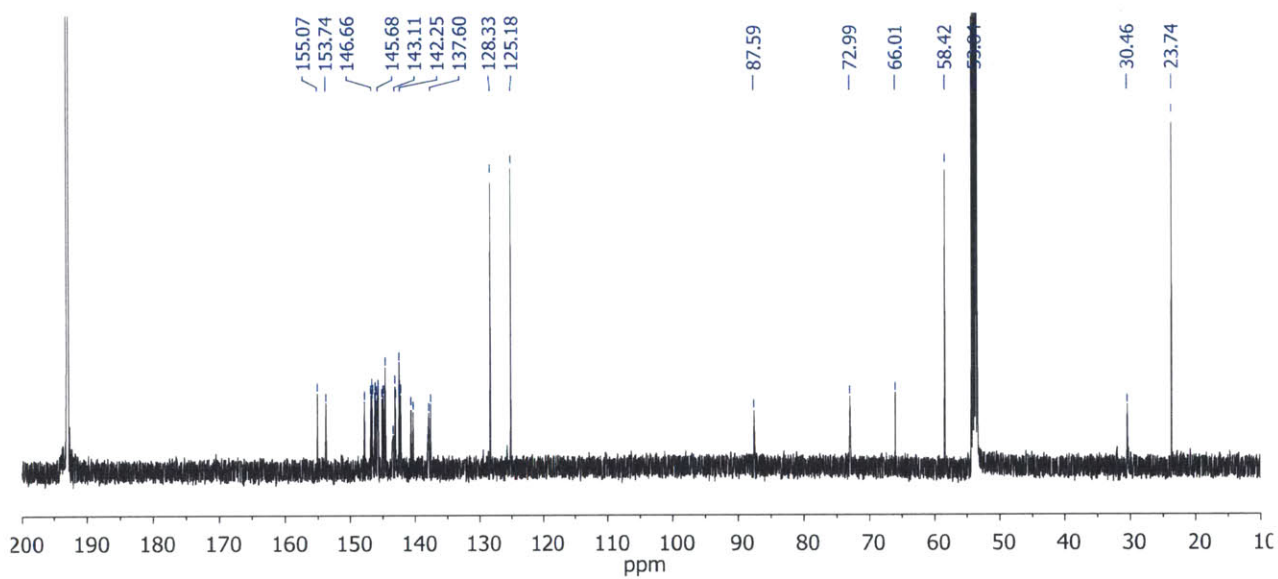
14. Laird, D. W. R., H.; Vejins, V.; Scott, L. T.; Lada, T. A. Organic photovoltaic devices comprising fullerenes and derivatives thereof and improved methods of making fullerene derivatives. *Patent* WO/2008/018931 A2.
15. Puplovskis, A.; Kacens, J.; Neilands, O. New route for [60]fullerene functionalisation in [4+2] cycloaddition reaction using indene. *Tetrahedron Lett.* **1997**, *38*, 285-288.
16. Tanida, H.; Tori, K.; Irie, T. Generation and Cycloaddition of 8,8-Dimethylisobenzofulvene. *Bull. Chem. Soc. Jpn.* **1972**, *45*, 1999-2003.
17. Warrenner, R. N.; Hammond, M. L. A.; Butler, D. N. The trapping of 6,6-dimethylisobenzofulvene by its 1,3-dipolar precursor: A rare example of a dipolar [6+4] cycloaddition. *Syn. Commun.* **2001**, *31*, 1167-1175.
18. Li, Y. F. Fullerene-Bisadduct Acceptors for Polymer Solar Cells. *Chem. Asian J.* **2013**, *8*, 2316-2328.
19. Lenes, M.; Wetzelaer, G. J. A. H.; Kooistra, F. B.; Veenstra, S. C.; Hummelen, J. C.; Blom, P. W. M. Fullerene Bisadducts for Enhanced Open-Circuit Voltages and Efficiencies in Polymer Solar Cells. *Adv. Mater.* **2008**, *20*, 2116-2119.
20. Khlyabich, P. P.; Burkhart, B.; Thompson, B. C. Efficient Ternary Blend Bulk Heterojunction Solar Cells with Tunable Open-Circuit Voltage. *J. Am. Chem. Soc.* **2011**, *133*, 14534-14537.
21. Kooistra, F. B.; Knol, J.; Kastenberg, F.; Popescu, L. M.; Verhees, W. J. H.; Kroon, J. M.; Hummelen, J. C. Increasing the Open Circuit Voltage of Bulk-Heterojunction Solar Cells by Raising the LUMO Level of the Acceptor. *Org. Lett.* **2007**, *9*, 551-554.
22. Troshin, P. A.; Hoppe, H.; Peregudov, A. S.; Egginger, M.; Shokhovets, S.; Gobsch, G.; Sariciftci, N. S.; Razumov, V. F. [70]Fullerene-Based Materials for Organic Solar Cells. *Chemosuschem*, **2011**, *4*, 119-124.
23. Delgado, J. L.; Oswald, F.; Cardinali, F.; Langa, F.; Martin, N. On the Thermal Stability of [60]Fullerene Cycloadducts: Retro-Cycloaddition Reaction of 2-Pyrazolino[4,5:1,2][60]fullerenes. *J. Org. Chem.* **2008**, *73*, 3184-3188.

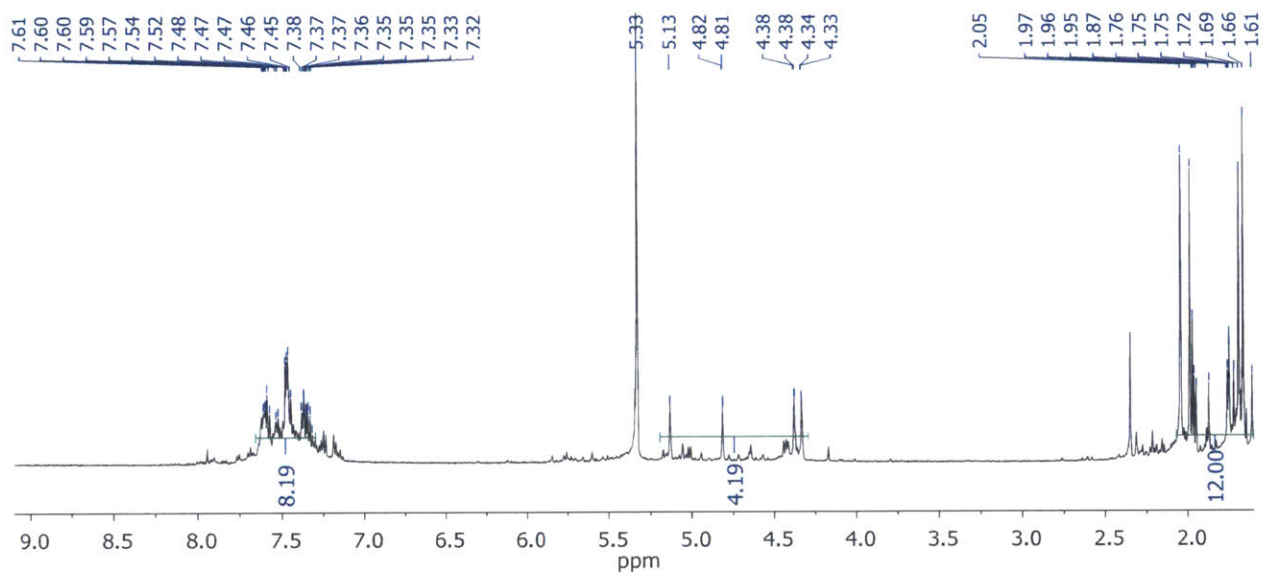
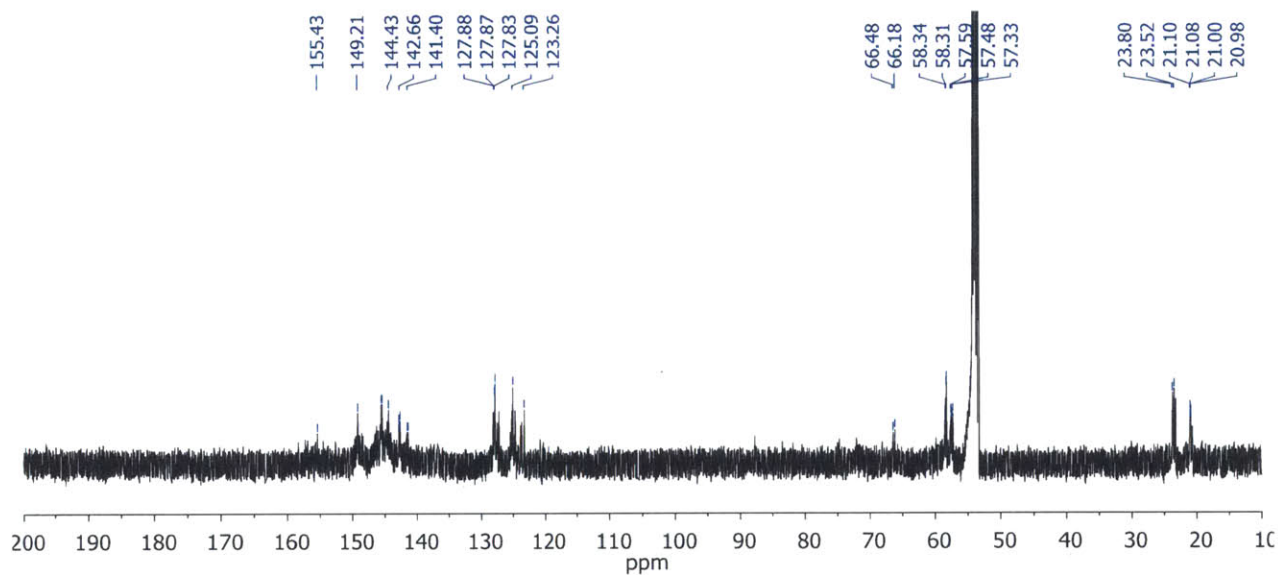
24. Martin, N.; Altable, M.; Filippone, S.; Martin-Domenech, A.; Echegoyen, L.; Cardona, C. M. Retro-Cycloaddition Reaction of Pyrrolidinofullerenes. *Angew. Chem. Int. Edit.* **2006**, *45*, 110-114.
25. Milliken, J.; Keller, T. M.; Baronavski, A. P.; Mcelvany, S. W.; Callahan, J. H.; Nelson, H. H. Thermal and Oxidative Analyses of Buckminsterfullerene, C₆₀. *Chem. Mater.* **1991**, *3*, 386-387.
26. Larson, B. W.; Whitaker, J. B.; Popov, A. A.; Kopidakis, N.; Rumbles, G.; Boltalina, O. V.; Strauss, S. H., Thermal [6,6] -> [6,6] Isomerization and Decomposition of PCBM (Phenyl-C-61-butyrlic Acid Methyl Ester). *Chem. Mater.* **2014**, *26*, 2361-2367.
27. Maurano, A.; Hamilton, R.; Shuttle, C. G.; Ballantyne, A. M.; Nelson, J.; O'Regan, B.; Zhang, W. M.; McCulloch, I.; Azimi, H.; Morana, M.; Brabec, C. J.; Durrant, J. R. Recombination Dynamics as a Key Determinant of Open Circuit Voltage in Organic Bulk Heterojunction Solar Cells: A Comparison of Four Different Donor Polymers. *Adv. Mater.* **2010**, *22*, 4987-4992.
28. Shaheen, S. E.; Brabec, C. J.; Sariciftci, N. S.; Padinger, F.; Fromherz, T.; Hummelen, J. C. 2.5% Efficient Organic Plastic Solar Cells. *Appl. Phys. Lett.* **2001**, *78*, 841-843.
29. Lombardo, L.; Wege, D.; Wilkinson, S. P. Reaction of Benzonorbomadiene and Related Compounds with Iron Carbonyls. *Aust. J. Chem.* **1974**, *27*, 143-152.

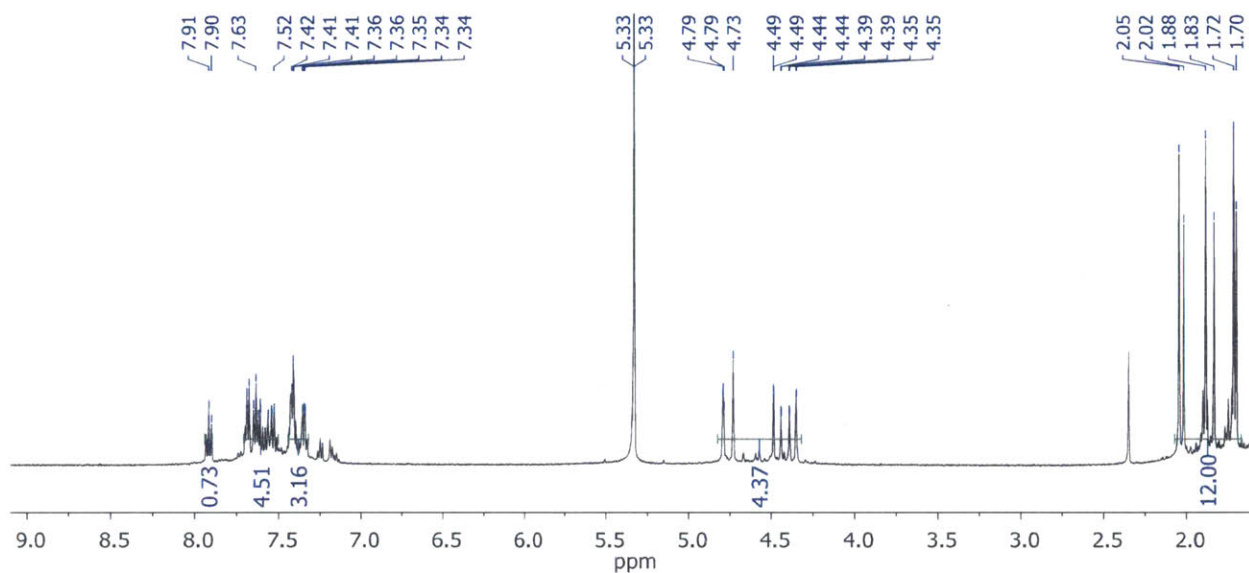
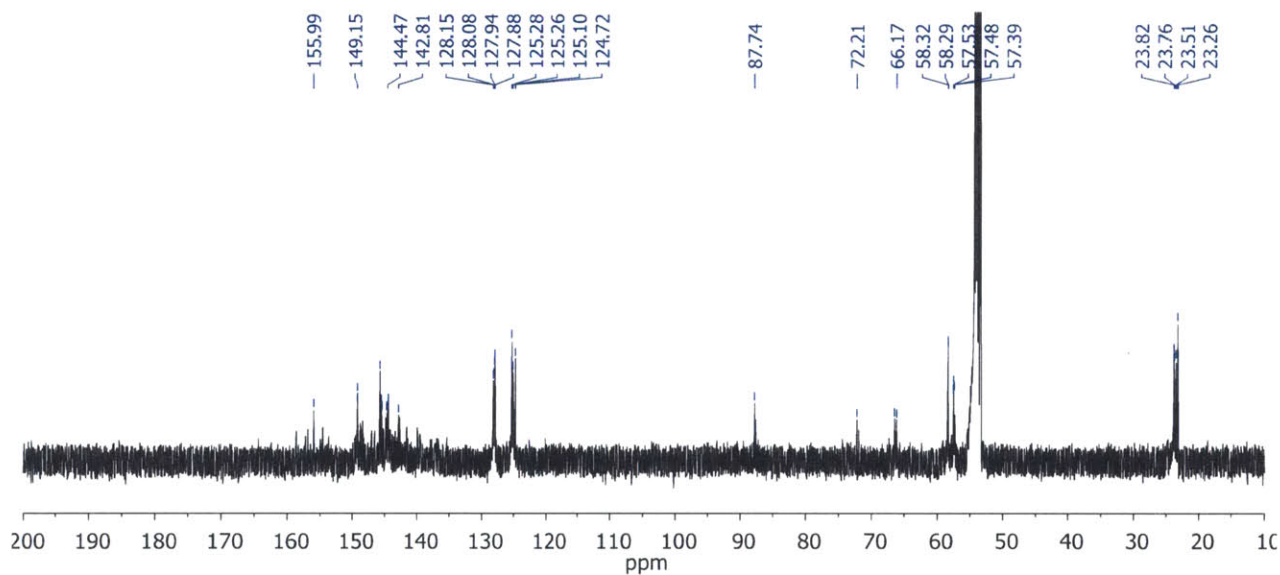
3.6. Appendix

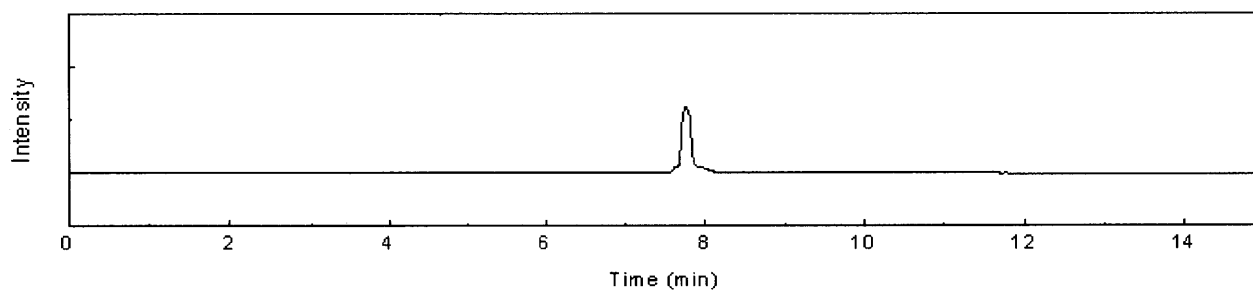
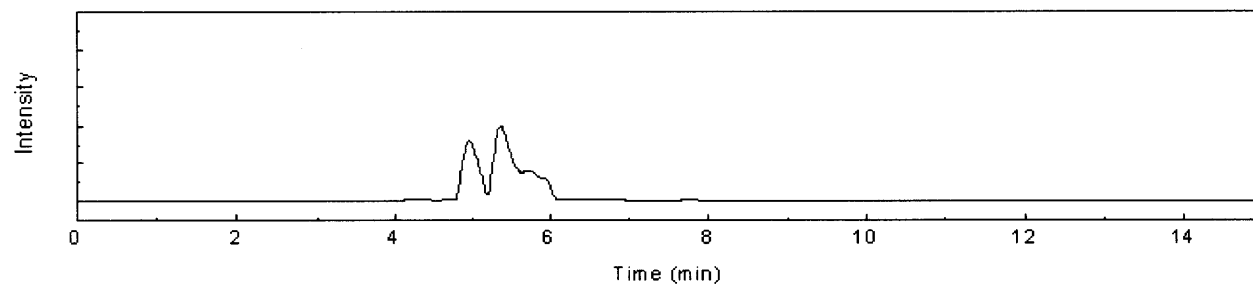
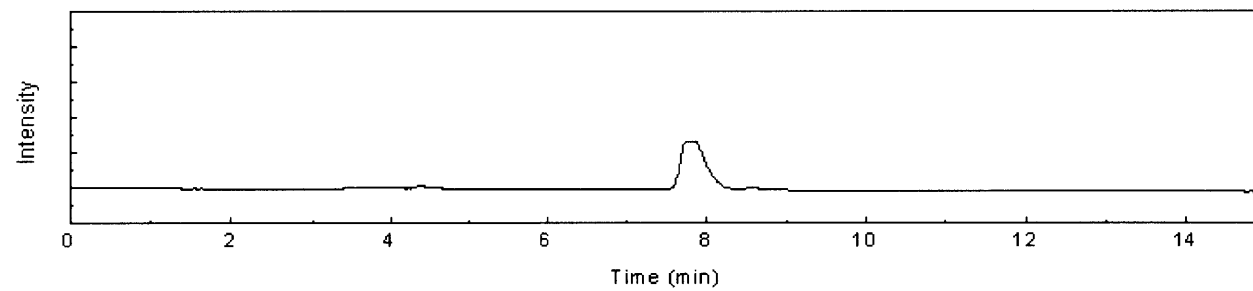
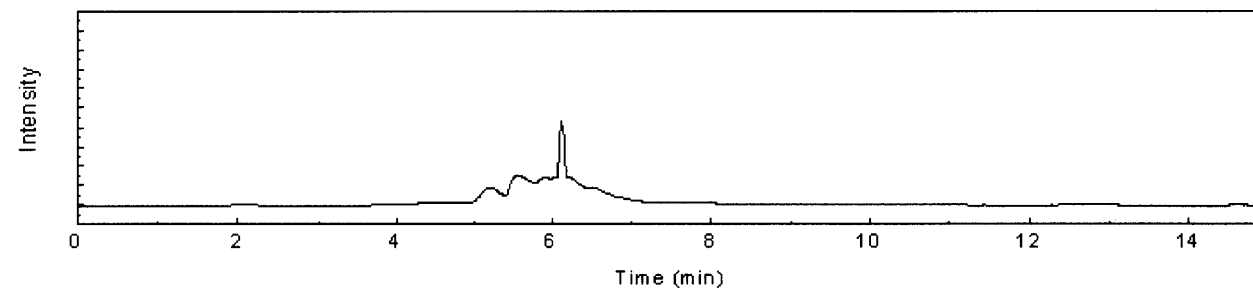
Spectrum 3.1. ¹H NMR of IBF-MonoSpectrum 3.2. ¹³C NMR of IBF-Mono

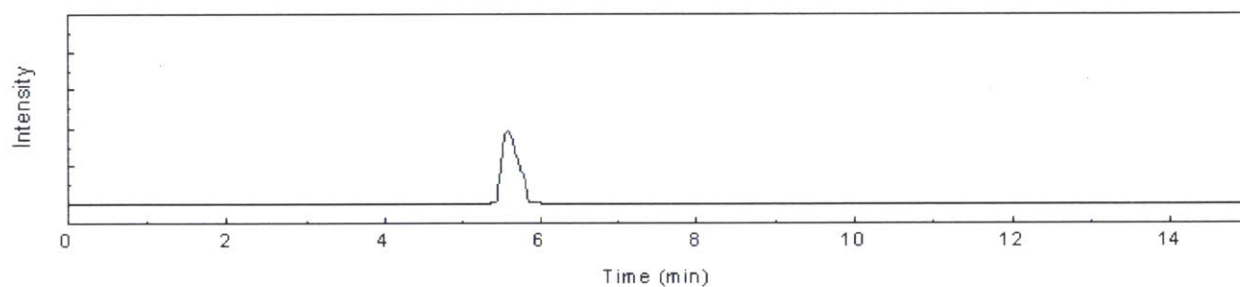
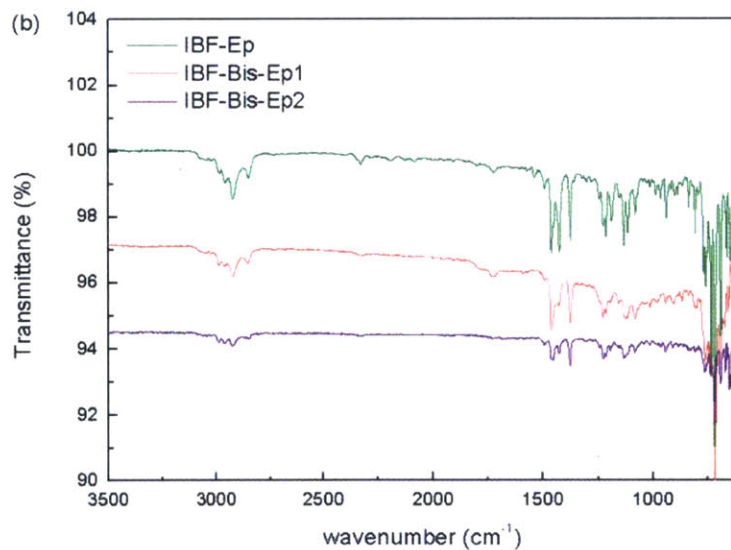
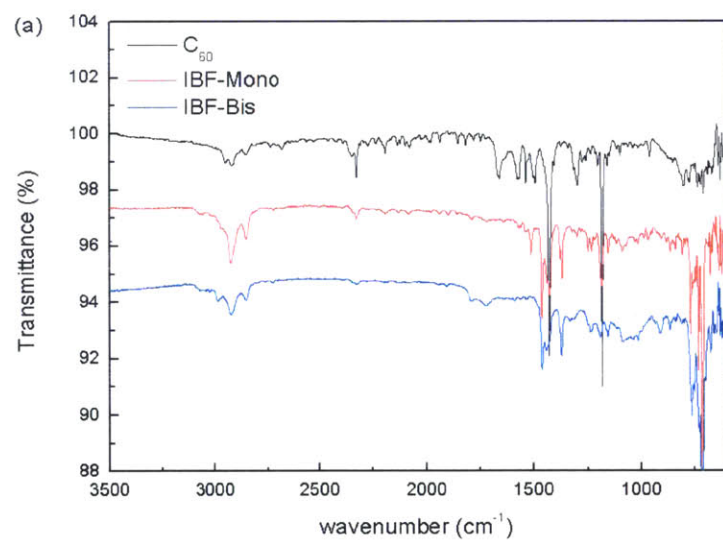
Spectrum 3.3. ^1H NMR of IBF-Bis**Spectrum 3.4.** ^{13}C NMR of IBF-Bis

Spectrum 3.5. ^1H NMR of IBF-Ep**Spectrum 3.6.** ^{13}C NMR of IBF-Ep

Spectrum 3.7. ^1H NMR of IBF-Bis-Ep1**Spectrum 3.8.** ^{13}C NMR of IBF-Bis-Ep1

Spectrum 3.9. ¹H NMR of IBF-Bis-Ep2**Spectrum 3.10.** ¹³C NMR of IBF-Bis-Ep2

Spectrum 3.11. HPLC trace of IBF-Mono**Spectrum 3.12.** HPLC trace of IBF-Bis**Spectrum 3.13.** HPLC trace of IBF-Ep**Spectrum 3.14.** HPLC trace of IBF-Bis-Ep1

Spectrum 3.15. HPLC trace of IBF-Bis-Ep2**Spectrum 3.16.** ATR-FTIR spectra of (a) C_{60} reference, IBF-Mono, IBF-Bis, (b) IBF-Ep, IBF-Bis-Ep1, and IBF-Bis-Ep2

CHAPTER 4
**Ambient-Processed Transition Metal Oxide Free-
Perovskite Solar Cells Enabled by
a New Organic Charge Transport Layer**

Adapted and reprinted in part from:

S. Chang[†], **G. D. Han[†]**, J. G. Weis, H. Park, T. M. Swager, and S. Gradečak.

“Ambient-Processed Transition Metal Oxide Free-Perovskite Solar Cells Enabled by a New Organic Charge Transport Layer.” [†]Equal Contribution.

4.1. Introduction

Recent achievements in high-efficiency organic/inorganic hybrid perovskite solar cells and other thin-film photovoltaics have been driven by developments in charge transfer materials with improved electronic properties and processability. A promising configuration for planar perovskite devices has been demonstrated by sandwiching the perovskite layer between a hole transport layer (HTL) and an electron transport layer (ETL). In particular, Spiro-OMeTAD (2,2',7,7'-tetrakis(*N,N*-di-*p*-methoxyphenylamine)-9,9'-spirobifluorene) has been widely used as a solid-state HTL because it can be deposited on top of a solution-processed methylammonium lead halide-based perovskite ($\text{CH}_3\text{NH}_3\text{PbX}_3$, X = Cl, Br, I) layer.¹⁻³ Recent studies demonstrate that the modification of two *p*-OMe substituents of Spiro-OMeTAD improves the power conversion efficiency (PCE) of perovskite solar cells up to 16.7%.⁴ Devices with record-high PCE of ~19.3% have been achieved using a Spiro-OMeTAD HTL and an yttrium-doped TiO_2 ETL.⁵ These studies reveal that the Spiro-OMeTAD HTL is optimally subjected to air oxidation to improve hole conductivity, which increases the PCE.⁶

A variety of transition metal oxides have been investigated as ETLs for perovskite solar cells.^{1,2,7} These solar cells are generally fabricated on nanostructured metal oxide substrates (e.g. TiO_2 , ZrO_2 , ZnO , and Al_2O_3) to maximize the interfacial area for efficient charge collection.^{2,8,9} However, the processing of the metal oxides involves a high-temperature sintering step, which makes them incompatible with perovskite layers that cannot tolerate temperatures above 100 °C. Therefore, the fabrication of inverted cells with metal oxide ETLs, where metal oxide layers are deposited on top of perovskite, has remained a challenge. To overcome this issue, organic electron transport materials such as C_{60} derivatives (e.g. phenyl- C_{61} -butyric acid methyl ester (PCBM)) have been used with an inverted structure,¹⁰ but the limited chemical and

morphological stability of PCBM under thermal annealing^{11, 12} may limit the performance of these solar cells. In addition, the production and stability of mixed lead halide-based perovskite solar cells in a normal structure with an underlying PCBM ETL have not been investigated under ambient conditions. Given the advantages of air oxidation of Spiro-OMeTAD as an effective HTL and the ease of non-glove box processing, it is desirable to develop an electron transport material that can tolerate ambient fabrication for this particular device architecture.

We report herein methylammonium mixed lead halide-based perovskite ($\text{CH}_3\text{NH}_3\text{PbI}_{3-x}\text{Cl}_x$) solar cells with a new organic electron transport material, isobenzofulvene- C_{60} -epoxide (IBF-Ep), generating a PCE of 6.9% in a normal structure and 9.0% in an inverted structure. In both configurations, the devices containing IBF-Ep ETL outperformed those with the conventional PCBM ETL. This advance is made possible by the superior morphological stability of IBF-Ep under thermal annealing conditions and its tolerance toward oxygen and moisture introduced under the ambient processing conditions.

4.2. Results and Discussion

4.2.1. Selection of Electron Transport Materials

The selection of new fullerene electron transport material was inspired by the investigation of the known ETL materials, PCBM and ICBA (indene- C_{60} bisadducts), both of which were successfully implemented in perovskite solar cells.^{13, 14} The chemical structures and the physical properties are highly correlated, thus we aim at selecting fullerenes that can be cast into smooth films by design. Inspired by indene- C_{60} adducts^{15, 16} we chose isobenzofulvene- C_{60} Diels-Alder adducts for ETL (Chapter 3), which possess 5- and 6-membered ring junctions with the pendant functional groups in contrast to the compact cyclopropane junction of PCBM. This structure has similarities to indene- C_{60} , but is augmented by an electron-rich tetra-substituted

alkene that interacts cofacially with the C₆₀. The bulky nature pendants on C₆₀ can suppress heterogeneity in fullerene phases that can occur in thermal annealing. The epoxide derivative (IBF-Ep) which exhibited the best performance in OPV (Chapter 3) among the isobenzofulvene-C₆₀ series was employed for ETL in perovskite solar cells, due to its superior processability and its LUMO level matching well with the conduction band edge of perovskite active layer.

4.2.2. Morphology of IBF-Ep and PCBM Thin Films and the Perovskite Layers on the Fullerene Films

A uniform morphology of perovskite layers is a key requirement for the reproducible manufacturing of quality solar cells. Therefore, we first investigated the thin film morphology of the underlying ETLs, which affect the morphology of the overlaid perovskite layers. IBF-Ep and PCBM were spin-coated in a N₂-filled glove box and annealed at 150 °C for 10 min to remove chlorobenzene. The thermal annealing of the organic ETLs (both IBF-Ep and PCBM) is necessary to improve the device performance as determined through control experiments (Appendix Figure 4.9). After annealing, the IBF-Ep films showed smooth morphology, whereas PCBM films exhibited aggregate features as large as 1 μm in diameter. The aggregating phenomenon of PCBM in bulk heterojunctions with various polymers is well known, and photo-oligomerization or the use of additives has been used to mitigate particle formation.¹⁷⁻²⁰ The origin of the differences in the extent of aggregation of IBF-Ep relative to PCBM is revealed in their dissimilar thermal properties measured by differential scanning calorimetry (DSC), as shown in Figure 4.1 (a). Consistent with literature reports,²¹⁻²³ PCBM was analyzed as received from a commercial source and it displays a residual solvent evaporation peak around 250 °C, a melting point at 282 °C on the first heating cycle, and a crystallization peak around 244 °C on the first cooling cycle. In contrast, under the same measurement conditions IBF-Ep does not exhibit

any measurable peaks (phase transitions) with the heating or cooling cycles. As reported for other bisadducts of fullerenes,^{22, 24} the absence of melting point and crystallization features indicates that the initially produced phase is stable over the temperature ranges studied.

To further investigate if there are thermally induced changes in the crystallinity of IBF-Ep and PCBM in the solid state, variable-temperature transmission-mode X-ray powder diffraction measurements were conducted. As shown in Figure 4.1 (b) and Figure 4.2, the crystalline phase of IBF-Ep powder remains unchanged upon heating up to 227 °C and cooling down to room temperature. In contrast, the diffraction pattern of PCBM displays slight changes upon heating and more after cooling (Figure 4.1 (c) and Figure 4.2). These studies reveal increased intensity in some peaks, new features and a reduction in other scattering. The loss of some of the broader features and enhancement of others are suggestive of an increase in crystalline domain sizes and/or changes in the relative amounts of different crystalline phases. Regardless of the explanation, it is clear that the morphology of PCBM is less stable under thermal annealing conditions, which results in the pronounced aggregation as shown in Figure 4.3 (b) and (d). This analysis is consistent with the chemical structures of IBF-Ep and PCBM; when compared to the functional group on PCBM, the epoxidized isobenzofulvene appendage of IBF-Ep is bulkier and lacks conformational flexibility which helps to suppress solid state phase transitions.

Figure 4.1. DSC traces of PCBM and IBF-Ep powder on the first heating and cooling cycles ranging from 25 °C to 350 °C. The decomposition temperatures of both materials are higher than 350 °C. Variable-temperature X-ray powder diffraction patterns of (b) IBF-Ep and (c) PCBM powder, packed in a capillary, measured at 25 °C (RT), 150 °C, 227 °C, and 25 °C again (RT') upon cooling. Dots indicate the peaks that developed after cooling of the capillary.

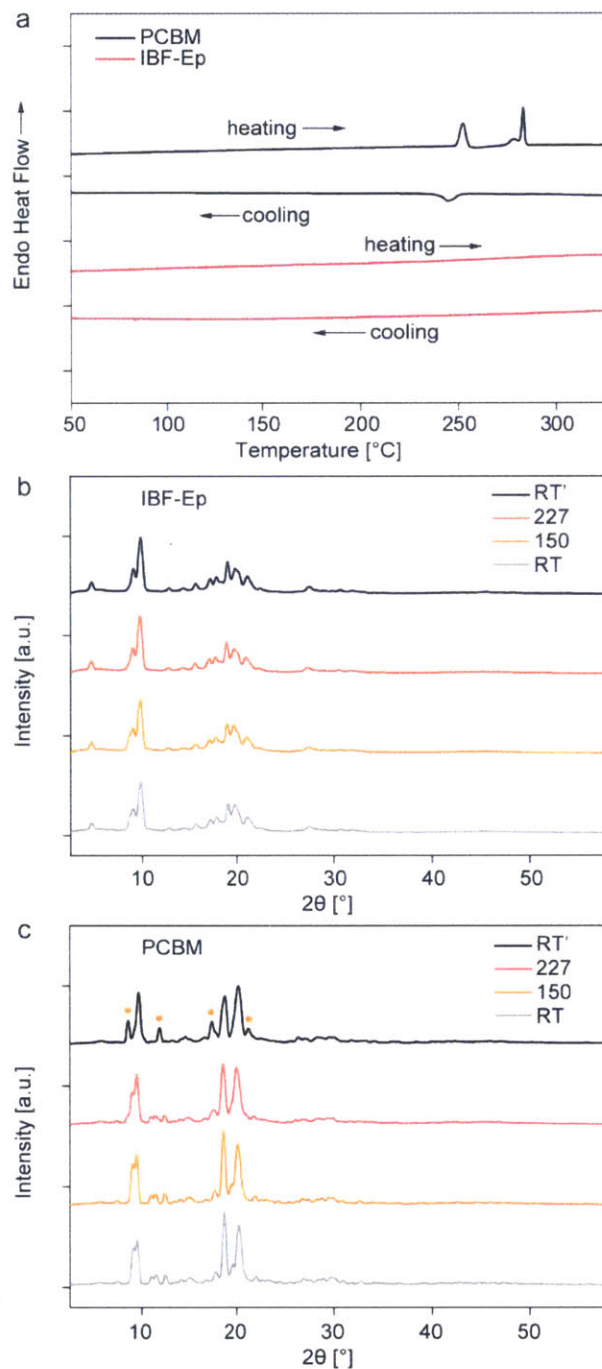
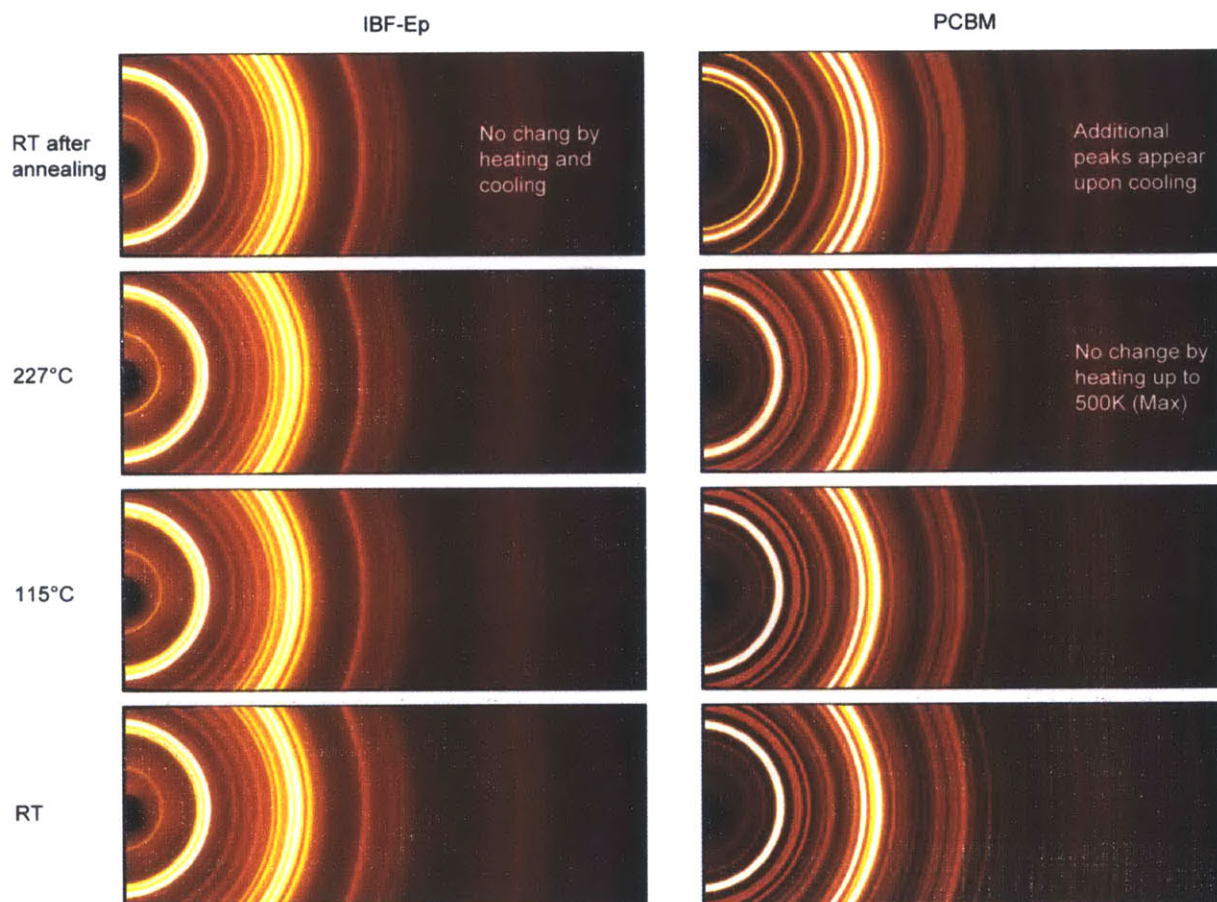


Figure 4.2. X-ray powder diffraction patterns of IBF-Ep and PCBM obtained at various temperatures. Four ranges of 2θ were collected subsequently and stitched together to cover the entire range shown here. The brighter parts represent higher intensities and correspond to the peaks in Figure 4.1 (b) and (c).



The morphologies of IBF-Ep and PCBM layers (Figure 4.3 (a-d)) investigated using atomic force microscopy (AFM) and scanning electron microscopy (SEM) corroborate the differential scanning calorimetry (DSC) and X-ray powder diffraction (XRD) measurements. The aggregation of PCBM is the result of instability of its solid-state phase upon thermal annealing, which may be also associated by the solvent desorption. The absence of aggregates on IBF-Ep films under the identical conditions is in accordance with thermal stability of IBF-Ep in the solid state observed by DSC and XRD. Furthermore, images of $\text{CH}_3\text{NH}_3\text{PbI}_{3-x}\text{Cl}_x$ perovskite layers spin-coated on IBF-Ep and PCBM ETLs under ambient conditions (Figure 4.3 (e-h)) show that the $\text{CH}_3\text{NH}_3\text{PbI}_{3-x}\text{Cl}_x$ sheets on the IBF-Ep ETL are smooth and uniform, whereas

perovskite films with a PCBM underlayer form particulates and have reduced coverage. As expected, the perovskite materials formed on either of the fullerene layers are nearly identical in terms of the UV-Vis absorption characteristics and the X-ray diffraction patterns (Figure 4.4). Therefore, we hypothesize that the observed morphological differences of ETLs (PCBM and IBF-Ep) directly influence the formation and coverage of perovskite active layer processed under ambient conditions, but do not affect its intrinsic properties.

Figure 4.3. AFM topographic images of (a) IBF-Ep and (b) PCBM. SEM images of (c) IBF-Ep and (d) PCBM. Fullerene aggregates were observed in PCBM films. (e-f) AFM topographic images of $\text{CH}_3\text{NH}_3\text{PbI}_{3-x}\text{Cl}_x$ perovskite layers spin-coated under ambient condition on IBF-Ep (e) and PCBM (f). (g-f) SEM images of perovskite layers on IBF-Ep ($70 \pm 5\%$ of perovskite coverage) (g) and PCBM ETLs ($60 \pm 5\%$ of perovskite coverage) (h). Particulates and lower coverage ($60 \pm 5\%$) of perovskite were seen on the films with PCBM ETLs.

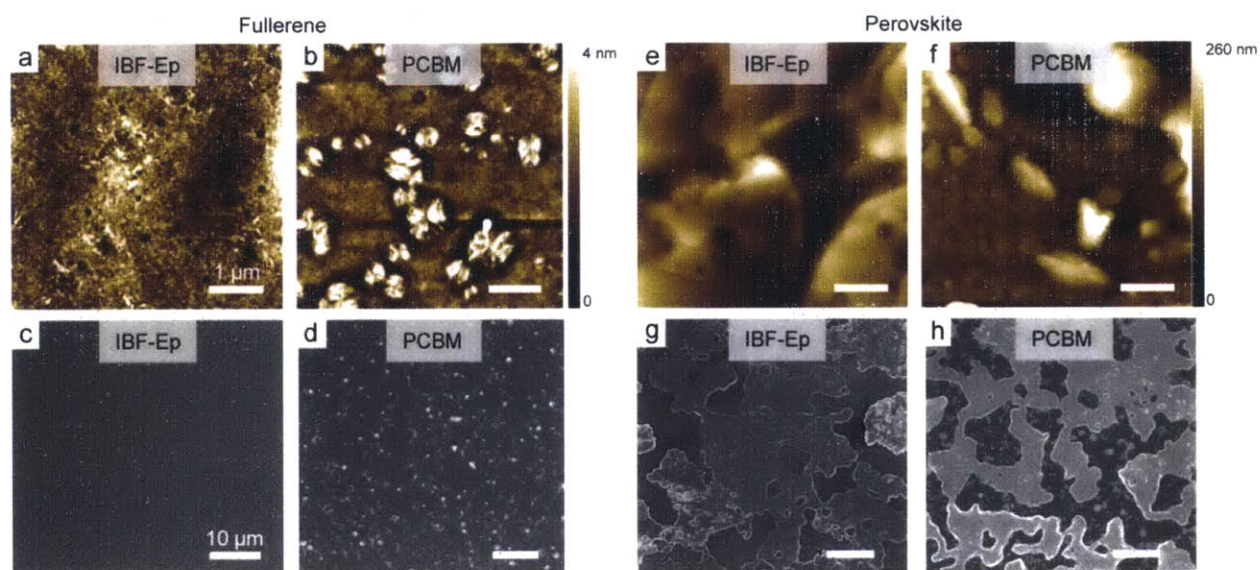
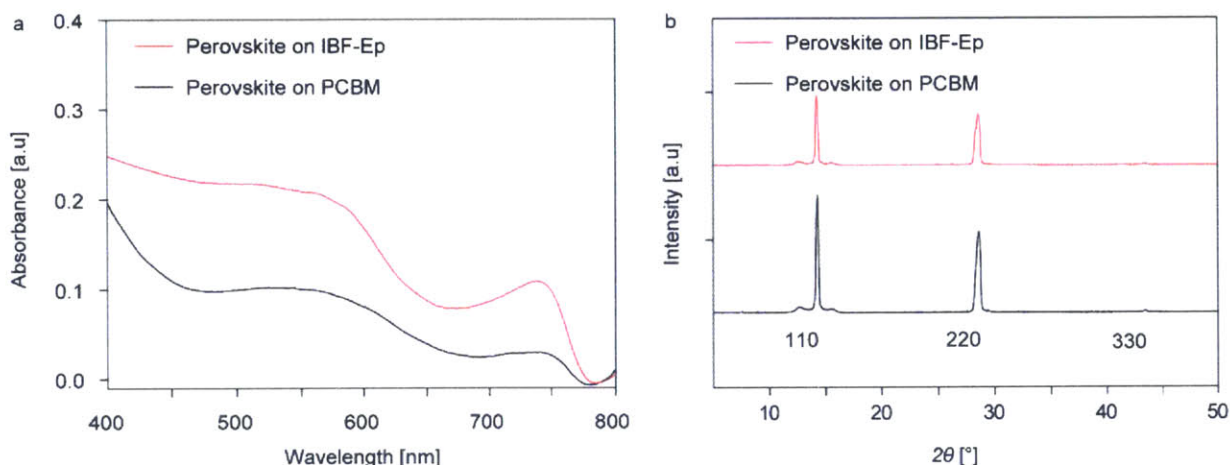


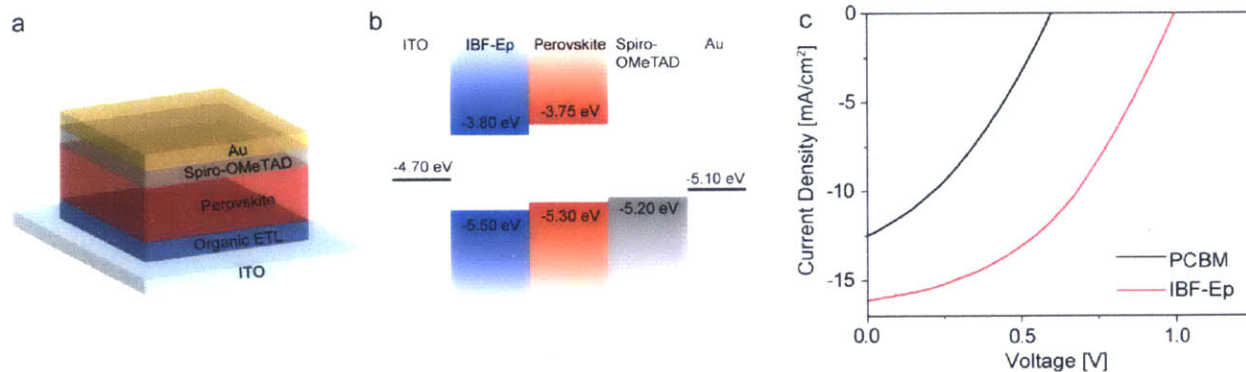
Figure 4.4. (a) UV-Vis absorption spectra and (b) X-ray diffraction patterns of $\text{CH}_3\text{NH}_3\text{PbI}_{3-x}\text{Cl}_x$ solar cells in a normal device structures measured under ambient conditions.



4.2.3. Normal Structure Devices

TiO₂ and ZnO, with conduction band edges of -4.0 eV and -4.3 eV, respectively,²⁵ are the two most commonly used transition metal oxide ETLs for perovskite solar cells. The LUMO level of IBF-Ep (-3.8 eV) is comparable to these materials, and as a result facile electron transfer from the conduction band edge of perovskite to IBF-Ep is expected. We have therefore replaced the transition metal oxide ETLs in the normal device structure with a functionalized fullerene that serves as the base layer upon which the perovskite is deposited. The normal device structure of the CH₃NH₃PbI_{3-x}Cl_x perovskite solar cells investigated in this study and the corresponding band diagram are shown in Figure 4.5 (a) and (b), respectively.

Figure 4.5. (a) A schematic of the normal CH₃NH₃PbI_{3-x}Cl_x perovskite solar cell structure. (b) The corresponding energy band diagram. (c) *J-V* characteristics of the CH₃NH₃PbI_{3-x}Cl_x perovskite solar cells with PCBM and IBF-Ep organic ETLs (measured under 100 mW/cm² AM1.5G illumination).



The J - V characteristics of the devices with different organic ETLs (IBF-Ep or PCBM), but otherwise identical architectures, are shown in Figure 4.5 (c) and their performance is summarized in Table 4.1. When compared to the reference device incorporating a conventional PCBM ETL, the solar cell with IBF-Ep exhibits significantly improved V_{oc} and J_{sc} . The measured record-high PCE of the IBF-Ep device is 6.9%, which is a major improvement compared to the best PCBM reference device with PCE of 2.5%. Considering the similar band offsets of IBF-Ep and PCBM, we attribute the V_{oc} differences to the improved overall morphology, as discussed previously. Although the perovskite active layers in both devices have similar crystallinity as determined by X-ray diffraction (Figure 4.4), their distinct phase and coverage (Figure 4.3) impact the device performance. Substantial phase separation and defects can lead to increased charge recombination, and as a result the morphological traits of the perovskite layer on the PCBM ETL layer can account for the attenuated V_{oc} . This effect emphasizes the superior potential of IBF-Ep as a bottom layer in PHJ solar cells.

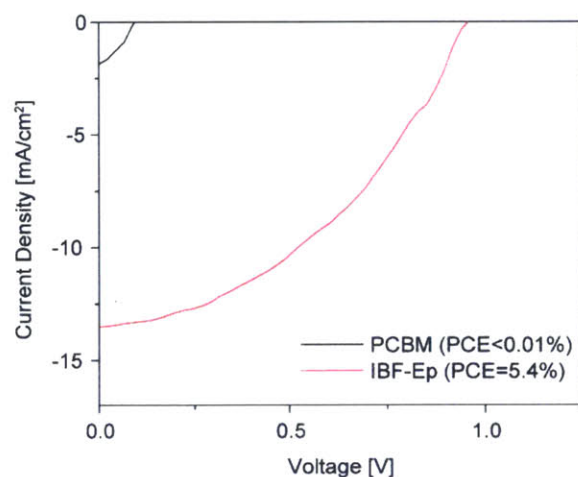
Table 4.1. Performance of $\text{CH}_3\text{NH}_3\text{PbI}_{3-x}\text{Cl}_x$ perovskite solar cells in the normal device architecture. For each structure, average values and standard deviation for five measured devices are indicated, as well as the champion device results (in parentheses).

Device	J_{sc} (mA/cm ²)	V_{oc} (V)	FF	PCE (%)
--------	--------------------------------	--------------	----	---------

PCBM	12.5 ± 0.8 (12.5)	0.55 ± 0.03 (0.59)	0.33 ± 0.01 (0.34)	2.3 ± 0.2 (2.5)
IBF-Ep	16.0 ± 0.7 (16.1)	0.95 ± 0.05 (1.00)	0.42 ± 0.02 (0.43)	6.4 ± 0.5 (6.9)

In addition to the superior device performance of the optimized devices, another key advantage of the IBF-Ep devices over the PCBM reference cells is their consistent superior performance independent of the humidity level in the processing environment (Figure 4.6). Day-to-day humidity is difficult to control under ambient processing conditions, and therefore a stable device performance tolerant of varying humidity is crucial for reliable manufacturing.²⁶ For IBF-Ep devices, a PCE in the range of 5.4–6.9% is maintained under conditions ranging from moderate (60%) to high (90%) relative humidity. In contrast to the IBF-Ep devices, the reference cells with a PCBM ETL show significantly poorer performance at higher relative humidity conditions; when fabricated under the condition of 90% relative humidity, the PCE of PCBM cells drops to below 0.01%.

Figure 4.6. J - V characteristics of $\text{CH}_3\text{NH}_3\text{PbI}_{3-x}\text{Cl}_x$ solar cells in a normal device structures fabricated in air of 90 % of relative humidity.



The lower environmental stability of PCBM devices relative to IBF-Ep cells could be attributed to three possible degradation mechanisms. First, the photo-oxidation of PCBM in the presence of oxygen and water can generate traps with lower LUMO levels.^{27,28} The formation of epoxide or carbonyl functional groups on the fullerene cage have been suggested as a consequence of photo-oxidation,^{29,30} and hence the photo-oxidative stability of PCBM and IBF-Ep are expected to be comparable. Second, the DMF solvent used in the perovskite deposition is prone to thermal decomposition in the presence of water to generate dimethylamine, a highly reactive nucleophile that can react with the PCBM ester groups. The epoxy group of the IBF-Ep is expected to be less reactive with dimethylamine because the fullerene and the steric bulk of the methyl groups block the nucleophilic ring-opening reaction. Lastly, the perovskite layer is inherently sensitive to moisture and a roughened morphology will have larger porosity and surface area (influenced by the aggregation of the PCBM ETL), making it more susceptible to hydrolytic degradation. Although a clear understanding of the degradation process for PCBM and IBF-Ep devices has yet to be realized, the consistent and significant performance differences of those devices indicate the importance of material selection for devices under ambient processing conditions.

4.2.4. Inverted Structure Devices

In addition to the normal device structure, we investigated an inverted device configuration to further evaluate the performance and utility of the IBF-Ep ETL material. The device structure and the corresponding band diagram are shown in Figure 4.7 (a) and (b), respectively. Poly(3,4-ethylenedioxythiophene) polystyrene sulfonate (PEDOT:PSS) was used instead of Spiro-OMeTAD as the HTL onto which the perovskite active layer was deposited, followed by the organic ETL film, and finally an evaporated calcium/aluminum cathode. An

SEM cross sectional image of the device is displayed in Figure 4.7 (c) from which different layers of the device can be recognized and their thickness determined. As recently reported, the thickness of the organic ETL influences the performance of the perovskite solar cells.³¹ An optimized performance of 9.0% was obtained with an IBF-Ep ETL thickness of 80 nm (corresponding results shown in Figure 4.7 (c) and (d) and summarized in Table 4.2). As in the case of the normal devices, inverted devices with IBF-Ep ETLs exhibited significantly higher performances than the corresponding PCBM reference devices with the best PCE of 5.3% (Figure 4.7 (d)). It is noteworthy that a higher PCE was obtained with the inverted structure (9.0%) than that obtained from the normal device structure (6.9%) with IBF-Ep ETLs.

Figure 4.7. (a) A schematic of the inverted $\text{CH}_3\text{NH}_3\text{PbI}_{3-x}\text{Cl}_x$ perovskite solar cell structure. (b) The corresponding energy band diagram. (c) An SEM cross section image of a device with an IBF-Ep ETL. (d) J - V characteristics under 100 mW/cm^2 AM1.5G illumination of the inverted $\text{CH}_3\text{NH}_3\text{PbI}_{3-x}\text{Cl}_x$ perovskite solar cell devices with PCBM and IBF-Ep organic ETLs.

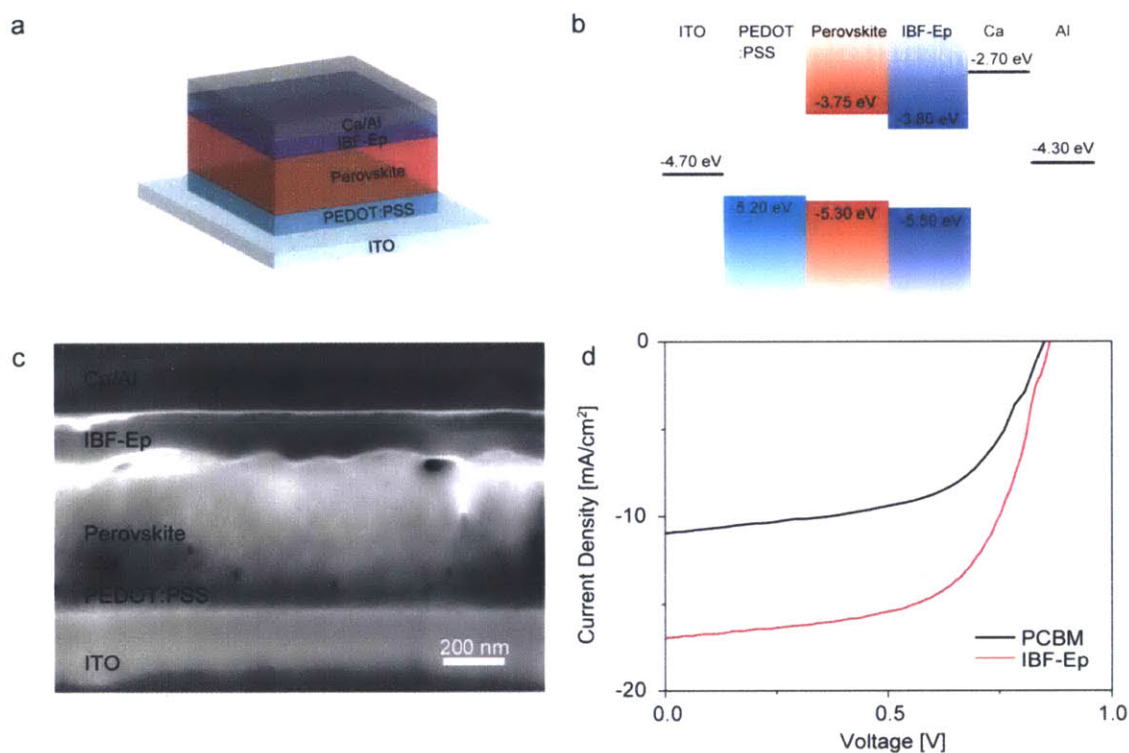
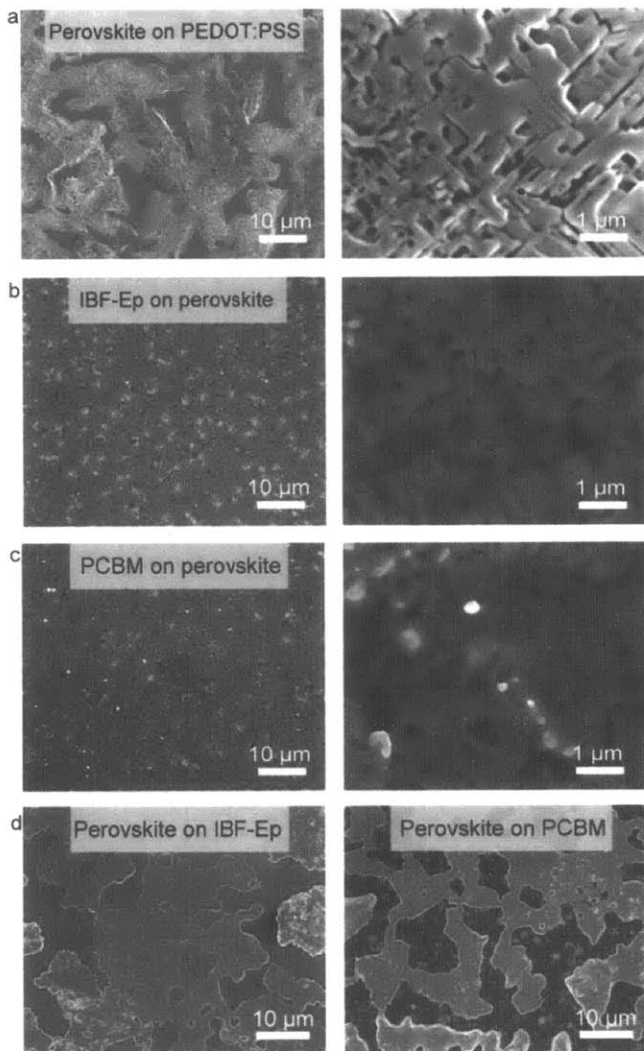


Table 4.2. Performance of $\text{CH}_3\text{NH}_3\text{PbI}_{3-x}\text{Cl}_x$ perovskite solar cells in the inverted structures device architecture with IBF-Ep ETLs. Average values and standard deviation for five measured devices are indicated, as well as the champion device results (in parentheses).

Device	J_{sc} (mA/cm ²)	V_{oc} (V)	FF	PCE (%)
PCBM	9.9 ± 1.1 (10.9)	0.87 ± 0.03 (0.84)	0.58 ± 0.01 (0.53)	5.1 ± 0.3 (5.3)
IBF-Ep	16.8 ± 0.4 (16.9)	0.85 ± 0.03 (0.86)	0.61 ± 0.01 (0.62)	8.6 ± 0.4 (9.0)

We hypothesize that the perovskite layer adopts a more uniform morphology and superior coverage when deposited on a PEDOT:PSS layer than the fullerene film, as can be seen by comparing Figure 4.8 (a) and (d). As shown in Figure 4.8, the morphologies of IBF-Ep and PCBM ETL deposited upon the perovskite active layer are comparable, although the PCBM layer contains larger round particles (about 100 nm in diameter) at a higher density as compared to the IBF-Ep layer. The presence of the particles, presumably caused by aggregation of PCBM, can lead to lower current and performance as depicted in the J - V characteristics of inverted PCBM devices. The dependence of perovskite formation on the polarity and crystallinity of the underlying layers (ETL or HTL) is of great interest and will be a continued topic of investigation to ascertain the mechanism controlling the performance of the perovskite solar cells.

Figure 4.8. SEM images of (a) $\text{CH}_3\text{NH}_3\text{PbI}_{3-x}\text{Cl}_x$ layer on PEDOT:PSS HTL, (b) IBF-Ep ETL, and (c) PCBM ETL on the perovskite layer on PEDOT:PSS HTL in an inverted structure. The images were taken at two different magnifications. (d) $\text{CH}_3\text{NH}_3\text{PbI}_{3-x}\text{Cl}_x$ layer on IBF-Ep and PCBM ETLs.



4.3. Conclusions

In conclusion, we have demonstrated the utility of the newly synthesized fullerene derivative, IBF-Ep, as an electron transport material in $\text{CH}_3\text{NH}_3\text{PbI}_{3-x}\text{Cl}_x$ perovskite solar cells with both normal and inverted configurations. The excellent morphological stability of IBF-Ep under thermal stress, its improved tolerance toward ambient processing conditions, and its compatibility with $\text{CH}_3\text{NH}_3\text{PbI}_{3-x}\text{Cl}_x$ perovskite fabrication combine to produce high performance solar cells with facile device fabrication steps. The superior performance of IBF-Ep

over PCBM as an ETL material in both device structures infers the versatility of IBF-Ep as an excellent alternative as electron acceptor in various structures of organic/inorganic hybrid solar cells. We also expect to present the broader utilization of this material as an n-type material for organic photovoltaic applications.

4.4. Experimental Section

Measurements. ^1H and ^{13}C NMR spectra were taken on Varian Inova-500 spectrometers. Chemical shifts were reported in ppm and referenced to residual solvent peaks (CD_2Cl_2 : 5.33 ppm for ^1H , 53.84 ppm for ^{13}C , CDCl_3 : 7.26 ppm for ^1H , 77.16 ppm for ^{13}C). Bruker Daltonics Omnisflex MALDI-TOF mass spectrometer was used for mass determination in a positive ion mode without the use of a matrix. ATR-FTIR (Attenuated total reflectance-Fourier transform infrared) spectra were acquired using a Thermo Scientific Nicolet 6700 FT-IR with a Ge crystal for ATR and subjected to the 'atmospheric suppression' correction in OMNICTM Spectra software. UV-Vis absorption spectra were obtained using a Cary 4000 UV-Vis spectrophotometer. X-ray diffraction patterns were collected on a Bruker Advance D8 diffractometer using Nickel-filtered Cu-K α radiation ($\lambda = 1.5418 \text{ \AA}$). X-ray diffraction samples were prepared by depositing perovskite on an organic ETL on a glass substrate. Variable-temperature transmission-mode X-ray powder diffraction was measured by Bruker X8 Dual ImuS APEX2 (temperature range from 100K to 500K) with Cu radiation. DSC analysis was conducted on TA Instruments Discovery. Electrochemical measurements were carried out in a glove box under nitrogen, using an Autolab PGSTAT 10 or PGSTAT 20 potentiostat (Eco Chemie) in a three-electrode cell configuration. A Pt button (1.6 mm in diameter) electrode, a Pt wire, and a quasi-internal Ag wire submerged in 0.01M AgNO_3 /0.1M tetrabutylammonium hexafluorophosphate (TBAPF_6) in acetonitrile were used as a working electrode, a counter electrode, and a reference electrode, respectively, in 0.1M

TBAPF₆ toluene/acetonitrile (4:1) solution. The ferrocene/ferrocenium (Fc/Fc⁺) redox couple was used as an internal standard, with the half-wave potentials observed between 0.193–0.205 V vs Ag/Ag⁺ in toluene/acetonitrile (4:1) solution. Scan rate of 0.1 V/s was applied.

Device Fabrication. Patterned ITO substrates (Thin Film Devices, 150 nm thick, 20 Ω/sq, 85%T) were cleaned by sonication in DI water with soap (Micro-90, Cole-Parmer), DI water, acetone and isopropanol, followed by oxygen plasma cleaning (100 W, Plasma Preen, Inc.) for 2 min. PCBM and IBF–Ep were dissolved in chlorobenzene (20 mg/ml) and spincoated on ITO substrates inside N₂-filled glove box. Methylammonium lead halide-based perovskite solution were prepared by mixing a 3:1 ratio of CH₃NH₃I (Luminescence Technology Corp.) and PbCl₂ (Sigma-Aldrich) with the concentration of 0.73 M and 2.2 M in dimethylformamide (DMF) and stirred at room temperature overnight. The mixed solution was spincoated on the ITO/PCBM or IBF–Ep at 2000 rpm for 30 sec under ambient condition, and annealed on a hotplate at 90 °C for 1 h then at 100 °C for 30 min. The aforementioned conditions were obtained by optimization to produce the best performance. When all the layers of the devices were processed exclusively in either air or N₂-filled glove box, the performance of them was not as good as those fabricated in the optimized condition (Appendix Figure 4.10 (a) and (b)). The spiro-OMeTAD solution in chlorobenzene (1 mL) with additives (45 μL LiTFSI in acetonitrile (170 mg/mL) (Sigma-Aldrich) and 10 μL *t*BP (Sigma-Aldrich)) was spincoated at 2000 rpm for 30 sec. The top gold electrode (Kurt J. Lesker, 3.175 mm pallets, 99.999%) was thermally evaporated through shadow masks at a base pressure of 2×10^{-6} Torr with rates about 1.0 Å/s. The device area defined by the overlap between the top and bottom electrodes was 5.44 mm².

For the inverted layout, poly(3,4-ethylenedioxythiophene):poly(styrenesulfonate) (PEDOT:PSS) (Clevios™ P VP AI 4083) was deposited on ITO by spincoating at 4000 rpm for 1 min and annealed at 150 °C for 10 min in air. The methylammonium lead halide-based perovskite solution was spincoated at 2000 rpm for 30 sec. PCBM and IBF-Ep were spincoated at 2000 rpm for 30 sec. Calcium and aluminum top electrodes were thermally evaporated through shadow masks at a base pressure of 2×10^{-6} Torr with rates of 0.5 Å/s and 1.0 Å/s, respectively.

Device Characterization. Current-voltage characteristics of the solar cell devices were recorded in a nitrogen-filled glove box using a computer-controlled Keithley 6487 picoammeter source-meter. 100 mW/cm² illumination was provided by a 150 W xenon arc-lamp (Newport 96000) equipped with an AM 1.5G filter. The PCEs for the normal structure were obtained from reverse bias scan with delay time of 0.02 ~ 1 sec. The PCEs for the inverted structure were obtained by averaging the forward and reverse bias scans with delay time of 0.02 ~ 1 sec. The absorption spectra of perovskite and fullerene films on glass substrates were measured by a Cary 4000 UV-Vis spectrophotometer. Scanning electron microscopy was performed with a Helios Nanolab 600 at 5 kV. AFM images were obtained with an Agilent 5100 atomic force microscope. The measurements were performed in ACAFM tapping mode using silicon tips with a force constant of 20–80 N/m.

4.5. References and Notes

1. Burschka, J.; Pellet, N.; Moon, S. J.; Humphry-Baker, R.; Gao, P.; Nazeeruddin, M. K.; Gratzel, M. Sequential Deposition as a Route to High-performance Perovskite-sensitized Solar Cells. *Nature* **2013**, *499*, 316-319.
2. Stranks, S. D.; Eperon, G. E.; Grancini, G.; Menelaou, C.; Alcocer, M. J. P.; Leijtens, T.; Herz, L. M.; Petrozza, A.; Snaith, H. J. Electron-Hole Diffusion Lengths Exceeding 1 Micrometer in an Organometal Trihalide Perovskite Absorber. *Science* **2013**, *342*, 341-344.
3. Noh, J. H.; Jeon, N. J.; Choi, Y. C.; Nazeeruddin, M. K.; Gratzel, M.; Seok, S. I. Nanostructured $\text{TiO}_2/\text{CH}_3\text{NH}_3\text{PbI}_3$ Heterojunction Solar Cells Employing Spiro-OMeTAD/Co-Complex as Hole-transporting Material. *J. Mater. Chem. A* **2013**, *1*, 11842-11847.
4. Jeon, N. J.; Lee, H. G.; Kim, Y. C.; Seo, J.; Noh, J. H.; Lee, J.; Seok, S. I. o-Methoxy Substituents in Spiro-OMeTAD for Efficient Inorganic-Organic Hybrid Perovskite Solar Cells. *J. Am. Chem. Soc.* **2014**, *136*, 7837-7840.
5. Zhou, H. P.; Chen, Q.; Li, G.; Luo, S.; Song, T. B.; Duan, H. S.; Hong, Z. R.; You, J. B.; Liu, Y. S.; Yang, Y. Interface Engineering of Highly Efficient Perovskite Solar Cells. *Science* **2014**, *345*, 542-546.
6. Abate, A.; Leijtens, T.; Pathak, S.; Teuscher, J.; Avolio, R.; Errico, M. E.; Kirkpatrick, J.; Ball, J. M.; Docampo, P.; McPherson, I.; Snaith, H. J. Lithium Salts as "Redox Active" P-type Dopants for Organic Semiconductors and Their Impact in Solid-state Dye-sensitized Solar Cells. *Phys. Chem. Chem. Phys.* **2013**, *15*, 2572-2579.
7. Qin, P.; Tanaka, S.; Ito, S.; Tetreault, N.; Manabe, K.; Nishino, H.; Nazeeruddin, M. K.; Gratzel, M. Inorganic Hole Conductor-based Lead Halide Perovskite Solar Cells with 12.4% Conversion Efficiency. *Nat. Commun.* **2014**, *5*, 1-6.
8. Lee, M. M.; Teuscher, J.; Miyasaka, T.; Murakami, T. N.; Snaith, H. J. Efficient Hybrid Solar Cells Based on Meso-Superstructured Organometal Halide Perovskites. *Science* **2012**, *338*, 643-647.

9. Bi, D. Q.; Moon, S. J.; Haggman, L.; Boschloo, G.; Yang, L.; Johansson, E. M. J.; Nazeeruddin, M. K.; Gratzel, M.; Hagfeldt, A. Using a Two-step Deposition Technique to Prepare Perovskite ($\text{CH}_3\text{NH}_3\text{PbI}_3$) for Thin Film Solar Cells Based on ZrO_2 and TiO_2 Mesostuctures. *RSC Adv.* **2013**, *3*, 18762-18766.
10. Malinkiewicz, O.; Yella, A.; Lee, Y. H.; Espallargas, G. M.; Graetzel, M.; Nazeeruddin, M. K.; Bolink, H. J. Perovskite Solar Cells Employing Organic Charge-transport Layers. *Nat. Photonics* **2014**, *8*, 128-132.
11. Li, Z.; Wong, H. C.; Huang, Z. G.; Zhong, H. L.; Tan, C. H.; Tsoi, W. C.; Kim, J. S.; Durrant, J. R.; Cabral, J. T. Performance Enhancement of Fullerene-based Solar Cells by Light Processing. *Nat. Commun.* **2013**, *4*, 1-7.
12. Bertho, S.; Janssen, G.; Cleij, T. J.; Conings, B.; Moons, W.; Gadisa, A.; D'Haen, J.; Goovaerts, E.; Lutsen, L.; Manca, J.; Vanderzande, D. Effect of Temperature on the Morphological and Photovoltaic Stability of Bulk Heterojunction Polymer: Fullerene Solar Cells. *Sol. Energ. Mat. Sol. C* **2008**, *92*, 753-760.
13. Jeng, J. Y.; Chiang, Y. F.; Lee, M. H.; Peng, S. R.; Guo, T. F.; Chen, P.; Wen, T. C. $\text{CH}_3\text{NH}_3\text{PbI}_3$ Perovskite/Fullerene Planar-Heterojunction Hybrid Solar Cells. *Adv. Mater.* **2013**, *25*, 3727-3732.
14. Wang, Q.; Shao, Y. C.; Dong, Q. F.; Xiao, Z. G.; Yuan, Y. B.; Huang, J. S. Large Fill-factor Bilayer Iodine Perovskite Solar Cells Fabricated by a Low-temperature Solution-process. *Energ. Environ. Sci.* **2014**, *7*, 2359-2365.
15. Puplovskis, A.; Kacens, J.; Neilands, O. New Route for [60]Fullerene Functionalisation in [4+2] Cycloaddition Reaction using Indene. *Tetrahedron Lett.* **1997**, *38*, 285-288.
16. Ren, S.; Zhao, N.; Crawford, S. C.; Tambe, M.; Bulović, V.; Gradečak, S. Heterojunction Photovoltaics Using GaAs Nanowires and Conjugated Polymers. *Nano Lett.* **2010**, *11*, 408-413.
17. Wong, H. C.; Li, Z.; Tan, C. H.; Zhong, H. L.; Huang, Z. G.; Bronstein, H.; McCulloch, I.; Cabral, J. T.; Durrant, J. R. Morphological Stability and Performance of Polymer-Fullerene Solar Cells

under Thermal Stress: The Impact of Photoinduced PC₆₀BM Oligomerization. *ACS Nano* **2014**, *8*, 1297-1308.

18. Lindqvist, C.; Bergqvist, J.; Feng, C. C.; Gustafsson, S.; Backe, O.; Treat, N. D.; Bounioux, C.; Henriksson, P.; Kroon, R.; Wang, E. G.; Sanz-Velasco, A.; Kristiansen, P. M.; Stingelin, N.; Olsson, E.; Inganäs, O.; Andersson, M. R.; Müller, C. Fullerene Nucleating Agents: A Route Towards Thermally Stable Photovoltaic Blends. *Adv. Energy Mater.* **2014**, *4*, 1301437.

19. Richards, J. J.; Rice, A. H.; Nelson, R. D.; Kim, F. S.; Jenekhe, S. A.; Luscombe, C. K.; Pozzo, D. C. Modification of PCBM Crystallization via Incorporation of C₆₀ in Polymer/Fullerene Solar Cells. *Adv. Funct. Mater.* **2013**, *23*, 514-522.

20. Liu, F.; Zhao, W.; Tumbleston, J. R.; Wang, C.; Gu, Y.; Wang, D.; Briseno, A. L.; Ade, H.; Russell, T. P. Understanding the Morphology of PTB7: PCBM Blends in Organic Photovoltaics. *Adv. Energy Mater.* **2014**, *4*, 1301377.

21. Dattani, R.; Bannock, J. H.; Fei, Z. P.; MacKenzie, R. C. I.; Guilbert, A. A. Y.; Vezie, M. S.; Nelson, J.; de Mello, J. C.; Heeney, M.; Cabral, J. T.; Nedoma, A. J. A General Mechanism for Controlling Thin Film Structures in All-conjugated Block Copolymer: Fullerene Blends. *J. Mater. Chem. A* **2014**, *2*, 14711-14719.

22. Liu, H. W.; Chang, D. Y.; Chiu, W. Y.; Rwei, S. P.; Wang, L. Fullerene Bisadduct as an Effective Phase-separation Inhibitor in Preparing Poly(3-hexylthiophene)-[6,6]-Phenyl-C₆₁-Butyric Acid Methyl Ester Blends with Highly Stable Morphology. *J. Mater. Chem.* **2012**, *22*, 15586-15591.

23. Trinh Tung, N.; Duc Nghia, N.; Van Tuyen, N., Glass transition of PCBM, P3HT and their blends in quenched state. *Adv. Nat. Sci.: Nanosci. Nanotechnol.* **2012**, *3*, 045001.

24. Cheng, Y. J.; Liao, M. H.; Chang, C. Y.; Kao, W. S.; Wu, C. E.; Hsu, C. S. Di(4-methylphenyl)methano-C₆₀ Bis-Adduct for Efficient and Stable Organic Photovoltaics with Enhanced Open-Circuit Voltage. *Chem. Mater.* **2011**, *23*, 4056-4062.

25. Boix, P. P.; Nonomura, K.; Mathews, N.; Mhaisalkar, S. G. Current Progress and Future Perspectives for Organic/inorganic Perovskite Solar Cells. *Mater. Today* **2014**, *17*, 16-23.

26. You, J.; Yang, Y.; Hong, Z.; Song, T.-B.; Meng, L.; Liu, Y.; Jiang, C.; Zhou, H.; Chang, W.-H.; Li, G.; Yang, Y. Moisture Assisted Perovskite Film Growth for High Performance Solar Cells. *Appl. Phys. Lett.* **2014**, *105*, 183902.
27. Hoke, E. T.; Sachs-Quintana, I. T.; Lloyd, M. T.; Kauvar, I.; Mateker, W. R.; Nardes, A. M.; Peters, C. H.; Kopidakis, N.; McGehee, M. D. The Role of Electron Affinity in Determining Whether Fullerenes Catalyze or Inhibit Photooxidation of Polymers for Solar Cells. *Adv. Energy Mater.* **2012**, *2*, 1351-1357.
28. Reese, M. O.; Nardes, A. M.; Rupert, B. L.; Larsen, R. E.; Olson, D. C.; Lloyd, M. T.; Shaheen, S. E.; Ginley, D. S.; Rumbles, G.; Kopidakis, N. Photoinduced Degradation of Polymer and Polymer-Fullerene Active Layers: Experiment and Theory. *Adv. Funct. Mater.* **2010**, *20*, 3476-3483.
29. Chambon, S.; Rivaton, A.; Gardette, J. L.; Firon, M. Photo- and Thermal Degradation of MDMO-PPV : PCBM Blends. *Sol. Energ. Mat. Sol. C* **2007**, *91*, 394-398.
30. Penn, S. G.; Costa, D. A.; Balch, A. L.; Lebrilla, C. B. Analysis of C₆₀ Oxides and C₁₂₀O_n (n=1,2,3) using Matrix Assisted Laser Desorption-ionization Fourier Transform Mass Spectrometry. *Int. J. Mass Spectrom.* **1997**, *169*, 371-386.
31. Seo, J.; Park, S.; Kim, Y. C.; Jeon, N. J.; Noh, J. H.; Yoon, S. C.; Sang, S. I. Benefits of Very Thin PCBM and LiF Layers for Solution-processed p-i-n Perovskite Solar Cells. *Energ. Environ. Sci.* **2014**, *7*, 2642-2646.

4.6. Appendix

Figure 4.9. *J–V* characteristics of CH₃NH₃PbI_{3–x}Cl_x solar cells fabricated in air without thermal annealing process of ETL. The decreased performance was obtained for devices with both PCBM and IBF–Ep, compared to the devices with annealed ETLs.

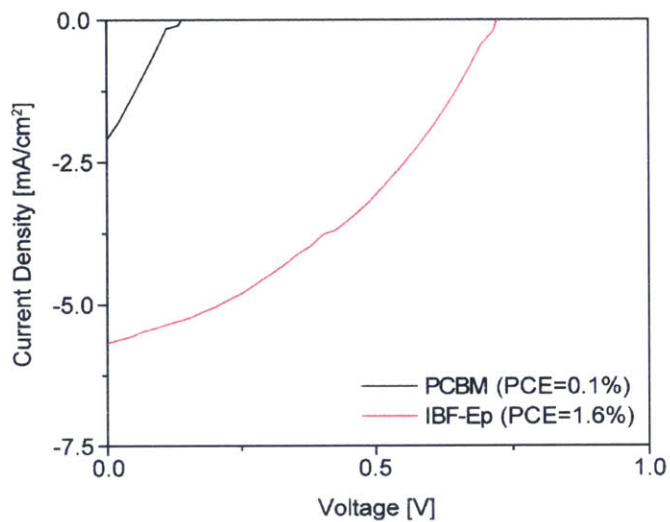
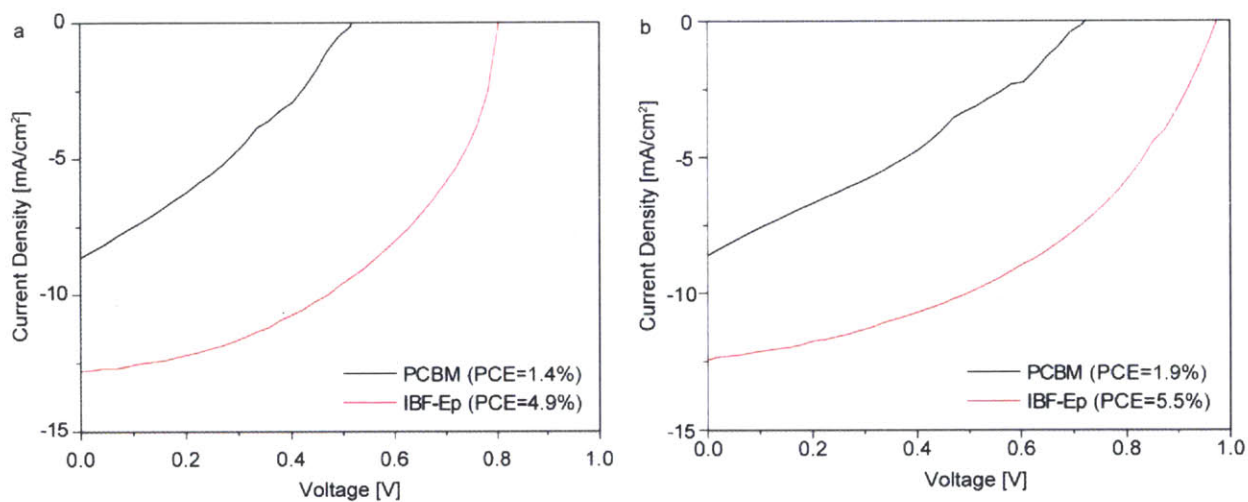


Figure 4.10. J - V characteristics of $\text{CH}_3\text{NH}_3\text{PbI}_{3-x}\text{Cl}_x$ solar cells fabricated exclusively (a) in a N_2 -filled glove box and (b) in air.



CHAPTER 5
Aryne-C₆₀ Additives for
Enhancing OPV Performances

5.1. Introduction

Polymer solar cells with bulk heterojunction (BHJ) active layers have attracted significant research interest due to their large surface area to volume ratio, abundant choices for active components, ease of processing, and potential low-cost.¹⁻⁴ The structure and properties of the components in the BHJ are the crucial factors that determine the power conversion efficiency (PCE) of solar cells. Therefore, there has been extensive investigation to develop high-performance p-type polymers by incorporating various donor-acceptor alternating units in their backbones. The push-pull conjugated polymers with low band gaps absorb a large fraction of the solar spectrum and generate significant current in solar cells.⁵⁻⁷ For the other component of BHJ the n-type acceptor, PCBM ([6,6]-phenyl-C₆₁-butyric acid methyl ester)⁸ and ICBA (indene-C₆₀ bisadduct)⁹ have been most widely utilized for their compatibility with commonly used polymers and for their good performance. Despite continuous efforts to develop alternative materials to PCBM or ICBA, not many fullerene derivatives or small molecules have shown to exceed the performance of those standard acceptors. Therefore, systematic studies of electron acceptors, particularly their structures, electronic properties, and interactions with polymer donors, are necessary to elucidate the mechanism that governs the behavior and efficiency of the n-type materials.

Film morphology of the BHJ active layer is another parameter which influences solar cell efficiency, thus the control of morphology has been a focus of extensive studies that involve an additive approach.¹⁰ A minority ternary component in addition to donor and acceptor in the active layer can significantly affect the performance of solar cells. For example, solvent additives with high boiling point or selective solubility of active materials have been demonstrated to improve the self-organization of polymer chains and the phase separation of donor and acceptor

in BHJ. The reported solvent additives include 1,8-diiodooctane,^{11,12} nitrobenzene,^{13,14} alkane-thiol,^{15,16} and 1-chloronaphthalene.¹⁷ Compared to the solvent additives, structurally designed polymer- or fullerene-based additives are less explored. An example of such designer additives is reported by Tada et al.,¹⁸ where the selective deposition of fluoroalkyl-functionalized P3HT or PCBM at the interface of bilayer OPV induces interfacial dipole moments. Another example of side-chain-functionalized polymer additives was reported by Lobez et al.,¹⁹ which describes that dipoles at the BHJ interface are induced by designer polythiophene additives and consequently enhance charge collection. A report on fullerene additives with polystyrene tethers²⁰ demonstrated that the film morphology is improved and the size of fullerene domain is reduced by the addition of the fullerene derivatives, resulting in the enhanced lifetime and efficiency.

We have been interested in understanding the correlation between the structural design of fullerene-based additives and the interface physics of the BHJ donor and acceptor phases. By studying the additives with various functional groups, one can build the effective structure of additives for enhanced charge transfer and improved morphology. Herein, we synthesize new fullerene derivatives to be employed as minority solar cell components to improve interfacial charge separation in conventional BHJ polymer photovoltaics composed of PTB7, Poly({4,8-bis[(2-ethylhexyl)oxy]benzo[1,2-*b*:4,5-*b'*]dithiophene-2,6-diyl}{3-fluoro-2-[(2-ethylhexyl)carbonyl]thieno[3,4-*b*]thiophenediyl}), and PCBM based on C_{60} and C_{70} . Interfacial properties are critical for PTB7:PCBM devices and are generally very sensitive to small changes in composition or processing conditions,²¹ which makes reliable reproducibility a challenge for both academia and large-scale industrial production. The fullerene derivatives with pendant aromatic groups oriented orthogonal to the fullerene surface were designed as the additives. Their distinct structures from that of PCBM are targeted to facilitate their physical separation

from PCBM domains. The assembly of the fullerene additives at interfaces between domains of PTB7 and PCBM modifies the interfacial properties to the benefit of the devices. Aromatic groups with well-designed substituents can promote stronger interactions with the polymer backbone than are observed for PCBM. We found that these additives result in an improvement of short-circuit current, fill factor, and overall efficiency of the devices. In addition, we noticed that these tailored additives also provide for robust interfacial properties of PTB7:PCBM devices and minimize variances from processing and/or minor compositional differences. It is notable that when PTB7:PCBM devices are in their most optimized forms (arising from optimized interfacial properties), the additives do not enhance the performance much, which is likely near intrinsic limits. However, with designer additives the probability that a high performance solar cell can be produced is enhanced. To clearly demonstrate these effects, we performed a statistical study varying multiple parameters and processing conditions and observed that the incorporation of the additives improves the overall PCE of devices having sub-optimal interfaces by up to 29%. The results illustrate how additives can solve the batch-to-batch reproducibility issue, which is crucial for the industrial production of the solar cells.

5.2. Results and Discussion

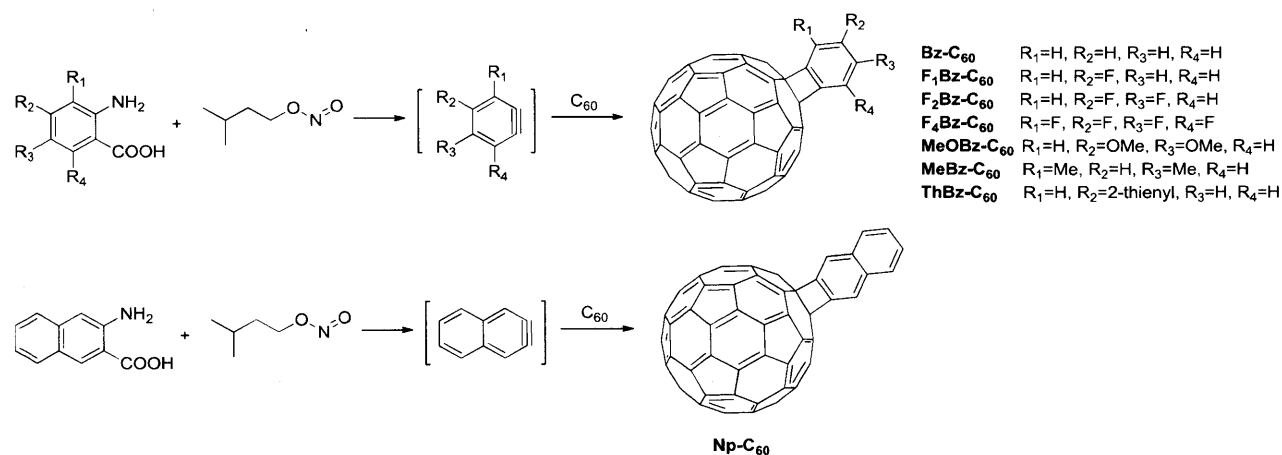
5.2.1. Syntheses of Aryne- C_{60} Adducts

Functional phenyl groups can be installed on the surface of C_{60} fullerenes via [2+2] cycloaddition of aryne intermediates and a double bond of C_{60} . Arynes can be generated from a variety of precursors including *o*-dihalophenyl derivatives, diphenyliodonium-2-carboxylate, *o*-halophenyl tosylates and triflates, and *o*-trimethylsilylphenyl triflate.²² Another method utilizing benzenediazonium-2-carboxylate precursor has been successfully employed to functionalize

fullerenes including C_{60} , C_{70} , and endohedral metallofullerenes.²³⁻²⁹ Recently, the [2+2] cycloaddition of C_{60} with the dinitrile-substituted (phenyl)[*o*-(trimethylsilyl)phenyl]iodonium triflate aryne precursor in the presence of tetra-*n*-butylammonium fluoride was shown to yield C_{60} functionalized with a dinitrilenaphthyl moiety.³⁰ These materials have a formal 4-membered ring in contrast to the previous examples that display a [5,6]-open structure such as the dibutoxyphenyl- C_{60} adduct, reported by Kim et al, using 2-amino-4,5-dibutoxybenzoic acid as the aryne precursor.³¹

As shown in Scheme 5.1, we have focused on anthranilic acid derivatives as aryne precursors and isoamyl nitrite as diazotization reagent. This functionalization method is simple and modular since the one-step reaction requires a very short time for conversion (less than 1 h in total) and a variety of the precursors are commercially available. The anthranilic acid derivatives with 4,5-dimethoxy group,²⁸ 4-fluoro group, 4,5-difluoro group, 3,4,5,6-tetrafluoro group, 3,5-dimethyl group, and 4-(2-thienyl) group were used, and for the larger aromatic pendant, 3-amino-2-naphthoic acid was employed as an aryne precursor. The corresponding aryne intermediates underwent [2+2] cycloaddition with C_{60} usually at 100 °C under argon, and the reactions were completed within 30 min. The reaction mixtures consisted of the monoadduct with minor amounts of bisadducts and multiadducts. The monoadducts were purified via silica gel column chromatography with toluene or CS_2 /hexane as elution solvents. For further purification, HPLC using a 5PBB Cosmosil column was employed with toluene elution. The structures of the synthesized compounds were characterized by 1H and ^{13}C NMR spectroscopy as well as mass spectrometry (MS).

Scheme 5.1. Various aryne formations and their [2+2] cycloaddition with C_{60} .

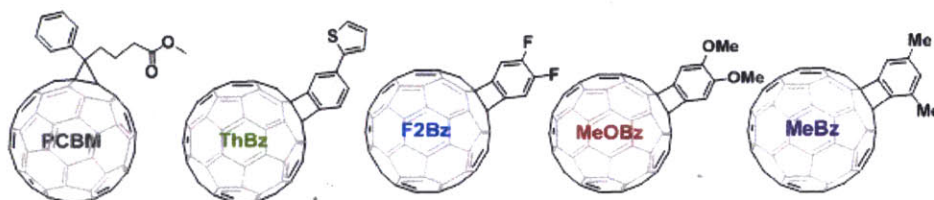
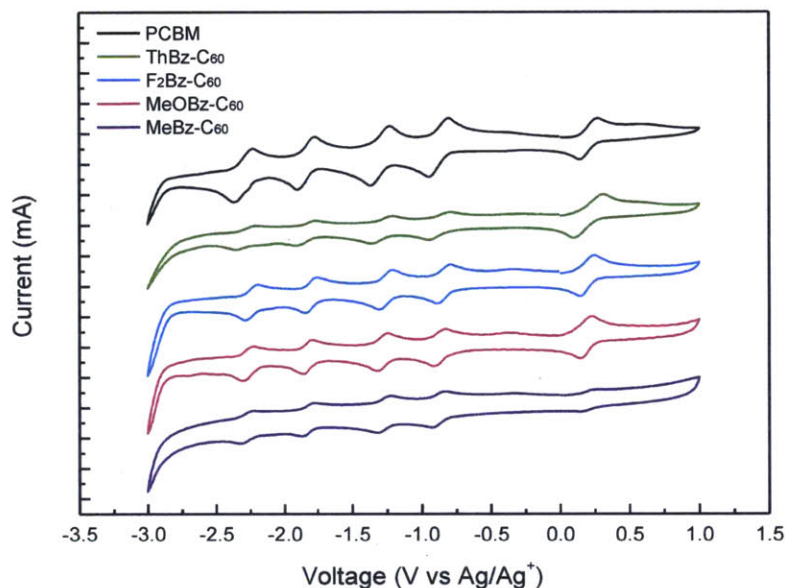


Four monoadducts (ThBz- C_{60} , F₂Bz- C_{60} , MeOBz- C_{60} , and MeBz- C_{60}) obtained with yields over 9 % were selected for device fabrication and further investigation (Figure 5.1). Other derivatives were obtained in trace amounts after the multi-step purifications due to either poor solubility or intrinsically poor reactivity. Given the low solubility of Bz- C_{60} , Np- C_{60} , and F₁Bz- C_{60} (containing less solubilizing groups) in common organic solvents, their yields decreased significantly during the separation of the products from the pristine C_{60} and the multiadducts. In the case of F₄Bz- C_{60} , even though the reaction was run at a higher temperature (120 °C) for a longer period of time (48 h), which can potentially be attributed to the high energy of the F₄Bz aryne intermediate, the isolation of the product proved challenging. We observed that reactivity decreases as more fluorine atoms were incorporated in the precursors of F₁Bz- C_{60} , F₂Bz- C_{60} , and F₄Bz- C_{60} . It is hypothesized that electron-withdrawing fluorine makes aryne precursors even more electron-deficient, which inhibits the generation of aryne intermediates. A computational study³² reported the formation energies of aryne species with different functional groups ranging from fluorine to methoxy groups. The calculations suggest that electron-withdrawing substituents raise the formation energy of arynes compared to electron-donating groups.

5.2.2. Electrochemical Properties

Cyclic voltammetry was conducted to measure the relative reduction potentials of the new C_{60} derivatives under anhydrous, air-free conditions with a ferrocene/ferrocenium (Fc/Fc^+) internal standard. In 0.1 M TBAPF₆ toluene/acetonitrile (4:1) solution, four reversible redox peaks are exhibited by each compound, and the relative positions of the onset reduction potentials are used to compare the LUMO energy levels of the fullerenes (Figure 5.1).^{33,34} The reduction onset potentials of the aryne- C_{60} adducts are within 20 mV of PCBM, which indicates that they can be expected to have similar LUMO levels and open-circuit voltage (V_{oc}) values in BHJ solar cells. Given the orthogonal geometry of the appended aryl groups and the fullerene, we expect negligible π - π intramolecular interaction between C_{60} and the aryl groups. This weak intramolecular interaction explains the similar electronic structures of the newly synthesized molecules with PCBM. These results are in contrast to our previously investigated C_{60} derivatives (shown in Chapter 2 and 3) that possess significant intramolecular π - π interaction and concomitantly noticeable elevation of LUMO levels.³⁵

Figure 5.1. Cyclic voltammograms of PCBM, ThBz- C_{60} , F₂Bz- C_{60} , MeOBz- C_{60} , and MeBz- C_{60} (under N₂, 0.1M Bu₄NPF₆ in toluene/acetonitrile (4:1), Pt (WE), Pt wire (CE), Ag/AgNO₃ (RE), scan rate 0.1 V/s, Fc/Fc^+ internal standard $E_{1/2}$ at 0.20 V) and the corresponding chemical structures of the fullerene derivatives.



5.2.3. Photophysical Properties

UV-Vis absorption spectroscopy was employed to study the optical properties of the new fullerenes in solution. These studies are critical to assess how functionalization affects the absorption of visible light by fullerenes, and increased absorbance can contribute to the increased short-circuit current density (J_{sc}) of solar cells.³⁶ The absorption spectra of the new fullerene derivatives and PCBM are plotted over the range of 400–800 nm in Figure 5.2. All of the adducts (ThBz- C_{60} , F₂Bz- C_{60} , MeOBz- C_{60} , MeBz- C_{60}) exhibit weak narrow peaks around 430 nm that are characteristic of fullerene derivatives formed by 1,2-addition. The absorption onset wavelengths, λ_{onset} , of the compounds are similar to that of PCBM, which further confirms the similar optical band gaps of these acceptors. The optical band gaps are used to approximate the

HOMO energy levels of the fullerenes by simple subtraction from the LUMO levels derived from cyclic voltammetry. The values obtained from the aforementioned experiments are summarized in Table 5.1, and the MO energy level diagrams of the fullerenes are depicted in Figure 5.3.

Figure 5.2. UV-Vis absorption spectra of PCBM (2.4×10^{-5} M), ThBz- C_{60} (2.3×10^{-5} M), F₂Bz- C_{60} (2.2×10^{-5} M), MeOBz- C_{60} (2.3×10^{-5} M), and MeBz- C_{60} (2.4×10^{-5} M) in CHCl₃.

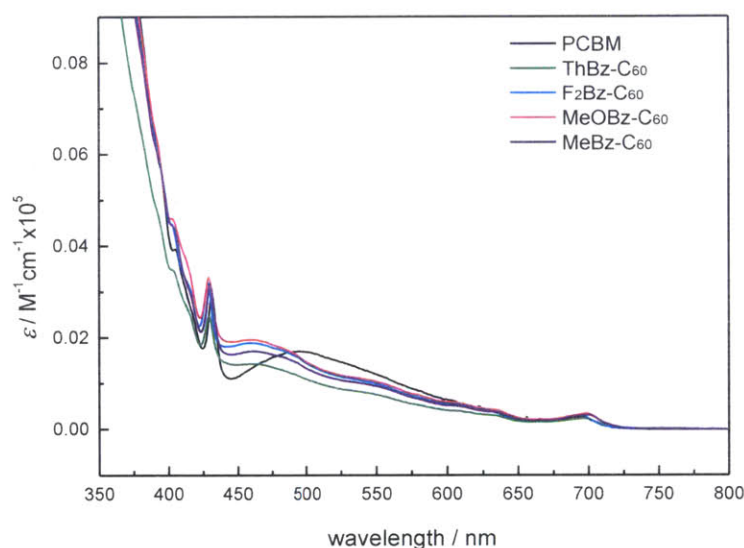
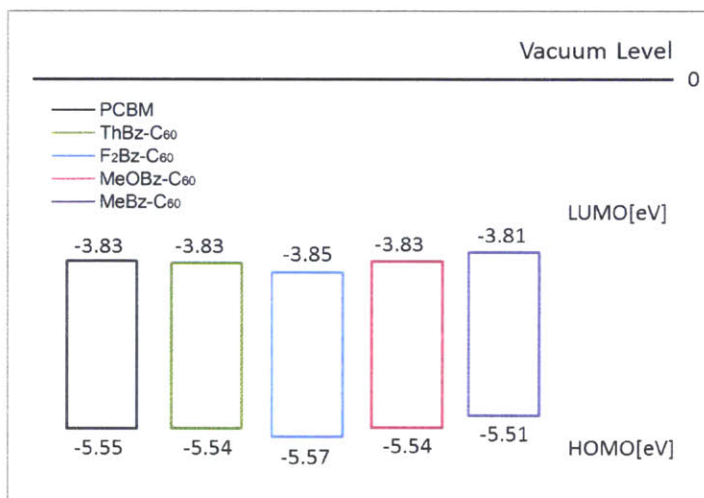


Table 5.1. HOMO and LUMO energies of fullerene derivatives calculated from UV-Vis absorption and cyclic voltammetry

C_{60} derivative	E_1 [V][a]	E_2 [V]	E_3 [V]	E_{onset} [V][b]	LUMO[eV][c]	λ_{onset} [nm][d]	HOMO[eV][e]	E_{gap} [eV][f]
PCBM	-0.87	-1.30	-1.83	-0.77	-3.83	723	-5.55	1.72
ThBz- C_{60}	-0.88	-1.29	-1.84	-0.77	-3.83	725	-5.54	1.71
F ₂ Bz- C_{60}	-0.84	-1.26	-1.80	-0.75	-3.85	722	-5.57	1.72
MeOBz- C_{60}	-0.87	-1.28	-1.83	-0.77	-3.83	728	-5.54	1.71
MeBz- C_{60}	-0.87	-1.27	-1.82	-0.79	-3.81	730	-5.51	1.70

[a] Half-wave potential, 0.5 (Ep.a.+Ep.c.); Ep.a., anodic peak potential; Ep.c. cathodic peak potential; [b] Onset reduction potential; [c] LUMO (eV) = $-e (E_{\text{onset}}+4.60)$; [d] Onset absorption wavelength; [e] HOMO = LUMO - E_{gap} [eV]; [f] Band gap = $hc/\lambda_{\text{onset}}$, converted [J] to [eV]; h, Planks constant; c, speed of light.

Figure 5.3. HOMO–LUMO energy diagrams of functionalized fullerenes. The MO energy levels were scaled relative to the vacuum level set to zero.

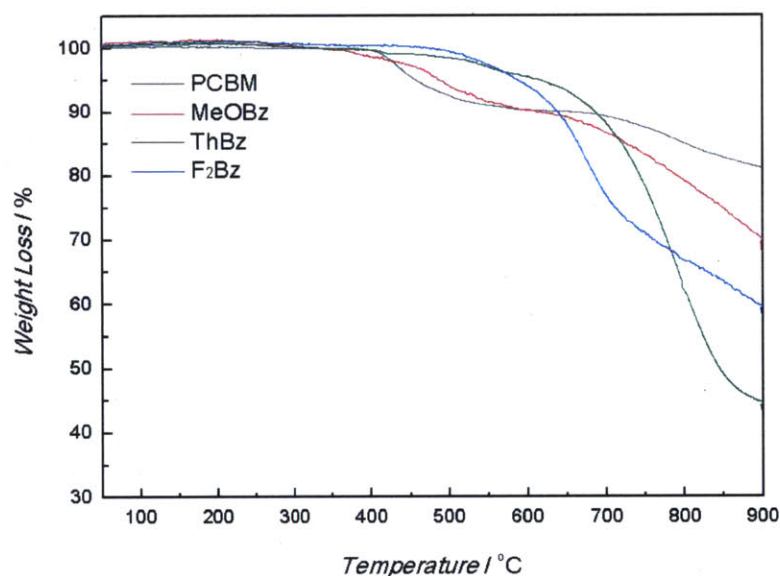


5.2.4. Thermal Properties

The retro-cycloaddition at elevated temperatures is a common decomposition mechanism of fullerene cycloadducts.^{37,38} In Chapter 2, we described retro Diels–Alder reaction of the tetramethylcyclobutadiene–C₆₀ multiadducts upon heating at 80 °C or above. The temperature at which the retro Diels–Alder reaction occurs thus determines the thermal stability of the fullerene derivatives. Here, the formation energy of the functionalized aryne intermediates can be predicted by the relative decomposition temperatures of the aryne–C₆₀ adducts. We selected three types of the functionalized aryne–C₆₀ adducts (ThBz–C₆₀, F₂Bz–C₆₀, MeOBz–C₆₀) to compare their thermal properties with that of PCBM. Prior to thermogravimetric analysis (TGA), all of the samples were dried overnight under vacuum at 150 °C to remove residual toluene. Figure 5.4 details the weight loss of the fullerene derivatives heated under nitrogen. For PCBM,

one-step weight loss starts at 405 °C before the C_{60} sublimation above 600 °C. The thermal decomposition of MeOBz- C_{60} consists of two weight losses, first at 365 °C and the second at 468 °C. ThBz- C_{60} shows the first small loss at 405 °C similar to that of PCBM, and the second at 535 °C. Even after the second step, the total weight loss of ThBz- C_{60} is less than 5% up to 600 °C, which indicates its high thermal stability. Lastly, the stability of F₂Bz- C_{60} is notable, as its first weight loss appears at 490 °C which is about 100 °C above the general decomposition temperatures of the fullerene adducts.

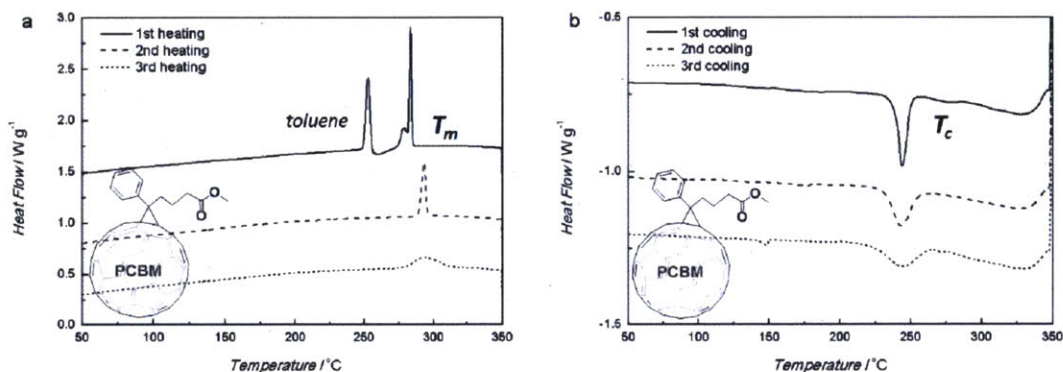
Figure 5.4. TGA of functionalized fullerenes under nitrogen condition with scan rate of 20° C/min from 50° C to 900° C.

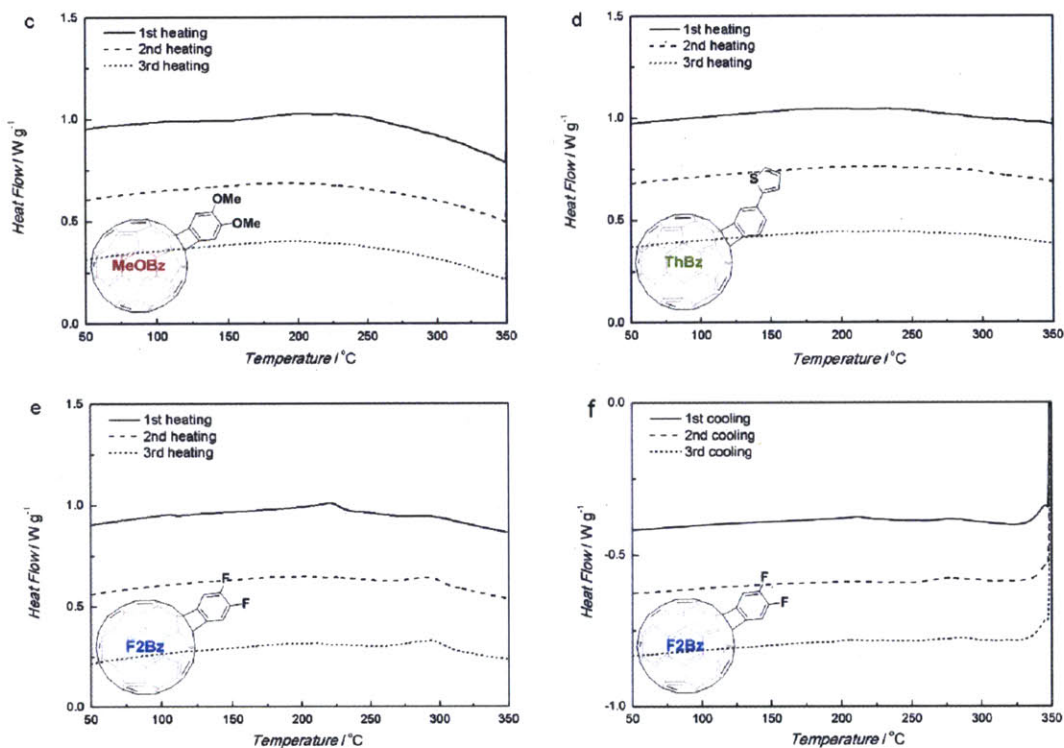


Although the mechanism of the thermal decomposition remains unclear, the relative barriers for the pendant detachment from fullerenes can be estimated. Our TGA results are in line with the computational results mentioned in Section 5.2.1 that electron-deficient arynes have higher formation energies than electron-rich ones. The lower decomposition temperature of MeOBz- C_{60} , the intermediate range for ThBz- C_{60} , and the highest temperature of F₂Bz- C_{60} follow the electron affinity trend of the substituents. We also explored the thermal transition of

the aryne-C₆₀ adducts below the decomposition temperatures using differential scanning calorimetry (DSC). In Figure 5.5, significantly different thermal behaviors are observed between PCBM and aryne-C₆₀ adducts. As discussed in Chapter 4, PCBM has a clear melting point at 282 °C on the first heating cycle and a crystallization peak around 244 °C on the first cooling cycle, indicating the labile phase transitions of PCBM (Figure 5.5 (a), (b)). In contrast, no such transition was detected for MeOBz-C₆₀ and ThBz-C₆₀ under identical conditions (Figure 5.5 (c), (d)). F₂Bz-C₆₀ displays a small endothermic bump at 290 °C on the second and third heating cycles, which is attributed to an impurity in the sample (detailed in Section 5.2.7). Figure 5.5 (f) shows cooling cycles of F₂Bz-C₆₀ without any transition characteristics such as a crystallization peak, demonstrating that the endothermic feature at 290 °C (Figure 5.5 (e)) does not indicate melting of the compound. Compared to PCBM with distinct melting and crystallization peaks, aryne-C₆₀ adducts without such transitions have higher thermal stability in the temperature range studied.

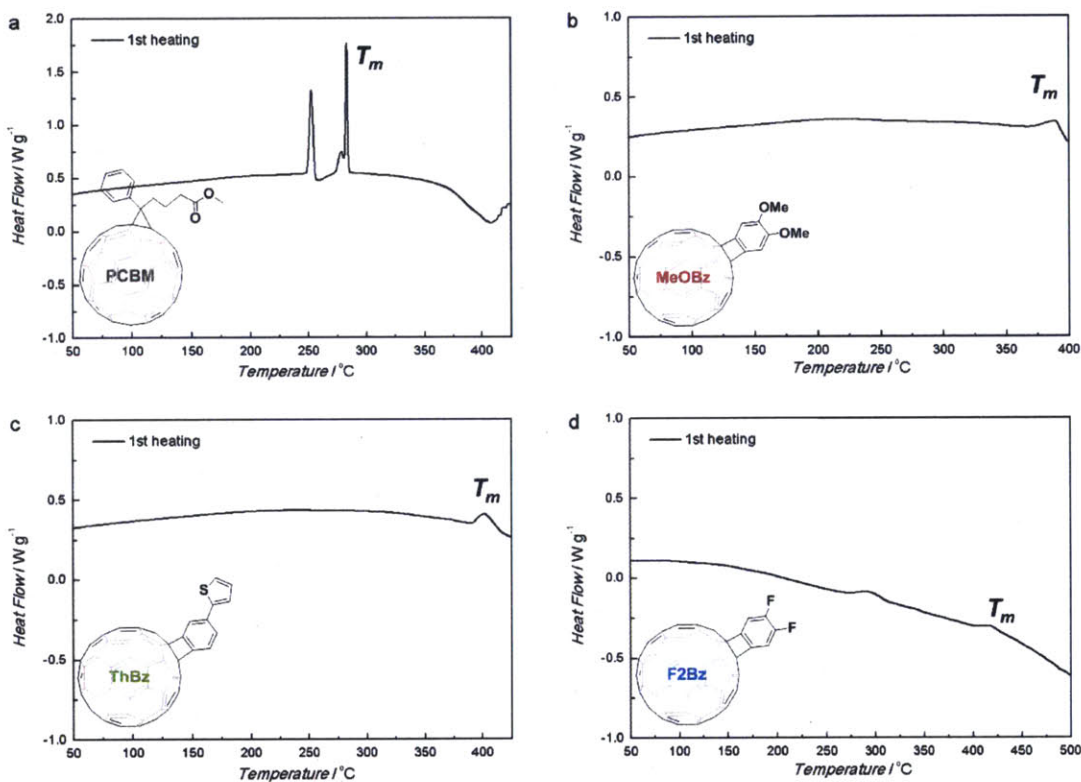
Figure 5.5. DSC measured on fullerene derivatives at the scan rate of 10° C/min over the range from 25 °C to 350 °C. (a) Three heating cycles of PCBM, (b) three cooling cycles of PCBM, three heating cycles of (c) MeOBz-C₆₀, (d) ThBz-C₆₀, (e) F₂Bz-C₆₀ and (f) three cooling cycles of F₂Bz-C₆₀. There was no endo- or exothermic feature on the cooling cycles of MeOBz-C₆₀ and ThBz-C₆₀.





As shown in Figure 5.6, DSC was also performed at higher temperatures slightly above the decomposition temperature (T_d) for each compound determined by TGA (Figure 5.4). For example, T_d of PCBM and ThBz- C_{60} (405 °C) was detected by TGA, and DSC was performed up to 425 °C. Likewise, MeOBz- C_{60} with T_d of 365 °C was heated up to 400 °C, and F₂Bz- C_{60} with T_d of 490 °C was heated up to 500 °C for DSC. Interestingly, PCBM showed exothermic behavior probably because of decomposition starting at 370 °C which is lower than its T_d . In contrast, MeOBz- C_{60} showed stable heat flow up to 400 °C and a melting point at 390 °C as shown in Figure 5.6 (b), as opposed to the predicted decomposition at 365 °C. The melting point of ThBz- C_{60} at 402 °C and that of F₂Bz- C_{60} at 416 °C were identified (Figure 5.6 (c) and (d)). The impurity peak (explained in Section 5.2.7) at 290 °C still remained in the F₂Bz- C_{60} sample. We note that the melting points of aryne- C_{60} adducts are more than 100 °C higher than that of PCBM (282 °C).

Figure 5.6. DSC characteristics of (a) PCBM, (b) MeOBz-C₆₀, (c) ThBz-C₆₀, and (d) F₂Bz-C₆₀ during the first heating cycle measured at the scan rate of 10° C/min over the range from 25 °C to 400, 425, or 500 °C. There was no endo/exothermic feature in the first cooling cycles and in the following heating/cooling cycles for all the compounds.



5.2.5. Decomposition Study by NMR

The chemical stability of the compounds was also investigated by NMR measurement after the annealing process at high temperatures. Significant differences between PCBM and aryne-C₆₀ adducts were observed (Figure 5.7–5.14). After the annealing at 425 °C, PCBM had entirely decomposed and none of the original peaks were detected by NMR (Figure 5.8). However, the NMR spectra of MeOBz-C₆₀ and ThBz-C₆₀ remained mostly unchanged even after the annealing at 400 °C and 425 °C, respectively (Figure 5.9–5.12). Some additional peaks with minor intensity were noticed as a sign of decomposition byproducts, but the presence and stability of the original adducts were clearly demonstrated. A similar stability was observed for

F₂Bz-C₆₀, and byproduct peaks were more noticeable because of the higher annealing temperature of 500 °C (Figure 5.13–5.14). The formation of pristine C₆₀ upon annealing was confirmed by thin layer chromatography (TLC), where the R_f value of C₆₀ is 0.85 and that of mono-functionalized C₆₀ is generally below 0.7 when eluted with a 1:1 mixture of CS₂/hexane. By TLC, minor C₆₀ and additional spots were observed for the annealed compounds. From the NMR studies, we learned that PCBM undergoes thermal decomposition at lower temperature than that determined by TGA. We also verified superior thermal stability of aryne-C₆₀ adducts which will enable device processing under high temperature conditions.

Figure 5.7. ¹H NMR spectrum of PCBM.

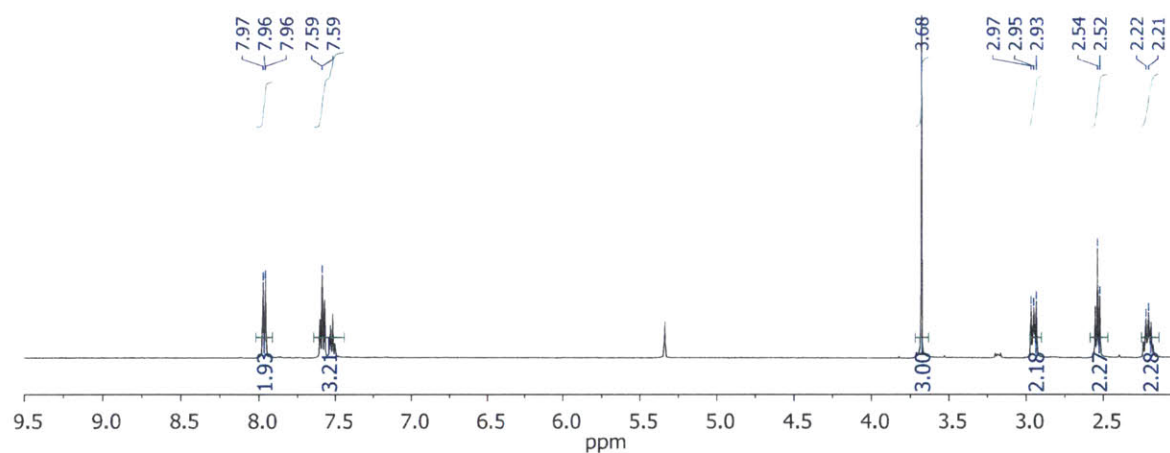


Figure 5.8. ¹H NMR spectrum of PCBM annealed at 425 °C.

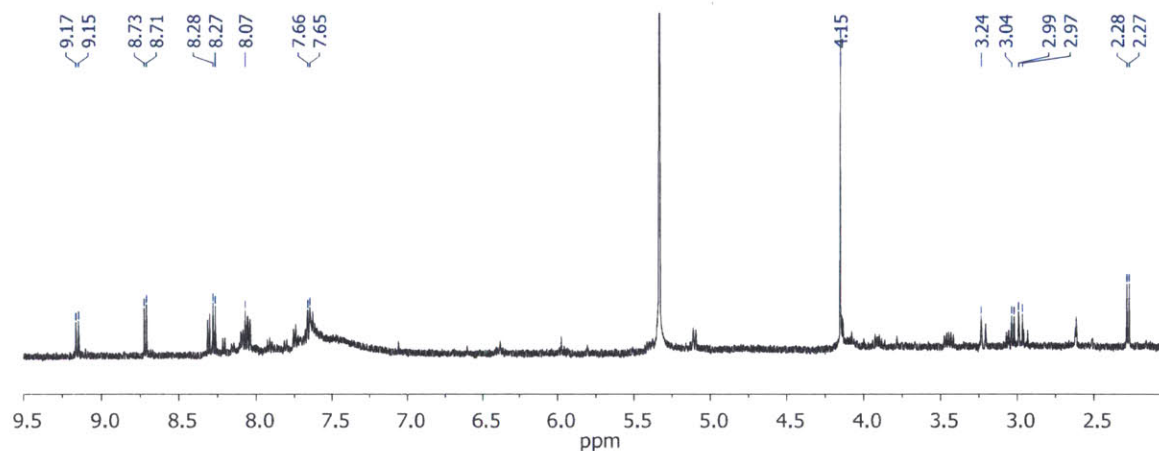


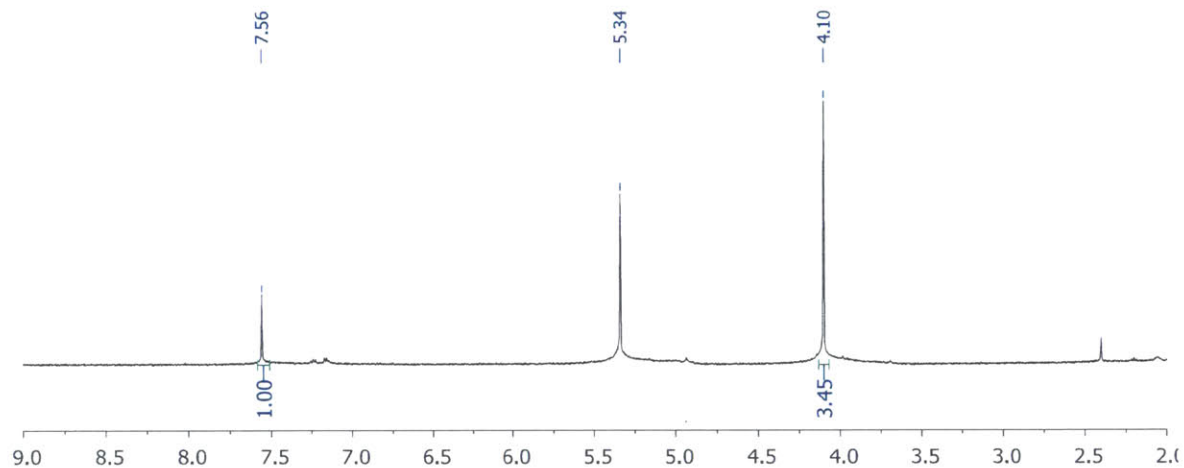
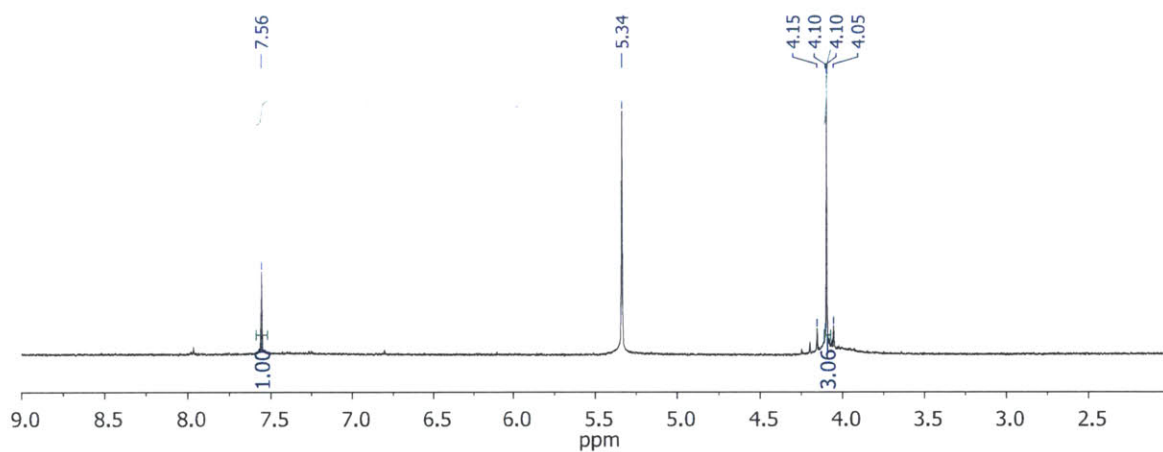
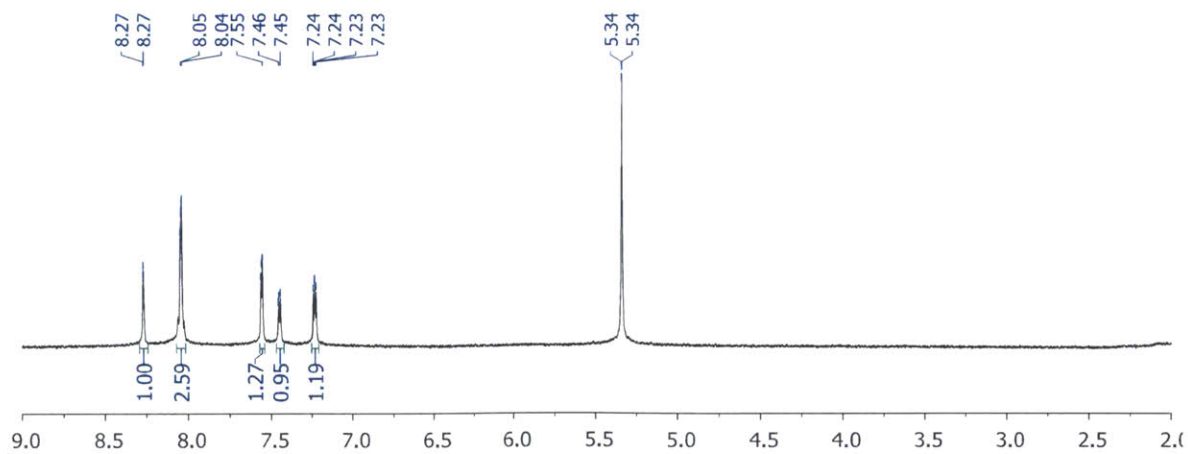
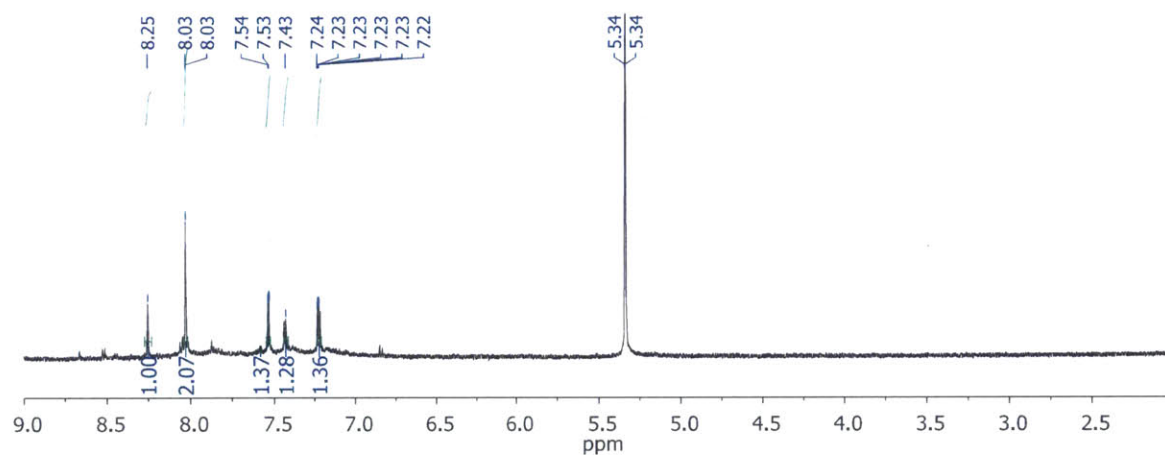
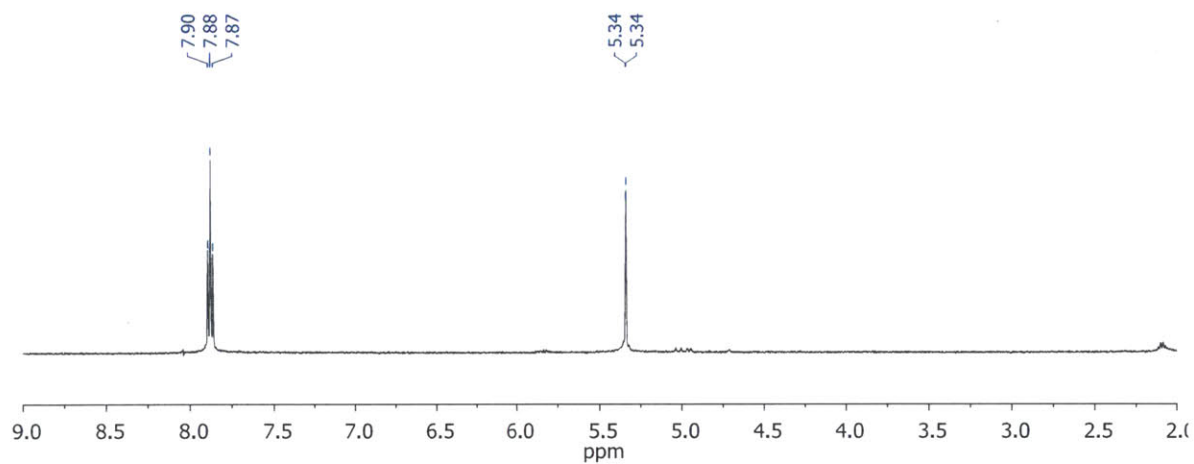
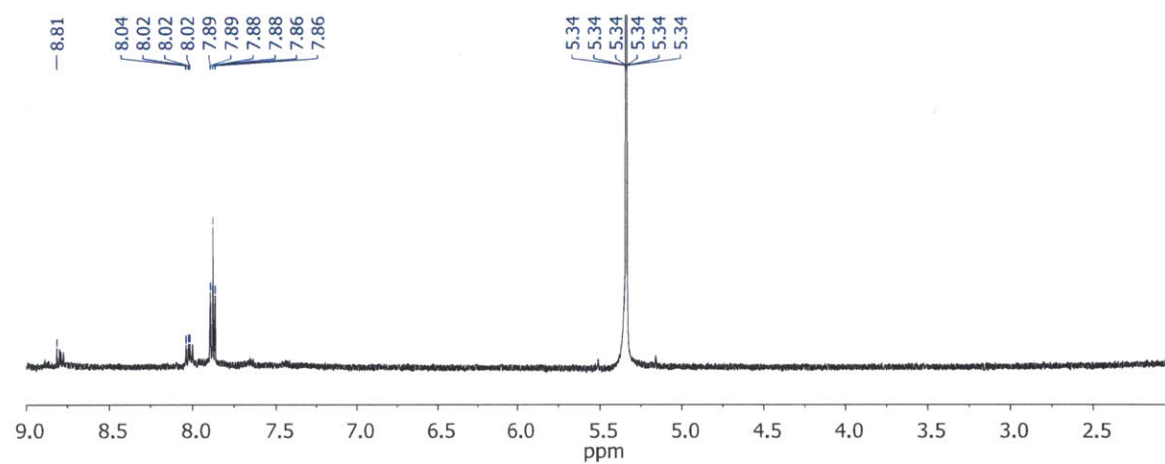
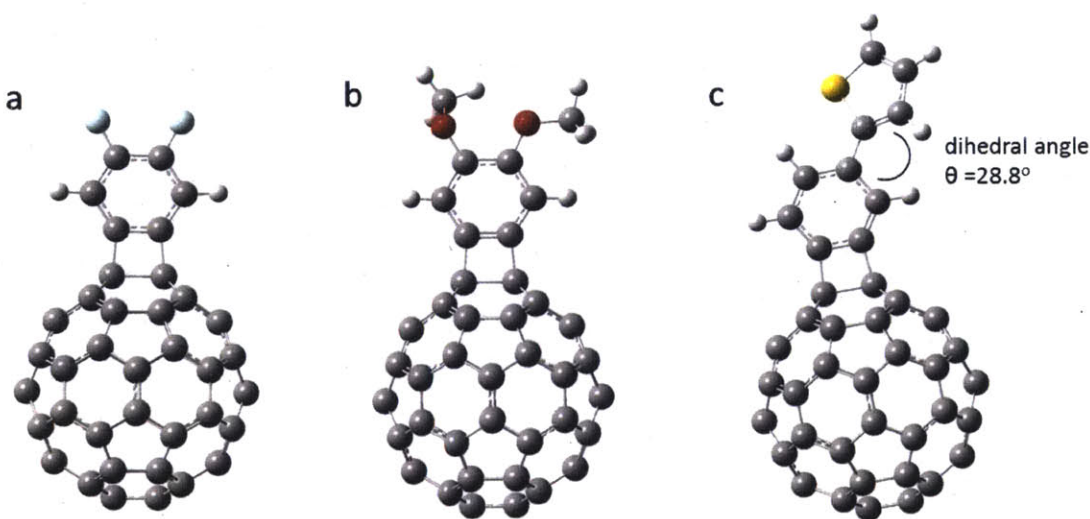
Figure 5.9. ^1H NMR spectrum of MeOBz- C_{60} .**Figure 5.10.** ^1H NMR spectrum of MeOBz- C_{60} annealed at 400 $^{\circ}\text{C}$.**Figure 5.11.** ^1H NMR spectrum of ThBz- C_{60} .

Figure 5.12. ¹H NMR spectrum of ThBz-C₆₀ annealed at 425 °C.**Figure 5.13.** ¹H NMR spectrum of F₂Bz-C₆₀.**Figure 5.14.** ¹H NMR spectrum of F₂Bz-C₆₀ annealed at 500 °C.

5.2.6. DFT Calculations

The optimized structures of F_2Bz-C_{60} , $MeOBz-C_{60}$, and $ThBz-C_{60}$ are obtained by DFT calculations and are displayed in Figure 5.15. The most noticeable structural difference among them is the degree of rotational freedom. F_2Bz-C_{60} has the most compact structure which does not allow rotation in the molecule. In $MeOBz-C_{60}$, however, the methyl groups can freely rotate around the C-O bond on the phenyl ring. The thiophene group in $ThBz-C_{60}$ can also rotate around the C-C bond attached to the phenyl ring, and the dihedral angle of 28.8° was calculated as a local energy minimum. The structural differences of aryne- C_{60} adducts are expected to influence the packing of the molecules and consequently their bulk physical properties.

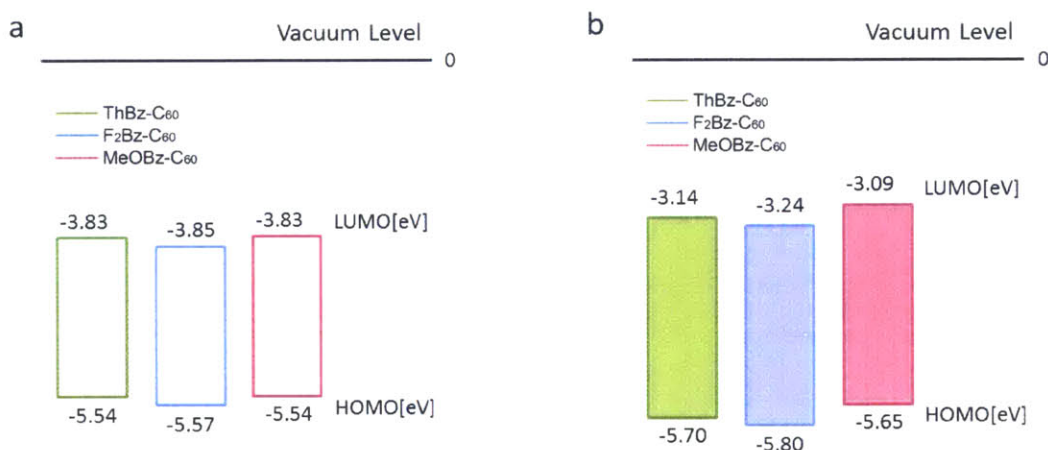
Figure 5.15. Optimized structures of (a) F_2Bz-C_{60} , (b) $MeOBz-C_{60}$, and (c) $ThBz-C_{60}$ by DFT calculations (B3LYP/ 6-31G (d,p)).



Electronic energy levels of aryne- C_{60} adducts were also calculated by DFT as shown in Figure 5.16 (b). The absolute values of experimental and computational results do not coincide, since compounds are in different forms for experiment (solution state) and calculation (gas phase), which generally leads to the discrepancy. However, the relative positions of LUMO and

HOMO levels among the series are consistent in both data sets. It is confirmed that electron-withdrawing fluorine groups lower the MO levels, and electron-donating methoxy groups raise them.

Figure 5.16. (a) Experimentally obtained and (b) DFT calculated MO energy levels of ThBz- C_{60} , F_2 Bz- C_{60} , and MeOBz- C_{60} .



5.2.7. Variable-Temperature Transmission-Mode X-Ray Powder Diffraction

We investigated the crystallinity of aryne- C_{60} adducts in the solid state by performing X-ray powder diffraction at room temperature. In order to check any change in the crystallinity of the compounds, the capillaries packed with the powders were heated up to 227 °C (the maximum temperature for the setup). The capillaries were then cooled down to room temperature, and the diffraction patterns were taken again. As shown in Figure 5.17, all of the aryne- C_{60} adducts exhibited great thermal stability as the diffraction pattern remained unchanged after the heating and cooling procedures. Figure 5.18 shows the original data which interestingly displays some single crystal diffraction patterns for F_2 Bz- C_{60} . The crystals do not disappear or undergo any changes throughout the heating and cooling cycles. After the XRD experiment, we isolated some colorless crystals from the sample, which was determined to be a simple salt in small

hexagonal unit cells. Therefore, the crystals seem to be impurities instead of the product, starting materials, or byproducts. This impurity explains the unexpected small endothermic bump around 290 °C observed by DSC (Figure 5.5 and 5.6).

Figure 5.17. VT-XRD spectra of (a) MeOBz- C_{60} , (b) ThBz- C_{60} , and (c) F₂Bz- C_{60} .

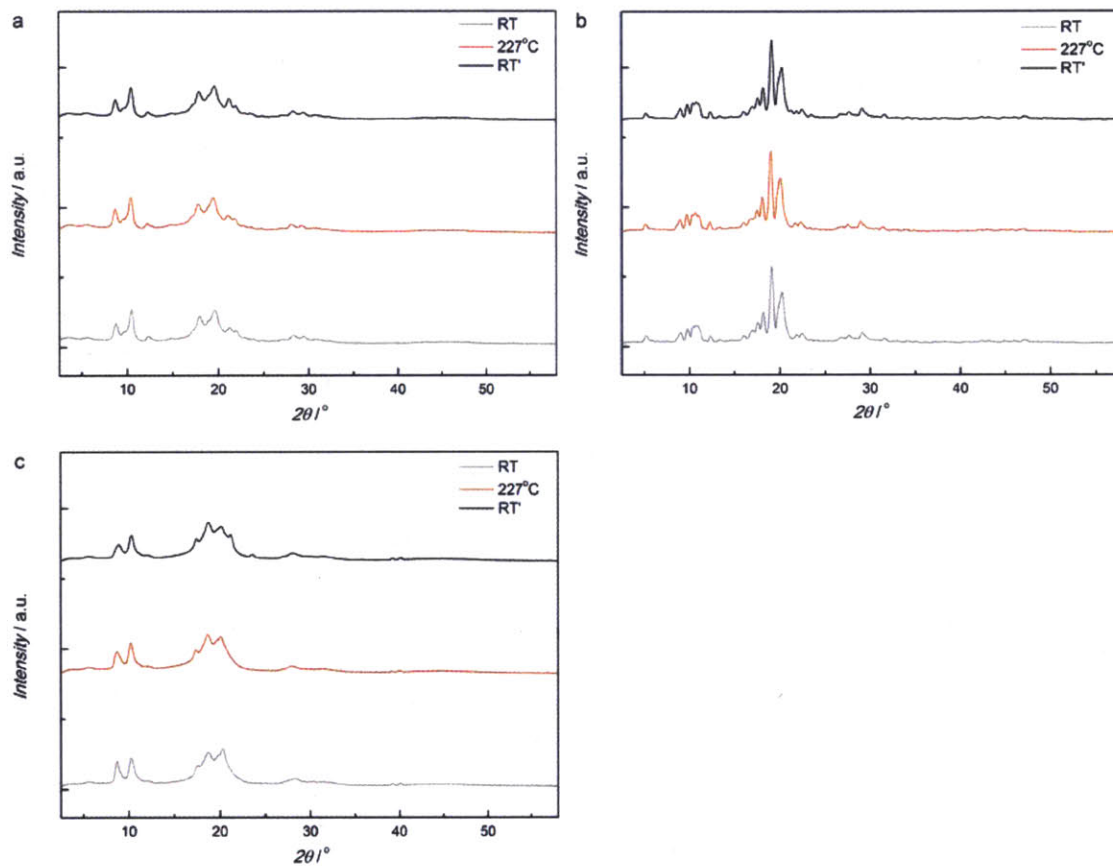
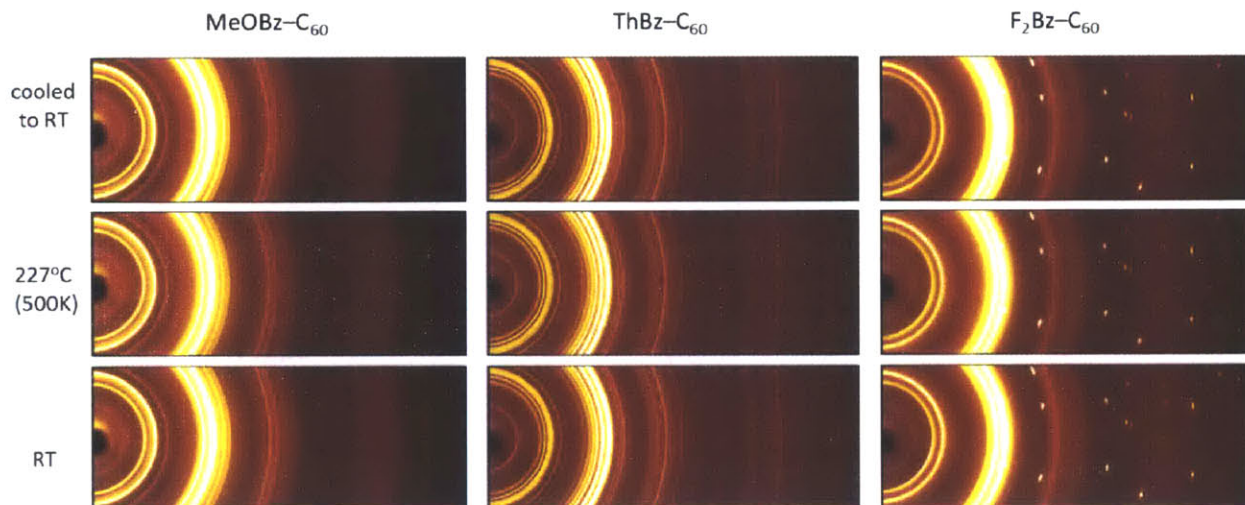


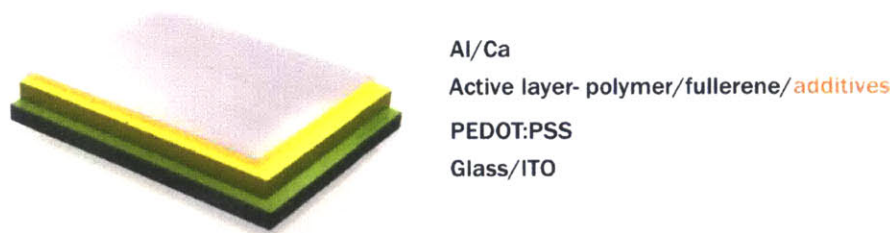
Figure 5.18. The original X-ray powder diffraction patterns of MeOBz- C_{60} , ThBz- C_{60} , and F₂Bz- C_{60} obtained at various temperatures. Four ranges of 2θ were collected subsequently and stitched together to cover the entire range shown here. The brighter parts represent higher intensities and correspond to the peaks in Figure 5.17.



5.2.8. Organic Photovoltaic Performances

We have fabricated BHJ solar cells with the device structure shown in Figure 5.19 using PTB7 donor and $PC_{61}BM$ or $PC_{71}BM$ acceptors for the photoactive components. We selected PTB7 polymer donor with a low band gap (1.6 eV)³⁹ which arises from its alternating donor-acceptor backbone (Figure 5.20 (b)). The BHJ devices with aryne- C_{60} n-type materials demonstrated low performance compared to PTB7:PCBM standard cells due to the poor solubility of aryne- C_{60} adducts in either chlorobenzene or *o*-dichlorobenzene processing solvent. Thus, we devised new BHJ compositions where aryne- C_{60} adducts were added as minority component in PTB7:PCBM standard cells. During the device optimization process, we varied multiple parameters (ratio of donor and acceptor, concentration of solutions, batches of commercially available PTB7 and PCBM, speed of spin coating, duration of drying, batches of PEDOT:PSS, and the thickness of calcium and aluminum electrodes) which produced devices with a wide range of efficiencies. Herein, we studied the impact of aryne- C_{60} additives on the devices with different levels of photovoltaic efficiency.

Figure 5.19. The device architecture of bulk heterojunction polymer solar cells.



The first devices were made with PC₆₁BM acceptor, and the preliminary device results are displayed in Figure 5.20 (a). The blends with 0.25% MeBz- C_{60} and MeOBz- C_{60} showed very similar performances compared to the standard cell in terms of V_{oc} , J_{sc} , and FF. On the other hand, the addition of ThBz- C_{60} and F₂Bz- C_{60} improved J_{sc} , FF, and consequently the overall efficiency (Table 5.2). V_{oc} remained unchanged as predicted by the similar LUMO levels of additives and the major acceptor PC₆₁BM. Fullerenes (both PCBM and aryne- C_{60} additives) are likely in contact with the acceptor unit (thienothiophene) of PTB7 rather than the sterically inaccessible donor unit (benzodithiophene with bulky alkyl chains).⁴⁰ Thus fullerenes that have stronger interaction with the fluorinated thienothiophene (F-TT) group will be located at the donor-acceptor interface and affect electron transfer. Non-covalent interactions such as fluorine-fluorine or fluorine-sulfur interactions and π - π stacking could attract F₂Bz- C_{60} and ThBz- C_{60} to the F-TT unit, which is expected to improve charge transfer dynamics.

Figure 5.20. (a) J - V characteristics of PTB7:PC₆₁BM and (b) structure of PTB7 donor.

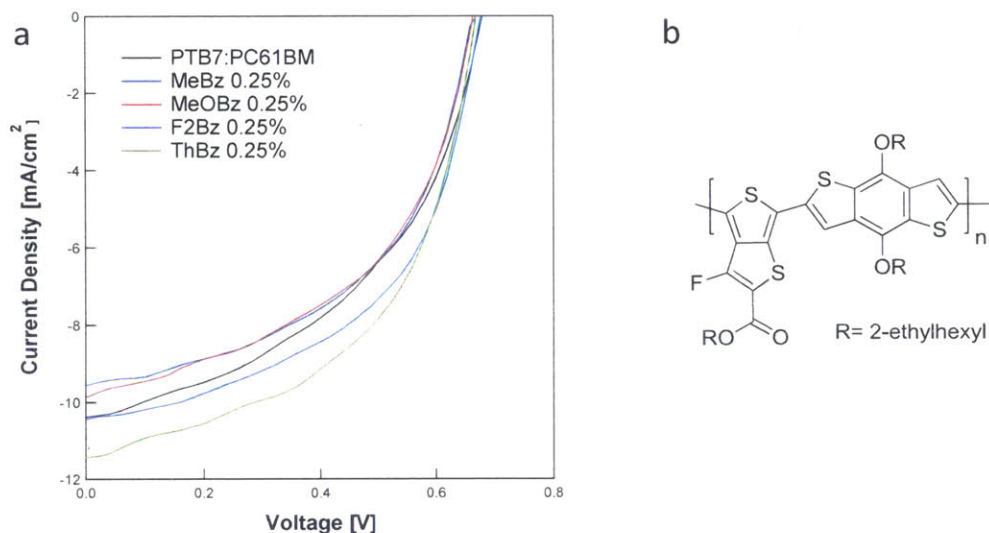


Table 5.2. OPV characteristics of the devices in Figure 5.20.

Device	J_{sc} (mA/cm ²)	V_{oc} (V)	FF	PCE (%)
Standard	10.4	0.67	0.46	3.2
MeBz	9.6	0.67	0.50	3.2
MeOBz	9.9	0.67	0.48	3.2
F2Bz	10.5	0.67	0.52	3.7
ThBz	11.4	0.67	0.51	3.9

Although fluorine-fluorine interactions are known to be very weak due to the low polarizability of the fluorine atom, some reports demonstrated stabilizing C-F \cdots F-C interactions and a shorter distance between fluorine atoms than the van der Waals radii of two fluorine atoms in the crystal structures.⁴¹⁻⁴⁴ In some cases fluorine-fluorine interactions play a prominent role in determining the crystal packing of molecules⁴⁵ and even the formation of transition metal complexes.⁴⁶ In an STM study of fluorinated anthradithiophene,⁴⁷ it was shown that both fluorine-fluorine and fluorine-sulfur interactions direct the self-assembly of the molecules. Therefore we hypothesize that F₂Bz- C_{60} additives are proximate to the fluorine and sulfur-containing unit of polymer and influence the donor-acceptor interfacial properties. Potential π - π

interactions between the thiophene moiety of ThBz- C_{60} and the thienothiophene group of polymer could selectively attract ThBz- C_{60} to the donor-acceptor boundary. Thus ThBz- C_{60} and F₂Bz- C_{60} are expected to self-organize preferably at the polymer-fullerene interface rather than to be randomly distributed in the PCBM domains. In contrast, MeOBz- C_{60} and MeBz- C_{60} do not possess functional groups that favorably interact with F-TT units. They are likely to intermix with PCBM in the acceptor phase due to the common alkyl or methoxy groups. MeOBz- C_{60} and MeBz- C_{60} did not exert performance enhancement, but they showed great compatibility with PCBM. As a result, the standard performance is maintained.

Next, PC₇₁BM instead of PC₆₁BM was employed as the n-type material, since C₇₀ derivatives have a higher extinction coefficient for light absorption compared to their C₆₀ counterparts. The best reported PCEs of PTB7:PC₇₁BM range from 6% to 8%, depending on the donor-acceptor compositions and processing conditions.^{39,48-51} Figure 5.21 (a) represents the blends under sub-optimal conditions with a standard PCE of 4.9% and low current, which could originate from poor morphology or interfacial properties. The 0.25% addition of ThBz- C_{60} and F₂Bz- C_{60} significantly increases J_{sc} and FF, resulting in an 18% and 29% improvement of the standard (Table 5.3). Figure 5.21 (b) shows a set of devices with an upgraded standard efficiency of 5.8% that was also improved with the additives (by 2% with ThBz- C_{60} and 12% with F₂Bz- C_{60}). The degree of PCE improvement by the additives is greater when the standard blend is under sub-optimal conditions.

Figure 5.21. J - V characteristics of PTB7:PC₇₁BM with (a) low and (b) upgraded standard.

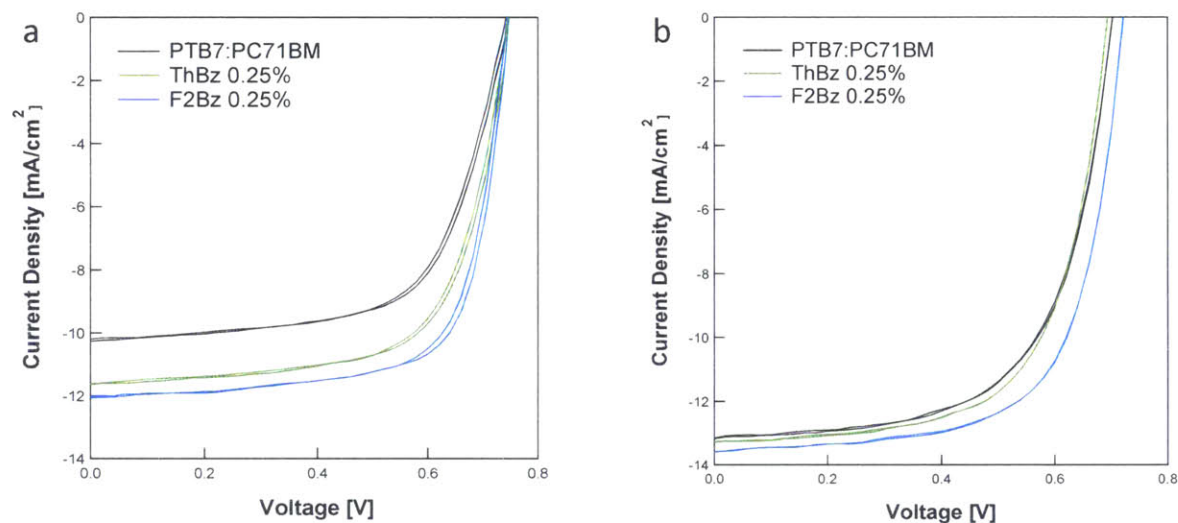


Table 5.3. OPV characteristics of the devices in Figure 5.21.

Device	J_{sc} (mA/cm ²)	V_{oc} (V)	FF	PCE (%)
Standard A	10.3	0.73	0.65	4.9
ThBz	11.7	0.75	0.66	5.8
F ₂ Bz	12.1	0.75	0.70	6.3
Standard B	13.2	0.71	0.62	5.8
ThBz	13.3	0.69	0.65	5.9
F ₂ Bz	13.6	0.73	0.66	6.5

Figure 5.22 and Table 5.4 exhibit the most optimized devices with 6.0% standard PCE that was further advanced by the additives (10% and 12% increment with ThBz- C_{60} and F₂Bz- C_{60} , respectively). The additives increase J_{sc} and FF concomitantly, which strongly suggests an improved charge transfer from polymer to fullerene. The interfacial properties are influenced by the type and amount of additives. When we varied the amount of F₂Bz- C_{60} additive from 0.1% to 5.0% (Figure 5.22 (b)), the best PCE of 6.7% was obtained with 0.25% and 1.0% doping, and the adverse effect on J_{sc} develops beyond 2.0% due to the unfavorable interfacial quality.

Excessive additives may inhibit the effective charge transfer because of the poor solubility of the aryne- C_{60} species.

Figure 5.22. J - V characteristics of optimized PTB7:PC₇₁BM devices with (a) 0.25% ThBz- C_{60} and F₂Bz- C_{60} and (b) a range of F₂Bz- C_{60} doping.

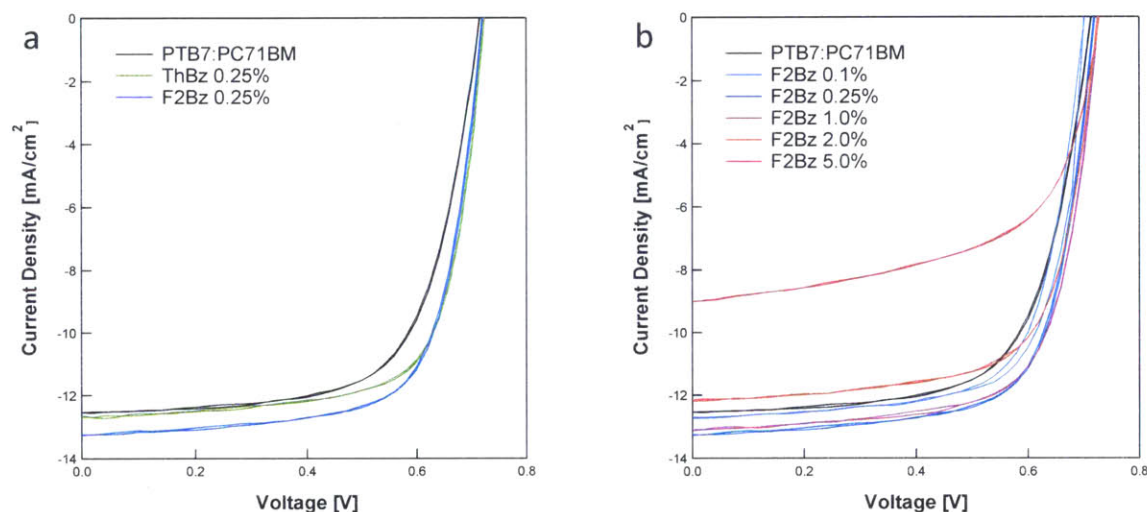


Table 5.4. OPV characteristics of the devices in Figure 5.20.

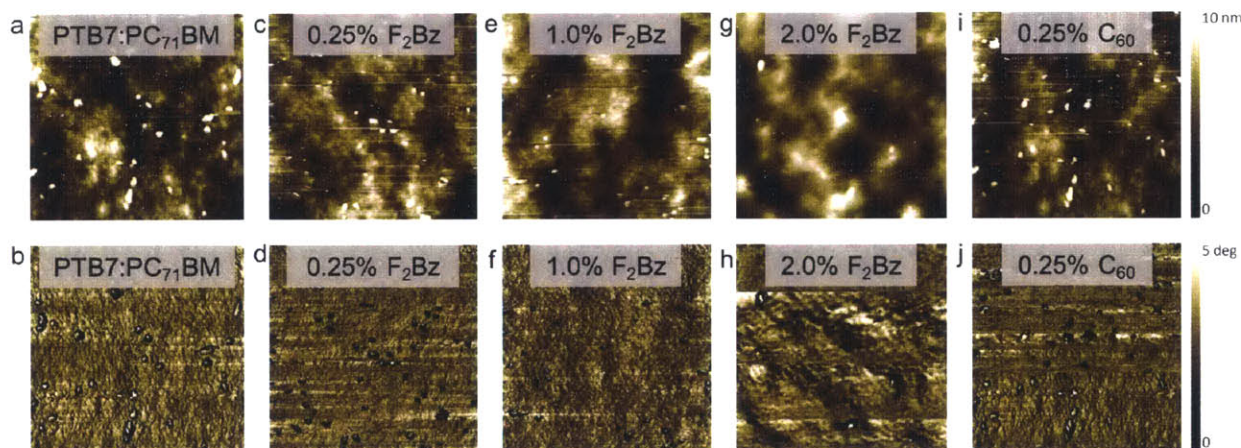
Device	J_{sc} (mA/cm ²)	V_{oc} (V)	FF	PCE (%)
Standard	12.5	0.71	0.67	6.0
ThBz 0.25%	12.7	0.73	0.71	6.6
F ₂ Bz 0.1%	12.7	0.71	0.71	6.4
F ₂ Bz 0.25%	13.2	0.73	0.70	6.7
F ₂ Bz 1.0%	13.1	0.73	0.70	6.7
F ₂ Bz 2.0%	12.2	0.73	0.69	6.1
F ₂ Bz 5.0%	9.0	0.73	0.59	3.9

5.2.9. Morphological Study

To assess the effect of additives on film morphology, we conducted atomic force microscopy (AFM) on the devices after the J - V measurements. Figure 5.23 shows the topography and phase of PTB7:PC₇₁BM devices with 0, 0.25, 1.0, and 2.0% additive. The

particles (30–100 nm) that appear in the standard PTB7:PC₇₁BM blend are the characteristic fullerene aggregates. The additives relieve PC₇₁BM aggregation, which becomes more apparent when doping exceeds 1.0%. There are fewer particles on the film with 1.0% F₂Bz- C_{60} , and they mostly disappear with 2.0% F₂Bz- C_{60} . The phenomena indicate that minority additives can drastically modify film morphology and impact photovoltaic performances. Though only marginal changes were detected by AFM on the films with 0.25% additives, the morphological effect on device performance should not be underestimated. We hypothesize that the combined effects of interfacial and morphological changes result in the PCE enhancement.

Figure 5.23. The topography (upper row) and phase (lower row) of PTB7:PC₇₁BM devices without additive (a, b), with 0.25% (c, d), 1.0% (e, f), 2.0% F₂Bz- C_{60} (g, h), and 0.25% C₆₀ (i, j). Each image is 1 μm \times 1 μm in scale. The white particles (high features) shown in the topography correspond to fullerene aggregates.

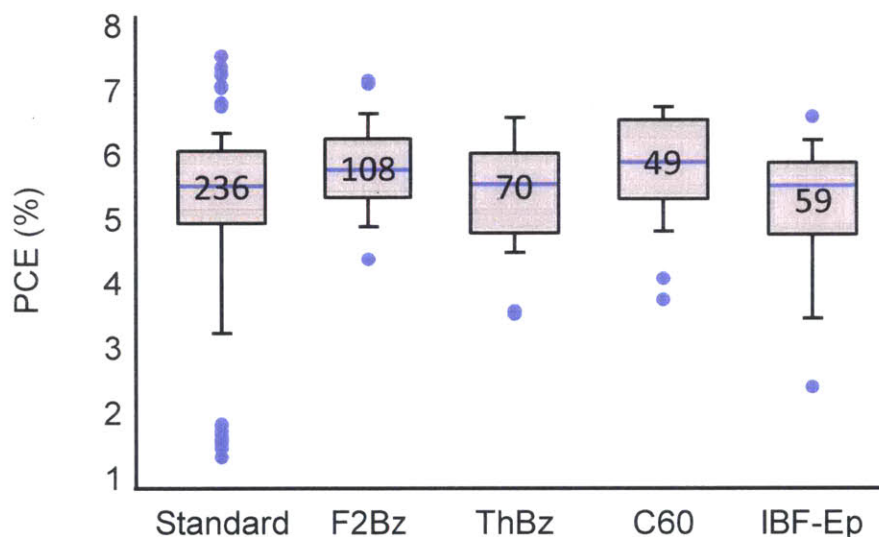


5.2.10. Statistical Analysis of Solar Cell Performances

We compiled all the results of functional devices, and a total of 522 devices was taken into account for statistical analysis (Figure 5.24). We note that more standard device results were available for analysis, since only the results with 0.25% and 1.0% doping were selected for additives (the number of devices for each entry can be found in the box). The box plot is an

effective way to present all PCE data, as it gives the 10th (bottom end), 25th (bottom of box), 50th (median, purple line), 75th (top of box), and 90th (top end) percentiles of the distribution as well as the outliers (purple dots). It is noted that standard device data has a broader distribution ranging from 1.3% to 7.5% than the blends with additives. The medians of all entries are similar (between 5% and 6%), but the spans of box and whiskers (two opposite ends) from top to bottom vary depending on the additives. F₂Bz- C_{60} and ThBz- C_{60} display narrower distribution than the reference cells, indicating better reproducibility. F₂Bz- C_{60} in particular makes more consistent devices with higher performance than the reference cells, as exemplified in the $J-V$ plots.

Figure 5.24. Statistical analysis of the PTB7:PC₇₁BM devices with no additives (standard) and 0.25% and 1.0% of additives (F₂Bz- C_{60} , ThBz- C_{60} , C₆₀, IBF-Ep). The number of devices for each entry is in the box. The purple line in the box indicates the median of distribution. The top and bottom of box represents the 75th and 25th percentiles, and the top and bottom ends show the 90th and 10th percentiles of the statistics. The purple dots are the outlier data. A broad distribution of standard performance implies a challenge for consistent device reproduction.



We extended our study to other additives (pristine C₆₀ and IBF-Ep as discussed in Chapters 3 and 4) for control experiments. C₆₀ lacks any functional group that can interact with

the polymer donor, and the substituents on IBF-Ep are not very distinct from those on PCBM. An interesting outcome is the similar behavior of C_{60} compared to that of F_2Bz-C_{60} or $ThBz-C_{60}$. As opposed to our prediction that C_{60} would have negligible impact, its addition produced higher median PCE and a narrower distribution than the reference cells. This result implies that C_{60} may separate from PCBM domains and self-organize at the donor-acceptor interface, which improves charge transfer. In contrast, the IBF-Ep control experiment result was similar to the reference cell distribution, which suggests that IBF-Ep intermixes well with PCBM in the acceptor domains and has no impact on interfacial properties. IBF-Ep, $MeBz-C_{60}$, $MeOBz-C_{60}$, and PCBM possess similar types of functional groups on C_{60} .

To summarize, F_2Bz-C_{60} , $ThBz-C_{60}$, and pristine C_{60} additives were effective in generating reproducible device performance with only 0.25% or 1.0% addition. Our hypothesis is that the additives enhance the charge transfer between the donor and acceptor; however, their contribution is the greatest when the composition and interface properties are sub-optimal, as seen in Figure 5.21 (a) with a 29% PCE improvement. When PTB7:PCBM reference devices are in their most optimized forms, their PCEs are likely to be near the intrinsic limits. In this case, the addition of a ternary component does not enhance the device performance as much, as shown in Figure 5.21 (b) and 5.22.

5.3. Conclusions

We have demonstrated that minority fullerene additives (0.25% or 1.0%) can enhance the photovoltaic performance of PTB7:PCBM polymer solar cells by increasing the current density and fill factor. The structural differences of additives and PCBM enable their phase separation and self-organization of dopants at the donor-acceptor interface. Also, the strong interaction of

the fluorine and thiophene substituents on aryne-C₆₀ with the F-TT unit on the polymer backbone can promote interfacial charge transfer. Through statistical analysis on a high number of device results, we confirmed that the additives effectively increase the reproducibility of high-performance devices, which can solve a critical problem in the industrial production of organic solar cells.

5.4. Experimental Section

Materials. PC₇₁BM and PTB7 were purchased from 1-Material and PEDOT:PSS was purchased from Stark. C₆₀ was purchased from SES Research. Anthranilic acid, 2-amino-4,5-dimethoxybenzoic acid, 2-amino-4-fluorobenzoic acid, 2-amino-4,5-difluorobenzoic acid, 2-amino-4-(2-thienyl)benzoic acid, and 3-amino-2-naphthoic acid were purchased from Alfa Aesar. PC₆₁BM, 2-amino-3,4,5,6-tetrafluorobenzoic acid, and 3,5-dimethylantranilic acid were purchased from Sigma-Aldrich. All compounds purchased from commercial sources were used as received. Other materials including solvents and electrolyte salt were also commercially available. Anhydrous solvents were obtained from a solvent purification system (Innovative Technologies).

Measurements. Reaction mixtures containing multiadducts of fullerenes were separated by 5PBB Cosmosil column (10 mm x 250 mm) from Nacalai Tesque, Inc. installed in Agilent Technologies ProsStar 210 High Pressure Liquid Chromatography (HPLC) system with 4mL/min elution of toluene. ¹H and ¹³C NMR spectra were taken on Varian Inova-500 spectrometers. Chemical shifts were reported in ppm and referenced to residual solvent peaks (CD₂Cl₂: 5.33 ppm for ¹H, 53.84 ppm for ¹³C). Bruker Daltonics Omnicflex MALDI-TOF mass spectrometer was used for mass determination without the use of matrix. UV-Vis absorption

spectra were obtained using a Cary 4000 UV-Vis spectrophotometer. Electrochemical measurements were carried out in a glove box under nitrogen, using an Autolab PGSTAT 10 or PGSTAT 20 potentiostat (Eco Chemie) in a three-electrode cell configuration. A Pt button (1.6 mm in diameter) electrode, a Pt wire, and a quasi-internal Ag wire submerged in 0.01M $AgNO_3/0.1M$ tetrabutylammonium hexafluorophosphate ($TBAPF_6$) in acetonitrile were used as a working electrode, a counter electrode, and a reference electrode, respectively, in 0.1M $TBAPF_6$ toluene/acetonitrile (4:1) solution. The ferrocene/ferrocenium (Fc/Fc^+) redox couple was used as an internal standard, with the half-wave potentials observed between 0.192–0.205 V vs Ag/Ag^+ in toluene/acetonitrile (4:1) solution. Thermogravimetric analyses were performed with a Discovery TGA and Discovery DSC (TA Instruments) under nitrogen. Variable-temperature transmission-mode X-ray powder diffraction was measured by Bruker X8 Dual ImuS APEX2 (temperature range from 100K to 500K) with Cu radiation. Gaussian 03 software package was used for the structure optimization and the frequency calculation at the DFT level. The B3LYP functional in conjunction with the 6-31G (d,p) basis set was used for the computation.

Synthesis of MeOBz- C_{60} . In a flame-dried 200 mL Schlenk flask, C_{60} (150 mg, 0.21 mmol) and 2-amino-4,5-dimethoxybenzoic acid (164 mg, 0.83 mmol) were dissolved in dry toluene (80 mL) and stirred at 100 °C under argon for 15 min. Isoamyl nitrite (112 μ L, 0.83 mmol) was then added dropwise to the solution which turned brown from purple. The solution was stirred for 30 min and slowly cooled down to room temperature. The solution was evaporated under reduced pressure, and 15 mL of the reaction mixture was left. The mixture was purified via SiO_2 column chromatography with toluene elution ($R_F \sim 0.5$), and 27.9 mg (15.6 %) of product was obtained. 113.4 mg (75.6 %) of C_{60} was recovered. 1H NMR (500 MHz, CD_2Cl_2/CS_2 , δ): 7.56 (s, 2H), 4.10

(s, 6H) ^{13}C NMR (500 MHz, $\text{CDCl}_3/\text{CS}_2$, δ): 193.27 (CS_2), 17 peaks found for C_{60} sp^2 carbons (156.02, 152.73, 147.47, 146.95, 146.74, 146.71, 146.04, 145.92, 145.24, 143.62, 143.59, 143.51, 142.98, 142.82, 141.77, 141.11, 139.79), 102.72 (aromatic), 78.18 (CDCl_3), 77.71 (C_{60} sp^3), 57.16 (2C), 30.79 (grease).

MS (MALDI-TOF, m/z): $[\text{M}]^+$ (monoisotopic mass) calcd for $C_{68}\text{H}_8\text{O}_2$, 856.0524; found, 856.06

Synthesis of $F_2\text{Bz}-C_{60}$. In a flame-dried 200 mL Schlenk flask, C_{60} (150 mg, 0.21 mmol) and 2-amino-4,5-difluorobenzoic acid (144 mg, 0.83 mmol) were dissolved in dry toluene (80 mL) and stirred at 100 °C under argon for 15 min. Isoamyl nitrite (112 μL , 0.83 mmol) was then added dropwise to the solution which turned brown from purple. The solution was stirred for 30 min and slowly cooled down to room temperature. The solution was evaporated under reduced pressure, and the dried reaction mixture was dissolved in toluene 15 mL. To the mixture was added EtOH (100 mL) to precipitate brown solid. The solid was purified via SiO_2 column chromatography with CS_2 /hexane (1:3 v/v) elution combined with HPLC with 5PBB Cosmosil column (toluene elution), and 9.0 mg (5.2 %) of product was obtained. 37.1 mg (24.7 %) of C_{60} was recovered. ^1H NMR (500 MHz, $\text{CD}_2\text{Cl}_2/\text{CS}_2$, δ): 7.88 (dd, 2H), 7.24, 7.17, 2.41 (m, m, s, toluene residue) ^{13}C NMR (500 MHz, $\text{CD}_2\text{Cl}_2/\text{CS}_2$, δ): 193.29 (CS_2), 15 peaks found for C_{60} sp^2 carbons (154.48, 147.58, 146.87, 146.81, 146.73, 146.27, 146.13, 145.25, 143.73, 143.68, 143.61, 143.06, 142.68, 141.27, 139.75), 114.40 (aromatic), 82.19 (C_{60} sp^3), 54.18 (CD_2Cl_2) *F-coupled carbons unseen due to the low intensity ^{19}F NMR (500 MHz, $\text{CD}_2\text{Cl}_2/\text{CS}_2$, δ): 102.04 (dd).

MS (MALDI-TOF, m/z): $[\text{M}]^+$ calcd for $C_{66}\text{H}_2\text{F}_2$, 832.0125; found, 832.06

Synthesis of MeBz- C_{60} . In a flame-dried 500 mL Schlenk flask, C_{60} (300 mg, 0.42 mmol) and 3,5-dimethylantranilic acid (274 mg, 1.66 mmol) were dissolved in dry toluene (200 mL) and stirred at 100 °C under argon for 15 min. Isoamyl nitrite (224 μ L, 1.66 mmol) was then added dropwise to the solution which turned brown from purple. The solution was stirred for 30 min and slowly cooled down to room temperature. The solution was evaporated under reduced pressure, and the dried reaction mixture was dissolved in toluene 30 mL. To the mixture was added EtOH (200 mL) to precipitate brown solid. The solid was purified by HPLC with 5PBB Cosmosil column (toluene elution) followed by SiO_2 column chromatography with CS_2 /hexane (1:1 v/v) elution, and 46.0 mg (14.1 %) of product was obtained. 1H NMR (500 MHz, CD_2Cl_2/CS_2 , δ): 7.65 (s, 1H), 7.37 (s, 1H), 2.80 (s, 3H), 2.70 (s, 3H) ^{13}C NMR (500 MHz, CD_2Cl_2/CS_2 , δ): 193.30 (CS_2), 29 peaks found for C_{60} sp^2 carbons (155.92, 155.44, 147.19, 147.03, 147.02, 146.78, 146.75, 146.11, 146.08, 146.00, 145.29, 145.27, 143.68, 143.64, 143.57, 143.04, 143.01, 142.99, 143.97, 143.94, 142.89, 142.87, 141.38, 141.23, 141.22, 141.20, 139.76, 139.65, 135.03), 132.56 (aromatic), 122.08 (aromatic), 68.85 (C_{60} sp^3), 68.27 (C_{60} sp^3), 54.18 (CD_2Cl_2), 23.42 (1C), 18.27 (1C).

MS (MALDI-TOF, m/z): $[M]^+$ calcd for $C_{68}H_8$, 824.0626; found, 824.07

Synthesis of ThBz- C_{60} . In a flame-dried 200 mL Schlenk flask, C_{60} (150 mg, 0.21 mmol) and 2-amino-4-(2-thienyl)benzoic acid (182 mg, 0.83 mmol) were dissolved in dry toluene (80 mL) and stirred at 100 °C under argon for 15 min. Isoamyl nitrite (112 μ L, 0.83 mmol) was then added dropwise to the solution which turned brown from purple. The solution was stirred for 30 min and slowly cooled down to room temperature. To the solution was added EtOH (100 mL) to precipitate brown solid. The solid was purified via SiO_2 column chromatography with

CS_2 /hexane (1:1 v/v) elution, and 28.0 mg (15.3 %) of product was obtained. 31.8 mg (21.2 %) of C_{60} was recovered. 1H NMR (500 MHz, CD_2Cl_2/CS_2 , δ): 8.27 (s, 1H), 8.04 (m, 2H), 7.56 (d, 1H), 7.45 (d, 1H), 7.23 (dd, 1H) ^{13}C NMR (500 MHz, CD_2Cl/CS_2 , δ): 193.29 (CS_2), 31 peaks found for C_{60} sp^2 carbons (155.31, 155.29, 150.51, 148.90, 147.52, 147.05, 147.03, 146.82, 146.81, 146.76, 146.17, 146.16, 146.10, 145.99, 145.28, 145.27, 145.00, 143.89, 143.68, 143.67, 143.60, 143.59, 143.06, 143.05, 142.85, 142.81, 143.28, 143.25, 139.75, 139.71, 137.38), 129.25 (aromatic), 128.84 (aromatic), 126.62 (aromatic), 124.88 (aromatic), 124.87 (aromatic), 121.92 (aromatic), 70.46 (C_{60} sp^3), 70.42 (C_{60} sp^3), 54.19 (CD_2Cl_2), under 33.14 (grease).

MS (MALDI-TOF, m/z): $[M]^+$ calcd for $C_{70}H_6S$, 878.0190; found, 878.09

Synthesis of Bz- C_{60} . In a flame-dried 200 mL Schlenk flask, C_{60} (150 mg, 0.21 mmol) and anthranilic acid (114 mg, 0.83 mmol) were dissolved in dry toluene (80 mL) and stirred at 100 °C under argon for 15 min. Isoamyl nitrite (112 μ L, 0.83 mmol) was then added dropwise to the solution which turned brown from purple. The solution was stirred for 30 min and slowly cooled down to room temperature. The solution was evaporated under reduced pressure, and the dried reaction mixture was purified via SiO_2 column chromatography with CS_2 /hexane (1:2 v/v) elution combined with HPLC with 5PBB Cosmosil column (toluene elution), and 6.6 mg (4.2 %) of product was obtained. 1H NMR (500 MHz, CD_2Cl_2/CS_2 , δ): 8.03 (d, 2H), 7.80 (d, 2H).

Synthesis of Np- C_{60} . In a flame-dried 200 mL Schlenk flask, C_{60} (150 mg, 0.21 mmol) and 3-amino-2-naphthoic acid (156 mg, 0.83 mmol) were dissolved in dry toluene (80 mL) and stirred at 100 °C under argon for 15 min. Isoamyl nitrite (112 μ L, 0.83 mmol) was then added dropwise to the solution which turned dark red from brown. The solution was stirred for 50 min and slowly

cooled down to room temperature. To the solution was added EtOH (200 mL) to precipitate brown solid. The solid was purified by HPLC with 5PBB Cosmosil column (toluene elution) followed by SiO_2 column chromatography with CS_2 /hexane (1:10 v/v) elution, and 9.2 mg (5.5 %) of product was obtained. 1H NMR (500 MHz, CD_2Cl_2/CS_2 , δ): 8.47 (s, 2H), 8.18 (d, 2H), 7.72 (d, 2H).

Synthesis of F_1Bz-C_{60} . In a flame-dried 200 mL Schlenk flask, C_{60} (150 mg, 0.21 mmol) and 2-amino-4-fluorobenzoic acid (129 mg, 0.83 mmol) were dissolved in dry toluene (80 mL) and stirred at 100 °C under argon for 15 min. Isoamyl nitrite (112 μ L, 0.83 mmol) was then added dropwise to the solution which turned brown from purple. The solution was stirred for 30 min and slowly cooled down to room temperature. To the solution was added EtOH (200 mL) to precipitate brown solid. The solid was purified via SiO_2 column chromatography with CS_2 /hexane (1:6 v/v) elution combined with HPLC with 5PBB Cosmosil column (toluene elution), and 8.1 mg (5.0 %) of product was obtained. 1H NMR (500 MHz, CD_2Cl_2/CS_2 , δ): 8.00 (dd, 1H), 7.75 (dd, 1H), 7.50 (m, 1H).

Synthesis of F_4Bz-C_{60} . In a flame-dried 200 mL Schlenk flask, C_{60} (150 mg, 0.21 mmol) and 2-amino-3,4,5,6-tetrafluorobenzoic acid (174 mg, 0.83 mmol) were dissolved in dry toluene (80 mL) and stirred at 100 °C under argon for 15 min. Isoamyl nitrite (112 μ L, 0.83 mmol) was then added dropwise to the solution which turned brown from purple. The solution was stirred at 120°C for 48 h and slowly cooled down to room temperature. The solution was evaporated under reduced pressure, and the dried reaction mixture was dissolved in toluene 10 mL. To the mixture was added EtOH (100 mL) to precipitate brown solid. The solid was purified via SiO_2 column

chromatography with CS₂/hexane (1:1 v/v) elution. Very low amount of the product was obtained and it could not be detected by NMR. The R_f value is 0.75 upon elution with toluene.

Device Fabrication. Patterned ITO substrates (Thin Film Devices, 150 nm thick, 20 Ω/sq, 85%T) were cleaned by sonication in DI water with soap (Micro-90, Cole-Parmer), DI water, acetone and isopropanol, followed by oxygen plasma cleaning (100 W, Plasma Preen, Inc.) for 2 minutes. Poly(3,4-ethylenedioxythiophene):poly(styrenesulfonate) (PEDOT:PSS) (Clevios™ P VP AI 4083) was deposited on ITO by spincoating at 4000 rpm for 1 min and annealed at 150 °C for 10 min in air. Chlorobenzene with 3 % diiodooctane (DIO) was prepared as a stock solution by adding 60 μL of DIO into 1.94 mL chlorobenzene. PTB7 and PC₇₁BM were dissolved in chlorobenzene/DIO mixture with the concentration of 12 mg/mL and 40 mg/mL, respectively, and the individual solutions were stirred at 70 °C for 90 min. For optimal results, two solutions were mixed by 2:1 volume ratio to make 21.3 mg/mL total concentration and stirred at 70 °C for 60 min. Each additive was dissolved in *o*-dichlorobenzene with 21.3 mg/mL concentration and added to the PTB7:PC₇₁BM blend solution by appropriate amount (from 0.1% to 5.0%). The active layer was spun at 1000 rpm for 2 min and dried in the nitrogen-filled glovebox for 3 h, then under vacuum for 1 h. The mixing ratio, duration of solution heating, spin-coating conditions, and drying conditions were varied to optimize the devices. Calcium (25 nm) and aluminum (100 nm) top electrodes were thermally evaporated through shadow masks at a base pressure of 2×10^{-6} Torr with rates of 0.5 Å/s and 1.0 Å/s, respectively.

Device Characterization. Current-voltage characteristics of the solar cell devices were recorded in a nitrogen-filled glove box using a computer-controlled Keithley 6487 picoammeter source-

meter. 100 mW/cm² illumination was provided by a 150 W xenon arc-lamp (Newport 96000) equipped with an AM 1.5G filter. AFM images were obtained with an Agilent 5100 atomic force microscope. The measurements were performed in ACAFM tapping mode using silicon tips with a force constant of 20–80 N/m.

5.5. References and Notes

1. Chen, J.; Cao, Y.: Development of Novel Conjugated Donor Polymers for High-Efficiency Bulk-Heterojunction Photovoltaic Devices. *Acc. Chem. Res.* **2009**, *42*, 1709-1718.
2. Roncali, J.: Molecular Bulk Heterojunctions: An Emerging Approach to Organic Solar Cells. *Acc. Chem. Res.* **2009**, *42*, 1719-1730.
3. Thompson, B. C.; Frechet, J. M. J.: Organic photovoltaics - Polymer-fullerene composite solar cells. *Angew. Chem. Int. Ed.* **2008**, *47*, 58-77.
4. Yu, G.; Gao, J.; Hummelen, J. C.; Wudl, F.; Heeger, A. J.: Polymer Photovoltaic Cells - Enhanced Efficiencies Via a Network of Internal Donor-Acceptor Heterojunctions. *Science* **1995**, *270*, 1789-1791.
5. Cheng, Y. J.; Yang, S. H.; Hsu, C. S.: Synthesis of Conjugated Polymers for Organic Solar Cell Applications. *Chem. Rev.* **2009**, *109*, 5868-5923.
6. Mühlbacher, D.; Scharber, M.; Morana, M.; Zhu, Z. G.; Waller, D.; Gaudiana, R.; Brabec, C.: High photovoltaic performance of a low-bandgap polymer. *Adv. Mater.* **2006**, *18*, 2884-2889.
7. Scharber, M. C.; Wühlbacher, D.; Koppe, M.; Denk, P.; Waldauf, C.; Heeger, A. J.; Brabec, C. L.: Design rules for donors in bulk-heterojunction solar cells - Towards 10 % energy-conversion efficiency. *Adv. Mater.* **2006**, *18*, 789-794.
8. Hummelen, J. C.; Knight, B. W.; Lepeq, F.; Wudl, F.; Yao, J.; Wilkins, C. L.: Preparation and Characterization of Fulleroid and Methanofullerene Derivatives. *J. Org. Chem.* **1995**, *60*, 532-538.

9. He, Y. J.; Chen, H. Y.; Hou, J. H.; Li, Y. F.: Indene-C₆₀ Bisadduct: A New Acceptor for High-Performance Polymer Solar Cells (vol 132, pg 1377, 2010). *J. Am. Chem. Soc.* **2010**, *132*, 5532-5532.
10. Liu, X.; Huettner, S.; Rong, Z.; Sommer, M.; Friend, R. H.: Solvent Additive Control of Morphology and Crystallization in Semiconducting Polymer Blends. *Adv. Mater.* **2012**, *24*, 669-674.
11. Peet, J.; Brocker, E.; Xu, Y. H.; Bazan, G. C.: Controlled beta-phase formation in poly(9,9-di-n-octylfluorene) by processing with alkyl additives. *Adv. Mater.* **2008**, *20*, 1882-1885.
12. Perez, L. A.; Chou, K. W.; Love, J. A.; van der Poll, T. S.; Smilgies, D. M.; Nguyen, T. Q.; Kramer, E. J.; Amassian, A.; Bazan, G. C.: Solvent Additive Effects on Small Molecule Crystallization in Bulk Heterojunction Solar Cells Probed During Spin Casting. *Adv. Mater.* **2013**, *25*, 6380-6384.
13. Moulé, A. J.; Meerholz, K.: Controlling Morphology in Polymer-Fullerene Mixtures. *Adv. Mater.* **2008**, *20*, 240-245.
14. van Duren, J. K. J.; Yang, X. N.; Loos, J.; Bulle-Lieuwma, C. W. T.; Sieval, A. B.; Hummelen, J. C.; Janssen, R. A. J.: Relating the morphology of poly(p-phenylene vinylene)/methanofullerene blends to solar-cell performance. *Adv. Funct. Mater.* **2004**, *14*, 425-434.
15. Peet, J.; Soci, C.; Coffin, R. C.; Nguyen, T. Q.; Mikhailovsky, A.; Moses, D.; Bazan, G. C.: Method for increasing the photoconductive response in conjugated polymer/fullerene composites. *Appl. Phys. Lett.* **2006**, *89*, 252105.
16. Pivrikas, A.; Sariciftci, N. S.; Juska, G.; Osterbacka, R.: A review of charge transport and recombination in polymer/fullerene organic solar cells. *Prog. Photovoltaics* **2007**, *15*, 677-696.
17. Chen, F. C.; Tseng, H. C.; Ko, C. J.: Solvent mixtures for improving device efficiency of polymer photovoltaic devices. *Appl. Phys. Lett.* **2008**, *92*, 103316.
18. Tada, A.; Geng, Y. F.; Wei, Q. S.; Hashimoto, K.; Tajima, K.: Tailoring organic heterojunction interfaces in bilayer polymer photovoltaic devices. *Nat. Mater.* **2011**, *10*, 450-455.
19. Lobez, J. M.; Andrew, T. L.; Bulovic, V.; Swager, T. M.: Improving the Performance of P3HT-Fullerene Solar Cells with Side-Chain-Functionalized Poly(thiophene) Additives: A New Paradigm for Polymer Design. *ACS Nano* **2012**, *6*, 3044-3056.

20. Moore, J. A.; Ali, S.; Berry, B. C.: Stabilization of PCBM domains in bulk heterojunctions using polystyrene-tethered fullerene. *Sol. Energ. Mat. Sol. Cells* **2013**, *118*, 96-101.
21. Liu, F.; Zhao, W.; Tumbleston, J. R.; Wang, C.; Gu, Y.; Wang, D.; Briseno, A. L.; Ade, H.; Russell, T. P.: Understanding the Morphology of PTB7:PCBM Blends in Organic Photovoltaics. *Adv. Energy. Mater.* **2014**, *4*, 1301377.
22. Kitamura, T.; Yamane, M.; Inoue, K.; Todaka, M.; Fukatsu, N.; Meng, Z. H.; Fujiwara, Y.: A new and efficient hypervalent iodine-benzyne precursor, (phenyl) [o-(trimethylsilyl)phenyl]iodonium triflate: Generation, trapping reaction, and nature of benzyne. *J. Am. Chem. Soc.* **1999**, *121*, 11674-11679.
23. Tsuda, M.; Ishida, T.; Nogami, T.; Kurono, S.; Ohashi, M.: Addition-Reaction of Benzyne to C₆₀. *Chem. Lett.* **1992**, 2333-2334.
24. Hoke, S. H.; Molstad, J.; Dilettato, D.; Jay, M. J.; Carlson, D.; Kahr, B.; Cooks, R. G.: Reaction of Fullerenes and Benzyne. *J. Org. Chem.* **1992**, *57*, 5069-5071.
25. Darwish, A. D.; Abdulsada, A. K.; Langley, G. J.; Kroto, H. W.; Taylor, R.; Walton, D. R. M.: Reaction of [70]Fullerene with Benzyne. *J. Chem. Soc., Chem. Comm.* **1994**, 2133-2134.
26. Darwish, A. D.; Avent, A. G.; Taylor, R.; Walton, D. R. M.: Reaction of benzyne with [70]fullerene gives four monoadducts: Formation of a triptycene homologue by 1,4-cycloaddition of a fullerene. *J. Chem. Soc. Perkin Trans. 2* **1996**, 2079-2084.
27. Meier, M. S.; Wang, G. W.; Haddon, R. C.; Brock, C. P.; Lloyd, M. A.; Selegue, J. P.: Benzyne adds across a closed 5-6 ring fusion in C₇₀: Evidence for bond delocalization in fullerenes. *J. Am. Chem. Soc.* **1998**, *120*, 2337-2342.
28. Nakamura, Y.; Takano, N.; Nishimura, T.; Yashima, E.; Sato, M.; Kudo, T.; Nishimura, J.: First isolation and characterization of eight regioisomers for [60]fullerene-benzyne bisadducts. *Org. Lett.* **2001**, *3*, 1193-1196.
29. Lu, X.; Akasaka, T.; Nagase, S.: Chemistry of endohedral metallofullerenes: the role of metals. *Chem. Commun.* **2011**, *47*, 5942-5957.

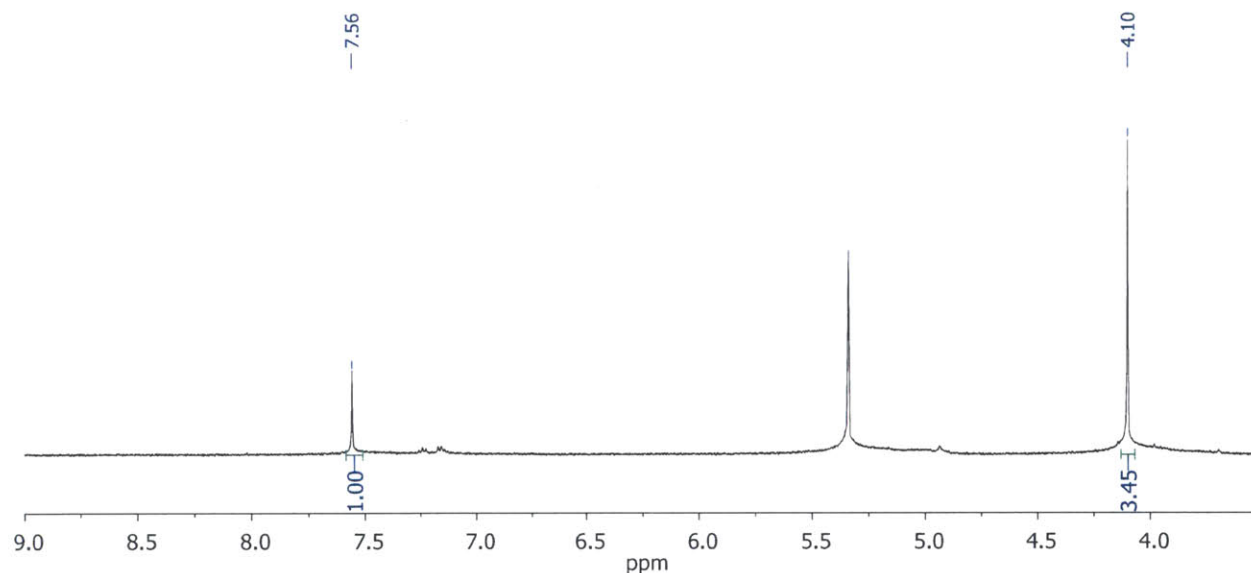
30. Fukuda, T.; Kikukawa, Y.; Takaishi, S.; Kobayashi, N.: Synthesis and Spectroscopic Properties of Phthalocyanine-[60]Fullerene Conjugates Connected Directly by Means of a Four-Membered Ring. *Chem. Asian J.* **2012**, *7*, 751-758.
31. Kim, G.; Lee, K. C.; Kim, J.; Lee, J.; Lee, S. M.; Lee, J. C.; Seo, J. H.; Choi, W. Y.; Yang, C.: An Unprecedented [5,6]-open Adduct via a Direct Benzyne- C_{60} Cycloaddition. *Tetrahedron* **2013**, *69*, 7354-7359.
32. Maurin, P.; Ibrahim-Ouali, M.; Parrain, J. L.; Santelli, M.: Structure of Substituted o-benzynes and Their Cycloaddition to Ketene Dialkyl Acetals. *J. Mol. Struct.Theochem.* **2003**, *637*, 91-100.
33. Khlyabich, P. P.; Burkhart, B.; Thompson, B. C.: Efficient Ternary Blend Bulk Heterojunction Solar Cells with Tunable Open-Circuit Voltage. *J. Am. Chem. Soc.* **2011**, *133*, 14534-14537.
34. Kooistra, F. B.; Knol, J.; Kastenberg, F.; Popescu, L. M.; Verhees, W. J. H.; Kroon, J. M.; Hummelen, J. C.: Increasing the Open Circuit Voltage of Bulk-heterojunction Solar Cells by Raising the LUMO Level of the Acceptor. *Org. Lett.* **2007**, *9*, 551-554.
35. Han, G. D.; Collins, W. R.; Andrew, T. L.; Bulovic, V.; Swager, T. M.: Cyclobutadiene- C_{60} Adducts: N-Type Materials for Organic Photovoltaic Cells with High V_{OC} . *Adv. Funct. Mater.* **2013**, *23*, 3061-3069.
36. Troshin, P. A.; Hoppe, H.; Peregudov, A. S.; Egginger, M.; Shokhovets, S.; Gobsch, G.; Sariciftci, N. S.; Razumov, V. F.: [70]Fullerene-Based Materials for Organic Solar Cells. *ChemSusChem* **2011**, *4*, 119-124.
37. Delgado, J. L.; Oswald, F.; Cardinali, F.; Langa, F.; Martin, N.: On the Thermal Stability of [60]Fullerene Cycloadducts: Retro-cycloaddition Reaction of 2-Pyrazolino[4,5 : 1,2][60]fullerenes. *J. Org. Chem.* **2008**, *73*, 3184-3188.
38. Martin, N.; Altable, M.; Filippone, S.; Martin-Domenech, A.; Echegoyen, L.; Cardona, C. M.: Retro-cycloaddition Reaction of Pyrrolidinofullerenes. *Angew. Chem. Int. Ed.* **2006**, *45*, 110-114.

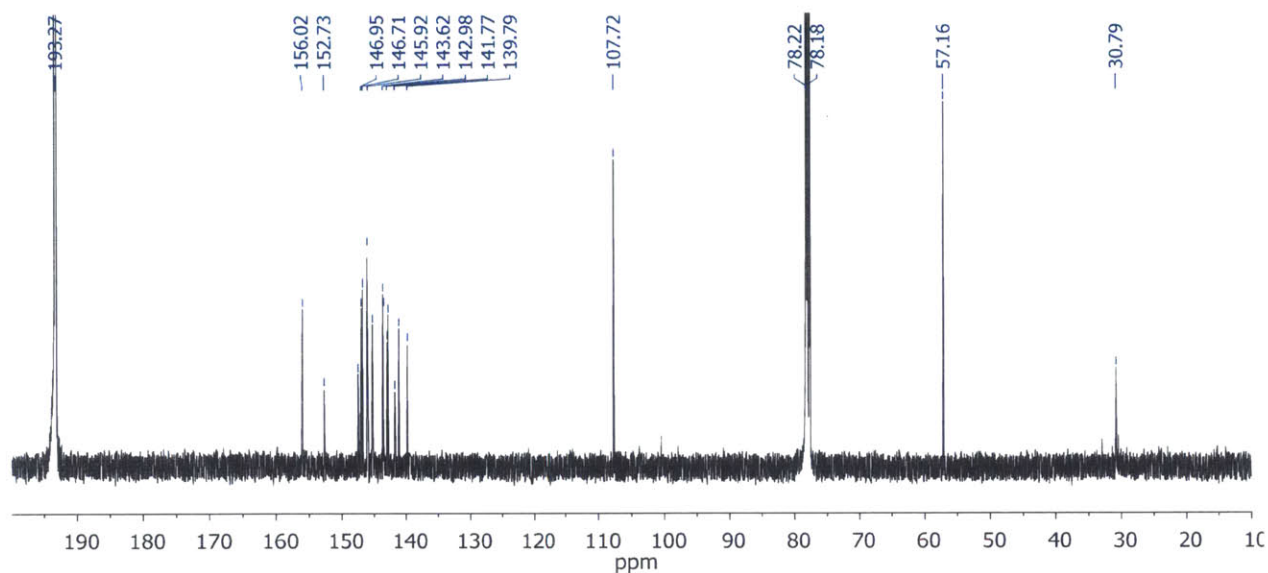
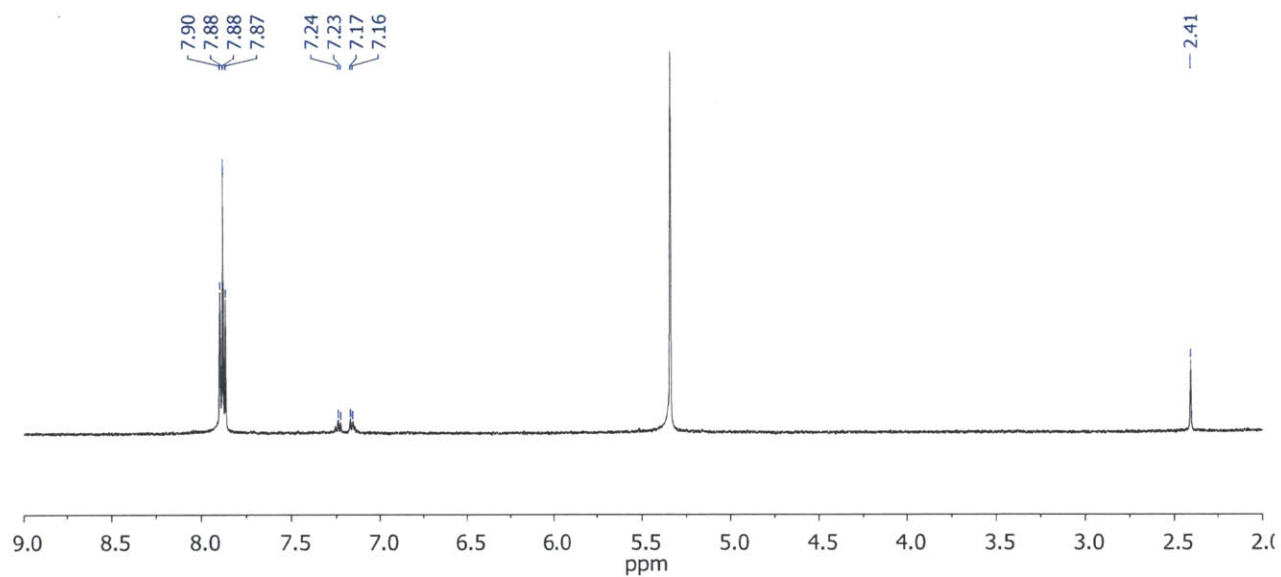
39. Liang, Y.; Xu, Z.; Xia, J.; Tsai, S.-T.; Wu, Y.; Li, G.; Ray, C.; Yu, L.: For the Bright Future—Bulk Heterojunction Polymer Solar Cells with Power Conversion Efficiency of 7.4%. *Adv. Mater.* **2010**, *22*, E135-E138.
40. Graham, K. R.; Cabanetos, C.; Jahnke, J. P.; Idso, M. N.; El Labban, A.; Ndjawa, G. O. N.; Heumueller, T.; Vandewal, K.; Salleo, A.; Chmelka, B. F.; Amassian, A.; Beaujuge, P. M.; McGehee, M. D.: Importance of the Donor:Fullerene Intermolecular Arrangement for High-Efficiency Organic Photovoltaics. *J. Am. Chem. Soc.* **2014**, *136*, 9608-9618.
41. Reichenbacher, K.; Suss, H. I.; Hulliger, J.: Fluorine in Crystal Engineering - "The Little Atom That Could". *Chem. Soc. Rev.* **2005**, *34*, 22-30.
42. Berger, R.; Resnati, G.; Metrangolo, P.; Weber, E.; Hulliger, J.: Organic Fluorine Compounds: A Great Opportunity for Enhanced Materials Properties. *Chem. Soc. Rev.* **2011**, *40*, 3496-3508.
43. Barcelo-Oliver, M.; Estarellas, C.; Garcia-Raso, A.; Terron, A.; Frontera, A.; Quinero, D.; Mata, I.; Molins, E.; Deya, P. M.: Experimental and Theoretical Study of Uracil Derivatives: The Crucial Role of Weak Fluorine-Fluorine Noncovalent Interactions. *CrystEngComm* **2010**, *12*, 3758-3767.
44. Baker, R. J.; Colavita, P. E.; Murphy, D. M.; Platts, J. A.; Wallis, J. D.: Fluorine-Fluorine Interactions in the Solid State: An Experimental and Theoretical Study. *J. Phys. Chem. A* **2012**, *116*, 1435-1444.
45. Chopra, D.; Row, T. N. G.: Role of Organic Fluorine in Crystal Engineering. *CrystEngComm* **2011**, *13*, 2175-2186.
46. Halper, S. R.; Cohen, S. M.: Self-assembly of Heteroleptic [Cu(dipyrrinato)(hfacac)] Complexes Directed by Fluorine-Fluorine Interactions. *Inorg. Chem.* **2005**, *44*, 4139-4141.
47. Huston, S. M.; Wang, J. Y.; Loth, M. A.; Anthony, J. E.; Conrad, B. R.; Dougherty, D. B.: Role of Fluorine Interactions in the Self-Assembly of a Functionalized Anthradithiophene Monolayer on Au(111). *J. Phys. Chem. C* **2012**, *116*, 21465-21471.

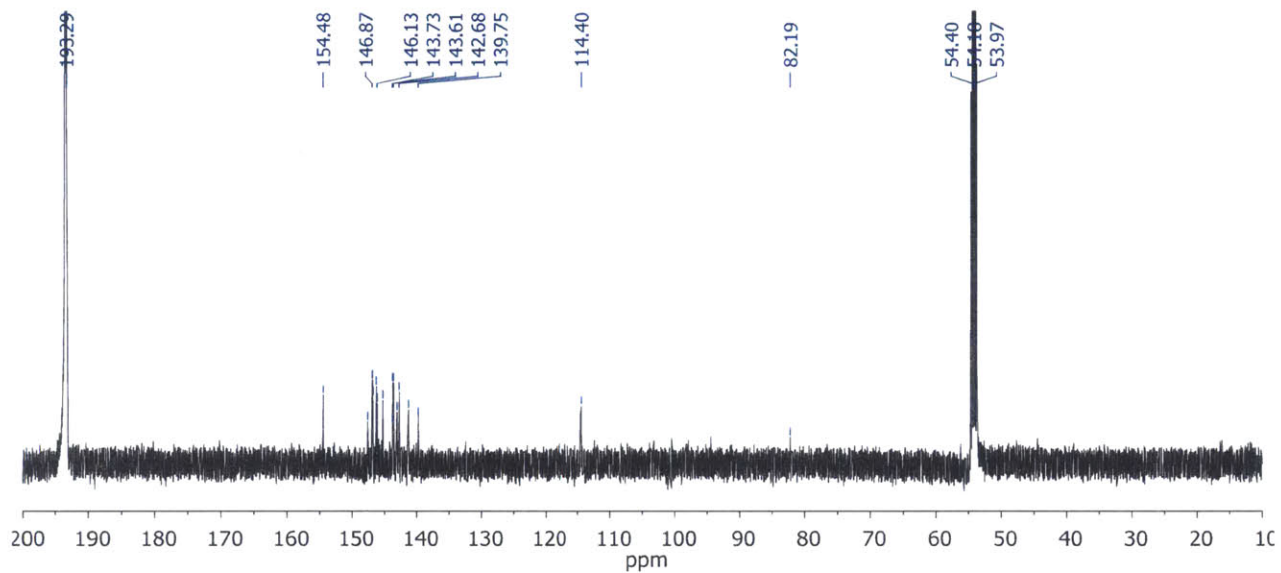
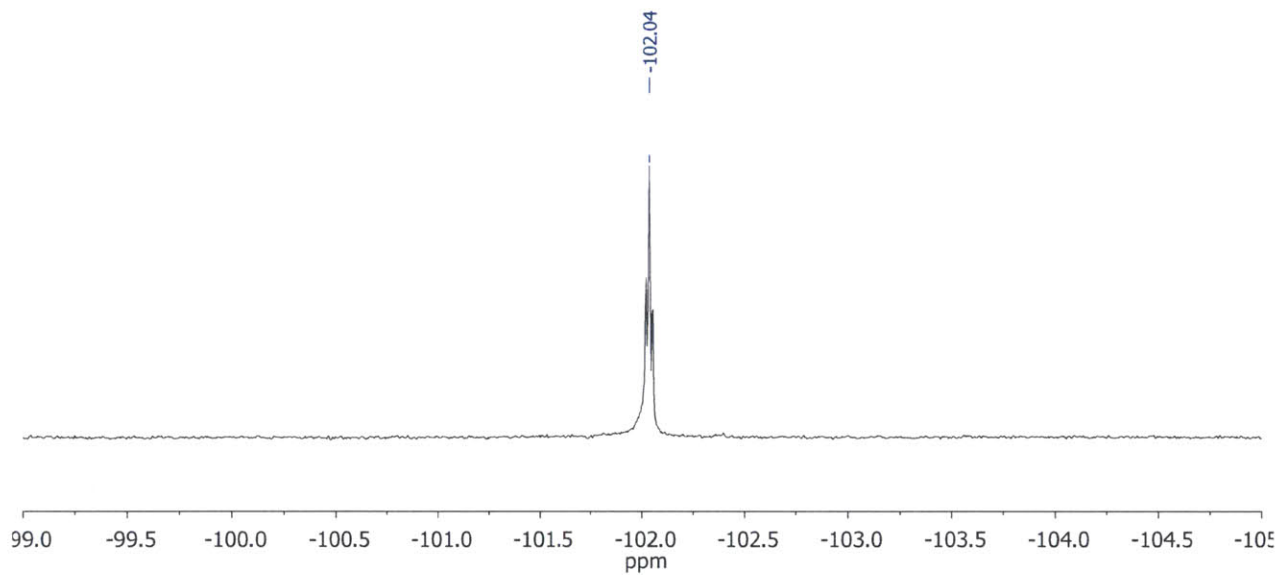
48. Gu, C.; Chen, Y. C.; Zhang, Z. B.; Xue, S. F.; Sun, S. H.; Zhong, C. M.; Zhang, H. H.; Lv, Y.; Li, F. H.; Huang, F.; Ma, Y. G.: Achieving High Efficiency of PTB7-Based Polymer Solar Cells via Integrated Optimization of Both Anode and Cathode Interlayers. *Adv. Energy. Mater.* **2014**, *4*, 1301771.
49. Hedley, G. J.; Ward, A. J.; Alekseev, A.; Howells, C. T.; Martins, E. R.; Serrano, L. A.; Cooke, G.; Ruseckas, A.; Samuel, I. D. W.: Determining the Optimum Morphology in High-performance Polymer-fullerene Organic Photovoltaic cells. *Nat. Commun.* **2013**, *4*, 2867.
50. Guerrero, A.; Montcada, N. F.; Ajuria, J.; Etxebarria, I.; Pacios, R.; Garcia-Belmonte, G.; Palomares, E.: Charge Carrier Transport and Contact Selectivity Limit the Operation of PTB7-based Organic Solar Cells of Varying Active Layer Thickness. *J. Mater. Chem. A* **2013**, *1*, 12345-12354.
51. He, Z. C.; Zhong, C. M.; Su, S. J.; Xu, M.; Wu, H. B.; Cao, Y.: Enhanced Power-conversion Efficiency in Polymer Solar Cells Using an Inverted Device Structure. *Nat. Photonics.* **2012**, *6*, 591-595.

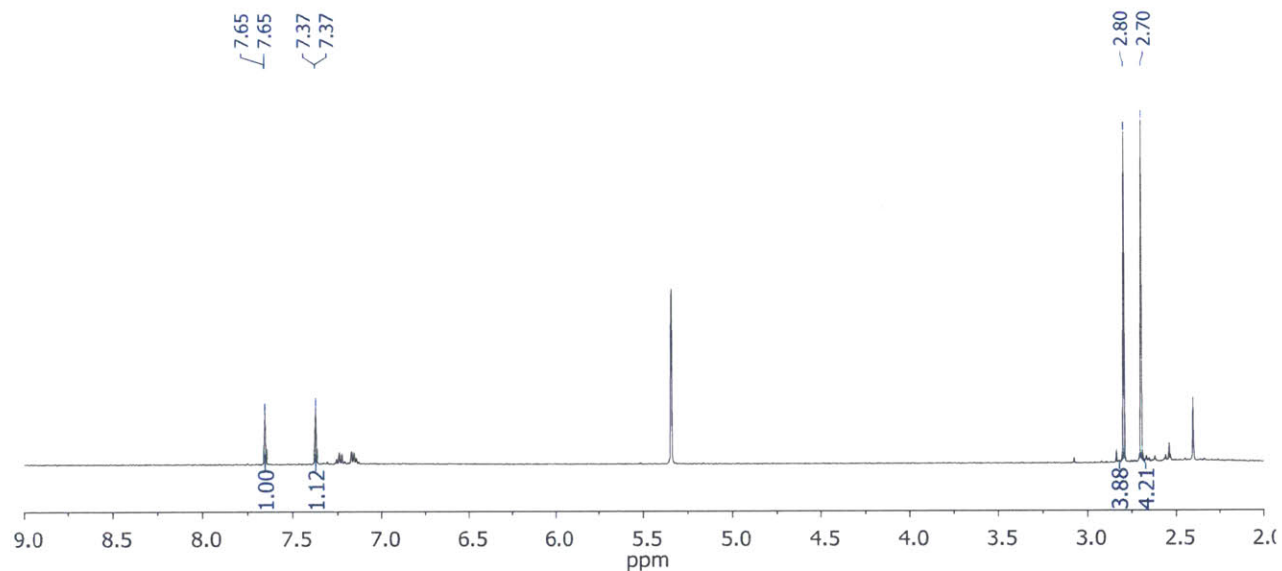
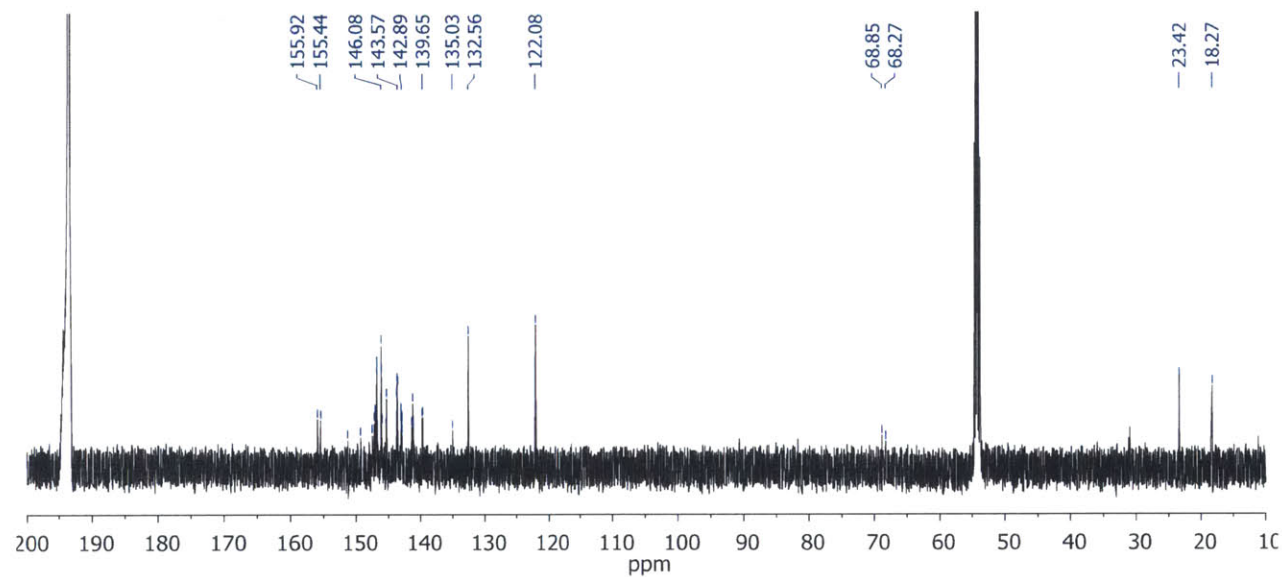
5.6. Appendix

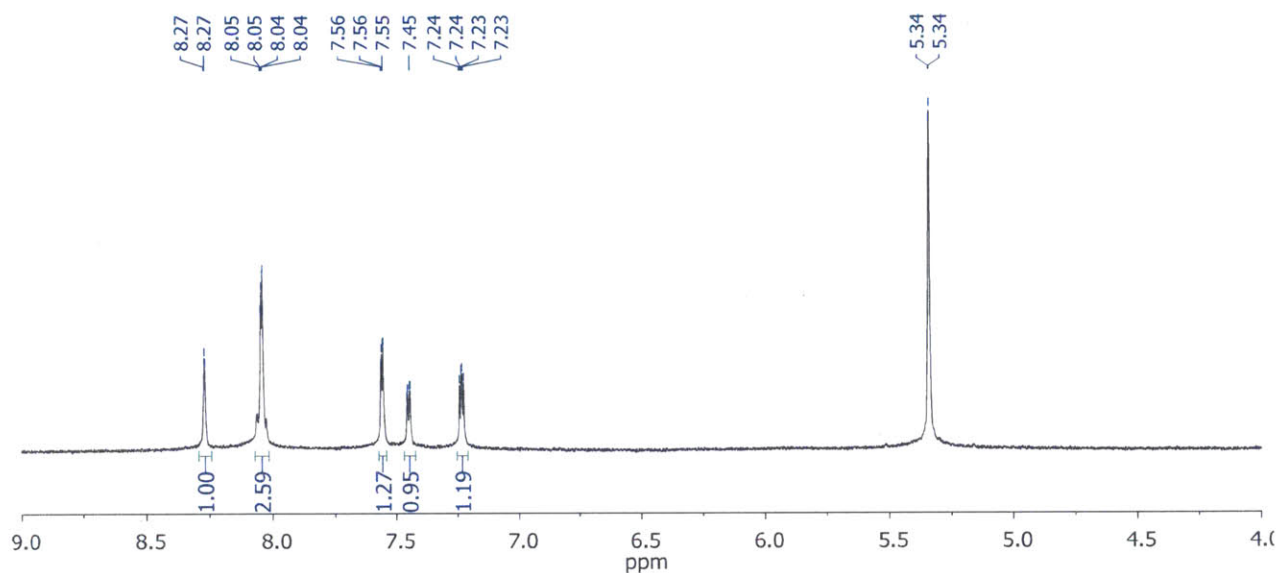
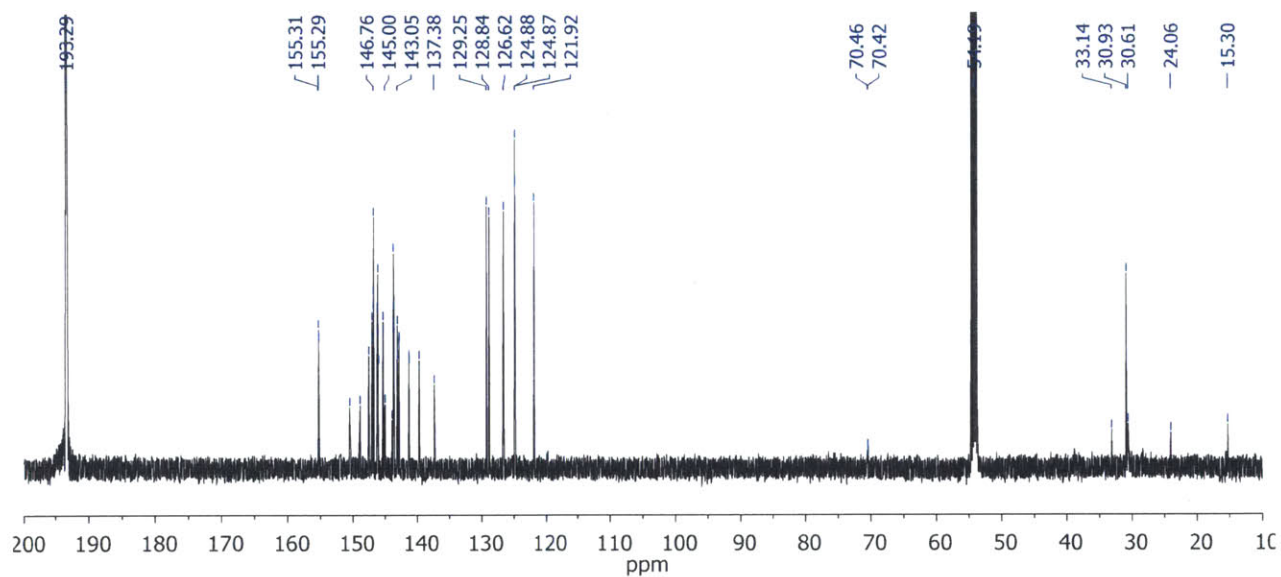
Spectrum 5.1. ^1H NMR of MeOBz- C_{60}

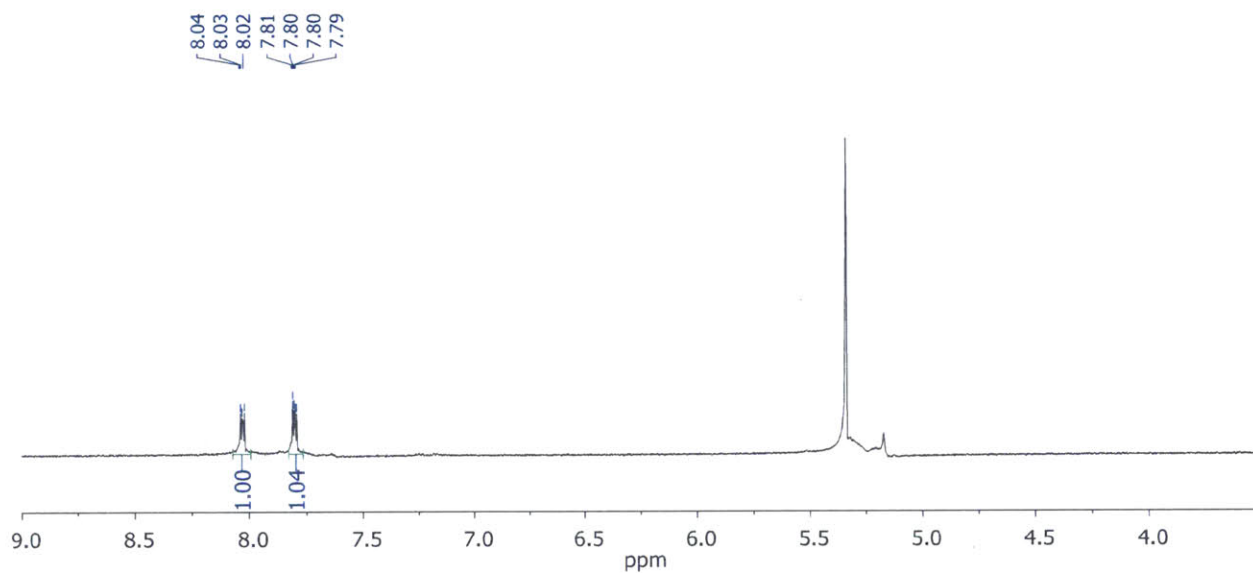
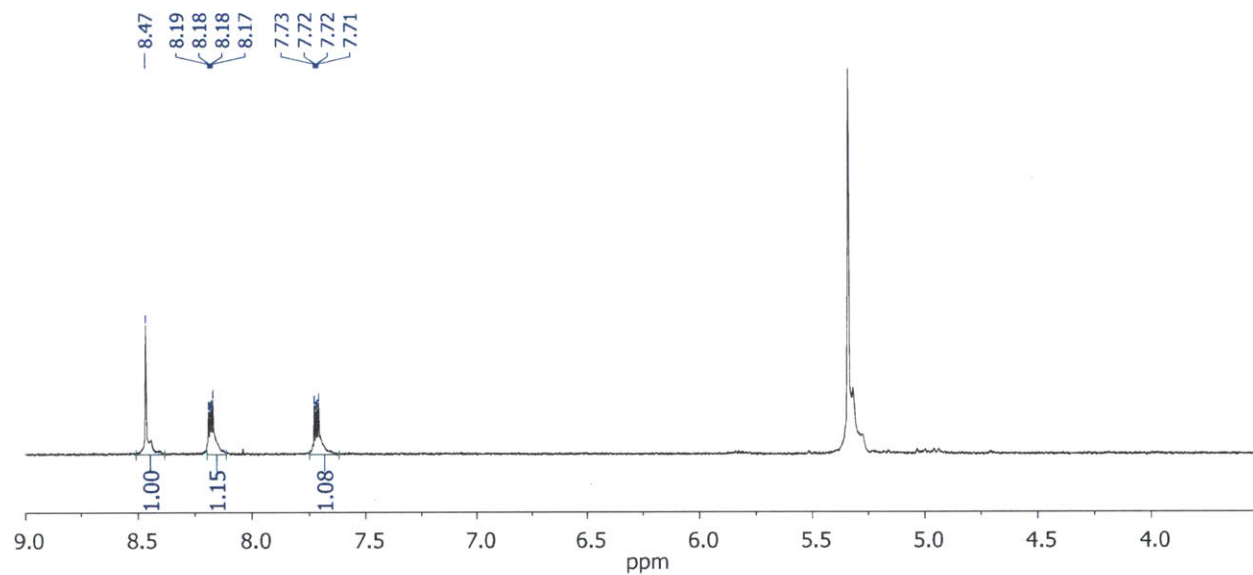


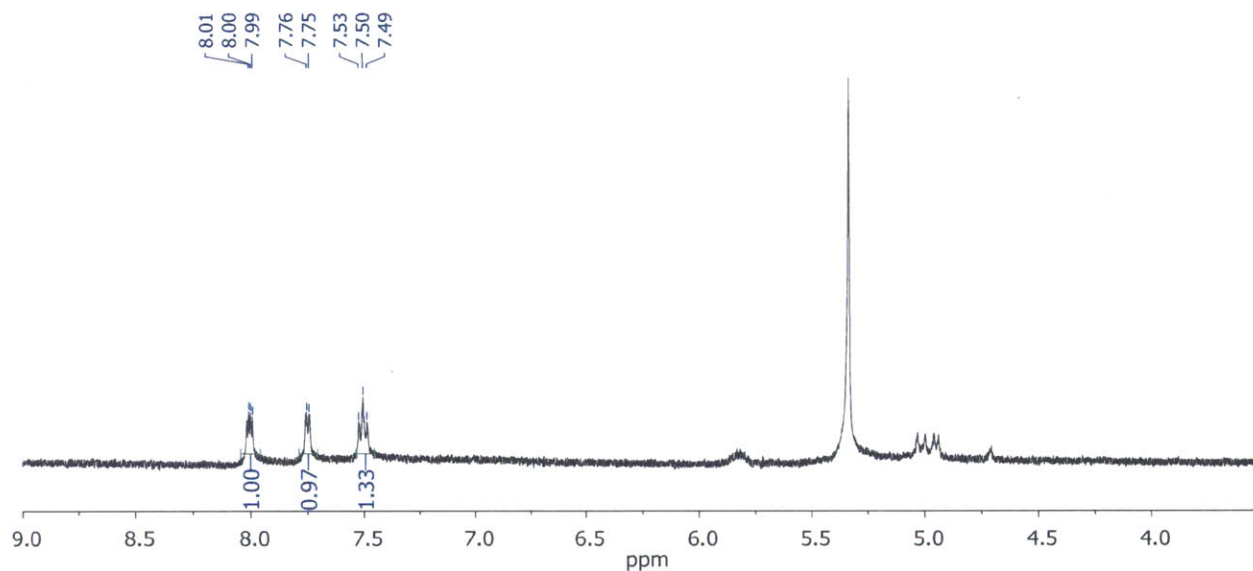
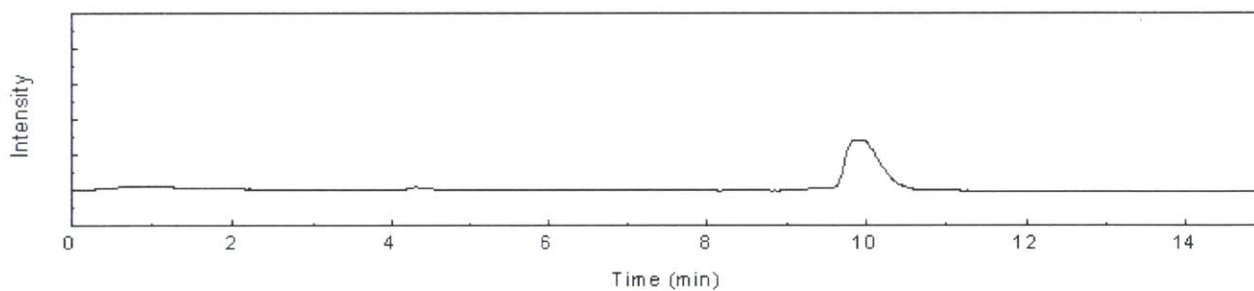
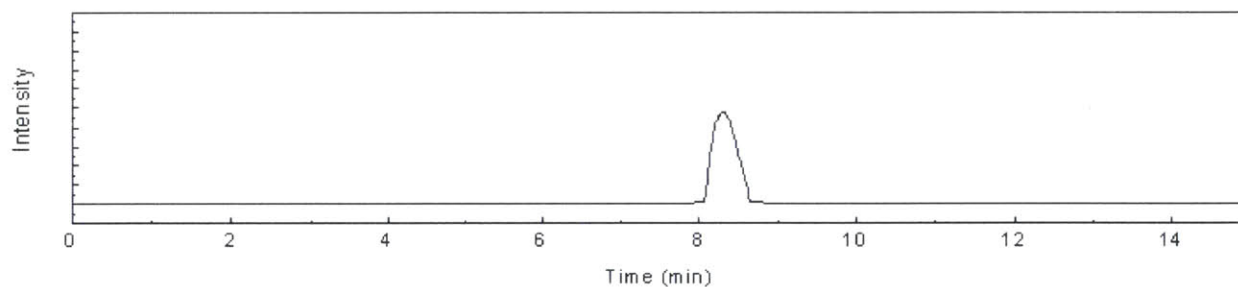
Spectrum 5.2. ¹³C NMR of MeOBz-C₆₀**Spectrum 5.3.** ¹H NMR of F₂Bz-C₆₀

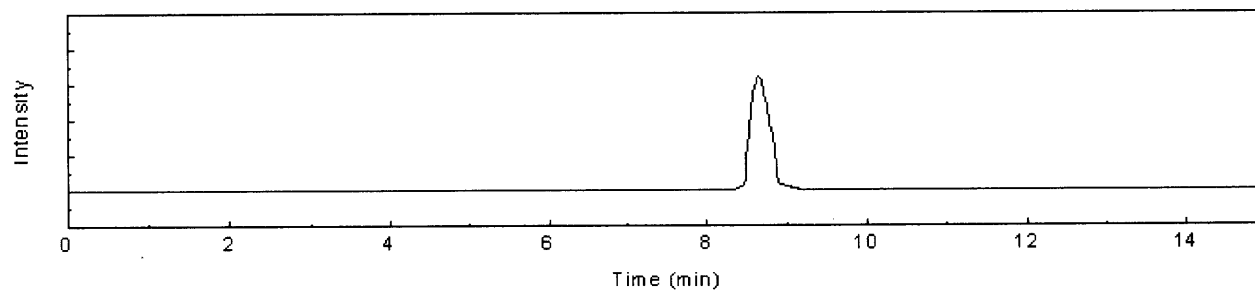
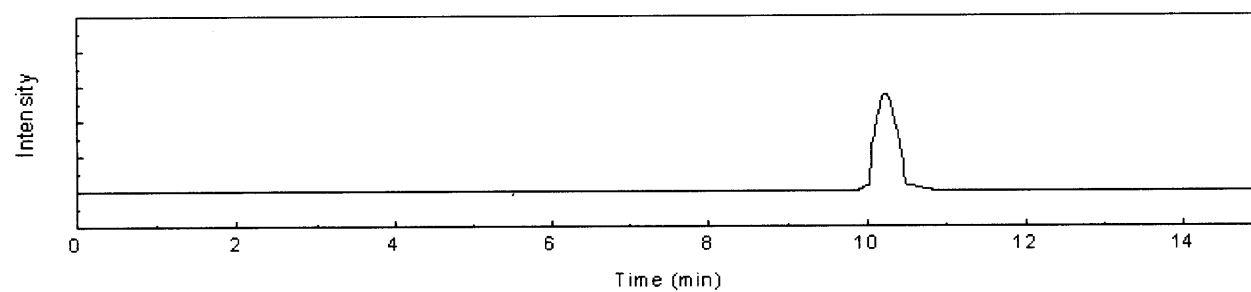
Spectrum 5.4. ^{13}C NMR of $\text{F}_2\text{Bz}-\text{C}_{60}$ **Spectrum 5.5.** ^{19}F NMR of $\text{F}_2\text{Bz}-\text{C}_{60}$ 

Spectrum 5.6. ¹H NMR of MeBz-C₆₀**Spectrum 5.7.** ¹³C NMR of MeBz-C₆₀

Spectrum 5.8. ¹H NMR of ThBz-C₆₀**Spectrum 5.9.** ¹³C NMR of ThBz-C₆₀

Spectrum 5.10. ¹H NMR of Bz-C₆₀**Spectrum 5.11.** ¹H NMR of Np-C₆₀

Spectrum 5.12. ¹H NMR of F₁Bz-C₆₀**Spectrum 5.13.** HPLC trace of MeOBz-C₆₀**Spectrum 5.14.** HPLC trace of F₂Bz-C₆₀

Spectrum 5.15. HPLC trace of MeBz- C_{60} **Spectrum 5.16.** HPLC trace of ThBz- C_{60} 

CHAPTER 6
Isoxazoline-Functionalized Nanocarbon Materials and
Their Transition Metal Complexes for
Electrocatalytic O₂ Reduction

6.1. Introduction

The polymer electrolyte membrane or proton exchange membrane (PEM) fuel cell is known for its high efficiency to produce electricity from fuels (typically hydrogen, methanol, ethanol, or formic acid) and oxidants (mostly dioxygen).¹ Two main reactions involved in the fuel cell are fuel oxidation at the anode and oxygen reduction reaction (ORR) occurring at the cathode.² Among these two, ORR is regarded as the bottleneck to achieving overall high efficiency of the cell as a result of its higher overpotential than that of hydrogen oxidation.³ To lower the overpotential, platinum catalysts are currently used as the state-of-the-art cathode materials, but the scarcity and high cost of the materials are limiting their utility and driving research efforts to replace them with non-precious metal catalysts such as cobalt or iron complexes.^{4,5} Some of the most widely explored non-precious metal ORR catalysts are cobalt macrocycles such as cobalt porphyrins or phthalocyanines, which have been studied in solution and on the surface of electrodes for homogeneous and heterogeneous catalysis.⁶⁻⁹ Nitrogen-containing polymers such as polypyrroles and polyacrylonitriles have shown ORR electrocatalysis upon binding cobalt ions in the presence of carbon supports.^{10,11} Cobalt and iron salts pyrolyzed with carbon and nitrogen sources also formed ORR catalysts, despite unclear mechanism and active site of ORR.^{12,13} From the examples of non-precious metal ORR catalysts, it is assumed that incorporation of nitrogen atoms on nanocarbon materials and their binding to metal ions (forming M–N–C units) are crucial for oxygen reduction.^{13,14} However, the lack of studies on the active site structures of these ORR catalysts remains a challenge, so the rational design of ligands and their attachment to nanocarbon materials via covalent bonding may elucidate the mechanism of the reactions and produce high-performance catalysts. Some recent reports^{14,15} describe the biomimetic iron-containing macrocycles tethered to carbon nanotubes

and their superior activity and stability as ORR electrocatalysts compared to platinum in alkaline media, emphasizing the importance of carefully designed structures and compositions of transition metal catalysts. Inspired by the recent studies and motivated to create more efficient ORR catalysts, we focused on developing covalent functionalization methods for nanocarbon materials such as fullerenes, carbon nanotubes (CNTs), and graphenes, which can be decorated with nitrogen-containing ligands to bind metals. The 1,3-dipolar cycloaddition of nitrile oxides was established as a modular functionalization route that can easily form isoxazoline derivatives on nanocarbon networks.^{16,17} In this work, we first demonstrate metal chelating ability of pyridyl or bipyridyl isoxazoline-functionalized fullerenes as a model system prior to the functionalization of carbon nanotubes. Conventional solution-state synthesis and mechanochemical (ball-mill) procedures are introduced for nanotube functionalization, and two types of metal complexes and composites are synthesized with the nanotubes containing ligand moieties. First, a direct chelation of cobalt(II) ions with a tridentate nitrogen-containing ligand is shown, then iron(II) phthalocyanine catalysts coordinated in the axial position by a pyridyl group tethered on CNTs will be presented. The relative ORR performance of the newly synthesized catalysts and that of platinum standard or their non-covalent counterparts are compared in alkaline media, and preliminary results from rotating disk electrode (RDE) and rotating ring-disk electrode (RRDE) experiments predict superior catalytic activity of the covalently-functionalized CNT–metal complexes than the physisorbed CNT/metal composites.

6.2. Results and Discussion

6.2.1. C₆₀ Ligands for Metal Chelation

Ramírez-Monroy and Swager reported transition metal chelation by fullerene derivatives incorporating various ligands as the pendant moieties.¹⁸ The isoxazolinofullerene derivatives

were synthesized by 1,3-dipolar cycloaddition of nitrile oxides generated from hydroximoyl halide precursors treated with triethylamine (Scheme 6.1). With the fullerene ligands, the authors successfully produced rhenium, platinum, and iridium complexes, opening up the potential of the fullerene derivatives to bind catalytically active transition metals (Figure 6.1).

Scheme 6.1. 1,3-dipolar cycloaddition of nitrile oxide derivatives to C₆₀.

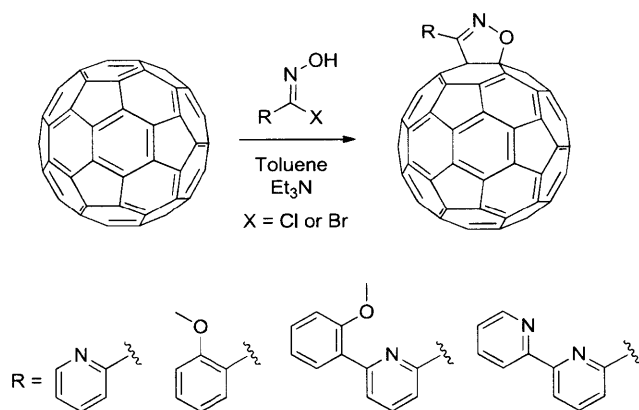
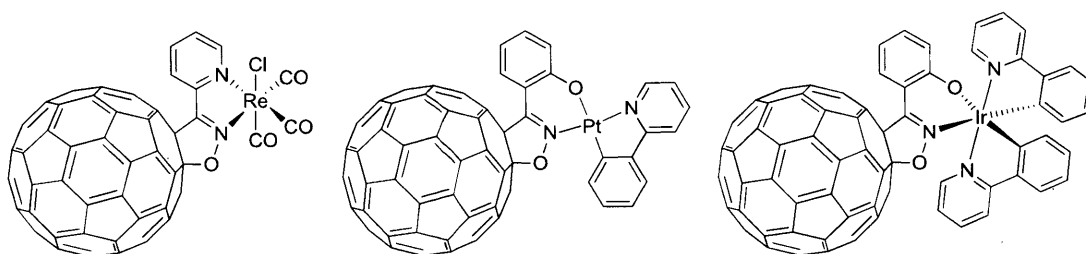
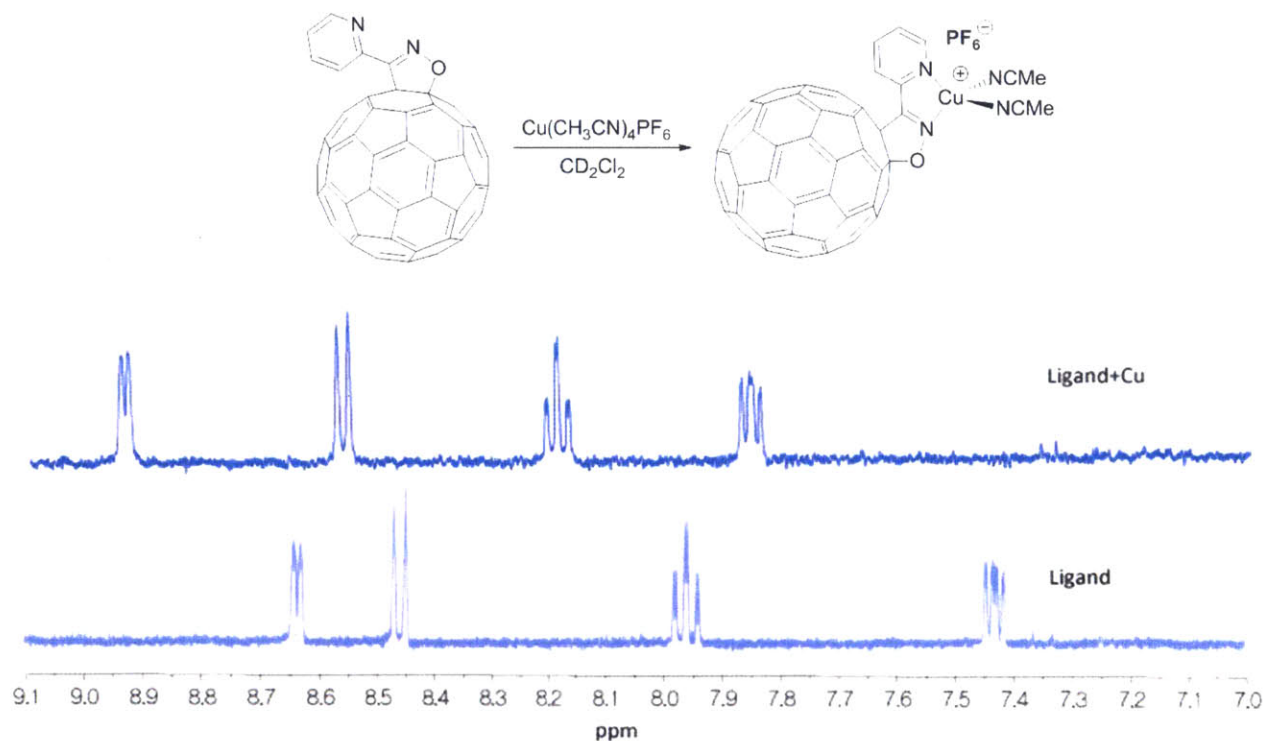


Figure 6.1. Transition-metal complexes of isoxazolinofullerene derivatives.



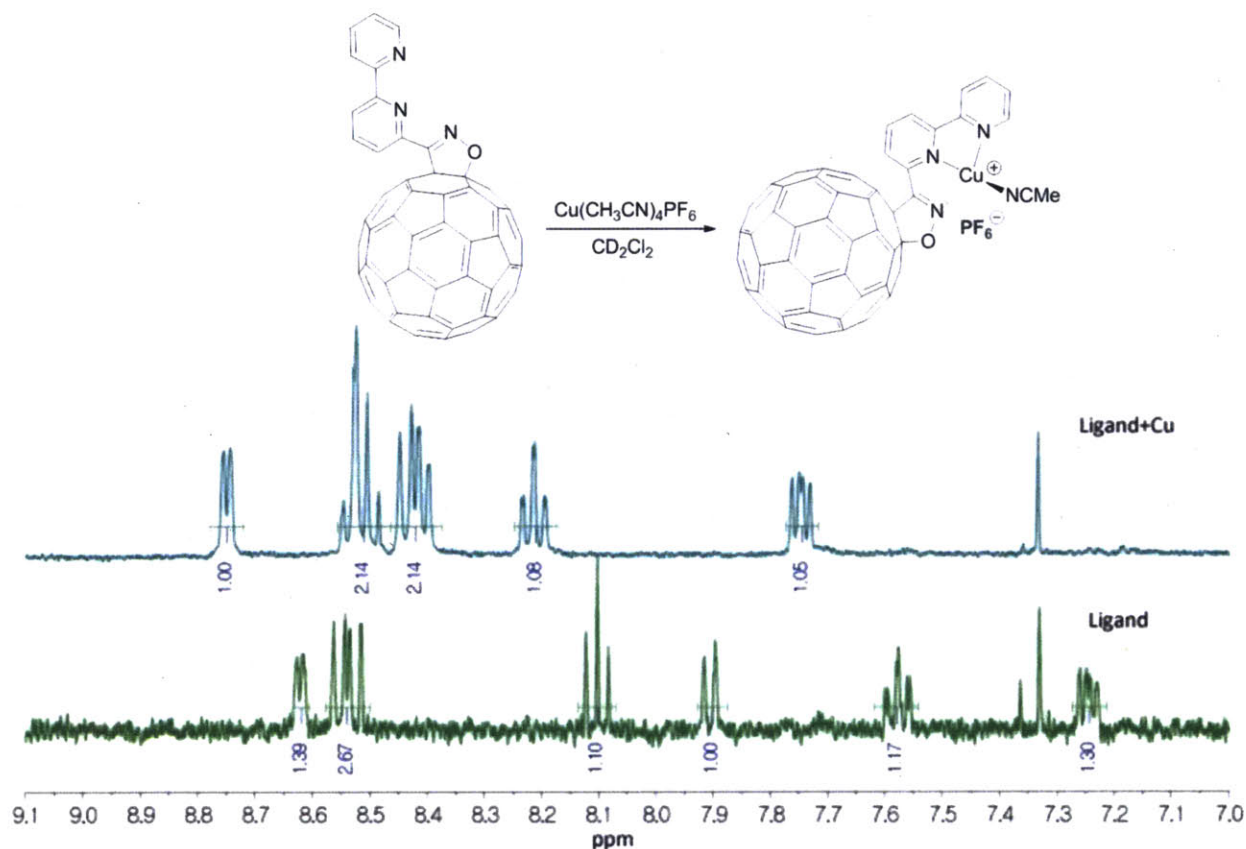
To expand the utility of the reported ligand system, other metal complexes were synthesized focusing on the nitrogen-containing ligands (pyridine and bipyridine). Scheme 6.2 shows the synthesis of a copper(I) complex with *o*-pyridyl isoxazolinofullerene and the detection of the product by ¹H NMR. The aromatic peaks on the ligand were downfield-shifted upon metal binding without broadening due to the diamagnetic nature of copper(I) complex.

Scheme 6.2. The proposed reaction and product of copper(I) complexation to *o*-pyridyl isoxazolinofullerene and the change in ^1H NMR spectra.



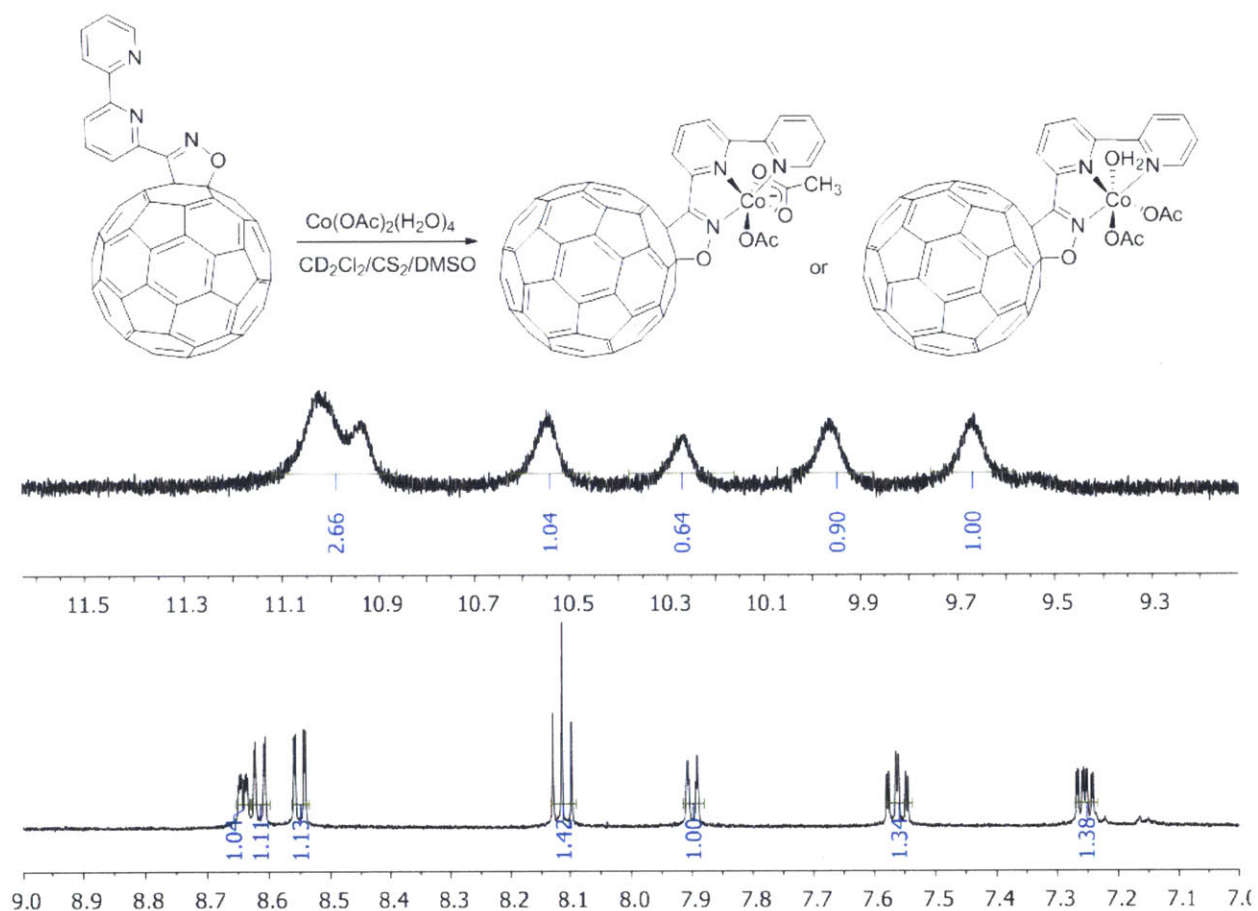
Similarly, a copper(I) complex with bipyridyl isoxazolinofullerene was synthesized, and the downfield shift of the aromatic peaks was observed by ^1H NMR spectroscopy (Scheme 6.3).

Scheme 6.3. The proposed reaction and product of copper(I) complexation to bipyridyl isoxazolinofullerene and the change in ^1H NMR spectra.



The binding of bipyridyl isoxazolinofullerene with cobalt(II) ions and the consequent formation of paramagnetic (d^7) complex was probed (Scheme 6.4). The broadening of the aromatic peaks and the significant shift of the peaks from 7.2–8.7 ppm to 9.5–11.3 ppm was observed upon the metal binding. For all experiments, the metal complexation occurred immediately upon mixing fullerenes and metal salts and was detected within 10–20 minutes.

Scheme 6.4. The proposed reaction and products of cobalt(II) complexation to bipyridyl isoxazolinofullerene and the change in ¹H NMR spectra.

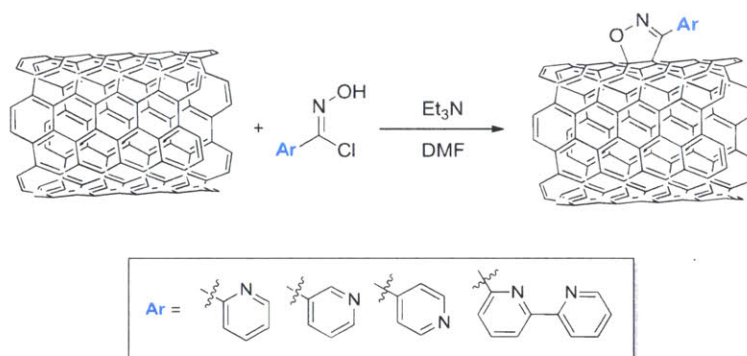


6.2.2. Carbon Nanotube Functionalization by 1,3-Dipolar Cycloaddition with Nitrile Oxides: Solution-State and Mechanochemical Syntheses

As discussed in Chapter 1, synthetic procedures of fullerene derivatives can be generally applied to carbon nanotube or graphene functionalization upon modification of reaction conditions. We targeted and synthesized four types of ligands on carbon nanotubes for potential oxygen reduction electrocatalysis application: *ortho*-, *meta*-, *para*-pyridyl, and bipyridyl moieties (Scheme 6.5). The precursor hydroximoyl chloride derivatives were synthesized following the literature procedures. Dehydrochlorination of hydroximoyl chlorides occurs upon the addition of triethylamine and generates nitrile oxides that undergo 1,3-dipolar cycloaddition with double bonds on the outer wall of carbon nanotubes. For the nanotubes, single-walled, double-walled,

and multi-walled carbon nanotubes (SWCNT, DWCNT, and MWCNT) were used and tested. From the preliminary oxygen reduction results of cobalt-complexed CNTs, we discovered that DWCNTs are the optimal platform for the application. DWCNTs have an intermediate curvature that is suitable for the covalent functionalization to occur, and it retains conductivity due to the intact inner wall despite the disrupted conjugation of the outer wall during the covalent modification. SWCNTs lose conductivity significantly upon the cycloaddition due to the broken conjugation, and MWCNTs are inherently less reactive and less conductive than SWCNTs and DWCNTs. Pristine CNTs were treated with nitric acid under refluxing conditions to remove residual metal impurities in the commercial CNT products prior to the functionalization reactions.

Scheme 6.5. The 1,3-dipolar cycloaddition of nitrile oxide derivatives to CNTs in solution.

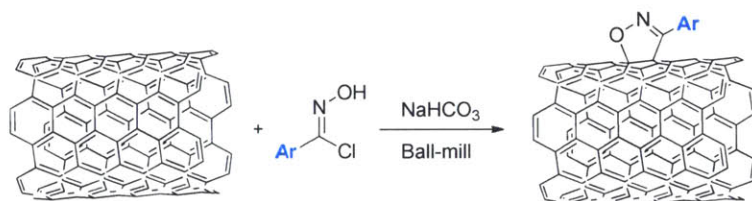


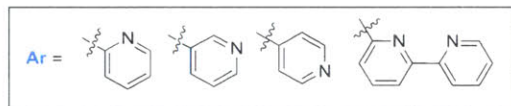
The solution-state functionalization of CNTs generally requires a large excess of reactants, high temperature conditions, and long reaction time due to the low reactivity of conjugated sp^2 network.¹⁹ In addition, the low dispersibility of nanotubes in common organic solvents, even in halogenated aromatic solvents or DMF, makes high-yield functionalization a challenge. The nitrile oxide cycloaddition reaction was also demanding since 10 equivalents of precursor were necessary to ensure high functional group density on the CNTs. The dropwise

addition of base was conducted over 6 h at 80 °C under anhydrous conditions (detailed in experimental section).

To reduce the difficulty of synthesis, we developed and optimized a mechanochemical method, a ball-mill process, and produced the identical functionalization products in comparable or higher yields. Ball-mill reactions use mechanical energy generated by the collision of steel or zirconium balls and chemicals in a reactor, which is shaken at a certain frequency.^{20,21} The advantage of the method is the solvent-free condition that is enabled by the mechanical milling and mixing of the contents by the balls.²² Since the poor dispersibility of carbon nanotubes in solution is problematic, the ball-mill reaction is a good option for making more homogeneous reaction conditions.²³ Ball-milling required shorter reaction times than solution-state syntheses, and the collection of nanotubes by scraping the solid-state reaction mixture was more convenient than the filtration or centrifugation of large volumes of CNT suspensions. We varied the types of solid base (Na_2CO_3 and NaHCO_3), the equivalent of reactant (0.5, 1.0, 1.25, and 2.5 eq per two carbon atoms), reaction time (5, 10, 15, 30, and 60 min), and frequency of ball-milling (10 Hz, 20 Hz, and 30 Hz) for the optimization of the reaction conditions. When *o*pyridyl hydroximoyl chloride was used as the test reagent, the best result (the highest functional group density on CNTs) was obtained with NaHCO_3 and 1.25 eq of reactant, ball-milled at 30 Hz for 30 min.

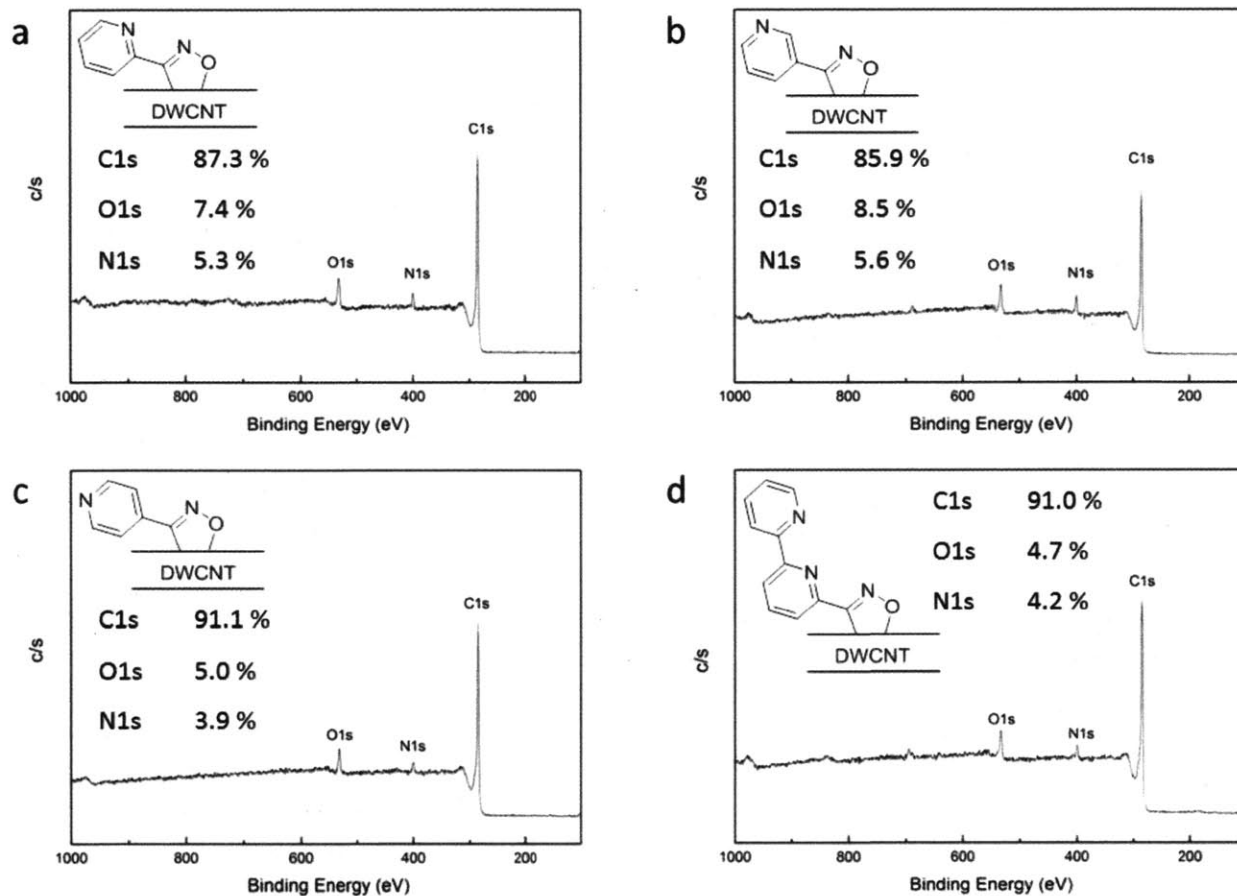
Scheme 6.6. Mechanochemical cycloaddition of nitrile oxide derivatives to carbon nanotubes.





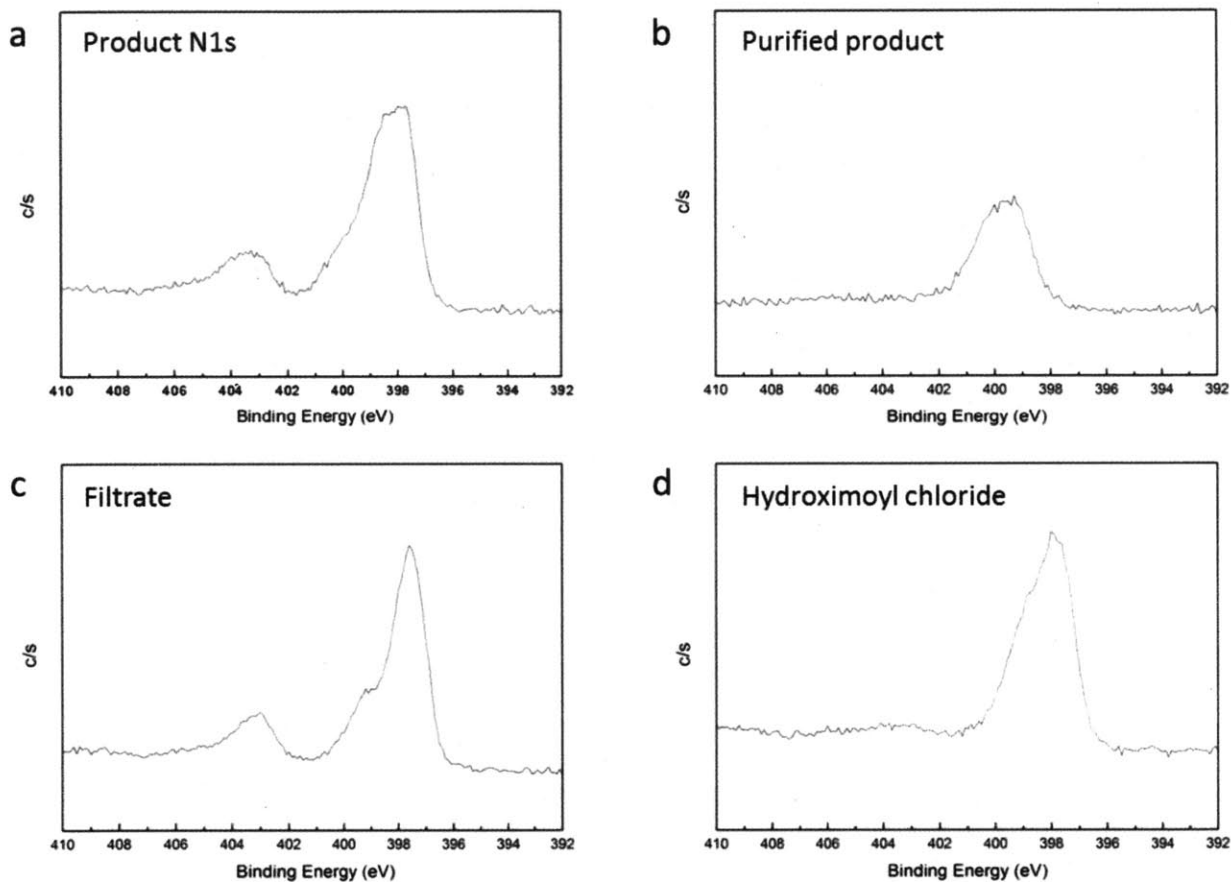
X-ray photoelectron spectroscopy (XPS) is a primary method for the characterization of the elemental contents in carbon nanotube chemistry. The presence of certain elements can determine the success of functionalization, and the atomic ratio of the marker elements to carbon can be used to calculate the functional group density on CNTs. Figure 6.2 describes XPS survey scans (0–1100 eV) of four optimized samples with different ligand moieties. C1s, N1s, and O1s peaks are observed within the range, and small peaks at around 690 eV are occasionally detected due to the impurity from the PTFE membranes used for the filtration of nanotube mixtures during the multi-step purification procedures. According to the atomic ratio of nitrogen to carbon shown in Figure 6.2, the functional group density of isoxazoline moiety is calculated for each sample: 1 *o*-pyridyl isoxazoline per 33 carbon atoms, 1 *m*-pyridyl isoxazoline per 31 carbon atoms, 1 *p*-pyridyl isoxazoline per 47 carbon atoms, and 1 bipyridyl isoxazoline per 65 carbon atoms. Given two-layer walls, the densities of the pyridyl groups are regarded to be in the high end.

Figure 6.2. XPS survey scans of the optimized products with (a) *o*-pyridyl, (b) *m*-pyridyl, (c) *p*-pyridyl, and (d) bipyridyl functional groups.



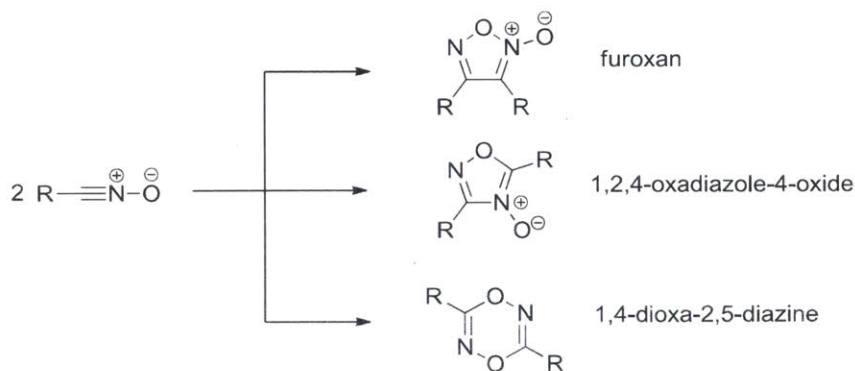
The nitrogen content in the CNT samples varies significantly depending on the extent of purification. For example, Figure 6.3 (a) shows the high-resolution N1s spectrum of a sample which was thoroughly washed with ethanol/water, acetone/water, ethyl acetate, dichloromethane, and hexane during the filtration process. The higher energy nitrogen peak (403 eV) is present due to the physisorbed impurity that is not removed by the washing process. When the CNT samples were sonicated and centrifuged multiple times in addition to the filtration and rinsing, the impurity peak disappears as shown in Figure 6.3 (b). The high energy peak was also detected in the dried filtrate sample (c) but not in the hydroximoyl chloride reagent (d), suggesting the formation of byproducts containing more electron-deficient nitrogen atoms.

Figure 6.3. High-resolution XPS spectra of N1s in (a) the product after one-step filtration and thorough washing, (b) after additional purification steps, (c) byproducts in filtrate, and (d) hydroximoyl chloride reagent.



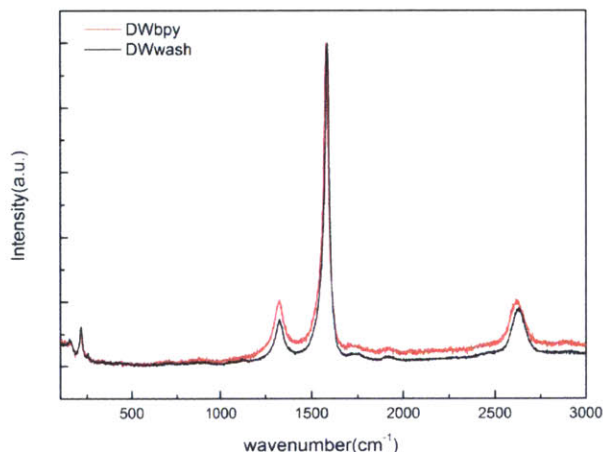
The byproducts were not isolated from the reaction mixtures, but the dimers of nitrile oxide are proposed to form the potential byproducts with electron-deficient nitrogen atoms (Scheme 6.7).²⁴ Due to the identical mass and similar ^1H NMR spectra, the dimers are difficult to distinguish.

Scheme 6.7. Mechanisms of byproduct formation from nitrile oxide intermediates.



Raman spectroscopy is an additional characterization method to measure the density of defects on carbon nanotubes, which can be correlated to the covalent functional group density of the sample.^{25,26} Lasers with wavelengths of 633 and 785 nm were used for measurements, and regardless of the wavelength, the D band to G band ratio increased with the functionalized CNTs compared to the acid-washed pristine CNTs. Figure 6.4 shows an example Raman spectrum of DWCNTs functionalized with bipyridyl isoxazoline moieties. When the G bands at around 1600 cm^{-1} are normalized, the intensities of D bands are compared. The higher D band of the functionalized sample compared to the acid-washed CNTs indicates the increased functional group density on the CNTs, consistent with the XPS results.

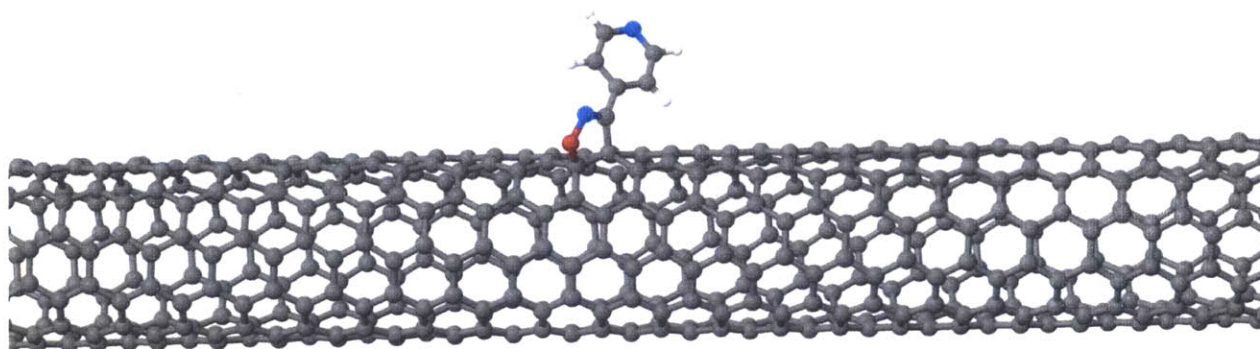
Figure 6.4. Raman spectra of covalently functionalized (red) and acid-washed (black) DWCNTs.



6.2.3. Computation of Isomeric Pyridyl Isoxazoline Structures on CNTs

Density functional theory (DFT) calculations were used to estimate the relative configuration of *ortho*-, *meta*-, and *para*-pyridyl isoxazoline moieties on CNTs. For the simplicity of calculation, a SWCNT with a (6,5) chirality was selected as a platform, and the optimized structures of the functionalized CNTs were calculated. Figure 6.5 shows a part of *para*-pyridyl isoxazoline-functionalized (6,5)-SWCNT around the pendant moiety. Two other isomeric structures were calculated under identical conditions (see experimental section).

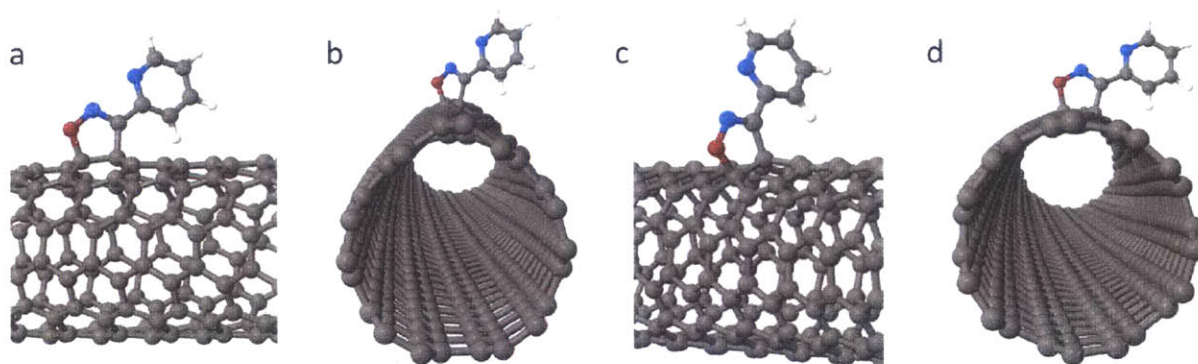
Figure 6.5. A representative view of the calculated structures of *p*-pyridyl isoxazoline-functionalized (6,5)-SWCNT.



There are two types of double bonds in the (6,5)-SWCNT that can be functionalized by 1,3-dipolar cycloaddition; one is diagonal, and the other is perpendicular to the long axis of CNT. As the addition reaction can take place on the both types of bonds, two structures were calculated as seen in Figure 6.6–6.8 for *ortho*-, *meta*-, and *para*-pyridyl isoxazoline substituents. In most cases, considerable torsional angles between two pendant rings were observed, except for the *ortho*-isomer attached diagonally to the CNT long axis (Figure 6.6 (a, b)). The *ortho*-isomer maintains the most planar geometry among the series, enabling the chelation of metal ions as tested on the fullerene derivatives. The bipyridyl isoxazoline group, which has an additional

pyridine ring on the 6-position of the *o*-pyridyl group, would make a relatively planar tridentate ligand on CNTs as observed with fullerene models (Scheme 6.3 and 6.4).

Figure 6.6. Calculated structures of *o*-pyridyl isoxazoline-functionalized (6,5)-SWCNT. Top-view and side-view of (a, b) diagonally attached and (c, d) perpendicularly attached *o*-pyridyl isoxazoline ring with respect to the long axis of the CNT. The torsional angle between the pyridine and the isoxazoline ring is 1.4° (a, b) and 12.4° (c, d).



The *meta*- and *para*-isomers in Figure 6.7 and 6.8 do not act as chelates, but the nitrogen atoms of the pyridyl groups are pointing toward the outer environment. Therefore, the coordination of the pyridine ligand to transition metal macrocycles with known catalytic activities is realized.

Figure 6.7. Calculated structures of *m*-pyridyl isoxazoline-functionalized (6,5)-SWCNT. Top-view and side-view of (a, b) diagonally attached and (c, d) perpendicularly attached *m*-pyridyl isoxazoline ring with respect to the long axis of the CNT. The torsional angle between the pyridine and the isoxazoline ring is 21.7° (a, b) and 18.5° (c, d).

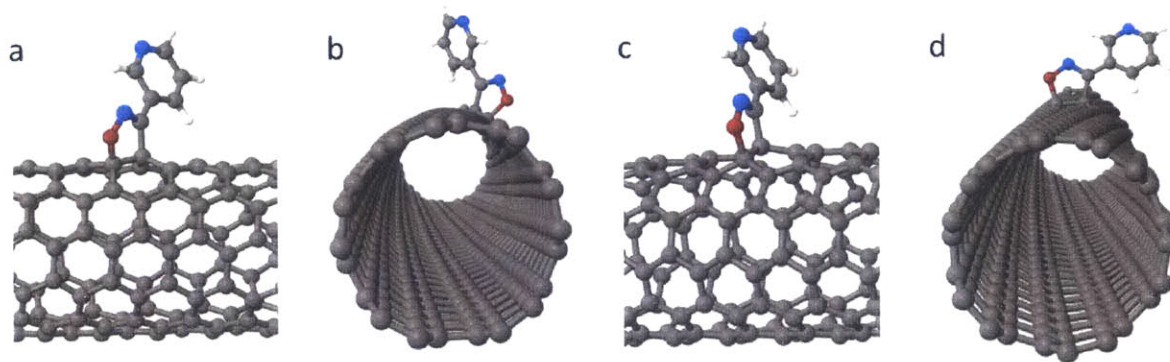
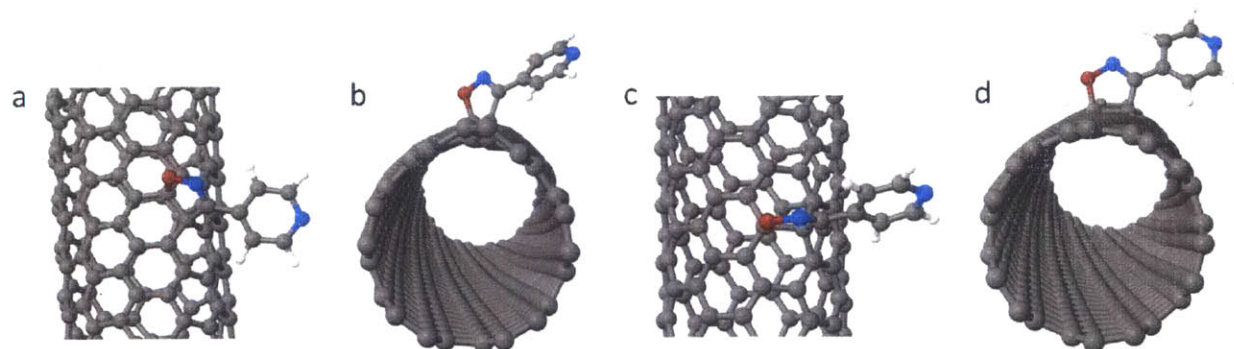


Figure 6.8. Calculated structures of *p*-pyridyl isoxazoline-functionalized (6,5)-SWCNT. Top-view and side-view of (a, b) diagonally attached and (c, d) perpendicularly attached *p*-pyridyl isoxazoline ring with respect to the long axis of the CNT. The torsional angle between the pyridine and the isoxazoline ring is 33.6° (a, b) and 18.8° (c, d).



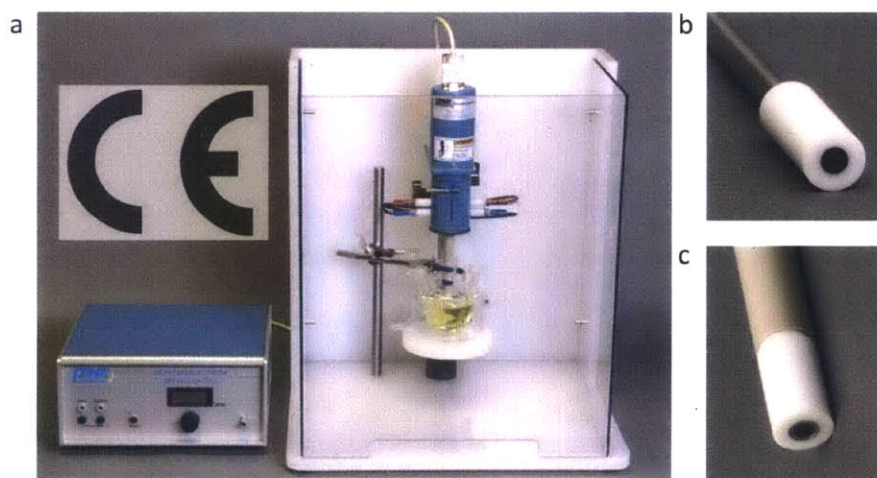
6.2.4. Metal Complexation and Electrocatalytic Performances

6.2.4.1. Chelation of Cobalt Ion with Tridentate Ligand

The first type of oxygen reduction catalyst we designed was the cobalt complex with bipyridyl isoxazoline-functionalized DWCNT, since cobalt(II) ions bound to nitrogen-containing ligands on nanocarbon supports (making M–N–C units) are known for oxygen reduction electrocatalysis in the literature, despite the lack of understanding of the exact active site and the catalytic mechanism. We used the bipyridyl-functionalized nanotubes (DWbpy) as the ligand to increase the potential to bind metal ions, and we used cobalt(II) acetate, chloride, tetrafluoroborate, or perchlorate as the metal source (synthesis detailed in experimental section).

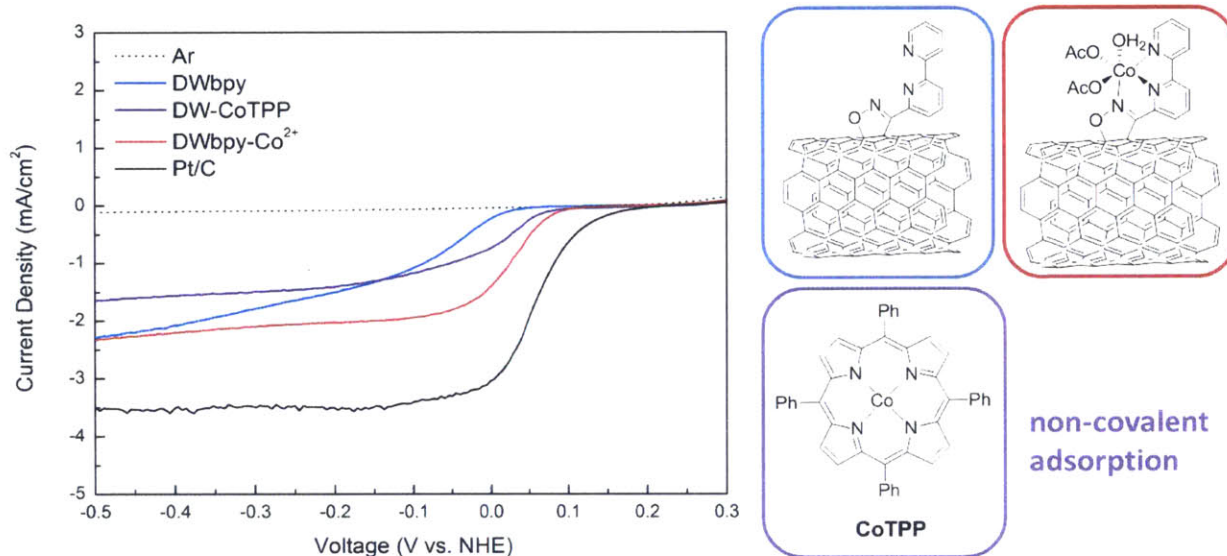
The cobalt complex did not form quantitatively as measured by XPS; the cobalt contents (measured by Co2p atomic ratio) in DWbpy–Co²⁺ catalyst were detected to be 0.5 % on average (approximately 2.5 wt %), which indicates incomplete binding of cobalt ions to the ligands. For the control experiment, cobalt(II) macrocycles (cobalt tetraphenylporphyrin, CoTPP) were physisorbed on unfunctionalized DWCNTs in 1% cobalt-to-carbon atomic ratio (DW–CoTPP). The electrocatalytic activities of nanotube samples were measured and compared using rotating disk electrode (RDE) and rotating ring-disk electrode (RRDE) techniques to prevent the diffusion-limited control of steady-state current (Figure 6.9). The nanotube samples in powder (DWbpy, DWbpy–Co²⁺, DW–CoTPP) and Pt/C standard (20 wt% Pt nanoparticles on carbon) were dispersed in aqueous isopropanol solution containing 0.5 wt% Nafion to make a catalyst ink in a concentration of 4 mg/mL. The ink was then deposited onto the surface of a polished glassy carbon (GC) disk electrode and dried under nitrogen gas flow to make uniform films (detailed in experimental section).

Figure 6.9. (a) Rotating electrode setup: a rotor with electrical connectors to working electrodes, a rotating shaft, a reaction flask, and a speed controller, (b) a GC rotating disk electrode, and (c) a rotating ring-disk electrode with a platinum ring and a GC disk.



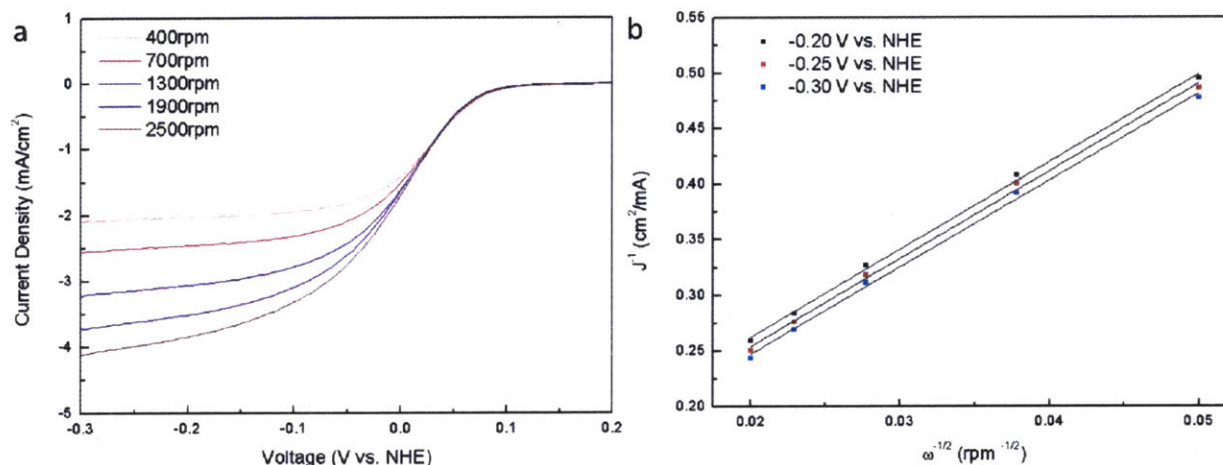
The ORR electrocatalytic activity of each sample was measured in 0.1 M KOH solution saturated with oxygen gas at a constant rotating speed. The linear sweep voltammetry (LSV) from 0.1 V to -0.8 V with reference to Ag/AgCl (1 M KCl) electrode or Hg/HgO (1 M NaOH) was performed with a scan rate of 10 mV/s, and the potential range was converted to NHE (normal hydrogen electrode) scale prior to data plotting. The background activity of all samples measured in argon-saturated solution was negligible as shown in Figure 6.10. The electrocatalytic activity of each catalyst at a rotating speed of 400 rpm is also exhibited in Figure 6.10. The bipyridyl-functionalized carbon nanotubes (DWbpy) showed high overpotential for oxygen reduction (about 150 mV higher than that of Pt/C), as marked with a blue line. The cobalt-complexed bipyridyl-functionalized nanotubes (DWbpy–Co²⁺) (red curve) possess lower overpotential than DWbpy by 60–70 mV. Although the catalyst is still less efficient than Pt/C with a 80–90 mV higher overpotential, the metal content in our sample (2.5 wt%) is significantly lower than 20 wt% platinum in carbon, which can contribute to lowering the cost of catalyst for large-scale applications. The purple curve represents the performance of the non-covalently functionalized carbon nanotubes with CoTPP. The physical adsorption of CoTPP onto DWCNTs leads to a considerably reduced current density for ORR, which may result from the less efficient electron transfer between the nanotubes and the catalytic active sites.

Figure 6.10. Linear sweep voltammograms of oxygen reduction electrocatalysis measured at a constant rotation speed of 400 rpm.



For the kinetic study of ORR activity, the linear sweep voltammetry was conducted at different rotation speeds (400, 700, 1300, 1900, and 2500 rpm) as plotted in Figure 6.11 (a) for DWbpy–Co²⁺. Applying the Koutecky–Levich (K–L) equation (Eq. 1), a K–L plot is obtained as shown in Figure 6.11 (b), and the number of electrons (n) participating in oxygen reduction can be derived from the slope of K–L plot (Eq. 2).²⁷ From the analysis, we obtained n of 3.6 for DWbpy–Co²⁺; the pronounced 4 e[−] selectivity over 2 e[−] pathway represents the preferred reduction of oxygen to water rather than to detrimental peroxide species by DWbpy–Co²⁺. The linear K–L plots and the parallel fitting lines indicate 1st-order reaction kinetics toward the oxygen concentration in solution.²⁸

Figure 6.11. (a) Linear sweep voltammograms of oxygen reduction electrocatalysis measured at various rotation speeds and (b) a K–L plot for DWbpy–Co²⁺.



$$I_{\text{lim}} = 0.2nFD^{2/3}v^{-1/6}C_0\omega^{1/2} \quad (\text{Eq. 1})$$

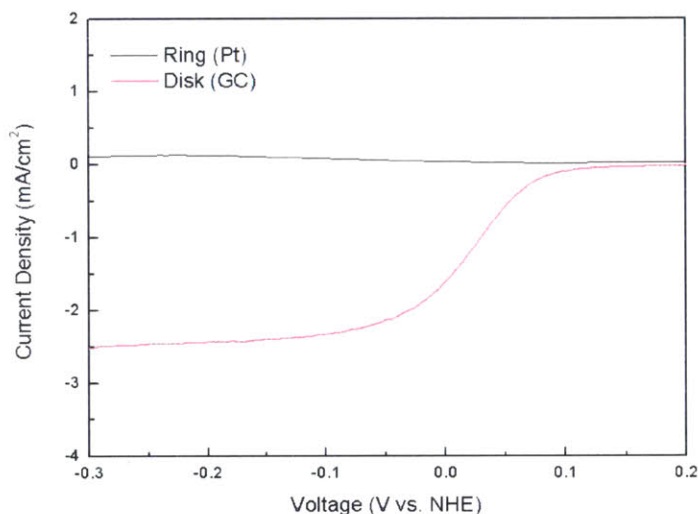
$$2B^{-1} = 0.2nFD^{2/3}v^{-1/6}C_0 \quad (\text{Eq. 2})$$

$[I_{\text{lim}}]$ diffusion-limiting current density; $[n]$ number of electrons transferred per reagent; $[F]$ Faraday constant (96485 C/mol); $[D]$ diffusion constant of O_2 in 0.1 M KOH ($1.9 \times 10^{-5} \text{ cm}^2/\text{s}$); $[v]$ kinetic viscosity of electrolyte ($1.1 \times 10^{-2} \text{ cm}^2/\text{s}$); $[C_0]$ concentration of O_2 in 0.1 M KOH ($1.2 \times 10^{-6} \text{ mol}/\text{cm}^3$)²⁹; $[\omega]$ angular rotation speed (rpm); $[B]$ Slope of K–L plot

In addition, a RRDE experiment was conducted to measure the relative production of peroxide species (HO_2^-) to water from ORR.³⁰ Catalyst ink was deposited onto the GC disk electrode surrounded by a platinum ring electrode. The potential range where the platinum electrode oxidizes peroxide species was 0.2–0.5 V vs. Ag/AgCl with a peak at 0.39 V as measured by cyclic voltammetry in 0.1 M KOH. Thus the ring potential was fixed at 0.39 V during the voltage sweep from 0.1 V to –0.8 V applied on GC working electrode for RRDE experiment. Figure 6.12 displays linear sweep voltammograms obtained from the disk and ring electrodes during ORR by the DWbpy– Co^{2+} catalyst, where the oxygen reduction disk-current is significantly higher than the peroxide oxidation ring-current. Using Eq. 3, the relative production of peroxide species to water was calculated to be 21.5 % by DWbpy– Co^{2+} . The number of electrons involved in ORR was obtained according to Eq. 4, and the result (n of 3.6) was

consistent with the previously obtained n from RDE experiment.³⁰ The numbers for other systems obtained from the identical procedure were 3.2 for DWbpy and DW–CoTPP and 4.0 for Pt/C, which implies increased 2 e[−] reduction characteristics for DWbpy and DW–CoTPP and a complete 4 e[−] reduction of oxygen to water by Pt/C.

Figure 6.12. Linear sweep voltammograms of disk-current (red) and ring-current (black) for oxygen reduction electrocatalysis measured at a constant rotation speed of 400 rpm.



$$\% \text{H}_2\text{O}_2 = 200 \times \frac{I_{\text{R}}/N}{I_{\text{D}} + I_{\text{R}}/N} \quad (\text{Eq. 3})$$

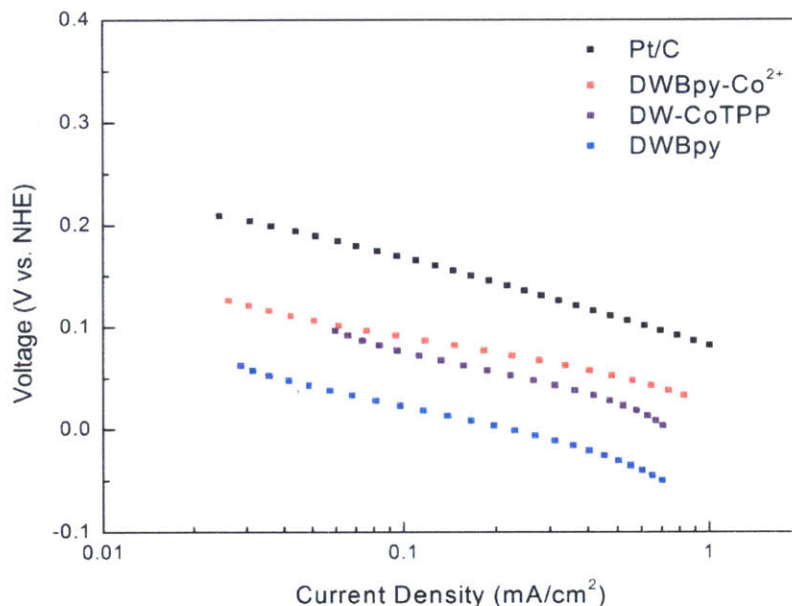
$$n = 4 \times \frac{I_{\text{D}}}{I_{\text{D}} + I_{\text{R}}/N} \quad (\text{Eq. 4})$$

$[I_{\text{R}}]$ ring current; $[I_{\text{D}}]$ disk current; $[N]$ number of electrons per O₂ reduction

The overpotential of each catalyst was more systematically compared in a Tafel plot (Figure 6.13). At a considerable current density close to 1 mA/cm², DWbpy–Co²⁺ shows lower overpotential than that of DW–CoTPP. The Tafel slope of the DWbpy–Co²⁺ catalyst is also slightly smaller than that of DW–CoTPP, which demonstrates superior electrocatalytic activity of the covalently-modified CNTs than that of non-covalent system. In summary, the higher current density, lower overpotential, and higher 4 e[−] selectivity of ORR with the covalent system

compared to its non-covalent counterpart suggest that electron transfer is more facile from the CNT network to the cobalt active sites that are covalently tethered than between CNTs and physisorbed cobalt macrocycles.

Figure 6.13. A Tafel plot of oxygen reduction electrocatalysis measured at a constant rotation speed of 400 rpm.



6.2.4.2. Axial Coordination of Pyridyl Ligand to Iron Macrocycle

Although the chelation mode of the tridentate ligand proved to be efficient, the cobalt complexes possess inherently high overpotential for ORR, which is a limitation to achieving catalysts that outperform the platinum standard.³¹ Alternative candidates for non-precious metal catalysis of ORR are iron(II/III) macrocycles, which have been known for their considerable ORR activities when supported by carbon materials.³² Recent studies have focused on the bio-inspired strategies to enhance the ORR activity of iron porphyrins or phthalocyanines via the axial coordination of nitrogen-containing heteroaromatic ligands to iron centers.^{14,15} Both SWCNTs and MWCNTs have been used for covalent functionalization to incorporate pyridine or imidazole pendants, accomplishing comparable or superior oxygen reduction efficiencies to that

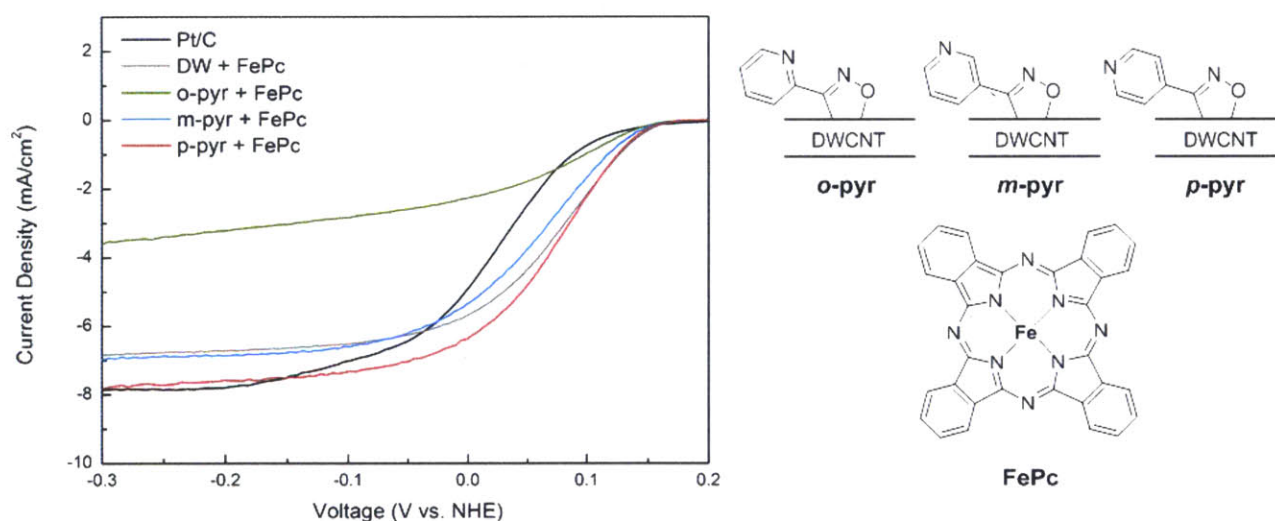
of the Pt/C standard. Despite the promising results of the covalently bound ligand–CNT systems, however, more non-covalent functionalization (physisorption) methods are reported in the literature,³³⁻³⁶ potentially due to the difficulty with the covalent grafting of CNTs.

The mechanochemical functionalization procedures that we developed and optimized with 1,3-dipolar cycloaddition reactions are simple, modular, and effective methods that can alleviate these difficulties. The isomeric structures of pyridyl isoxazoline moieties on CNTs (previously shown in Figure 6.6–6.8) were compared in terms of their ability to coordinate to the macrocycles and to enhance the ORR catalysis compared to that of non-covalent system. The catalysts were prepared by mixing iron phthalocyanine (FePc) with the functionalized CNTs (1:2 ratio by weight), and CNT ink was made following the identical procedure used for cobalt–CNT catalysts (experimental section). The mixture of FePc and DWCNTs was particularly well-dispersed in aqueous isopropanol solutions, making homogeneous films deposited on the working electrode, which is attributed to the significant π -interaction between CNT surface and the macrocycles. Less homogeneous films and solutions were obtained with SWCNT derivatives, which have less effective π -interaction with FePc due to the size mismatch; SWCNTs have a diameter of 0.7–0.9 nm, which is smaller than that of FePc (1.3 nm),³⁷ while DWCNTs are about 5 nm in diameter, which is wide enough to interact with the macrocycle.

The ORR electrocatalytic activity of FePc/CNT complexes were measured under conditions identical to those used for cobalt catalysts (in 0.1 M KOH solution saturated with oxygen). Figure 6.14 shows the performance of isomeric pyridyl-functionalized DWCNTs and the control sample (DW, unfunctionalized DWCNT/FePc composite) relative to Pt/C standard. The overpotentials of all FePc catalysts were lower than that of Pt/C, as similarly reported in the literature. The limiting current density of Pt/C and that of *p*-pyridyl isomer were similar, from

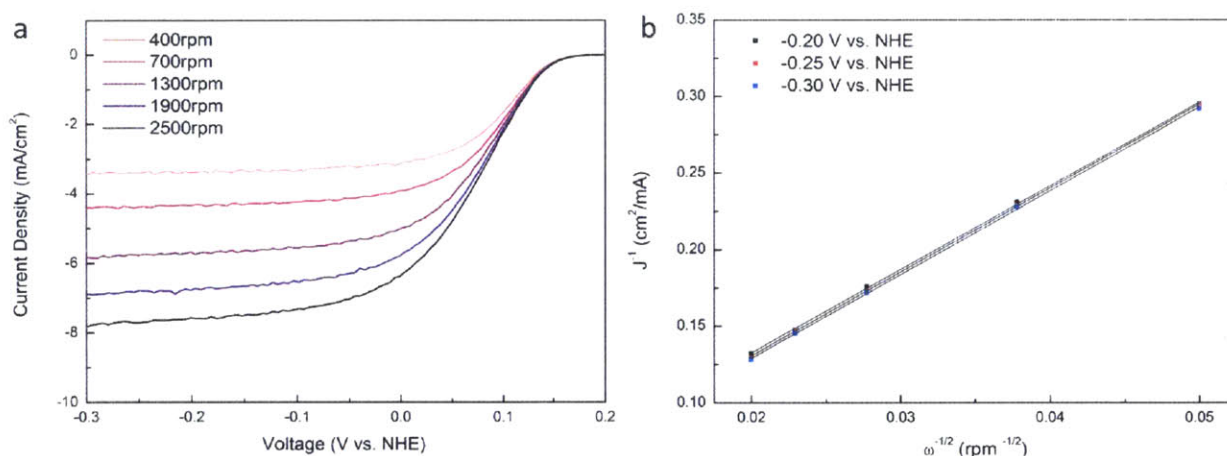
−0.2 V to −0.3 V, and the *meta*-isomer showed slightly reduced current. The *ortho*-isomer exhibited significantly lower current density compared to other samples, which was predicted from the restricted configuration of its pyridyl group for the coordination to FePc (Figure 6.6). According to the DFT calculation results, the *meta*- and *para*-isomers have suitable geometry to coordinate to the axial position of FePc. An interesting result was the unexpectedly high current observed with the non-covalent control sample (DW in Figure 6.14). Unlike the poor activities of macrocycle/pristine CNT composites reported in the literature, the considerable current density obtained with our FePc/DWCNT composite suggests facile oxygen reduction via efficient electron transfer between DWCNT and FePc. Since the non-covalent interaction serves as one of the major components to facilitate electron transfer, the additional effect of axial coordination to FePc was not as significant as expected, and only marginal improvement was made by varying the pyridyl group density on CNTs. For the *ortho*-isomer, even lower current was obtained by increasing the functional group density on CNTs.

Figure 6.14. Linear sweep voltammograms of oxygen reduction electrocatalysis measured at a constant rotation speed of 2500 rpm.



We further analyzed the performance of the catalysts by varying the rotation speed of RDE as shown in Figure 6.15. From the K–L plot, we obtained n of 3.9 for *p*-pyridyl, 3.8 for *m*-pyridyl, 3.0 for *o*-pyridyl derivative, and 3.4 for the non-covalent composite (DW) as the number of electrons involved in the oxygen reduction. Further investigation on peroxide production by RRDE experiment, long-term stability, and resistance toward carbon monoxide or methanol poisoning will be the focus of continuing research, and mechanistic studies of ORR in the system will be conducted.

Figure 6.15. (a) A representative linear sweep voltammogram of oxygen reduction electrocatalysis measured at various rotation speeds and (b) K–L plot for *p*-pyridyl isoxazoline-functionalized DWCNT/FePc composite.



6.3. Conclusions

We synthesized a series of covalently-functionalized DWCNTs bearing ligand moieties for cobalt or iron complexation by simple and efficient mechanochemical method. The generated catalysts exhibited enhanced ORR electrocatalytic activity relative to that of the non-covalent system or that of Pt/C standard. It is demonstrated that electron transfer is facilitated between the covalently linked conductive nanocarbon and the catalytic active site. The number of electrons

that participate in the reduction process is estimated to be 3.6 for the DWbpy–Co²⁺ catalyst and 3.9 for the *p*-pyridyl DWCNT/FePc composite, which represents a preferred 4-electron reduction pathway to water rather than a 2-electron reduction to peroxide species for both catalysts. ORR exhibits dependence on the relative configuration of the isomeric pyridyl groups attached to carbon nanotubes, which is correlated to the coordination capability of the ligand to the FePc axial position. Further studies on the long-term stability and the optimization of catalytic system are expected to continue based on the preliminary results presented in this chapter.

6.4. Experimental Section

Materials. SWCNT (carbon > 90%, SWCNT > 77%, (6,5) chirality) and DWCNT (carbon > 90%, DWCNT 50–80%) were purchased from Sigma–Aldrich. MWCNT (carbon 98%, 3–6 walls) were purchased from SouthWest Nanotechnologies. Platinum on graphitized carbon (Pt/C) purchased from Sigma–Aldrich contains 20 wt% Pt nanoparticles (<5 nm) on Vulcan XC72. Nafion (ca. 5%) in a mixture of low aliphatic alcohols and water was purchased from Sigma–Aldrich. Oxygen gas was purchased from Airgas. All other main chemicals were purchased from Sigma–Aldrich and used as received. Other materials including electrolyte salts were commercially available. Purified water was obtained from Barnstead Nanopure Diamond Water Purification Systems. Anhydrous solvents were obtained from a solvent purification system (Innovative Technologies). The membrane filters (fluoropore PTFE 0.2 μm and polypropylene 0.6 μm) were purchased from EMD Millipore.

Measurements. ¹H NMR spectra were recorded on Varian Inova-500 spectrometers. Chemical shifts were reported in ppm and referenced to residual solvent peaks (DMSO-d₆: 2.50 ppm, DMF-d₇: 8.02 ppm) Electrochemical measurements were carried out under atmospheric

condition using an Autolab PGSTAT 10 or PGSTAT 20 potentiostat (Eco Chemie) in a three-electrode cell configuration. A Pt wire and Ag/AgCl electrode (1 M KCl, CH Instruments) were used as a counter electrode and a reference electrode, respectively, in 0.1 M KOH solution. Hg/HgO electrode (1 M NaOH) was also used as a reference electrode for more reliable results in the alkaline media. Rotating disk electrode (glassy carbon disk, 2.5 mm diameter) and rotating ring-disk electrode (glassy carbon disk, 5.61 mm outer diameter, and platinum ring, 6.25 mm inner and 7.92 mm outer diameter, 320 μm ring–disk gap, 37% collection efficiency) (Pine Instrument Company) were used as working electrodes. Raman spectra were measured on a Horiba LabRAM HR Raman Spectrometer using the excitation wavelengths of 633 and 785 nm. XPS spectra were obtained by a Versaprobe II X-ray Photoelectron Spectrometer.

DFT Calculations. DFT calculations were performed using the Vienna Ab initio Simulation Packages (VASP)³⁸ with the generalized gradient approximation of Perdew-Burke-Ernzerhof (PBE)³⁹ for the exchange and correlation functional. The projector-augmented-wave method was adopted to describe the core electrons. A Monkhorst-Pack k-point sampling of 1X1X3 and an energy cutoff of 400eV were used. A large vacuum spacing of > 15 Å (in x- and y-directions, both CNT radial) was used to prevent spurious interactions between adsorbate and CNT. CNT bearing the adsorbate was fully relaxed using the conjugate gradient method until the energy difference between two consecutive ionic steps is less than 10^{-4} eV.

Synthesis of o-Pyridinecarbohydroximoyl Chloride. 2-Pyridylamidoxime (5.0 g, 36.5 mmol) was dissolved in 100 mL water at 0 °C, and 37.5 mL of concentrated hydrochloric acid was added. Sodium nitrate (3.0 g, 43.8 mmol) in 18 mL of water was added dropwise to the stirred solution,

and after 2 h sodium bicarbonate (about 30 g) was slowly added until pH 4 was reached. The white precipitate was filtered, washed with cold water, and dried under vacuum. The product was obtained in 92 % yield (5.22 g).

Synthesis of m-Pyridinecarbohydroximoyl Chloride. 3-Pyridylamidoxime (1.22 g, 10.0 mmol) was dissolved in 10 mL DMF, and *N*-chlorosuccinimide (1.36 g, 10.2 mmol) was added portion-wise to solution. The solution was heated at 60 °C for 30 min and then cooled in an ice bath. The precipitate was filtered and dried, and the product was obtained in 25 % yield (0.39 g).

Synthesis of p-Pyridinecarbohydroximoyl Chloride. 4-Pyridylamidoxime (0.98 g, 8.0 mmol) was dissolved in 10 mL DMF, and *N*-chlorosuccinimide (1.1 g, 8.2 mmol) was added portion-wise to solution. The solution was heated at 60 °C for 90 min, and cooled to room temperature. 400 mL of cold water was added to solution, and the precipitate was filtered and dried. The product was obtained in 40 % yield (0.50 g).

Synthesis of Bipyridinecarbohydroximoyl Chloride. 2,2'-Bipyridine-6-carbaldehyde oxime (0.85 g, 4.27 mmol) was dissolved in 15 mL DMF, and *N*-chlorosuccinimide (0.93 g, 6.9 mmol) was added portion-wise to solution. The solution was heated at 60 °C for 30 min, and stirred for 4 h at room temperature. Cold water was added to solution, and the precipitate was filtered and dried. The product was obtained in 88 % yield (0.88 g).

Pristine CNT Purification Procedures. Carbon nanotubes were treated with 3 M nitric acid in water under reflux condition for 15 hours. After the acid treatment, the solution was diluted with water, and the carbon nanotubes precipitated. The clear supernatant was decanted multiple times

and the solution was diluted again with water until the solution became neutral (pH 6–7). CNTs were then filtered on a hydrophilic membrane (Milipore, mixed cellulose esters) and dried under reduced pressure at 200 °C overnight.

Solution-State Functionalization of CNTs. In a flame-dried Schlenk flask, DWCNT (18 mg, 0.75 mmol of 2C) was dispersed in anhydrous DMF (40 mL) and sonicated for 2 h under Ar. Hydroximoyl chloride derivatives (7.5 mmol) in 10 mL DMF and triethylamine (0.88 ml, 7.5 mmol) in 20 mL DMF were concomitantly added drop-wise to the CNT dispersion at 80 °C over 6 h. The reaction mixture was stirred at 80 °C overnight, and 500 mL of ethanol was added to precipitate the CNTs. The precipitate was filtered on a fluoropore PTFE membrane (0.2 μm) and rinsed with copious ethanol/water, acetone/water, ethyl acetate, dichloromethane, and hexane to remove any byproducts and/or unreacted reagents. The product was dried under vacuum at 100 °C overnight. 10–20 mg of functionalized CNT was obtained depending on the extent of purification.

Mechanochemical Functionalization of CNTs. In a stainless-steel or zirconium jar (10 mL), DWCNT (15 mg, 0.625 mmol of 2C), hydroximoyl chloride derivatives (0.78 mmol), and NaHCO₃ (0.78 mmol) were added with two balls and shaken with a constant frequency for 10–30 min. The reaction mixture was transferred to a 50 mL centrifuge tube filled with methanol and water. After 5 min sonication, the mixture was centrifuged for 20 min, and the supernatant was carefully removed. After 2 or 3 cycles of dispersion, sonication, and centrifugation, the CNT was filtered on a polypropylene hydrophobic membrane (0.6 μm) and rinsed with copious methanol/water, acetone/water, acetone, ethyl acetate, and dichloromethane. The product was

dried under vacuum at 100 °C overnight. 10–20 mg of CNT was obtained depending on the extent of purification.

One-Pot Functionalization of CNTs. For both solution-state and mechanochemical methods, oxime derivatives instead of hydroximoyl chloride derivatives can be used in combination with equimolar *N*-chlorosuccinimide (NCS) or *N*-bromosuccinimide (NBS) to generate nitrile oxide intermediates. For solution-state reactions, NBS was mixed with oxime and added drop-wise to the CNT dispersion while triethylamine was concomitantly added. For ball-mill process, NCS was added to the reactor with oxime and NaHCO₃ before the reaction. The yield of the one-pot synthesis was comparable to that of the analogous reaction starting from hydroximoyl chloride.

Preparation of CNT–Metal Complexes. For cobalt chelation project, excess cobalt(II) acetate, chloride, tetrafluoroborate, or perchlorate salts dissolved in acetone or ethanol were mixed with functionalized CNTs dispersed and sonicated (5 min) in dichloromethane. The mixture was stirred at 40 °C overnight and filtered on a PTFE membrane. After rinsing with acetone, ethanol, and dichloromethane, the CNT sample was dried under vacuum at 40 °C overnight. For macrocycle coordination project, iron(II) phthalocyanine was mixed with CNTs (by weight ratio of 1:2) in dichloromethane, sonicated for 10–15 min, and dried under atmospheric conditions.

Preparation of CNT Ink and CNT Films. CNT samples in powder were first added to aqueous isopropanol solution (H₂O and *i*PrOH in 2.5:1 volume ratio) containing 0.5 wt % Nafion and sonicated for 10–15 min to make dispersion in 4 mg/mL concentration. Pt/C standard was also prepared in solution with 4 mg/mL concentration. Glassy carbon (GC) disk electrode and GC/Pt

ring-disk electrode were polished with alumina slurry (with 0.05, 0.3, 1.0 μm particles in sequence) and washed with water and acetone to obtain a mirror-like surface prior to CNT ink deposition. 12.5 μL of ink was drop-casted onto a GC disk electrode, and 17.5 μL of ink was drop-casted on the GC disk of a ring-disk electrode. After drying under nitrogen gas flow, uniform films covering the entire surface of GC disk were formed.

6.5. References and Notes

1. Rajashekara, K.: Hybrid fuel-cell strategies for clean power generation. *IEEE Trans. Ind. Appl.* **2005**, *41*, 682-689.
2. Gewirth, A. A.; Thorum, M. S.: Electroreduction of Dioxygen for Fuel-Cell Applications: Materials and Challenges. *Inorg. Chem.* **2010**, *49*, 3557-3566.
3. Gasteiger, H. A.; Panels, J. E.; Yan, S. G.: Dependence of PEM fuel cell performance on catalyst loading. *J. Power Sources* **2004**, *127*, 162-171.
4. Bashyam, R.; Zelenay, P.: A class of non-precious metal composite catalysts for fuel cells. *Nature* **2006**, *443*, 63-66.
5. Lefèvre, M.; Proietti, E.; Jaouen, F.; Dodelet, J.-P.: Iron-Based Catalysts with Improved Oxygen Reduction Activity in Polymer Electrolyte Fuel Cells. *Science* **2009**, *324*, 71-74.
6. Jasinski, R.: A New Fuel Cell Cathode Catalyst. *Nature* **1964**, *201*, 1212-1213.
7. Collman, J. P.; Anson, F. C.; Barnes, C. E.; Bencosme, C. S.; Geiger, T.; Evitt, E. R.; Kreh, R. P.; Meier, K.; Pettman, R. B.: Further studies of the dimeric .beta.-linked "face-to-face four" porphyrin: FTF4. *J. Am. Chem. Soc.* **1983**, *105*, 2694-2699.
8. Durand, R. R.; Bencosme, C. S.; Collman, J. P.; Anson, F. C.: Mechanistic aspects of the catalytic reduction of dioxygen by cofacial metalloporphyrins. *J. Am. Chem. Soc.* **1983**, *105*, 2710-2718.

9. Chang, C. J.; Baker, E. A.; Pistorio, B. J.; Deng, Y.; Loh, Z.-H.; Miller, S. E.; Carpenter, S. D.; Nocera, D. G.: Structural, Spectroscopic, and Reactivity Comparison of Xanthene- and Dibenzofuran-Bridged Cofacial Bisporphyrins. *Inorg. Chem.* **2002**, *41*, 3102-3109.
10. Yuasa, M.; Yamaguchi, A.; Itsuki, H.; Tanaka, K.; Yamamoto, M.; Oyaizu, K.: Modifying Carbon Particles with Polypyrrole for Adsorption of Cobalt Ions as Electrocatalytic Site for Oxygen Reduction. *Chem. Mater.* **2005**, *17*, 4278-4281.
11. Gupta, S.; Tryk, D.; Bae, I.; Aldred, W.; Yeager, E.: Heat-treated polyacrylonitrile-based catalysts for oxygen electroreduction. *J. Appl. Electrochem.* **1989**, *19*, 19-27.
12. Dignard-Bailey, L.; Trudeau, M. L.; Joly, A.; Schulz, R.; Lalande, G.; Guay, D.; Dodelet, J. P.: Graphitization and particle size analysis of pyrolyzed cobalt phthalocyanine/carbon catalysts for oxygen reduction in fuel cells. *J. Mater. Res.* **1994**, *9*, 3203-3209.
13. Scherson, D. A.; Gupta, S. L.; Fierro, C.; Yeager, E. B.; Kordesch, M. E.; Eldridge, J.; Hoffman, R. W.; Blue, J.: Cobalt tetramethoxyphenyl porphyrin—emission Mossbauer spectroscopy and O₂ reduction electrochemical studies. *Electrochim. Acta* **1983**, *28*, 1205-1209.
14. Cao, R.; Thapa, R.; Kim, H.; Xu, X.; Gyu Kim, M.; Li, Q.; Park, N.; Liu, M.; Cho, J.: Promotion of oxygen reduction by a bio-inspired tethered iron phthalocyanine carbon nanotube-based catalyst. *Nat. Commun.* **2013**, *4*, 2076.
15. Wei, P.-J.; Yu, G.-Q.; Naruta, Y.; Liu, J.-G.: Covalent Grafting of Carbon Nanotubes with a Biomimetic Heme Model Compound To Enhance Oxygen Reduction Reactions. *Angew. Chem. Int. Ed.* **2014**, *53*, 6659-6663.
16. Yurovskaya, M. A.; Trushkov, I. V.: Cycloaddition to buckminsterfullerene C-60: advancements and future prospects. *Russ. Chem. Bull.* **2002**, *51*, 367-443.
17. Alvaro, M.; Atienzar, P.; de la Cruz, P.; Delgado, J. L.; Troiani, V.; Garcia, H.; Langa, F.; Palkar, A.; Echegoyen, L.: Synthesis, Photochemistry, and Electrochemistry of Single-Wall Carbon Nanotubes with Pendent Pyridyl Groups and of Their Metal Complexes with Zinc Porphyrin. Comparison with Pyridyl-Bearing Fullerenes. *J. Am. Chem. Soc.* **2006**, *128*, 6626-6635.

18. Ramírez-Monroy, A.; Swager, T. M.: Metal Chelates Based on Isoxazoline[60]fullerenes. *Organometallics* **2011**, *30*, 2464-2467.
19. Hirsch, A.; Vostrowsky, O.: Functionalization of carbon nanotubes. *Top Curr. Chem.* **2005**, *245*, 193-237.
20. James, S. L.; Adams, C. J.; Bolm, C.; Braga, D.; Collier, P.; Friscic, T.; Grepioni, F.; Harris, K. D. M.; Hyett, G.; Jones, W.; Krebs, A.; Mack, J.; Maini, L.; Orpen, A. G.; Parkin, I. P.; Shearouse, W. C.; Steed, J. W.; Waddell, D. C.: Mechanochemistry: opportunities for new and cleaner synthesis. *Chem. Soc. Rev.* **2012**, *41*, 413-447.
21. Wang, G.-W.: Mechanochemical organic synthesis. *Chem. Soc. Rev.* **2013**, *42*, 7668-7700.
22. Stolle, A.; Szuppa, T.; Leonhardt, S. E. S.; Ondruschka, B.: Ball milling in organic synthesis: solutions and challenges. *Chem. Soc. Rev.* **2011**, *40*, 2317-2329.
23. Zhu, S.-E.; Li, F.; Wang, G.-W.: Mechanochemistry of fullerenes and related materials. *Chem. Soc. Rev.* **2013**, *42*, 7535-7570.
24. Yu, Z.-X.; Caramella, P.; Houk, K. N.: Dimerizations of Nitrile Oxides to Furoxans Are Stepwise via Dinitrosoalkene Diradicals: A Density Functional Theory Study. *J. Am. Chem. Soc.* **2003**, *125*, 15420-15425.
25. Dresselhaus, M. S.; Dresselhaus, G.; Saito, R.; Jorio, A.: Raman spectroscopy of carbon nanotubes. *Phys. Rep.* **2005**, *409*, 47-99.
26. Dresselhaus, M. S.; Dresselhaus, G.; Jorio, A.; Souza Filho, A. G.; Saito, R.: Raman spectroscopy on isolated single wall carbon nanotubes. *Carbon* **2002**, *40*, 2043-2061.
27. Tammeveski, K.; Tenno, T.; Claret, J.; Ferrater, C.: Electrochemical reduction of oxygen on thin-film Pt electrodes in 0.1 M KOH. *Electrochim. Acta* **1997**, *42*, 893-897.
28. Mayrhofer, K. J. J.; Strmcnik, D.; Blizanac, B. B.; Stamenkovic, V.; Arenz, M.; Markovic, N. M.: Measurement of oxygen reduction activities via the rotating disc electrode method: From Pt model surfaces to carbon-supported high surface area catalysts. *Electrochim. Acta* **2008**, *53*, 3181-3188.

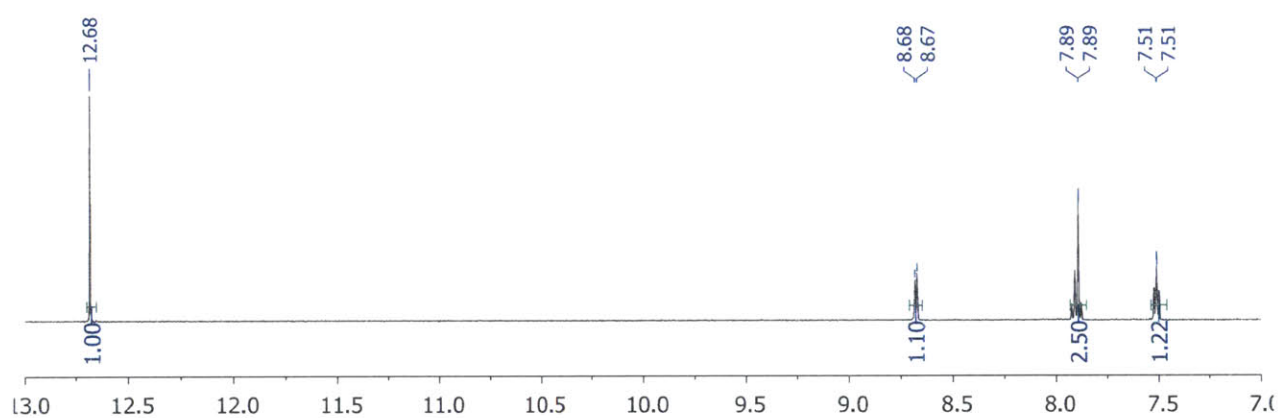
29. Davis, R. E.; Horvath, G. L.; Tobias, C. W.: The solubility and diffusion coefficient of oxygen in potassium hydroxide solutions. *Electrochim. Acta* **1967**, *12*, 287-297.
30. Paulus, U. A.; Schmidt, T. J.; Gasteiger, H. A.; Behm, R. J.: Oxygen reduction on a high-surface area Pt/Vulcan carbon catalyst: a thin-film rotating ring-disk electrode study. *J. Electroanal. Chem.* **2001**, *495*, 134-145.
31. Chen, R.; Li, H.; Chu, D.; Wang, G.: Unraveling Oxygen Reduction Reaction Mechanisms on Carbon-Supported Fe-Phthalocyanine and Co-Phthalocyanine Catalysts in Alkaline Solutions. *J. Phys. Chem. C* **2009**, *113*, 20689-20697.
32. Li, W.; Yu, A.; Higgins, D. C.; Llanos, B. G.; Chen, Z.: Biologically Inspired Highly Durable Iron Phthalocyanine Catalysts for Oxygen Reduction Reaction in Polymer Electrolyte Membrane Fuel Cells. *J. Am. Chem. Soc.* **2010**, *132*, 17056-17058.
33. Meier, H.; Tschirwitz, U.; Zimmerhackl, E.; Albrecht, W.; Zeitler, G.: Application of radioisotope techniques for the study of phthalocyanine catalyzed electrochemical processes in fuel cells. *J. Phys. Chem.* **1977**, *81*, 712-718.
34. van der Putten, A.; Elzing, A.; Visscher, W.; Barendrecht, E.: Redox potential and electrocatalysis of O₂ reduction on transition metal chelates. *J. Electroanal. Chem. Interfacial Electrochem.* **1987**, *221*, 95-104.
35. Baranton, S.; Coutanceau, C.; Roux, C.; Hahn, F.; Léger, J. M.: Oxygen reduction reaction in acid medium at iron phthalocyanine dispersed on high surface area carbon substrate: tolerance to methanol, stability and kinetics. *J. Electroanal. Chem.* **2005**, *577*, 223-234.
36. Baker, R.; Wilkinson, D. P.; Zhang, J.: Facile synthesis, spectroscopy and electrochemical activity of two substituted iron phthalocyanines as oxygen reduction catalysts in an acidic environment. *Electrochim. Acta* **2009**, *54*, 3098-3102.
37. Milev, A. S.; Tran, N.; Kamali Kannangara, G. S.; Wilson, M. A.; Avramov, I.: Polymorphic Transformation of Iron-Phthalocyanine and the Effect on Carbon Nanotube Synthesis. *J. Phys. Chem. C* **2008**, *112*, 5339-5347.

38. Kresse, G.; Furthmüller, J.: Efficiency of ab-initio total energy calculations for metals and semiconductors using a plane-wave basis set. *Comput. Mater. Sci.* **1996**, *6*, 15-50.

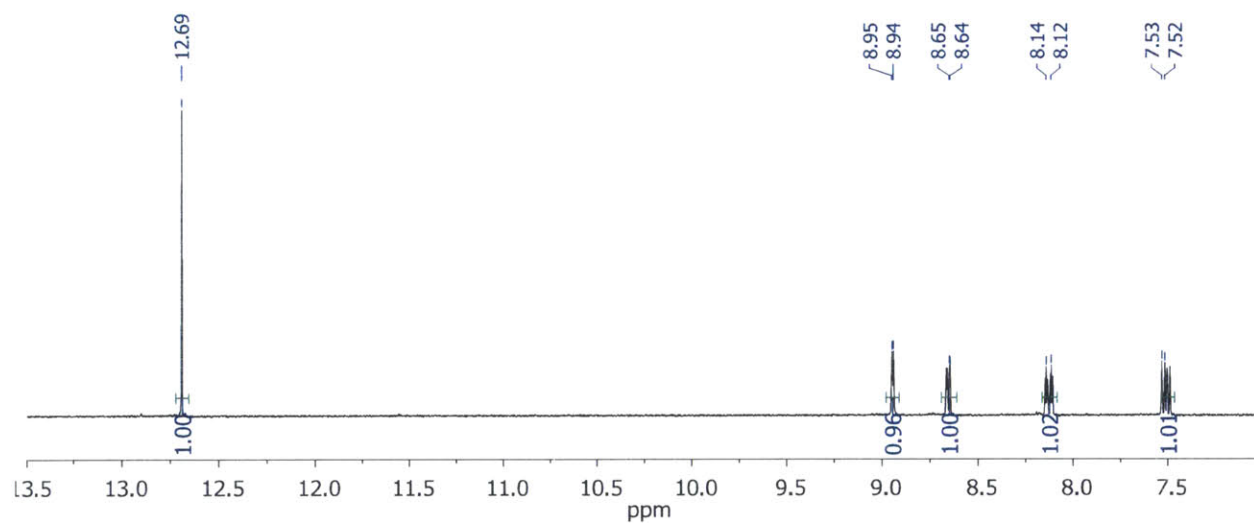
39. Perdew, J. P.; Burke, K.; Ernzerhof, M.: Generalized Gradient Approximation Made Simple. *Phys. Rev. Lett.* **1996**, *77*, 3865-3868.

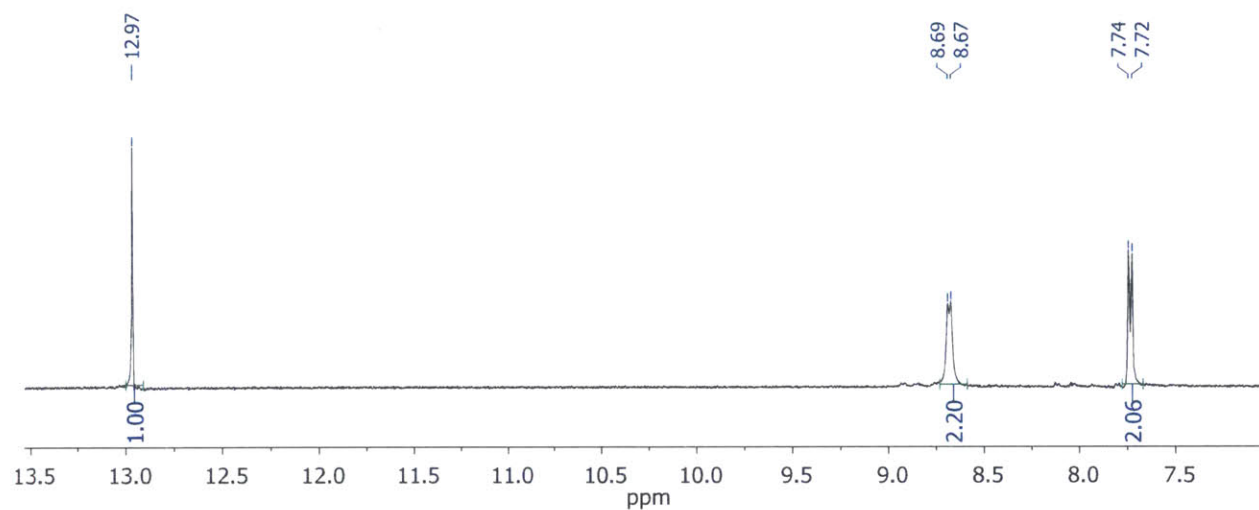
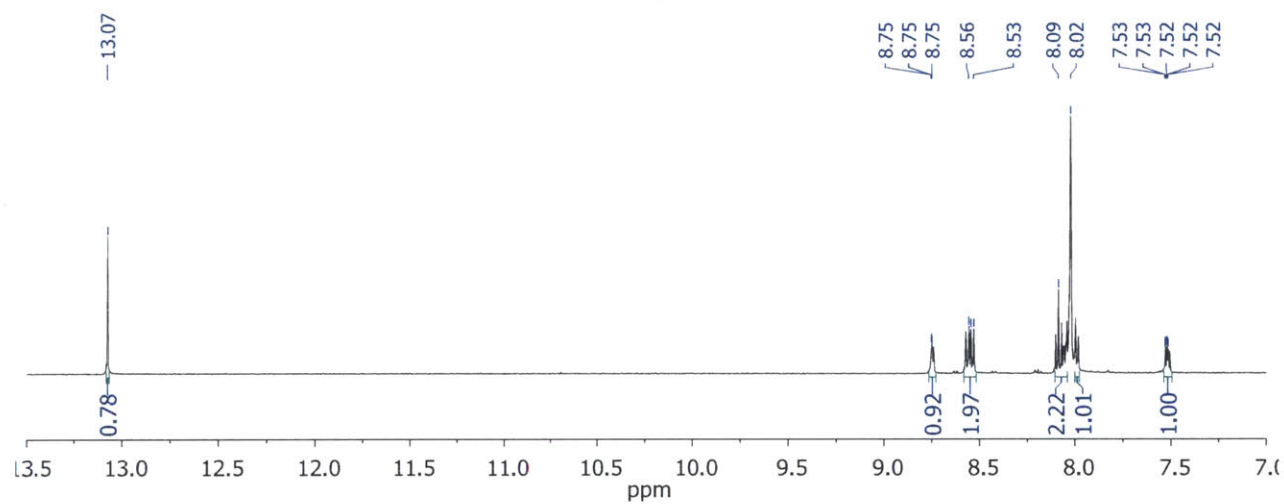
6.6. Appendix

Spectrum 6.1. ^1H NMR of *o*-pyridinecarbohydroximoyl chloride in $\text{DMSO-}d_6$.



Spectrum 6.2. ^1H NMR of *m*-pyridinecarbohydroximoyl chloride in $\text{DMSO-}d_6$.



Spectrum 6.3. ^1H NMR of *p*-pyridinecarbohydroximoyl chloride in $\text{DMSO-}d_6$.**Spectrum 6.4.** ^1H NMR of bipyridylamidochloride in $\text{DMF-}d_7$.

Ggoch Ddeul (Grace) Han

77 Massachusetts Avenue, 18-014
Cambridge, MA 02139
617-599-2257
gracehan@mit.edu

EDUCATION

Massachusetts Institute of Technology (MIT), Cambridge, MA

Ph.D. in Inorganic Chemistry GPA: 4.9/5.0 2010-2015

Pohang University of Science and Technology (POSTECH), Pohang, South Korea

Bachelor of Science in Chemistry, summa cum laude GPA: 4.1/4.3 2006-2010

University of California at Berkeley (UC Berkeley), Berkeley, CA

Exchange Program in Chemistry GPA: 3.6/4.0 2008-2009

AWARDS AND FELLOWSHIPS

MIT Energy Initiative Graduate Student Travel Funds 2013
Departmental Nominee for Collamore-Rogers Fellowship 2013
Department of Chemistry Award for Outstanding Teaching at MIT 2012
Robert T. Haslam Presidential Fellowship at MIT 2010
Korea Presidential Scholarship for Outstanding Science & Engineering Students 2006-2009

RELEVANT SKILLS

Instrument Thermal evaporator, Spin coater, Solar simulator, XPS, XRD, Raman, FT-IR, UV-Vis absorption and fluorescence spectroscopy, Profilometer, Four point probe, TGA, DSC, MALDI-TOF, NMR, HPLC, Glove box usage and maintenance, Electrochemical potentiostat, Rotating electrode system, etc.
Software Gaussian (DFT calculation), Autodesk 3dsMax

RESEARCH EXPERIENCE

Research projects with Prof. Timothy M. Swager at MIT 2010-2015

Designed and synthesized n-type materials and fabricated organic and hybrid photovoltaics

- Project 1: Fullerene-based electron acceptors with high LUMOs for bulk-heterojunction organic solar cells
 - Covalently functionalized fullerenes with cyclobutadiene moieties by Diels–Alder cycloaddition
 - Characterized electrochemical, photophysical, and thermal properties of the new materials
- Project 2: Fullerene-based electron transporting materials for perovskite solar cells
 - Synthesized isobenzofulvene-functionalized fullerenes and their epoxide derivatives
 - Fabricated $\text{CH}_3\text{NH}_3\text{PbI}_{3-x}\text{Cl}_x$ perovskite solar cells with fullerene electron transporting layers
- Project 3: Donor–acceptor interfacial additives for low-bandgap polymer solar cells
 - Synthesized benzyne–fullerene adducts with various functional groups
 - Fabricated and characterized bulk-heterojunction solar cells with fullerenes additives
- Project 4: Templating fullerenes by domain boundaries of a nanoporous network
 - Studied the interaction of fullerenes with nanoporous networks by STM
 - Explored the behaviors of various fullerenes used as common electron acceptors for photovoltaics
- Project 5: Electrocatalysis of oxygen reduction by carbon nanotubes/transition metal complex hybrid
 - Covalently functionalized carbon nanotubes with organic ligands and transition metal complexes
 - Characterized oxygen reduction reaction using rotating electrode system

Undergraduate research project with Prof. Jeffrey R. Long at UC Berkeley 2009
Synthesized and characterized metal–organic frameworks incorporating 1,3,5-Benzenetripyrazole

TEACHING AND LEADERSHIP

- Teaching Certificate Program at MIT* 2014
- Participated in classes and microteaching sessions on STEM education offered by Teaching and Learning Laboratory at MIT
- Head teaching assistant for Organic Chemistry I (5.12)* 2012 Fall
- Organized interactive teaching methods, conducted recitations, exam preparation, proctoring, and grading
- Teaching assistant for Principles of Chemical Science (5.112)* 2011 Fall
- Conducted recitations, exam proctoring, exam grading and problem set grading
- Team leader of nanocarbon subgroup in Swager group* 2011-2013
- Organized weekly meetings on literature discussion and research updates

PROFESSIONAL ACTIVITIES

- Contributor of SYNFACTS – Synthesis of Materials and Unnatural Products* 2010-2011
- Highlighted latest research and commented on the significance of the work for 12 volumes of the journal
- Session Chair at 2014 MRS Fall Meeting & Exhibit – Design of Organic Electronic Materials II (Q7)* 2014

PUBLICATIONS

- S. Chang†, **G. D. Han**†, J. G. Weis, H. Park, S. Gradečak, and T. M. Swager. New Organic Charge Transport Layer for Transition Metal Oxide Free- Perovskite Solar Cells. *ACS Nano*. Under Review. †Equal Contribution.
- G. D. Han**†, A. Maurano†, J. G. Weis, V. Bulović, and T. M. Swager. V_{OC} Enhancement in Polymer Solar Cells with Isobenzofulvene- C_{60} Adducts. *In Preparation*. †Equal Contribution.
- D. den Boer, **G. D. Han**, and T. M. Swager. Templating Fullerenes by Domain Boundaries of a Nanoporous Network. *Langmuir* **2014**, 762-767.
- G. D. Han**, W. R. Collins, T. L. Andrew, V. Bulović, and T. M. Swager. Cyclobutadiene- C_{60} Adducts: N-Type Materials for Organic Photovoltaic Cells with High V_{OC} . *Adv. Funct. Mater.* **2013**, 23, 3061-3069.
- V. Colombo, S. Galli, H. J. Choi, **G. D. Han**, A. Maspero, G. Palmisano, N. Masciocchi and J. R. Long. High thermal and chemical stability in pyrazolate-bridged metal-organic frameworks with exposed metal sites. *Chem. Sci.* **2011**, 2, 1311-1319.

PATENTS

- G. D. Han**, S. Chang, S. Gradečak, and T. M. Swager. Devices Including Photovoltaic Devices and Functionalize-d Nanostructures. U.S. Provisional Application No. 62/140,242.
- G. D. Han**, A. Maurano, R. Po, A. Pellegrino, V. Bulović, and T. M. Swager. Functionalized Fullerenes for Enhanced Photovoltaic Efficiency. PCT/US2015/026379.
- G. D. Han**, T. L. Andrew, V. Bulović, and T. M. Swager. Functionalized Nanostructures and Related Devices. PCT/US2013/029079, WO2014/062213. European Patent 138471537.

PRESENTATIONS

- G. D. Han**, A. Maurano, J. G. Weis, V. Bulović, and T. M. Swager. Efficiency Enhancement of Polymer Solar Cells by Diels-Alder Fullerene Modification. *2014 MRS Spring Meeting & Exhibit*, San Francisco, CA, April 21-25, **2014**.
- G. D. Han** and T. M. Swager. Covalently Functionalized Carbon Nanotubes for Electrocatalytic Oxygen Reduction Reaction. *245th ACS National Meeting*, New Orleans, LA, April 7-11, **2013**.
- G. D. Han**, W. R. Collins, T. L. Andrew, V. Bulović, and T. M. Swager. Cyclobutadiene- C_{60} Adducts: N-Type Materials for Organic Photovoltaic Cells with High V_{OC} . *2013 MRS Spring Meeting & Exhibit*, San Francisco, CA, April 1-5, **2013**.
- J. M. Schnorr, **G. D. Han**, A. Ramirez-Monroy, T. M. Swager. Functionalized Carbon Nanotubes as Soluble Molecular Wires. *International Symposium on Advancing the Chemical Science – Challenges in Renewable Energy (ISACS4)*, Boston, MA, July 5-8, **2011**.

Acknowledgements

First of all, I would like to express my deepest appreciation to Prof. Tim Swager for his guidance, support, and hearty care for the past years. Tim has shown how to conduct creative and honorable research, how to respect and lead people, how to deal with challenges, and how to contribute to society by his own examples. He has been always encouraging, particularly during the hard times, and led me to find my own answers and to grow stronger. I truly enjoyed being a member of his group and a TA for his class, and I'm grateful for the countless opportunities that he has provided. I will always remember his mentorship and will be proud to be a Swager graduate.

I would like to thank all of the faculty members in the inorganic chemistry division, particularly Prof. Mircea Dincă and Prof. Steve Lippard for their guidance during my coursework, oral exams, and annual meetings. Prof. Dincă has inspired my research from the undergraduate years and continuously provided a broad perspective encompassing inorganic and materials chemistry. Prof. Lippard has been a great model for an excellent teacher, and his enthusiasm for teaching has inspired me as a student and a TA for his classes.

Prof. Vladimir Bulović has been a great mentor for my solar cell research through our collaborations. Without his generous support, the completion of my projects would have not been possible. Prof. Silvija Gradečak has given significant guidance for our collaboration on perovskite solar cells, and I would like to thank her for the support.

I would like to thank Prof. Jeffrey Long and Prof. Sung-Kee Chung for the opportunities to work in their groups as an undergraduate student and for their tremendous support on my way to a graduate school. I appreciate my undergraduate academic advisor, Prof. Mahn-Joo Kim, who has given critical guidance and advice on my career decisions.

Working on the boundaries of chemistry and engineering, I was fortunate to collaborate with many of the exceptionally talented colleagues making great teams. I would like to thank Dr. Andrea Maurano for leading me to the solar cell world and for his devotion to our projects. I feel grateful to have a chance to work with Dr. Sehoon Chang who has provided wise advice on science and a listening ear for life challenges. I thank my fellow Jon Weis who has contributed to essential parts of my research and has given kind help when it is the most needed. Dr. Duncan den Boer has been a good friend and a mentor, and it was a pleasant experience to work with him and to share the moments of cuteness of Julius. I thank other collaborators who have made my journey more enjoyable and the fullest: Byungjin, Georgios, Jisun, Sébastien, Yoshi, Tran, Donghun, Bill, Trisha, Hyoungwon, Carlos Z., John F., David B., Sophie, and Lauren. In addition, I would like to thank Patrick, Joel, Farnaz, Apoorva, and Anna for their openness and significant help at onelab, Lionel for being the master guardian of TGA and DSC, and Dr. Peter Mueller for his guidance at the X-ray facility. I gratefully acknowledge Eni S.p.A. under the Eni-MIT alliance solar frontiers program for providing funding for all of my projects.

The Swager group has been the best place to interact with talented people with great mind. I would like to thank Jon, Kelvin, and John in my year for supporting each other through many challenges. I appreciate all of my past and present office and bay mates including Becca, Shuang, Jan, Jose, Jeewoo, Balta, Kat, Sébastien, Olesya, Duncan, Sophie, Derik, Silvia, Joe W., Julia, Sibó, Graham, and Maggie for the unforgettable memories and laughter in the basement. I would like to thank the fellow captains and members of NanoC and Excitons subgroups for the great discussions, particularly during the CPR (critical problems of research) sessions which have been incredible. Even with a large number of members, the Swager group has been running as one body thanks to the efforts of Kathy, Caitlin, Brian, and Joe, and I can't thank them enough. I would like to give special thanks to Sarah, Kelvin, and Jon for helping me on my practice talk and interview, and to Greg, Julia, Sophie, Byungjin, Georgios, and Sarah for their amazing help on proofreading my thesis. Lastly I thank Bora, Jisun, Byungjin, and Intak for sharing difficult moments and recovery food together and for being cheerful friends. I'm so grateful that I have met great colleagues and have made friends through this invaluable experience in the team.

I appreciate all my friends out of the lab including Bonjun, Hyangsoo, Woonju, Jon A., Mik, Mike, Miller, Carl, Sarah P., Hong Geun, and Suheol in the department of chemistry for their support and our fun times together. I would like to thank my Korean friends in the same year and in the 1988 group who have made my life as a graduate student much more interesting. My special thanks go to my dearest friends Hyangsoo, Bonjun, Bora, and Daryl for their unconditional friendship and for sharing countless moments of joy and sorrow for the past years. I would have never been able to go through this journey without you.

마지막으로 한국에 계신 부모님께 모든 감사를 바칩니다. 학업과 진로 뿐 아니라 인생의 많은 부분에서 제가 독립적으로 결정을 내릴 수 있게 믿고 존중해 주셔서, 또한 아낌없는 응원과 기도를 해주셨기에 지금의 제가 있습니다. 비록 멀리 있어서 매년 몇 주 뵙지 못하지만, 부모님의 따뜻한 격려가 항상 힘이 되었습니다. 헌신적으로 우리 가족을 이끌어오신 할머니, 우리 수아, 뉴저지에 계신 할아버지와 가족들, 모두 사랑합니다.